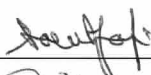
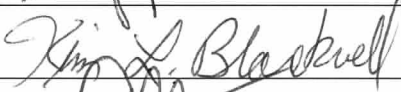

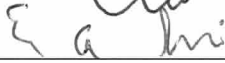

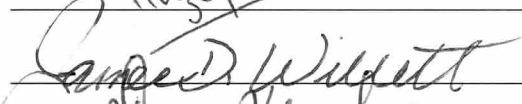

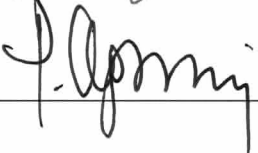


COMPUTATIONAL STUDIES OF Ca^{2+} DYNAMICS IN CARDIAC CELLS USING GPGPU

by

Hoang-Trong Minh Tuan
A Dissertation
Submitted to the
Graduate Faculty
of
George Mason University
in Partial Fulfillment of
The Requirements for the Degree
of
Doctor of Philosophy
Bioinformatics and Computational Biology

Committee:

	Dr. M. Saleet Jafri, Dissertation Director
	Dr. Avrama Blackwell, Committee Member
	Dr. Dmitri Klimov, Committee Member
	Dr. Eric Sobie, Committee Member
	Dr. Huzefa Rangwala, Committee Member
	Dr. James D. Willett, Director, School of Systems Biology
	Dr. Donna M. Fox, Associate Dean, Office of Academic Affairs and Special Programs, College of Science
	Dr. Peggy Agouris, Dean, College of Science
Date: <u>21/07/2014</u>	Summer Semester 2014 George Mason University Fairfax, VA

Computational Studies Of Ca^{2+} Dynamics In Cardiac Cells Using GPGPU

A dissertation submitted in partial fulfillment of the requirements for the degree of
Doctor of Philosophy at George Mason University

By

Hoang-Trong Minh Tuan
Master of Engineering
Chonnam National University, South Korea, 2008

Director: M. Saleet Jafri, Professor
School of System Biology
Department of Bioinformatics and Computational Biology

Summer Semester 2014
George Mason University
Fairfax, VA

© Hoang-Trong Minh Tuan 2014
All rights reserved

ACKNOWLEDGEMENTS

This dissertation presents the results of my research during the time I worked with my advisor, Professor M. Saleet Jafri, and the end of my journey in obtaining my Ph.D. There are so many people that have supported me to make this possible and an unforgettable experience. First and foremost, I want to express my sincere thanks to Saleet for his continuous support since my first days at Mason. I still remember he was the first person I met at the Department, and coincidentally, he was assigned as my temporary advisor. It went so well that I continued working with him as my academic and research advisor. I have learnt a lot from working with him, and Saleet has given me the opportunities to develop my skills and to involve in multiple projects.

Most of the results described in this dissertation would not have been possible without a close collaboration with Professor W. Jonathan Lederer, George Blair Williams, Aristide Chikando, Niall McQuaide, Karin Sipido, Stephan E. Lehnart, and Brian Hagen. I owe them a great deal of appreciation and gratitude.

I would like to expand my thanks to Professors Avrama Blackwell, Eric Sobie, Dmitri Klimov and Huzefa Rangwala for their helpful comments on my dissertation and my defense. I also want to thank Diane St. Germain and Andrea Nikoi for providing information and assistance during the years I was a student at Department of Bioinformatics and Computational Biology. My six years at George Mason has been a great time thanks to my friends and classmates, Aman Ullah, Sangeeta Shukla, Sarita Limbu, and Rashmi Kumar.

Last but not least, I would like to dedicate this dissertation to my family. First is my parents, Ba Thằng and Mẹ Nhận, who have always been with me, educating me, and giving me encouragement and inspiration. I would like to thank my two lovely siblings, my brother Vĩ and my sister Nguyệt. They are the best and I know I always have them to count on. Finally, the last three years of my Ph.D. has been wonderful with the support of my dear wife, Thùy. Thank you all very much!

Hoang-Trong Minh Tuan
George Mason University
July, 2014

TABLE OF CONTENTS

	Page
List of Tables.....	vii
List of Figures	viii
List of Abbreviations and Symbols	xii
Abstract	xiv
Chapter 1: INTRODUCTION.....	1
Abstract	1
Cardiac ventricular myocytes	3
Cellular structure	5
Cardiac calcium homeostasis	10
Calcium-induced calcium release.....	13
Local control theory: high gain and gradedness release of calcium	13
Calcium release units: calcium spark	15
General-purpose GPU (GPGPU).....	16
Scalar Processor (SP) or CUDA core	18
Streaming Multiprocessor (SM)	20
Texture Processor Cluster (TPC) to Graphics Processor Cluster (GPC)	22
Memory architecture	23
CUDA Programming model.....	25
Kernel	26
Thread hierarchy (block and grid).....	27
Warp scheduling.....	29
Review of Computational Models	30
Research Objectives	34
References	36
Chapter 2: ULTRA-FAST MARKOV-CHAIN MONTE CARLO ALGORITHM FOR CHANNEL GATING SIMULATION.....	46
Abstract	46
Introduction	48
Algorithm Development	51
Vectorized-gating of a continuous-time, discrete-state Markov chain	54

Ultra-fast Markov chain Monte-Carlo algorithm (version 1)	60
Ultra-fast Markov chain Monte-Carlo algorithm (version 2)	64
Implementation and Performance analysis	66
Appendix	68
Generate the compact-form matrix for a single cluster.	68
Generate the compact-form matrix for the heterogeneous cluster	68
Program structure	69
References	73
Chapter 3: A LOCAL CONTROL RAT VENTRICULAR MYOCYTE YIELDS NOVEL	
UNDERSTANDING OF THE MECHANISM OF CARDIAC ARRHYTHMIA AND THE NUMBER OF	
CELLS AS A TRIGGER POINT	
Abstract	78
Introduction	80
Model development	83
Calcium release site (CRU)	85
Ryanodine receptor type-2 model	86
L-type Ca^{2+} channel model	88
Na^{+} channel model	92
K^{+} channel model	97
SL pumps/exchangers	98
Background currents	98
SR pumps	99
Calcium-bound to buffers	101
Numerical Methods	101
Dynamics of calcium sparks and calcium leak	102
Dynamics of calcium during a twitch-relaxation cycle	105
T-tubule remodelling and Heart failure	109
Calciums alternans	117
How many cells to trigger a sustained electrical response	137
Supplemental data	142
References	146
Chapter 4: FUNCTIONAL CONSEQUENCE OF RYR CLUSTER FRAGMENTATION AND	
REDISTRIBUTION IN PERSISTENT ATRIAL FIBRILLATION	
Abstract	161
Introduction	163
Computational modelling	167
Results	174
RyR cluster size and Ca^{2+} spark frequency	174

Functional RyR cluster	178
Modeling sarcomeric Ca^{2+} propagation.....	180
Discussion	181
References	185
Chapter 5: TEMPORO-SPATIAL MODEL OF CARDIAC CELLS TO STUDY Ca^{2+} WAVES INDUCED BY SR Ca^{2+} OVERLOAD	190
Abstract	190
Introduction	191
Model development.....	194
Sarcolemma(SL) and T-tubule membrane	196
Calcium release site.....	198
Spatial placement of CRUs	199
Spatial placement of $\text{Na}^+/\text{Ca}^{2+}$ exchangers, SERCA pump, SR and SL buffers.....	201
Diffusion of ions.....	203
Model formulation in spatial cell	205
Computational methods.....	208
Results	210
Ca^{2+} transient.....	210
Ca^{2+} spark-induced Ca^{2+} sparks	212
Ca^{2+} waves.....	218
Conclusion.....	227
Appendix	230
Program design.....	230
Methods to place CRUs.....	231
Parameters	233
References	235
Chapter 6: CONCLUSION AND FUTURE DIRECTION	244
Conclusion.....	244
Future directions.....	251
References	253
BIOGRAPHY.....	259
Published/In-preparation works.....	259

LIST OF TABLES

Table	Page
Table 1. Performance comparison.....	67
Table 1. Comparison of measured T-tubule at less than 3 μm from the surface between using confocal vs STED mode (* $p < 0.001$).	112
Table 2. The fraction of LCCs (from the CRUs which are Activated) in each state at the beginning of the stimulus at each beat [S2 = open, S3 = open, S4 = Ca^{2+} -dependent inactivation, S5 = Vm-dependent inactivation].....	126
Table 3. The fraction of LCCs (from the CRUs which are Inactivated) in each state at the beginning of the stimulus at each beat [S2 = open, S3 = open, S4 = Ca^{2+} -dependent inactivation, S5 = Vm-dependent inactivation].....	126
Table 4 Number of Myocytes with the instantaneous and gradual current injection in 1D, 2D and 3D tissue.	141
Table 5. Constant data and whole-cell level data	142
Table 6. Initial values	143
Table 7. Calcium buffers	143
Table 8. Parameters for L-type Ca^{2+} channel model	144
Table 9. Fluxes' parameters	145
Table 1. Parameters in the model	173
Table 1. Po, trigger when $[\text{Ca}^{2+}]_{\text{myo}} = 0.156 \mu\text{M}$, and $[\text{Ca}^{2+}]_{\text{sr}} = 1.3\text{mM}$. The latter case assumes luminal Ca^{2+} sensitivity saturate at 1.13 mM	215
Table 2. Parameters in the model	233

LIST OF FIGURES

Figure	Page
Figure 1. (A) The heart in the body; (B) A cross-section of the human heart (looking from the front)	3
Figure 2. (A) A single cardiac myocyte; (B) An electron microscope image of striated muscle where the sarcomere is the basic functional unit (courtesy Roger Craig, University of Massachusetts)	6
Figure 3. A schematic diagram of ionic channels across the sarcolemma of a typical heart cell (Hund & Rudy, 2004).....	7
Figure 4. Distribution of tubule diameter (Soeller & Cannell, 1999).....	9
Figure 5. A schematic diagram of calcium-induced calcium-release mechanism in a cardiac myocyte (Williams et al., 2011).....	10
Figure 6. (A) Schematic cardiac AP (the horizontal lines at the bottom shows the contribution of the ionic currents); (B) The AP waveforms at different regions of the heart (S. Nattel, Maguy, Le Bouter, & Yeh, 2007)	12
Figure 7. Distance between adjacent RyR2 clusters from longitudinal section images (Chen-izu et al., 2006).	16
Figure 8. Schematic diagrams that show the difference in hardware architecture between G80, GT200 GPUs and Niagara-2 CPU from Sun	19
Figure 9. A GT80 and GT200 architecture.....	22
Figure 10. A single GPC in GF100 architecture.....	23
Figure 11. CUDA programming model.....	25
Figure 12. An example of two different kernels, organized with two different thread hierarchies	28
Figure 13. A warp scheduler in Fermi.....	30
Figure 1. Calcium release sites (Adapted from (Donald M Bers, 2002)	49
Figure 2. Markov-model of L-type Ca^{2+} channel (A) (Sun, Fan, Clark, & Palade, 2000), (B) (Morotti, Grandi, Summa, Ginsburg, & Bers, 2012)	51
Figure 3. An example of a Petri Net for (A) a system of chemical reactions; (B) channel gating	53
Figure 4. (A) A minimal 2-state model of RyR, (B) A 7-state model of LCC	55
Figure 5. (A) A state diagram with Y is the current state, while X, Z are two potential future state. (B) A uniform pseudo-random number [0,1] determines the state transition	56
Figure 6. A two-state model of RyR (Williams et al., 2011).....	57
Figure 7. An example of a compact-form component-matrix $\text{cK}[]$. (A) and (B) are two different segments of the matrix $\text{cK}[]$. The left-most non-zero elements in each row display rate-constants of the reachable states in $\text{cK}[]$ whose true state-indices are kept in the corresponding column in the compact-form index-matrix $\text{iK}[]$	63
Figure 1. Calcium transport in the ventricular myocytes (Donald M Bers, 2002).	82
Figure 2. Schematic diagram of a ventricular cell that shows only 2 T-tubule branches	84
Figure 3. Schematic diagram of the model for the L-type calcium channel (DHPR channel), $\text{C4}=\text{Ca}^{2+}$ -dependent inactivation, $\text{C5}=\text{V}_m$ -dependent inactivation.....	88
Figure 4. The fraction of LCC channels in different states during the voltage-clamp of $\text{V}_{\text{stim}} = +10 \text{ mV}$ for 200ms	92
Figure 5. Dynamics of Na^+ gating variables during an AP: (A) Luo-Rudy-94 model at 37°C for guinea pig, (B) Pandit et al.-2001 model at 23°C for rat	92
Figure 6. Experimental data from rat ventricular myocyte at 23°C (Brette & Orchard, 2006).....	94

Figure 7. (A-B) gating variables; (C-D) time constants at different voltages. (E) I-V curve, (F) dynamics of gating variables of the proposed model during an AP	95
Figure 8. Comparison three common model formulation: Tran-Crampin (solid line), Shannon (dashed-line) and Inesi (dotted line), where SERCA2a pump flux vs. (A) $[Ca]_i$ and (B) $[Ca]_{sr}$ (Williams et al., 2011) ...	101
Figure 9. Calcium in the subspaces during (A) Ca^{2+} sparks and (B) Ca^{2+} quarks, (C) Dynamics of jSR Ca^{2+} release, (D) Number of RyR openings, (E) Ca^{2+} -bound calmodulin complex	104
Figure 10. Quantitatives Ca^{2+} fluxes during excitation-contraction coupling. The integrated fluxes during twitch relaxation in rat ventricular myocytes (Donald M Bers, 2002)	105
Figure 11. (A) $[Ca]_{myo}$, (B) Action potential (AP), (C) $[Ca]_{nsr}$, (D) opening probability of RyR, (E) opening probability of LCC, (F) subspace free $[Ca]_{ds}$, (G) L-type current density; (H) NCX current density; (I) PMCA current density; (J) Na^+ current density; (K) Na/K exchanger current density; (L) K1 current density; (M) slow component of transient-outward K^+ current, (N) fast-component of transient-outward K^+ current, (O,P,Q) background currents.	108
Figure 12. A long trace of calcium dynamics in the (A) myoplasm, (B) network SR, and (C) AP	109
Figure 13. A schematic diagram of dyadic junctions in healthy and diseased cardiac cells (adopted from (Polakova & Sobie, 2013))	111
Figure 14. Dynamics change of Potassium currents during HF	113
Figure 15. (A) Cytosolic $[Ca^{2+}]$, (B) SR $[Ca^{2+}]$, (C), subspace $[Ca^{2+}]_{ds}$, (D) AP	115
Figure 16. (A) LCC current, (B) Probability of RyR opening, (C) Integrated RyR Ca^{2+} flux during diastole and systole	116
Figure 17. (A) Cytosolic calcium, (B) SR $[Ca^{2+}]$, (C) P_o of RyR2	120
Figure 18. Calcium alternans at 8Hz: (A) Cytosolic calcium, (B) P_o (RyR2), (C) V_m , (D) I_{CaL} , (E) I_{Na}	121
Figure 19. (A) beat-to-beat variation in CRU's states where we examine Act-Act (the fraction of CRU that Activate in beat-i, and continue to Activate in beat-(i+1), similarly with Act-Inact, Inact-Inact, and Inact-Act, (B) The probability of RyR opening at each beat (red = open, black = closed)	123
Figure 20. An example that show a CRU that fires at two contiguous beats, e.g. (X) marks the release sites that is Act-Act	123
Figure 21. Ca^{2+} /CaM complex at the subspace during 8Hz and 1Hz pacing frequency	125
Figure 22. LCC opening (S2 and S3) at each beat	125
Figure 23. The fraction of LCCs in the opening states at the beginning of the stimulus from Inact-Inact CRUs	127
Figure 24. From rabbit ventricular myocyte: (A)a. alternans with alternation in diastolic SR $[Ca^{2+}]$ at 2.2Hz, (A)b. no alternans at 1.5Hz, (B) alternans without alternation in diastolic SR $[Ca^{2+}]$ at 2Hz (Picht et al., 2006)	128
Figure 25. (A) The diastolic $[Ca^{2+}]_{jSR}$ right before the stimulus from CRUs in two groups: red = Act, blue = Inactivate. (B) The upper black line shows the average $[Ca^{2+}]_{SR}$ level right before the I_{stim} is applied, and the lower red line shows the nadir of average $[Ca^{2+}]_{SR}$ level at the corresponding beat	130
Figure 26. The fraction of CRUs that has 1 or more RyR openings during each beat (black = beat-1, red = beat-2, blue = beat-3, yellow=beat-4, green=beat-5)	130
Figure 27. 8Hz pacing with $[Na^+]_i = 15mM$: (A) The average of $[Ca^{2+}]_{jSR}$ right before the stimulus from CRUs in two groups: red = Act, blue = Inactivate, and the nadir value. (C) calcium transient	133
Figure 28. LCC opening (S2,S3) when (A) $[Na^+]_i = 15mM$, (B) NCX expression 1.5x increase	133
Figure 29. Calcium transient in (A) 8Hz and $[Na]_i = 15mM$; (B) 8Hz and NCX downregulated 0.5x	134
Figure 30. SR $[Ca^{2+}]$ at (A) 8Hz pacing rate, (B) 8Hz pacing rate + $[Na^+]_i = 15mM$, (C) 8Hz pacing rate + $[Na^+]_i = 20mM$, (D) 8Hz pacing and NCX upregulated 1.5-fold, (E) 8Hz pacing and NCX udownregulated 0.5-fold	135
Figure 31. At $[Na^+]_i = 20mM$ and 8Hz	136
Figure 32. Alternans at high pacing rate (8Hz) using Na^+ stochastic modelled at 23°C, (A) action potential, (B) I_{CaL} current; (C) cytosolic calcium, (D) opening probability of whole-cell ryanodine receptors	137
Figure 33. Schematic of a 1-D tissue, cells are coupled by the gap junction conductance g_{gap} . Stimulus is applied to cells on the left side.	139

Figure 34. (A) The heart has many fine structures such as Purkinje fibers and trabeculae (lining the chambers of the heart) that are in effect 1-D structure or small-size 3D structure that extend from the atrioventricular. (A) The schematic diagram of a trabeculae that interface with the heart wall.	139
Figure 1. Schematic diagrams that show ECG recordings with (A) a normal sinus rhythm, and (B) an AF. The rapid and irregular AF activation is showed on ECG as an undulating baseline (the dotted lines show the continuous activity of atrial activation during QRS and T wave phases). During AF, ventricular activations (QRS complex) are driven by fibrillating atria which weaken the cardiac contraction efficiency and causing clinical symptoms (adapted from (Wakili et al., 2011))	165
Figure 2. Schematic diagram of a release site (with 25 RyRs) that sense calcium from 2 voxels of size 100nm x 100nm.....	169
Figure 3. Deconvolved STED microscopy resolves RyR sub-cluster formations in atrial myocytes. A. Images show average of the same 3 fluorescent beads aligned on their peaks from confocal (i) and STED (ii) recordings. B. RyR antibody labelling in an atrial myocyte visualized using confocal microscopy. Allowing a ~4-6x improvement in resolution. The much reduced Gaussian half maximal fit, with 2 possible fits has been reported before (5). This may allow further improvements the resolution of closely packed clusters of proteins. C-F Optical and software-based methods used to allow sub-cluster resolution (region outlined in red is shown in ii). C. A confocal image the sub-region used in subsequent imaging steps. D. The STED image of this region shows a marked improvement in resolution. E Deconvolution of the image in (D) allows further improvements in image, with reduced noise and more defined edges of each sub-cluster. F. RyR clusters are segmented using the Otsu thresholding method to allow further quantification of their size and shape. G. Here, the colors delineate the 10 RyR clusters detected in Fii. H. Illustration of RyR cluster size quantification. A grid of single RyRs (blue squares) are superimposed on the thresholded image to count the number of RyRs which would fit. (extract from Niall's study)	175
Figure 4. Computational modeling of intraCRU activation: Activation of large clusters by release from small RyR clusters. Insert shows release from small RyR within the CRU which can activate the larger RyR cluster. The small clusters are triggers simultaneously and the central cluster is activated by the diffusion of released Ca^{2+} . Red arrows depict the sequence of activation. Distance shown is edge-to-edge. A. Simulation of spark frequency of clusters with 5, 25 and 49 RyRs, revealing an order of magnitude increased frequency from smaller clusters. B. The probability (i) and delay(ii) of triggering release from a 25 RyR cluster by varying numbers small clusters placed 100 nm away which are triggered simultaneously.	177
Figure 5. Computational modeling of intraCRU activation: Activation of small cluster by release from large RyR clusters. Insert shows release from one large RyR within the CRU which can activate the smaller RyR cluster. The small cluster is activated by the diffusion of released Ca^{2+} from the larger cluster. Red arrows depict the sequence of activation. A. Waterfall plot of F/F_0 and (B) total Ca^{2+} signals from 2 the release sites depicted in the inset; The 49 RyR is 200 nm edge-to-edge away from the 5 RyR cluster. A smaller, more prolonged release from the small cluster is visible, after activation by Ca^{2+} released from the main cluster. B Plots show spatial profiles of fluorescence (i) and total Ca^{2+} released (ii). Cluster interaction is only evident on the free Ca^{2+} plot at -0.1 and -0.2 distances, however this is not visible on the simulated linescan F/F_0 image. C. (i) The relationship between the probability of triggering release from a small cluster ($P_{trigger}$) vs. distance from a larger site and the corresponding delay of activation (ii). This shows a high likelihood of activation and <2 ms delay if small clusters are ≤ 150 nm away from a larger one.....	179
Figure 6. Simulation of neighboring CRU activation during a macrospark. Inset shows schematic of model. 2 CRUS with one central 25 RyR cluster and 3 subclusters with 5 RyR. Edge to edge distance from the large cluster was varied from 400-700 nm. A. The resultant probability of propagation between adjacent clusters, mimicking the effect of altering the longitudinal separation between CRUs and macrospark formation. B. Simulated linescan image of a typical macrospark event. Two CRUs were placed 400 nm apart; The central release site from one site was triggered, releasing Ca^{2+} . This then diffused to raise Ca^{2+} local to the neighboring site triggering its release.	181
Figure 1. A schematic diagram of ventricular myocyte modeled as a hypercube	195
Figure 2. Three-dimensional skeleton of the TATS system in rat ventricular myocytes reconstructed from fluorescence micrograph [from (Soeller and Cannell 1999)]	197
Figure 3. The schematic diagram of a single dyad spreading into multiple grid points	199

Figure 4. Distribution of nearest neighbor distance of CRUs along different directions	200
Figure 5. The placement of calcium release sites (A) at one z-depth, (B) at one Z-disc. The inset in (A) shows the CRUs on two T-tubule at two adjacent Z-discs. The distribution of inter-CRU distance is derived based on the experimental data.....	200
Figure 6. (A) A single rat ventricular myocyte stained with anti-SERCA2a primary antibody, (B) enlarged view of eight sarcomere in panel A, and the plot of immunofluorescence distribution (adapted from (Smith, Keizer et al. 1998)).....	202
Figure 7. Calcium transient during an action potential (AP).....	211
Figure 8. Using different distances between the two CRUs, (i) shows the probability of one CRU to trigger the neighboring one, and (2) shows the delay of the activation. (A) The normal condition at diastolic phase is used ($[Ca^{2+}]_{myo} = 0.096 \mu M$, and $[Ca^{2+}]_{nsr} = 1.02 mM$), (B) The high cytosolic calcium ($[Ca^{2+}]_{myo} = 0.4 \mu M$, and $[Ca^{2+}]_{nsr} = 1.02 mM$)	212
Figure 9. Using different distances between the two CRUs, (i) shows the probability of one CRU to trigger the neighboring one, and (2) shows the delay of the activation. The overload condition (A) ($[Ca^{2+}]_{myo} = 0.156 \mu M$, and $[Ca^{2+}]_{nsr} = 1.70 mM$), and (B) ($[Ca^{2+}]_{myo} = 0.156 \mu M$, and $[Ca^{2+}]_{nsr} = 1.30 mM$).....	215
Figure 10. (A) A simulated calcium sparks, (B) Free calcium shows the underlying structure of release site (the delayed activation of the two satellite clusters are invisible under fluorescence profile, (C) The profile of a calcium spark giving FWHM=1.85um (each color represents the snapshot at different time point after the peak (e.g. bk=0 means black line at 0ms delayed); (D) The free calcium profile using back-calculation method agrees with experimental estimates, however, it underestimates the real free myoplasmic calcium amplitude.....	216
Figure 11. Using different distances, (i) shows the probability of one CRU to trigger the neighboring one, and (2) shows the delay of the activation. The overload condition (B) ($[Ca^{2+}]_{myo} = 0.156 \mu M$, and $[Ca^{2+}]_{nsr} = 1.30 mM$) where each CRU has 3 satellite clusters of 10 RyRs each at distance 0.2 μm	217
Figure 12. Simulation setting to study spark-induced waves (X = CRU location). Black X = the activated CRU, Blue X = the CRU to be activated by diffusing Ca^{2+} , Green X = intermediate RyR cluster	219
Figure 13. The $P_{o,trigger}$ of Ca^{2+} release from 9 activated CRUs on one Z-line on the CRU at different distance, and the time delay for the activation	220
Figure 14. The $P_{o,trigger}$ of Ca^{2+} release from 9 activated CRUs on one Z-line, with 1 intermediate RyR cluster in the middle, on the CRU at the next Z-line of different distance, and the time delay for the activation.....	221
Figure 15. Calcium overload ($[Ca]_{nsr}=1.7mM$, $[Ca]_i=0.15\mu M$), this computational model of the rat ventricular myocyte can reproduce a repetitive sustained calcium wave which typically initiates at one end of the cell. The initiation site typically occurs where release sites are closer together or at a boundary.....	223
Figure 16. Calcium waves under $[Ca]_o = 5mM$ overload condition, the repetitive waves occur at a particular sites for each cell. This suggest there is a more density of release sites surrounding that region that allows mass calcium release is high enough to trigger the wave. Some waves can sustain to the next end, while some decay and stop in between, which suggests a stochastic nature of the waves (extract from Brian Hagen's experiment).	223
Figure 17. (A) uniform SERCA; (B) block SERCA 90%	225
Figure 18. Given the initial $[Ca]_{nsr}=1.7mM$, to derive the triggering of the wave, the simulation suggested that an overload of 1.5M is enough to trigger the repetitive calcium waves.	226

LIST OF ABBREVIATIONS AND SYMBOLS

API	application programming interface
AF	atrial fibrillation
APD	action potential duration
Ca^{2+}	calcium
Calm	calmodulin (CALcium-MODULated proteIN)
CaMKII	Ca^{2+} /Calmodulin-dependent protein kinase II
CICR	Ca^{2+} -induced Ca^{2+} -release
CRU	Calcium Release Unit (Calcium Release Site)
CTMT	continuous-time discrete-state Markov chain
CUDA	Compute-Unified device architecture
DAD	delayed-after depolarization
DHPR	dihydropyridine receptor (see LCC)
FDHM	full-duration half-max
FWHM	full-width half-max
GPU	graphics processing unit
HF	heart failure
IP3R	inositol triphosphatase receptor
FP	floating-point
jSR/nSR	junctional SR/network SR
LCC	L-type calcium channel (see DHPR)
LSCM	laser-scanning confocal microscopy

MCMC	Markov-Chain Monte-Carlo
NCX	$\text{Na}^+/\text{Ca}^{2+}$ exchanger
PLB	phospholamban
PRNG	pseudo-random number generator
RyR2	ryanodine receptor type 2
SERCA	sarcoplasmic/endoplasmic reticulum Ca^{2+} -ATPase
SAN	stochastic automata network
SCD	sudden cardiac death
SL	sarcolemma
SR	sarcoplasmic reticulum
SP	streaming processor
SPN	stochastic Petri nets
SM	streaming multiprocessor
SFU	special functional unit (see CRU)
STED	stimulated emission depletion
TPC	thread processor cluster
Tpn-C	Troponin-C
UMCMC	Ultra-fast Markov-chain Monte carlo

ABSTRACT

COMPUTATIONAL STUDIES OF Ca^{2+} DYNAMICS IN CARDIAC CELLS USING GPGPU

Hoang-Trong Minh Tuan, Ph.D.

George Mason University, 2014

Dissertation Director: M. Saleet Jafri, Ph.D.

Calcium release in the heart plays a central role regulating and linking the electrical excitation of the heart with contraction. The molecular and cellular processes that govern calcium release are stochastic in nature involving over 1,000,000 stochastic ion channels. This creates a highly computationally expensive problem that necessitated the creation of novel algorithms that exploited advanced computational architectures. The studies presented in this dissertation started with introducing a fast, high-memory efficiency algorithm to simulate stochastic gating of ion channels. The method was then implemented using the novel computing platform GPU which utilizes Compute Unified Device Architecture (CUDA) programming model, and to apply it in developing experimentally-based models of the rat ventricular myocytes. There are two levels of modelling were developed in this dissertation: the stochastic compartmental model that incorporate a mechanistic representation of the calcium-induced calcium-release (CICR) mechanism, and a stochastic temporal-spatial model that incorporate the spatial placement of all the calcium release units (CRU) in the myocyte. The presented work was used to answer specific scientific questions to the morphologies of ionic currents under heart failure (HF) condition, calcium alternans and the critical number of cells in order to trigger a spontaneous ectopic heart beat. Then, the spatial model was used to study the dynamic changes in calcium sparks under atrial fibrillation (AF) conditions. The integrated whole-cell temporal spatial model for the rat was used to study calcium waves, which do not

occur during normal conditions, but are important as they can cause membrane depolarizations under certain conditions as the result of the life threatening cardiac arrhythmias.

CHAPTER 1: INTRODUCTION

Abstract

The heart is a muscular organ of the circulatory system that constantly pumps the blood to the whole body. Even though this pumping function is very well regulated, a multitude of pathological conditions may develop that can be the result of structural and/or functional changes at the cellular or subcellular level. Heart disease is the leading causes of death, with 24.6% of total death in the United States (Kochanek, Xu, Murphy, Minino, & Kung, 2009). Among them, sudden cardiac death (SCD) is the largest cause of death, about 325,000 adults each year. Sudden cardiac arrest occurs when the electrical system to the heart malfunctions and the heart beat becomes irregular, known as *arrhythmias*. The heart may not pump enough blood to the body, reducing blood supply to the brain, that cause a person losing consciousness in just a few minutes. In over half of the cases, however, sudden cardiac arrest occurs without prior symptoms. Until today, the underlying cellular mechanism is still unclear; with the most common life-threatening arrhythmia is ventricular fibrillation.

Since 1950s with the first computational model for the squid giant axon by Hodgkin-Huxley (Hodgkin & Huxley, 1952), using computational cellular models has become a useful mean to provide predictions or explanations of the underlying cellular processes. Therefore, the goal of this thesis is first to advance simulation algorithm, then

using it to investigate cardiac calcium regulatory mechanism. It is aimed first to provide a more accurate representation of the cardiac calcium cycling mechanism, and second to acquire novel insights into the pathophysiology of heart failure.

The first part of this chapter focuses on introducing the cellular structure of a cardiac ventricular myocytes, along with calcium dynamics in the cell to provide readers with adequate background to facilitate the understanding of the works. The second part introduces general-purpose GPU (GPGPU), a new generation of computing technology using GPU as the massively parallel computing device. The CUDA technology is the backbone of the computing technology for developing the computational model for the ventricular myocytes in this thesis.

Cardiac ventricular myocytes

A heart is a complicated organ located between the two lungs, slightly to the left of the center of your chest. The “tips” (the *apex*) of the heart points downward and toward the left, Figure 1 (A). Anatomically, the heart has four chambers. The two upper chambers are called left/right *atrium*; while the two lower chambers are called left/right *ventricles* (LV/RV), Figure 1 (B). The atrium collects the blood coming to the heart, and deliver it to the lower chambers. The right ventricle pumps the deoxygenated blood to the lung via pulmonary artery; while the left ventricle pumps the oxygen-rich blood to all parts of the body through powerful, rhythmic contractions.

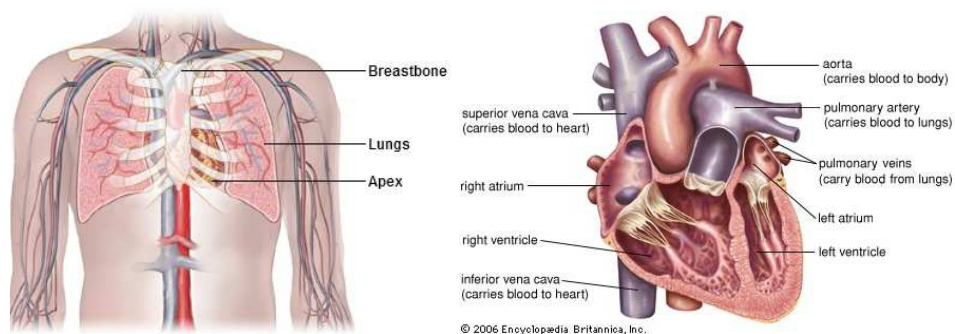


Figure 1. (A) The heart in the body¹; (B) A cross-section of the human heart (looking from the front)²

Among the different parts of the heart structure, the wall of the ventricles is of particular important as it's where the blood is pumped to the whole body. This makes the

¹ http://www.bostonscientific-international.com/templatedata/imports/HTML/CRM-Intl/heart/heart_intro.html

² <http://www.britannica.com/EBchecked/media/121131/Cross-section-of-the-human-heart>

left ventricular wall 3 times thicker than that of the right ventricle. In general, the muscular wall of the ventricle is composed of 3 major layers. The innermost layer of the cardiac tissues that lines the chamber of the heart is called **endocardium** (*endow-* = within, inward). The outermost layer is called **epicardium** (*epic-* = on, upon). The middle and also the thickest layer is the **myocardium** that is responsible for the excitation-contraction of the ventricle.

Excitation-contraction coupling (ECC) is the process of converting the electrical signal into a mechanical response in which the blood is rhythmically pumped out of the heart. At each heart beat, the fraction of blood pumped out of a chamber is called the ejection fraction (EF). This is smaller than one, and for a normal person, the EF for LV is about 50-70%. The dysfunction to the ECC may result in the loss of the heart's ability to adequately pump the blood. This can result to various types of cardiac arrhythmia in which ventricle fibrillation is the most common life-threatening arrhythmia.

At different regions in the heart, there are different cell types, with different fractions and densities of cellular components. There are 3 main types of cells: atrial cells, ventricular cells and excitatory/conducting cells. The excitatory/conducting cells have the capability of autonomous excitation, and are composed of sinoatrial (SA) nodes, atrio-ventricular (AV) nodes and Purkinje fibers. We will focus on ventricular myocytes as this is the cell type to be modelled.

Cellular structure

A typical ventricular myocyte has a long, narrow shape, with about 10-25 μm in diameter, and 50-130 μm in length (D M Bers, 2001; Opie, 2004), Figure 2(A). Adjacent cells are tightly connected via a junction called an *intercalated disc* to allow electrical, chemical and physical signals to be transferred between cells. In the cell, the contractile proteins (the myofilaments) make up almost one-half of the cell volume (rat: 48-50%). Most of the remaining volume is occupied by the mitochondria (rat: 35%), and a small fraction (rat: 3%) is occupied by the nuclei. The cell volume varies between species and at different stages of development. In rat, the cell volume is in the range from 20-40 (pL).

The proteins comprising the myofilaments, including actin, myosin, troponin and other proteins, form the striated structure of the myocyte, Figure 2(B1). The sarcomere is the basic functional unit of the striated structure, separated at each end by the so-called Z-disc (or Z-line). Each sarcomere has a dark band (A-band or anisotropic band) that consists mainly thick myosin filaments. The light band (I-band or isotropic band) consists mainly the thin actin filament. The Z-line bisects the I-band Figure 2 (B2).

Around each cell is a phospholipid plasma membrane known as the sarcolemma (SL). The ionic species (Ca^{2+} , Na^{+} , K^{+} ...) are distributed unequally across the SL of the cells by the action of ionic pumps and exchangers. This generates an electrochemical gradient between extracellular and intracellular ion concentration that helps maintain a proper transmembrane potential V_m . The cell harnesses these electrochemical gradients by allowing ions to cross the membrane through transmembrane proteins forming selective gating channels or ionic pumps/exchangers. Depending on the permeated ions,

the proteins are named accordingly, e.g. Na^+ channels, K^+ channels (I_{Ktof} , I_{Ktos} , I_{K1} , I_{Kss}), L-type Ca^{2+} channels (DHPR), $\text{Na}^+/\text{Ca}^{2+}$ exchanger (NCX), Na^+/K^+ exchanger, plasma membrane $\text{Ca}^{2+}/\text{ATP-ase}$ (PMCA), Figure 3.

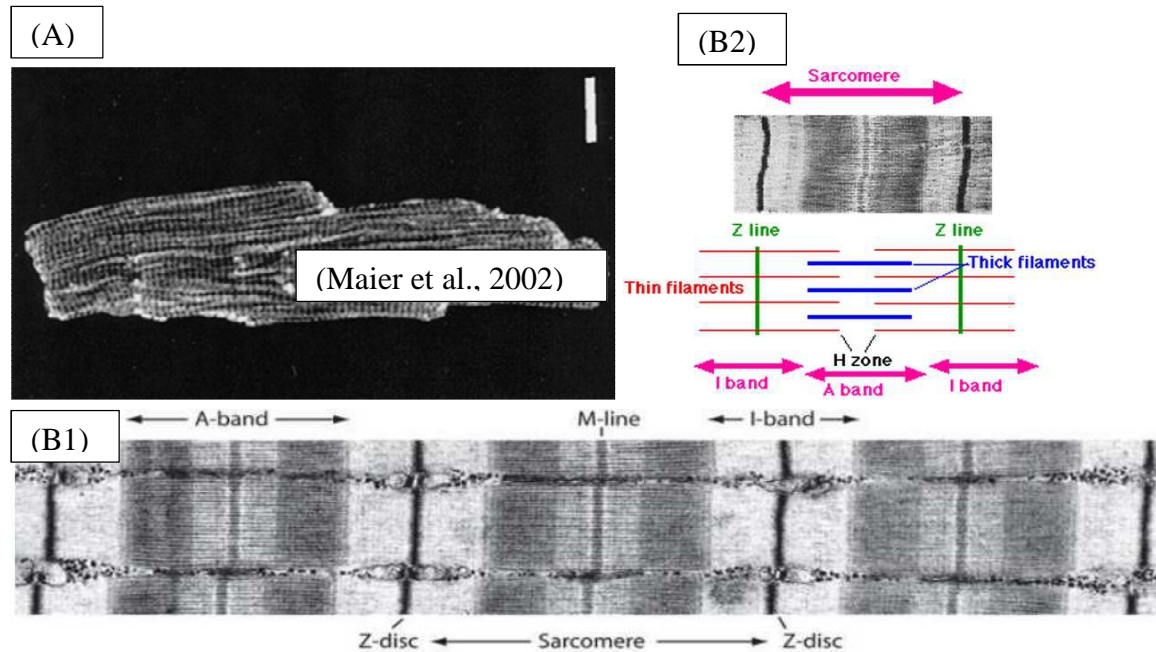


Figure 2. (A) A single cardiac myocyte; (B) An electron microscope image of striated muscle where the sarcomere is the basic functional unit (courtesy Roger Craig, University of Massachusetts)

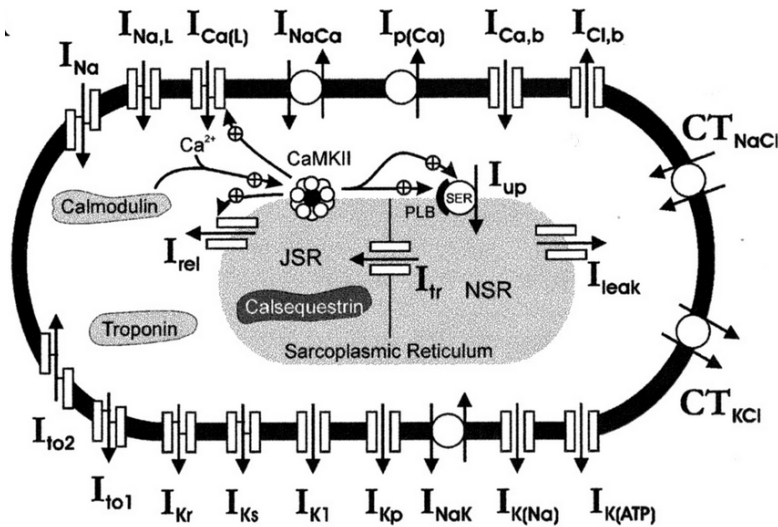


Figure 3. A schematic diagram of ionic channels across the sarcolemma of a typical heart cell (Hund & Rudy, 2004)

A significant amount of the sarcolemma forms transverse-tubular (T-tubule) system (rat: 21-33% of the total sarcolemma surface area). The first evidence of this contiguous tubules in mammalian heart muscle dated back to 1897 by Nyström who injected Indian ink and used light microscopy to detect dark lines trasversely crossing the ardiac fiber (see (Huxley, 1971). 60 years later, using electron microscopy (EM), (Lindner, 1957) was able to identified T-tubule systems in ventricular musculature of the dog. T-tubular system is continuous with the sarcolemma, invaginated deep into the inner side of the cell and located at the level of the Z-lines (Girardier & Pollet, 1964), Figure 5. However, the physiological role of these invaginations was not appreciated until T-tubules were seen in skeletal muscle and were implicated in ECC (A. Fabiato & Fabiato, 1977). The extremely fast in conduction of electrical signal on the sarcolemma to trigger uniformly Ca^{2+} release even in the center of the cell cannot be explained by the

simple chemical diffusion (Huxley & Taylor, 1955), and this can be explained by the functional role of T-tubule systems in contiguous with the outer surface membrane to transmit the electrical signal.

T-tubules have been found in the cardiac tissues of all mammalian species (e.g. rat, mice, guinea pigs, dogs, rabbits, and humans), but appear to be absent in avian, reptile, and amphibian cardiac tissue (Brette & Orchard, 2003). Interestingly, T-tubules are far less developed in atrial, pacemaker cells, with about 50% of atrial myocytes having a sparse irregular T-tubular system (Kirk et al., 2003; Richards et al., 2011). Although about one-third of the entire cell membrane area form the T-tubule networks, the total volume density is very small, e.g. about 1-3% (Page, McCallister, & Power, 1971; Soeller & Cannell, 1999).

The name T-tubular system was given due to the transversal direction of the invagination. However, subsequent studies shown that a considerable amount of tubules run in the axial direction (Forbes, Hawkey, & Sperelakis, 1984; Forssmann & Girardier, 1970). A better descriptive name was suggested as “transverse-axial tubular system” (TATS or T-Ax) (Forbes et al., 1984). Another name – Sarcolemma Z rete - was also proposed due to the fact that there is a large number of tubules that run neither axial nor transversal directions (Soeller & Cannell, 1999). EM also suggested that about 51% of tubules are between 180-280nm wide in rat, Figure 4, and the mean width is ~ 400nm in rabbit and human (M. B. Cannell, Crossman, & Soeller, 2006; Savio-Galimberti et al., 2008).

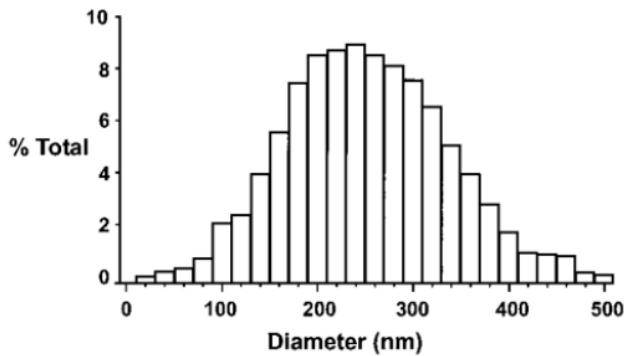


Figure 4. Distribution of tubule diameter (Soeller & Cannell, 1999)

Among the different organelles in the cell, sarcoplasmic reticulum (SR) is the major internal calcium storage organelle (rat: 3-4% of cell volume). SR is structurally divided into two parts: the network SR (nSR) and the junctional SR (jSR). nSR is the major structure of the SR and consists of 25-60 nm diameter sarcotubules organized into a network that surrounds the myofibrils fairly uniformly along the entire length of the sarcomere (Jorgensen, Shen, Arnold, McPherson, & Campbell, 1993). jSR is in closed proximity to the T-tubules or to the external sarcolemma at a small distance (10-15nm) and physically connects to the wall via the ‘feet’ structure. The tiny space formed by walls of a jSR and the T-tubules are called the dyadic subspace. These sites, known as calcium release sites (CRU), locate the majority of L-type calcium channels and ryanodine receptor type 2 (RyR2), Figure 5.

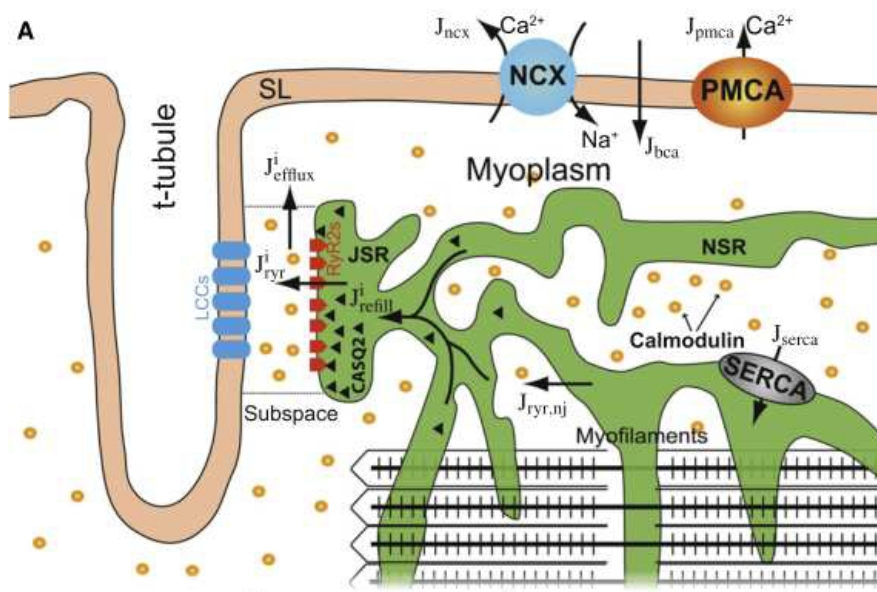


Figure 5. A schematic diagram of calcium-induced calcium-release mechanism in a cardiac myocyte (Williams et al., 2011)

Cardiac calcium homeostasis

Calcium is the ubiquitous second messenger that is involved in myriad intracellular signaling processes (for review: in animal (Berridge, 1998; Berridge, Lipp, & Bootman, 2000; Clapham, 2007; Gaspers, Pierobon, & Thomas, 2005), and in plants (Dodd, Kudla, & Sanders, 2010)). The multiple reasons pointed out by (Schaub & Heizmann, 2008) for the important roles of calcium were that (1) calcium is abundant, (2) compared to monovalent cations, the divalent cations (Ca^{2+} , Mg^{2+}) can form more stable and specific complexes with organic substances, yet not forming covalent bond in biology, (3) calcium with 4 electron shells, i.e. a more complex configuration than Mg^{2+} (three electron shells) allows a greater flexibility in forming interaction with protein

ligands, (4) the kinetics of ligand binding with Ca^{2+} is much faster than with Mg^{2+} (i.e. about 1000x).

More than a hundred years ago (in 1880s), the role of calcium in excitation-contraction of mammalian cells was first confirmed by Ringer in a series of his papers when doing experiments with frog heart (review: (Fye, 1984; Orchard, Eisner, Allen, & Ringer, 1994)). Since then, the role of calcium has been extensively studied, both in nerves and cardiac cells, though there are still many unresolved questions regarding its role in pathological genesis (Review: (Berridge, Bootman, & Roderick, 2003; Keating & Sanguinetti, 2001; Stanley Nattel, Maguy, Bouter, & Yeh, 2007; Pazoki, Wilde, & Bezzina, 2010; ter Keurs & Boyden, 2007)).

The calcium homeostasis is regulated via a number of special transmembrane protein complexes known as pumps and exchangers, e.g. plasma membrane ATP-driven pumps (PMCA), $\text{Na}^+/\text{Ca}^{2+}$ exchanger (NCX), intracellular SR/ER Ca^{2+} -ATPase (SERCA) pumps, mitochondrial calcium uniporter (MCU) and ion channels such as the RyR2 and IP₃R. In addition to its gradient across the SL, calcium is also sequestered into the SR leading to a large concentration gradient (about 10000-fold) between the SR lumen and the cytosol. In cardiac cells, under physiological conditions, to avoid calcium toxicity, when the cell is at rest, cytosolic calcium concentration is kept at a low level ($[\text{Ca}^{2+}]_i \sim 0.1\mu\text{M}$). During contraction, this concentration can increase up to 10-fold within tens to a few hundreds of milliseconds, depending upon species (Donald M Bers, 2002).

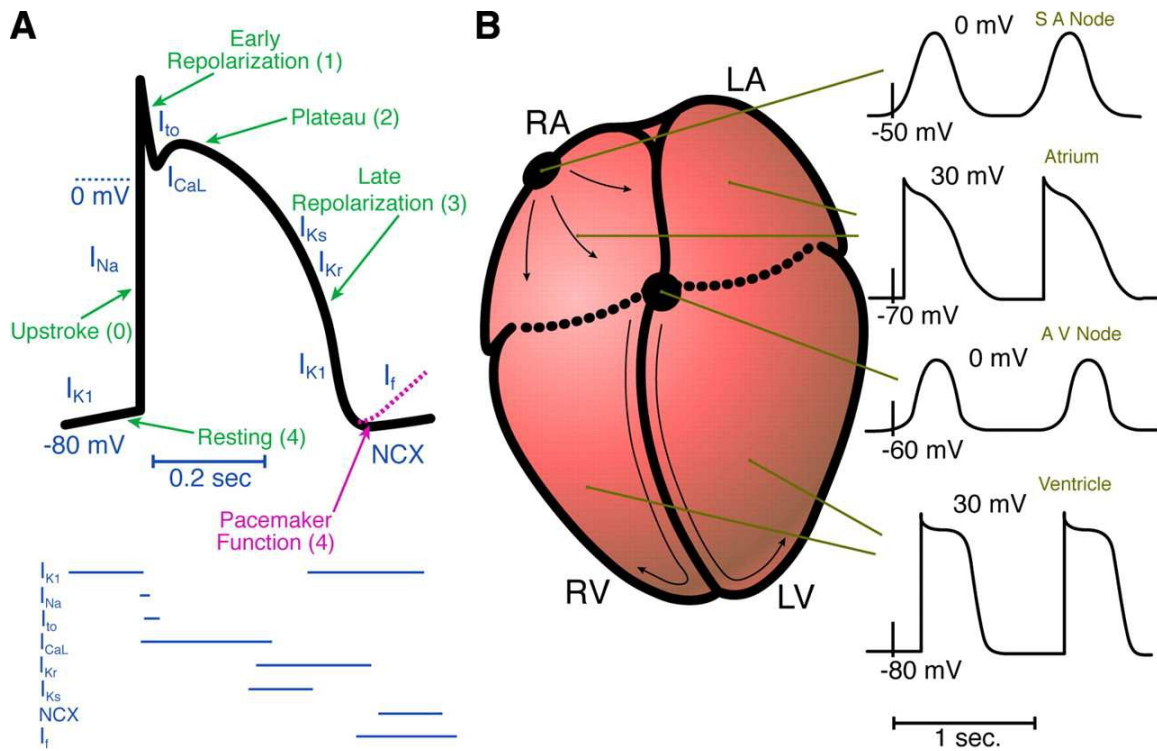


Figure 6. (A) Schematic cardiac AP (the horizontal lines at the bottom show the contribution of the ionic currents); (B) The AP waveforms at different regions of the heart (S. Nattel, Maguy, Le Bouter, & Yeh, 2007)

During ECC, at the cellular level, the initiating event is the depolarizing of the transmembrane potential, known as action potential (AP), which results in an increase in cytosolic calcium. Depending on the region and the cell types, the AP can have different waveform, Figure 6. In cardiac cells, the AP is mainly regulated by three ions: Na^+ , K^+ and Ca^{2+} in which Ca^{2+} plays the major role to the contractile. The elevation of cytosolic calciums triggers the contractile proteins, resulting in myocyte contraction. At the end of a normal excitation-contraction cycle, cytosolic calcium is brought back to the normal diastolic level by SERCA uptake (rat: nearly 90% uptake), by NCX extrusion

(rat: nearly 7%) (D M Bers, 2001), by mitochondria (1-2%) (D. M. Bers, Bassani, & Bassani, 1996) and sarcolemma Ca^{2+} -ATPase (1%) (D. M. Bers, 2000).

Calcium-induced calcium release

The physiological mechanism for calcium transient inside cardiac cells was coined calcium-induced calcium release (CICR) (Alexandre Fabiato, 1983; Alexandre Fabiato & Fabiato, 1975) where transmembrane voltage (V_m) plays no direct role in the mechanism. In skeletal cells, CICR has limited physiological role, and it was suggested that depolarization can induce calcium release via RyR type-1, i.e. voltage-induced Ca^{2+} release (VICR) (Schneider & Chandler, 1973). CICR is a regenerative process in which, upon membrane depolarization, a small influx of calcium via voltage gated L-type calcium channels (LCC) can elevates the calcium concentration in the dyadic cleft to a level high enough to bind to the activating sites of intracellular Ca^{2+} channels (the ryanodine receptor) and triggers the release of calcium from the intracellular calcium store - the sarcoplasmic reticulum (SR) in cardiac cell (Endo, 2009; Meissner, 1994). The dominant isoform of RyR in ventricular myocytes is type 2 (RyR2), while that in skeletal muscle cell is type 1 (S. O. Marx, 1998; Steven O. Marx et al., 2001) . In essence, the coupling between the voltage membrane and calcium forms the basis of excitation-contraction (EC) coupling.

Local control theory: high gain and gradedness release of calcium

With the advances in whole-cell recording techniques, experimental data have shown that calcium transient in cardiac cells is not an all-or-none process but possesses two important properties: high gain (or amplification, where a small influx of Ca^{2+}

triggers a much higher Ca^{2+} release from SR) (Beuckelmann and Wier, 1988) and gradedness (the elevation of cytosolic $[\text{Ca}^{2+}]$ is gradedness at different voltage clamps) (Fabiato, 1985). This leads to the hypothesis that CICR follows a local control mechanism, i.e. at the site where Ca^{2+} are released, the channels see a much higher calcium concentration than the bulk cytosolic calcium (Michael D Stern et al., 1999). The idea of local control was first suggested by Niggli-Lederer in which they suggested a local increase of $[\text{Ca}^{2+}]_i$ close to the sarcolemmal (including the T-tubular) higher and more rapidly than that in the inner region of the cell (Niggli & Lederer, 1990). The local region was suggested the term “fuzzy space” for the case of NCX (Lederer, Niggli, & Hadley, 1990). The hypothesis was then experimentally confirmed with the observation of local elevations of calcium known as Ca^{2+} sparks using confocal microscope (Cheng, Lederer, & Cannell, 1993; Niggli & Lederer, 1990). Since then, the local control theory has been verified on different cell types, especially cardiac cells (Mark B Cannell, Cheng, & Lederer, 1995; Wier, Egan, López-López, & Balke, 1994) where the small influx of calcium causes a local elevation ($>100 \mu\text{M}$) which is much higher than bulk cytosolic calcium (Klein et al., 1996; Peskoff & Langer, 1998; Santana, Cheng, Gómez, Cannell, & Lederer, 1996). It was estimated that there are $\sim 20,000$ of such calcium release sites in a single cardiac cell of volume $\sim 20 \text{ pL}$ (Cheng et al., 1993).

Calcium release units: calcium spark

At a single calcium release site, the calcium release channels (RyRs), associated with one face of one junctional T-tubule segment, form a functional unit that was coined couplon in skeletal muscle (Stern et al., 1997), and calcium release units (CRU) in cardiac cells (Franzini-Armstrong et al., 1999). At each release site, the restricted space or dyadic subspace is limited by one side the T-tubule membrane and the SR membrane on the other side. With local control, in the cardiac dyad, the influx of calcium via LCC is sensed by the closely apposed cluster of RyR2s, triggering the release of calcium from the SR and yielding a local increase in $[Ca^{2+}]$, i.e. $[Ca^{2+}]_{ds}$. These spatially localized events occurring at the “calcium release unit” (CRU) can be detected using fluorescent dyes which then can be quantified using the full-width half-max (FWHM), time-to-peak, half-decay time and full-duration half-max (FDHM) (Cheng and Lederer, 2008). At the time point where the Ca^{2+} spark reaches the peak, FWHM is the spatial distance between two locations at which the amplitude is half of the peak. If we assume the line-scan going through the center of the release site, FDHM is the time period from the two time points at which the value is half peak. In cardiac cells, FWHM of a Ca^{2+} spark is wide ($\sim 2 \mu m$), yet do not trigger neighboring sites under normal physiological conditions. In ventricular cardiac cells, the mean inter-release site distance is about $1.6 \mu m$ longitudinal and $0.8 \mu m$ in the axial direction (Bers, 2001). (Chen-izu et al., 2006) was first to quantify the distribution of the nearest neighbor distance between the CRUs along the transversal and longitudinal directions, Figure 7.

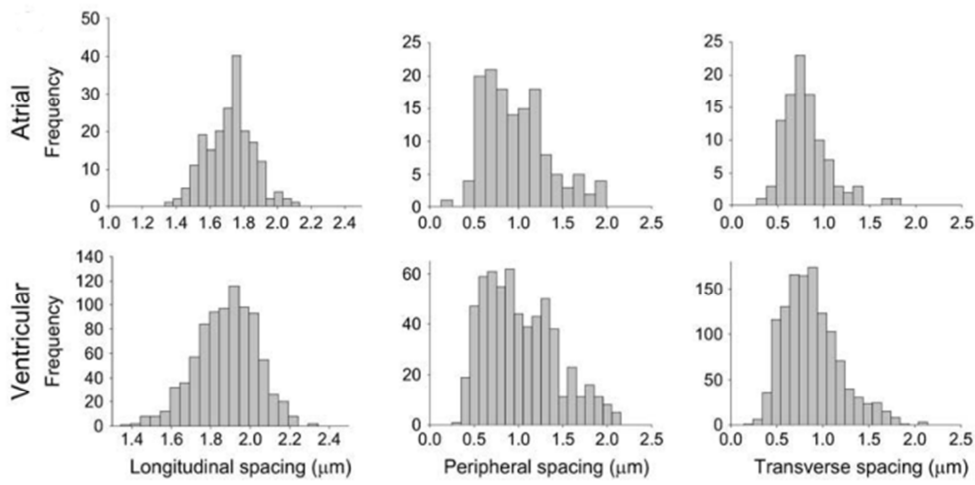


Figure 7. Distance between adjacent RyR2 clusters from longitudinal section images (Chen-izu et al., 2006).

General-purpose GPU (GPGPU)

GPUs are conventionally developed for video accelerator. Recently, the shift in GPU architecture and the extension of the GPU instruction set have enabled GPU to handle intensive parallel computational applications. However, conventional programming languages are designed to compile the code running on CPU. Programming languages designed to compile the code, into binary files that run code on GPU, is not easy for non-graphical programmers due to the fact that input data need to be interpreted as graphical data which requires the programmers to have a certain level of understanding of graphical programming. These binary files that run on GPU are called shaders (the term shader also refers to the GPU core in charge of doing shading).

To handle images and video processing, some GPU core are designed for pixel shading, and some are designed for vertex shading, or geometry shading. The concept of

“cores” are two different things between CPU vs. GPU. A GPU core (known as a shader (in computer graphics field) or a streaming processor (SP) (universal shader architecture) or CUDA core (Nvidia)) is more likely an ALU (arithmetic logic unit) - a functional unit in CPU core. The unified architecture means that all GPU core are identical and they can do the same thing (vertex, pixel, geometry and compute kernels). Even though ATI was the first to develop the unified architecture, it is NVIDIA that bring general purpose GPU (GPGPU) to the hype - with the name Compute Unified Device Architecture (CUDA).

A typical element of input data to GPU cores is a pixel which is a vector of 4 components (RGBA – red/green/blue/alpha) or can be XYZW since they don’t necessarily represent color information. At each clock cycle, a single instruction is issued to operate on the 4 different pixels. However, in many cases, each component in a pixel need to use a different instruction. To improve performance, AMD/ATI shader cores are capable of simultaneously processing 2 instructions. This is known as ‘co-issued’ or multiple-instructions multiple-data (MIMD) architecture. Nvidia used a different approach, called single-instruction multiple-data (SIMD). With SIMD, instead of processing 4 pixels of 4 components per cycle, since Nvidia G80/G92 GPUs, each GPU core processes only one component from 16 different pixels. This is the first unified shader, and thus given the name scalar processor (SP), which later was named streaming processor (SP).

NVIDIA’s unified approach started with G80 chips in 2006. In the context of CUDA, any shaders are now called scalar (streaming) processors (SP) or thread processor (as each SP process an instruction from a single thread). To make programming on

GPGPU accessible to a broader class of programmers, in 2007, Nvidia developed CUDA library, an extension to C language that can recognize the section of C code designed to run on GPU and compile it separately. The library was then ported to be used by different programming languages (Fortran, Python, MatLab, etc.). Nevertheless, there is a limitation in the number of features that can be used in these languages compared to CUDA C.

The first GPU device dedicated only to high-performance computing was named Tesla (GT200). The second generation of Tesla card was called Fermi (GF110). The third generation was called Kepler (GK20); and the coming generation in 2014 is Maxwell which is expected to bring 2-3x faster performance than Kepler. At each generation, there are certain changes in the architecture and improvements. They will be briefly described in the subsequent subsections. Each CUDA-capable device is organized in a hierarchical manner in memory architecture and data processing hardware architecture. The GPU hardware being used mainly in this study is Fermi architecture.

Scalar Processor (SP) or CUDA core

A G80 chip has 128 SPs; while GT200 chip (T10 architecture) has 240 SPs, and GF100 chip (Fermi) has 512 SPs. The newer generation, GK104 (Kepler) has 1536 SPs. GT200 is the first Tesla device dedicated to high-performance computing from Nvidia, and the hardware components in a single SP at different generations can be different.

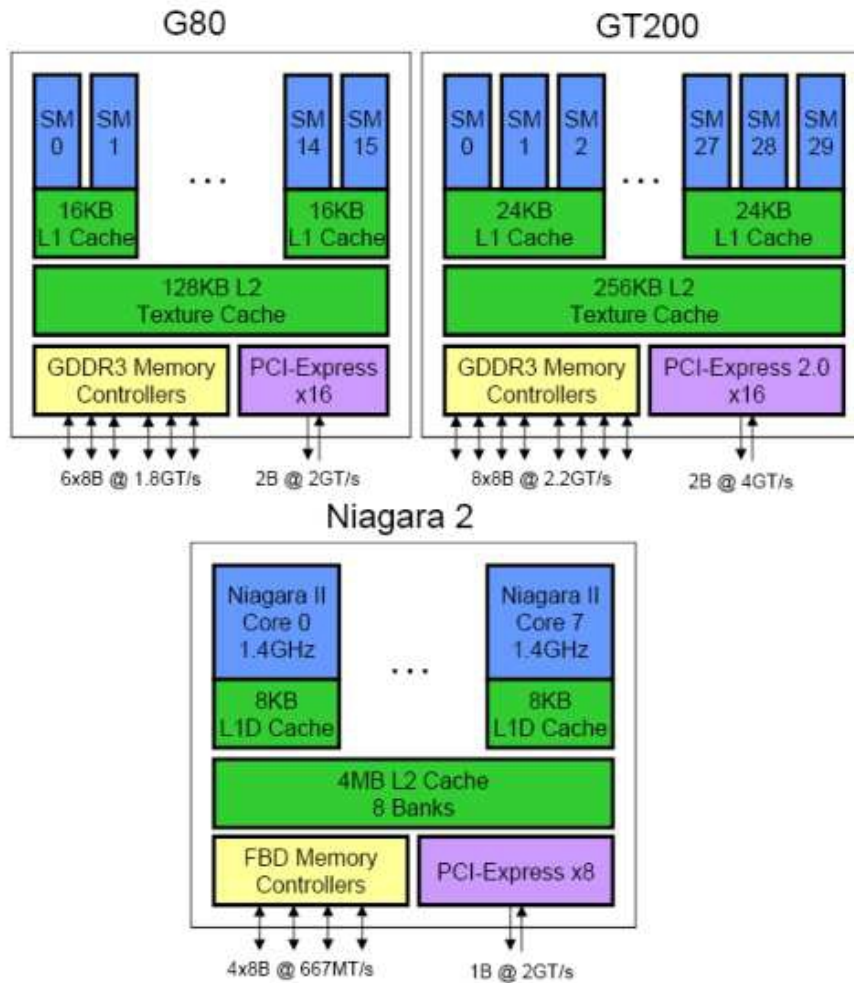


Figure 8. Schematic diagrams that show the difference in hardware architecture between G80, GT200 GPUs and Niagara-2 CPU from Sun

In G80/G92 chips, each SP or GPU core, however, lacks a complete front-end that can fetch and schedule instructions independently. Thus, SP is most closely corresponding to an issue pipeline or a modern multi-threaded CPU. In addition, an SP in G80/G92 chips can only do simple arithmetic operations (MAD/MUL), e.g. 32-bit floating-point multiply-add (MAD FP32) or 32-bit integer addition (ADD INT32) or 24-

bit integer multiplication (MUL INT24). To do complicated functions (EXP, LOG, RCP, RSQ, SIN, COS), a separate unit, known as special functional unit (SFU), is required. Due to the nature of graphical application where the speed is more important than the precision, G80 chips and other earlier model of CUDA-capable devices, all execution units in GPU only support 32-bit operations, but not 64-bit (FP64) operations. Fermi is the first CUDA-capable device that supports FP64 operations optimally, i.e. about 7x times faster than GT200.

An SP in GT200 chips can do 24-bit integer arithmetic operations in 24-bit in hardware, while 32-bit operations need to use software emulation. Since GK100 (Fermi), each SP has a newly designed INT unit and FP unit that support full 32-bit operations for all instructions in hardware (IEEE 754-2008 standard), with 64-bit operations are optimized so that two 32-bit ALUs can functions as one double-precision unit, giving about half the performance compared to 32-bit FP operations.

In G80/G92 chips, one instruction takes 4 clock cycles; while transcendental functions executed by SFU take 16 clock cycle latency and can be 32 clock cycles or longer to execute for more complicated functions (e.g. square roots or exponential function).

Streaming Multiprocessor (SM)

A streaming multiprocessor (SM) is a complete processor which is a collection of SPs and some other hardware units. In G80/G92 chips, each SM is composed of 8 SPs, 2 SFUs, 1 multithread instruction fetch/issue unit (MT issue), an instruction cache (I-cache), a read-only constant cache (C-cache), 16 KB read/write shared memory, 16KB

L1 texture-cache, 8K 32-bit registers and one WARP scheduler. Thus, each G80/G92 has 16 SMs.

GT200 chips have 32 SMs, double-precision was supported with one 64-bit MAD unit for each SM. A SM in this generation has more data: 24KB shared memory, 24 KB L1 texture cache, 16K 32-bit registers. In addition, a brand new 64-bit FMAD unit was added to shared by the entire SM integer and floating-point operations. FMAD supports standard IEEE 754-1985 to perform fused multiply-add with a single rounding on the result to give more accurate result, especially on iterative algorithms. Even though FMAD improve the accuracy, it decreases the performance as the number of FMAD units is one fourth of the double-precision units. Double-precision-based computation is expected 1/8 of single-precision-based computation in performance due to the number of 64-bit FP units is 1/8 of the 32-bit FP units.

The third generation SM in Fermi-based GPUs has a lot of innovations, especially the number of SP is 32 (in GF100) and 48 (in GF104), instead of 8. A GF100 chip has 14 SMs (ideally 16, but two were disabled). Each SM is composed of 32 SPs, 4 SFUs, 1 MT issue, 1 I-cache, 1 uniform-cache (replacement for C-cache), 64 KB shared-memory/L1 cache, 12KB texture-cache, 32K 32-bit registers, 2 WARP schedulers, 2 dispatch units, 4 TEX units, 1 PolyMorph engine, 16 load/store units (LD/ST). The new share-memory/L1 cache configurable memory allows compiler to manage between 16/48 (suitable for graphics applications) and 48/16 (suitable for compute applications). L2 cache is shared by all SMs and is particularly useful when all SMs need to access shared data. Now, two

SPs can do 64-bit operations, so the 64-bit MAD units were removed, and the performance in DP is expected to be $\frac{1}{2}$ of that in SP.

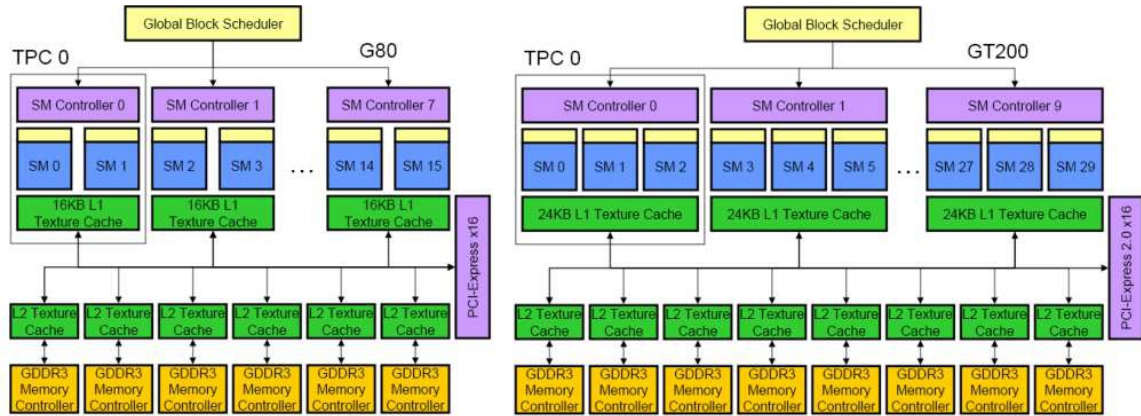


Figure 9. A GT80 and GT200 architecture

Texture Processor Cluster (TPC) to Graphics Processor Cluster (GPC)

At a higher level, in G80/G92 chips, 2 SMs combined with one texture memory unit (TMU or TEX engine), one geometry controller (i.e. PolyMorph unit) and one shared-memory controller (SMC) form a texture processor cluster (TPC). A complete G80/G92 GPU is the assemble of 8 TPCs. GT200 chips have 10 TPCs, with each TPC encloses 3 SMs, rather than 2, Figure 9.

Since GK100 chip (Fermi), the texture unit and PolyMorph engine is moved into the SM. So, TPC is replaced by a new concept called graphics processing cluster (GPC). A GPC has 4 SM, one Raster Engine that makes it functions a self-contained GPU,

Figure 10. Ideally, a GK100 chip has 4 full GPCs. However, due to the limitation of 40nm architecture, two SMs are disabled in the last GPC.

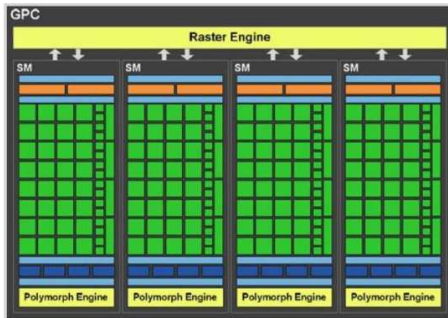


Figure 10. A single GPC in GF100 architecture

Memory architecture

There are two main types of memory: Dynamic random access memory (DRAM) and static RAM (SRAM). DRAM has cheaper cost per bits, yet has long latency, and thus is used as the main memory. SRAM is faster (6-8x faster than DRAM), yet it costs more per bit. SRAM is mainly used to produce cache memory. In CPU, to maximize sequential executions, a large amount of cache memory with different level was used (L1/L2/L3 caches). In GPU, the amount of cache memory are limited due to the large number of cores in one GPU. Thus, optimizing the utilization of cache and register files is a critical factor in developing a fast code in GPU. Memory spaces on GPU are hierarchically organized into

1. Register: extremely fast (zero clock cycle)
2. Shared memory: single cycle

3. Constant memory: C-cache, with 1, 10s, or 100s of clock cycles, depending on cache locality
4. Texture memory: L1 texture cache, with 1, 10s or 100s of clock cycles, depending on cache locality
5. Instruction memory (invisible to programmer): I-cache
6. Local memory: reside on global memory, but visible to one thread only. It is not cached, and thus is slow
7. Global memory: reside on global memory, and visible to all threads. It is not cached, and thus is slow.

G80/G92 chips has total 8192 32-bit registers, i.e. each SP can have 1K entries to be used by 96 active threads. GT200 has 16384 32-bit registers, i.e. each SP has 2K entries to be used by up to 128 threads. In GT200, each individual thread can have minimum 4, and maximum 128 registers. GK100 chip (Fermi) has 32768 32-bit registers. In Fermi, each individual thread can have minimum 21 registers and maximum 63 registers. The limit numbers of register files per thread requires a kernel to be designed so that it is not too big; otherwise memory spilling may occur and the overall performance can be compromised.

G80/G92 doesn't have shared memory. Since GT200, 16KB of shared memory was added to each SM. In Fermi, the amount of shared memory can be configurable between share/L1-cache configuration of total 64KB memory in each SM.

CUDA Programming model

CUDA programming model is a set of application programming interfaces (APIs) developed at different levels, Figure 11 . The lowest level is CUDA driver, which has the most capabilities with all hardware instructions (PTX language) but is extremely hard to use. CUDA runtime, developed by Nvidia from CUDA driver's APIs, provides the ease of programming. Using APIs from either CUDA runtime or CUDA driver (but not both), different CUDA libraries, written by different programmers, can be created. Many of them were developed by Nvidia, e.g. CUBLAS, CUFFT.

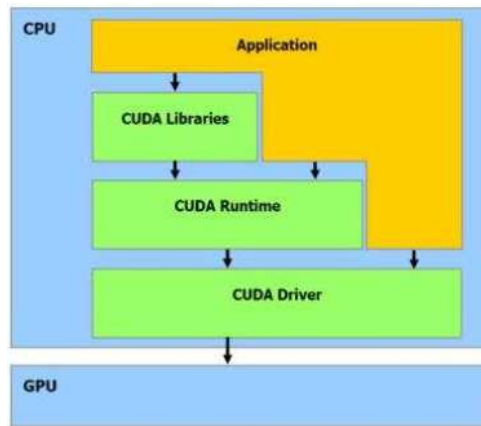


Figure 11. CUDA programming model

Initially, CUDA is a C-language extension that contains some new keywords that allows the driver tool (*nvcc*) to recognize, extract the CUDA code and compile the functions which are designed to run on CUDA-capable devices. These functions are called **kernels**, each of which is instantiated into a number of parallel logical threads. Each logical thread is put to one physical SP for executing the thread's instructions.

Threads from a single kernel are organized in a hierarchical structure of **grid** and **threadblock**.

A CUDA program must be initiated and run on CPU first. During the execution, some of its code can run on GPU asynchronously, allowing the program to continue the execution of other CPU codes. The basic CUDA execution model involves

1. Choose the GPU to use
2. Allocate the memory on device
3. Copy the data from host memory (CPU) to device memory
4. Asynchronous/Synchronous launch the kernel
5. Do other things on CPU (for asynchronous) or wait for the kernel to complete (synchronous)
6. Copy-out the result (if necessary) from device memory back to host memory
7. Deallocate the memory (CPU/GPU) at the end of the program

Kernel

A CUDA kernel is a function that only run on GPU. A kernel must be a ‘void’ function in CUDA C and a subroutine in CUDA Fortran. Any data returned must be passed via arguments or using global ‘device’ data. To define a new function as a kernel, depending on the programming languages, some new keywords were added

```
__global__ void mykernel() { // CUDA C
}
attributes(global) subroutine mykernel() !! CUDA Fortran
end subroutine
```

When a kernel is evoked, the kernel is instantiated into thousands of copies, known as threads, each one operate on one or a few particular data element using some

mechanism to map the thread index to the right data element(s) to process. The threads are organized into a number of threadblocks, and the threadblocks are organized into a single grid. In early versions of CUDA, a grid is 1-dimension; while a threadblock can be 1-, 2- or 3-dimension, depending on the nature of the problem. This hierarchical structure allows mapping perfectly the matrix-wise based applications to GPU.

Thread hierarchy (block and grid)

As mentioned in the previous subsection, a kernel is instantiated into thousands of light-weight threads. The organization of these threads need to be specified at each call to a kernel from the code. This is known as the execution configuration, using *chevron syntax*, which requires two facts: grid structure and threadblock structure.

```
grid = 1; block = N
call VecAdd<<<grid, block>>>( n, a , x , y )

.....

attributes ( global ) subroutine VecAdd(N, A, B, C)
  real , dimension (N) : : A, B, C
  integer i = threadIdx .x;
  if ( i .le. N) C(i) = A(i) + B(i);
end subroutine
```

In many practical problems, the data is in the form of a matrix in 2D or 3D. Thus, the threads can be organized into 2D or 3D threadblocks. If the number of data elements to be processed exceed the size of a threadblock, then multiple threadblocks are used and organized into a single grid of 1D or 2D. Depending on the generation of CUDA-capable device, there are certain restrictions and limitations. In particular, there is a maximum number of threads in a threadblock, and the maximum number of threadblocks per grid.

Up to GT200, the maximum number of threads per block is 512, while on Fermi, it's 1024. As critical resources like register files are statistically allocated to each thread, thread switching is very quick, as there is no need to save the thread's state when switching from one threads to another. Thread switching is done in groups of fixed size known as *warp*.

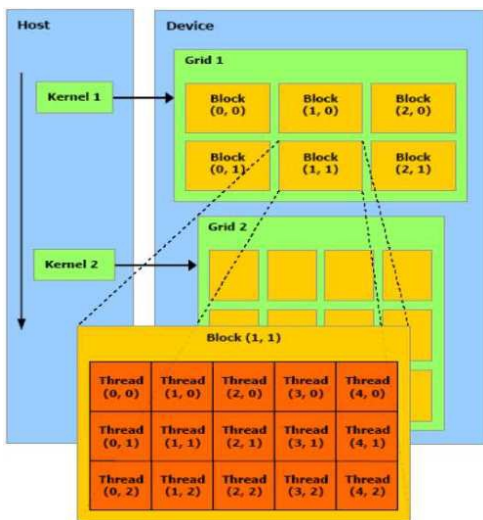


Figure 12. An example of two different kernels, organized with two different thread hierarchies

Given the large amount of threads, while there are only a few hundreds of CUDA core in a single GPU, a dedicated hardware will determine which threads/blocks to be activated (resident). The resident threads will be executed in groups of threads in the same threadblocks. The excessive blocks will be launched after the resident threads are finished. The next section will described how threads are activated.

Warp scheduling

At the chip level, threadblocks are distributed to different SM via the GigaThread Engine (*global block scheduler*) in a round-robin fashion. The GigaThread engine in G80 can manage up to 12,288 threads (i.e. each SM in G80/G92 can handle 768 threads, in G92 can handle 768 threads, in GT200 can handle 1024 threads); while that in Fermi it can support up to 24,576 threads at the same time (i.e. each SM can handle 1536 threads), and reduce context switching down to 20 microseconds. Then, at the SM level, a *local warp scheduler* will distribute threads to the CUDA cores. Giving a large number of threads, and a smaller number of SPs, only a numbers of threads are active at a time, i.e. those that can use the hardware resources to do the job. Threads are activated in groups of fixed size called **warp**. Current CUDA-capable devices uses warp size as 32.

Since GK100 (Fermi), with 2 WARP schedulers and 2 instruction dispatch units, two warps can be executed concurrently, Figure 13. For each warp, an instruction is issued to a group of 16 cores, or 16 LD/ST units, or 4 SFU units. So, as long as the threads in the first half or the second-half of a warp call the same instructions, there will be no divergence in the code. Otherwise it cause the CUDA cores to run threads in each branch sequentially. Note that double-precision and special-purpose operations like `exp()`, `sin()` do not support dual-dispatch with any other operations. There are two types of controllers in an SM: (1) geometry controller, (2) SM controller. Geometry controller maps the operations to SM that need to use 2D texture cache; while SM controller does the jobs for non-texture operations. In a high-performance computing application, most of the time, non-texture operations are used.

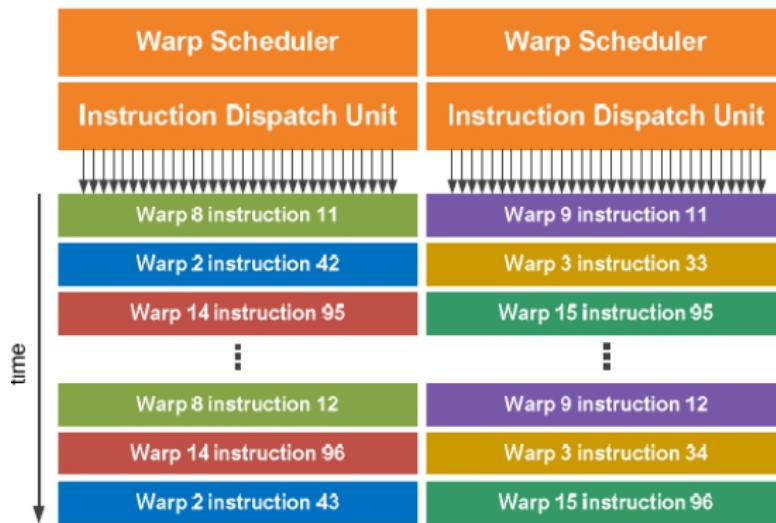


Figure 13. A warp scheduler in Fermi

Review of Computational Models

In 1950s, Hodgkin-Huxley developed the first electrophysiological model to study the dynamics changes of ionic concentration in nerve cells (Hodgkin & Huxley, 1952). Since then, there have been myriad efforts to develop cellular models for other types of cells (Denis Noble, Garny, & Noble, 2012). Nowadays, computational models have become a valuable tool to provide a quantitatively look into the dynamics of a system. Particularly, in order to understand the mechanism of excitation-contraction of the heart under normal and pathological conditions, there have been a plethora of developed computational models targeted to different types of cardiac cells: Purkinje fibres (DiFrancesco & Noble, 1985; McAllister, Noble, Tsien, & Haven, 1975), nodal cells (Hagiwara, Irisawa, & Kameyama, 1988; D Noble & Noble, 1984), atrial cells (Courtemanche et al., 1998; Earm & Noble, 1990; Hilgemann & Noble, 1987; Lindblad,

Murphey, Clark, & Giles, 1996; Nygren et al., 1998), ventricular myocytes (Beeler & Reuter, 1977; Chudin, Goldhaber, Garfinkel, Weiss, & Kogan, 1999; C.-H. Luo & Rudy, 1991; C. H. Luo & Rudy, 1994; Shannon, Wang, Puglisi, Weber, & Bers, 2004; Snyder, Palmer, & Moore, 2000; Winslow, Rice, Jafri, Marbán, & O'Rourke, 1999), etc. These models are considered to be “common pool” models because all the Ca^{2+} released flow into a single compartment which is either the bulk myoplasm or the lumped subspace.

Regardless of the many advances in channel gating's formulation, “common-pool” model for cardiac cells is a much simplified representation of the underlying cellular calcium dynamic. To reproduce the high gain and gradedness release, many of these models face the problem of instabilities, i.e. a small change in parameters can lead to numerical instabilities. From the view point of computer simulation, Stern suggested that “common-pool” models have to be reconsidered to avoid such problem (M D Stern, 1992). Phenomenological models derived from Luo-Rudy model although can possess high gain and gradedness property of local control mechanism (Faber & Rudy, 2000; Fox, McHarg, & Gilmour, 2002; Priebe & Beuckelmann, 1998); they lack a mechanistic description of the processes underlying the CICR mechanism.

In a single ventricular myocyte, there are many, in the order of 10^4 , CRUs and the accepted hypothesis is that global calcium transient is the result of the recruitment of the activations of many CRUs (M B Cannell, Cheng, Lederert, & Lederer, 1994; Cleemann, Wang, & Morad, 1998). To account for this local control mechanism, a computational model needs to incorporate distinct restricted subspaces (dyadic subspaces) for the CRUs. At each CRU, calcium influx flows into the subspace before it diffuses into the cytosol.

Jafri-Rice-Winslow model (Jafri, Rice, & Winslow, 1998) was the first one to introduce a restricted Ca^{2+} subspace into the model and using Markov state model for L-type Ca^{2+} channel. However, due to computational expense, early models assumed a lumped dyadic subspace in the simulation setting (Jafri et al., 1998; Winslow et al., 1999) and thus still belong to the class of common-pool model. In these models, the spatially diffuse tubular network SR is divided into two regions: the network SR (NSR) and junctional SR (JSR) (Sobie, Dilly, dos Santos Cruz, Lederer, & Jafri, 2002). Some studies also divide the cytoplasm into two regions: the subsarcolemmal compartment and the bulk myoplasm based on the inference that NCXs sense a calcium concentration different from that in the bulk myoplasm (Mahajan et al., 2008; Shannon et al., 2004; Shiferaw, Watanabe, Garfinkel, Weiss, & Karma, 2003).

With the number of junctions in the order of 10^4 , attempts to resolve the calcium dynamics at this microdomain level in time and space have been computationally intractable for modeling arrhythmogenesis at tissue and organ level. As a matter of fact, many models (for review, see (Williams, Smith, Sobie, & Jafri, 2010; Winslow et al., 2011)), although can simulate graded release, and reproduce some pathological conditions (e.g. the alternation in action potential - alternans, and early afterdepolarization - EAD), lack a mechanistic description in which the release from SR is the summation of discrete events (Chudin et al., 1999; Faber & Rudy, 2000; Faber, Silva, Livshitz, & Rudy, 2007; Viswanathan & Rudy, 1999). In an effort to incorporate a more realistic description of how calcium is regulated using local-control mechanism,

many of the whole-cell models consider a few hundred or a few thousands of them and stochastic simulation is therefore required.

To reproduce graded release, Rice-Jafri-Winslow (Rice, Jafri, & Winslow, 1999) assumed 500 CRUs whose activity was being simulated stochastically. Greenstein and Winslow (Joseph L Greenstein & Winslow, 2002) presented the first local-control model to integrate the system with 12,500 CRUs. However, the model didn't produce a proper Ca^{2+} spark feature; as the local calcium concentration is expected to reach $\sim 100\mu\text{M}$ and did not explain the role of invisible calcium leak in resting calcium homeostasis. Also, due to the computational demand, a smaller fraction, 20%, of the CRUs were used in the simulations (Joseph L. Greenstein, 2002).

To avoid high computational cost, (Joseph L Greenstein, Hinch, & Winslow, 2006) used deterministic approach, Williams et al. proposed probability density function concept or moment closure to avoid high computational demand (Williams, Huertas, Sobie, Jafri, & Smith, 2007, 2008). These algorithms can reproduce high gain and gradedness; yet the approaches require simplification of the model for the CRU based on average (deterministic) behavior and fail to capture stochastic events at individual CRU which are believed to play a role in triggering spontaneous calcium waves (Cheng, Lederer, Lederer, & Cannell, 1996; Izu, Wier, & Balke, 2001; Keizer & Smith, 1998). As a result, some of them don't feature Ca^{2+} sparks and thus cannot be used to simulate calcium dynamics in a temporal-spatial whole-cell model setting. Chikando and Jafri (Chikando, 2008) introduced the first rat ventricular myocyte model with 20,000 release sites. However, the large computational cost associated with the model limited its use for

extensive modeling studies. Some initial efforts were made to create temporal spatial of the cardiac cells in 2D (Rovetti, Cui, Garfinkel, Weiss, & Qu, 2010) and 3D (Restrepo & Karma, 2009), however, they didn't incorporate a proper spark model or didn't feature the realistic placement of CRUs as well as the non-uniform distribution of other transmembrane proteins.

Research Objectives

Due to the extensive computational high demand of developing a mechanistic whole-cell model that is able to capture the calcium dynamics at the single-channel level, the main objective of the work described in this document is to introduce a novel computational algorithm, called Ultra-fast Markov-chain Monte Carlo method. The method was effectively implemented on GPGPU, and then is used to implement the stochastic gating of ion channels in the calcium release sites to develop the stochastic compartmental model for the rat ventricular myocytes. The model integrates, and improves upon, features from other computational models to provide a novel tool for studying calcium dynamics at different pathophysiological conditions, particularly heart failure, cardiac alternans and catecholamine polymorphism ventricular tachycardia (CPVT). Next, the model is incorporated in a tissue model to provide the first stochastic tissue model that can be used to study the critical point of number of cells for triggering cardiac arrhythmias. Finally, the temporal-spatial model for the rat ventricular myocytes was developed that incorporate the spatial placement of all calcium release sites in the heart, as well as non-uniform distribution of ion channels, and exchangers on the sarcolemma, including the external surface and the T-tubule systems. The model provides

an unprecedented tool to study calcium waves, and the role of T-tubule detubulation in cardiac diseases.

REFERENCES

- Beeler, G. W., & Reuter, H. (1977). Reconstruction of the action potential of ventricular myocardial fibres. *Journal of Physiology*, 268, 177-210.
- Berridge, M. J. (1998). Neuronal calcium signaling. *Neuron*, 21, 13-26. doi: 10.1098/rstb.2008.0093
- Berridge, M. J., Bootman, M. D., & Roderick, H. L. (2003). Calcium signalling: dynamics, homeostasis and remodelling. *Nature reviews. Molecular cell biology*, 4, 517-529. doi: 10.1038/nrm1155
- Berridge, M. J., Lipp, P., & Bootman, M. D. (2000). The versatility and universality of Calcium signalling. *Nature reviews. Molecular cell biology*, 1, 11-21.
- Bers, D. M. (2000). Calcium Fluxes Involved in Control of Cardiac Myocyte Contraction. *Circulation Research*, 87, 275-281. doi: 10.1161/01.RES.87.4.275
- Bers, D. M. (2001). *Excitation-Contraction Coupling and Cardiac Contractile Force*. (2nd ed.). Dordrecht, Netherlands: Kluwer Academic Publishers.
- Bers, D. M. (2002). Cardiac excitation-contraction coupling. *Nature*, 415, 198-205.
- Bers, D. M., Bassani, J. W., & Bassani, R. A. (1996). Na-Ca exchange and Ca fluxes during contraction and relaxation in mammalian ventricular muscle. [Research Support, U.S. Gov't, P.H.S. Review]. *Ann N Y Acad Sci*, 779, 430-442.
- Brette, F., & Orchard, C. (2003). T-tubule function in mammalian cardiac myocytes. *Circulation research*, 92, 1182-1192. doi: 10.1161/01.RES.0000074908.17214.FD
- Cannell, M. B., Cheng, H., & Lederer, W. J. (1995). The control of calcium release in heart muscle. *Science (New York, N.Y.)*, 268, 1045-1049.

- Cannell, M. B., Cheng, H., Lederer, W. J., & Lederer, W. J. (1994). Spatial non-uniformities in $[Ca^{2+}]$ in Cardiac Myocytes during excitation-contraction coupling in cardiac myocytes. *Biophys. J.*, 67, 1942-1956.
- Cannell, M. B., Crossman, D. J., & Soeller, C. (2006). Effect of changes in action potential spike configuration, junctional sarcoplasmic reticulum micro-architecture and altered t-tubule structure in human heart failure. [Research Support, Non-U.S. Gov't]. *J Muscle Res Cell Motil*, 27(5-7), 297-306. doi: 10.1007/s10974-006-9089-y
- Chen-izu, Y., McCulle, S. L., Ward, C. W., Soeller, C., Allen, B. M., Rabang, C., . . . Izu, L. T. (2006). Three-dimensional distribution of ryanodine receptor clusters in cardiac myocytes. *Biophysical journal*, 91, 1-13. doi: 10.1529/biophysj.105.077180
- Cheng, H., Lederer, M. R., Lederer, W. J., & Cannell, M. B. (1996). Calcium sparks and $[Ca^{2+}]_i$ waves in cardiac myocytes. *The American journal of physiology*, 270, C148-159.
- Cheng, H., Lederer, W. J. J., & Cannell, M. B. (1993). Calcium Sparks: Elementary Events Underlying Excitation-Contraction Coupling in Heart Muscle. *Science*, 262, 740-744.
- Chikando, A. C. (2008). A Computational Study of Excitation-Contraction Coupling: Mechanisms of Sarcoplasmic Reticulum Calcium Leak and the Role of Mitochondria in Myoplasmic Calcium Regulation (pp. 187).
- Chudin, E., Goldhaber, J. I., Garfinkel, A., Weiss, J. N., & Kogan, B. (1999). Intracellular Ca^{2+} dynamics and the stability of ventricular tachycardia. *Biophysical journal*, 77, 2930-2941. doi: 10.1016/S0006-3495(99)77126-2
- Clapham, D. E. (2007). Calcium signaling. *Cell*, 131, 1047-1058. doi: 10.1016/j.cell.2007.11.028
- Cleemann, L., Wang, W., & Morad, M. (1998). Two-dimensional confocal images of organization, density, and gating of focal Ca^{2+} release sites in rat cardiac myocytes. *Proceedings of the National Academy of Sciences of the United States of America*, 95, 10984-10989.
- Courtemanche, M., Ramirez, R. J., Nattel, S., Stella, A., Genovesi, S., Physiol, A. J., & Circ, H. (1998). Ionic mechanisms underlying human atrial action potential properties: insights from a mathematical model. *The American journal of physiology*, 275, H301-321.

- DiFrancesco, D., & Noble, D. (1985). A Model of Cardiac Electrical Activity Incorporating Ionic Pumps and Concentration Changes. *Philosophical Transactions of the Royal Society of London, Series B, Biological Sciences*, 307, 353-398.
- Dodd, A. N., Kudla, J., & Sanders, D. (2010). The language of calcium signaling. *Annual review of plant biology*, 61, 593-620. doi: 10.1146/annurev-arplant-070109-104628
- Earm, Y. E., & Noble, D. (1990). A model of the single atrial cell: relation between calcium current and calcium release. *Proceedings of the Royal Society of London. Series B, Containing papers of a Biological character. Royal Society (Great Britain)*, 240, 83-96.
- Endo, M. (2009). Calcium-Induced Calcium Release in Skeletal Muscle. *Physiological Reviews*, 89, 1153-1176. doi: 10.1152/physrev.00040.2008.
- Faber, G. M., & Rudy, Y. (2000). Action potential and contractility changes in [Na(+)](i) overloaded cardiac myocytes: a simulation study. *Biophysical journal*, 78, 2392-2404. doi: 10.1016/S0006-3495(00)76783-X
- Faber, G. M., Silva, J., Livshitz, L., & Rudy, Y. (2007). Kinetic Properties of the Cardiac L-Type Ca²⁺ Channel and Its Role in Myocyte Electrophysiology: A Theoretical Investigation. *Biophysical Journal*, 92, 1522-1543. doi: 10.1529/biophysj.106.088807
- Fabiato, A. (1983). Calcium-induced release of calcium from the cardiac sarcoplasmic reticulum. *American journal of physiology. Cell physiology*, 245, C1-C14. doi: 10.1016/0022-2828(92)90114-F
- Fabiato, A., & Fabiato, F. (1975). Contractions induced by a calcium-triggered release of calcium from the sarcoplasmic reticulum of single skinned cardiac cells. *Journal of Physiology*, 249, 469-495.
- Fabiato, A., & Fabiato, F. (1977). Calcium release from the sarcoplasmic reticulum. [Research Support, U.S. Gov't, P.H.S. Review]. *Circ Res*, 40(2), 119-129.
- Forbes, M. S., Hawkey, L. A., & Sperelakis, N. (1984). The transverse-axial tubular system (TATS) of mouse myocardium: its morphology in the developing and adult animal. [Research Support, Non-U.S. Gov't Research Support, U.S. Gov't, P.H.S.]. *Am J Anat*, 170(2), 143-162. doi: 10.1002/aja.1001700203

- Forssmann, W. G., & Girardier, L. (1970). A study of the T system in rat heart. *J Cell Biol*, 44(1), 1-19.
- Fox, J. J., McHarg, J. L., & Gilmour, R. F. (2002). Ionic mechanism of electrical alternans. *American journal of physiology. Heart and circulatory physiology*, 282, H516-530. doi: 10.1152/ajpheart.00612.2001
- Fye, W. B. (1984). Sydney Ringer, calcium, and cardiac function. *Circulation*, 69, 849-853. doi: 10.1161/01.CIR.69.4.849
- Calcium signaling 211-221 (2005).
- Girardier, L., & Pollet, M. (1964). [Demonstration of the Continuity between the Interstitial Space and the Lumen of the Intracellular Canals in the Rat Myocardium]. *Helv Physiol Pharmacol Acta*, 22, C72-73.
- Greenstein, J. L. (2002). Local control of calcium release and its implications for cardiac myocyte properties *Heart Failure* (pp. 281).
- Greenstein, J. L., Hinch, R., & Winslow, R. L. (2006). Mechanisms of excitation-contraction coupling in an integrative model of the cardiac ventricular myocyte. *Biophysical journal*, 90, 77-91. doi: 10.1529/biophysj.105.065169
- Greenstein, J. L., & Winslow, R. L. (2002). An integrative model of the cardiac ventricular myocyte incorporating local control of Ca²⁺ release. *Biophysical journal*, 83, 2918-2945. doi: 10.1016/S0006-3495(02)75301-0
- Hagiwara, N., Irisawa, H., & Kameyama, M. (1988). Contribution of two types of calcium currents to the pacemaker potentials of rabbit sino-atrial node cells. *Journal of Physiology*, 395, 233-253.
- Hilgemann, D. W., & Noble, D. (1987). Excitation-contraction coupling and extracellular calcium transients in rabbit atrium: reconstruction of basic cellular mechanisms. [Research Support, Non-U.S. Gov't
- Review]. *Proc R Soc Lond B Biol Sci*, 230(1259), 163-205.
- Hodgkin, A. L., & Huxley, A. F. (1952). A quantitative description of membrane current and its application to conduction and excitation in nerve. *Journal of Physiology*, 117, 25-71.
- Hund, T. J., & Rudy, Y. (2004). Rate dependence and regulation of action potential and calcium transient in a canine cardiac ventricular cell model. [Research Support, N.I.H., Extramural
- Research Support, Non-U.S. Gov't

- Research Support, U.S. Gov't, P.H.S.]. *Circulation*, 110(20), 3168-3174. doi: 10.1161/01.CIR.0000147231.69595.D3
- Huxley, A. F. (1971). The activation of striated muscle and its mechanical response. [Review]. *Proc R Soc Lond B Biol Sci*, 178(50), 1-27.
- Huxley, A. F., & Taylor, R. E. (1955). Function of Krause's membrane. *Nature*, 176(4492), 1068.
- Izu, L. T., Wier, W. G., & Balke, C. W. (2001). Evolution of Cardiac Calcium Waves from Stochastic Calcium Sparks. 80, 103-120.
- Jafri, M. S., Rice, J. J., & Winslow, R. L. (1998). Cardiac Ca²⁺ dynamics: the roles of ryanodine receptor adaptation and sarcoplasmic reticulum load. *Biophysical journal*, 74, 1149-1168. doi: 10.1016/S0006-3495(98)77832-4
- Jorgensen, A. O., Shen, A. C., Arnold, W., McPherson, P. S., & Campbell, K. P. (1993). The Ca²⁺-release channel/ryanodine receptor is localized in junctional and corbular sarcoplasmic reticulum in cardiac muscle. [Research Support, Non-U.S. Gov't
- Research Support, U.S. Gov't, P.H.S.]. *J Cell Biol*, 120(4), 969-980.
- Keating, M. T., & Sanguinetti, M. C. (2001). Molecular and cellular mechanisms of cardiac arrhythmias. *Cell*, 104, 569-580.
- Keizer, J., & Smith, G. D. (1998). Spark-to-wave transition: saltatory transmission of calcium waves in cardiac myocytes. *Biophysical chemistry*, 72, 87-100.
- Kirk, M. M., Izu, L. T., Chen-Izu, Y., McCulle, S. L., Wier, W. G., Balke, C. W., & Shorofsky, S. R. (2003). Role of the transverse-axial tubule system in generating calcium sparks and calcium transients in rat atrial myocytes. *The Journal of physiology*, 547, 441-451. doi: 10.1113/jphysiol.2002.034355
- Klein, M. G., Cheng, H., Santana, L. F., Jiang, Y.-H., Lederer, W. J. J., & Schneider, M. F. (1996). Two mechanisms of quantized calcium release in skeletal muscle. *Nature*, 379, 455-459.
- Kochanek, K. D., Xu, J., Murphy, S. L., Minino, A. M., & Kung, H.-C. (2009). Deaths: Final Data for 2009. *National Vital Statistics Reports*, 60(3).
- Lederer, W. J., Niggli, E., & Hadley, R. W. (1990). Sodium- Calcium in Excitable Exchange Cells : Fuzzy Space. *Science*, 248, 283-284.

- Lindblad, D. S., Murphey, C. R., Clark, J. W., & Giles, W. R. (1996). A model of the action potential membrane currents in a rabbit atrial cell. *Am J Physiol Heart Circ Physiol*, 271, H1666-H1696.
- Lindner, E. (1957). Die submikroskopische Morphologie des Herzmuskels. *Zeitschrift für Zellforschung und mikroskopische Anatomie*, 45, 702-746.
- Luo, C.-H., & Rudy, Y. (1991). A Model of the Ventricular Cardiac Action Potential. Depolarization, repolarization, and their interaction. *Circulation Research*, 68, 1501-1526. doi: 10.1161/01.RES.68.6.1501
- Luo, C. H., & Rudy, Y. (1994). A dynamic model of the cardiac ventricular action potential. I. Simulations of ionic currents and concentration changes. *Circulation research*, 74, 1071-1096.
- Mahajan, A., Shiferaw, Y., Sato, D., Baher, A., Olcese, R., Xie, L.-H., . . . Weiss, J. N. (2008). A rabbit ventricular action potential model replicating cardiac dynamics at rapid heart rates. *Biophysical journal*, 94, 392-410. doi: 10.1529/biophysj.106.98160
- Maier, S. K., Westenbroek, R. E., Schenkman, K. A., Feigl, E. O., Scheuer, T., & Catterall, W. A. (2002). An unexpected role for brain-type sodium channels in coupling of cell surface depolarization to contraction in the heart. [In Vitro
- Research Support, Non-U.S. Gov't
- Research Support, U.S. Gov't, P.H.S.J. *Proc Natl Acad Sci U S A*, 99(6), 4073-4078. doi: 10.1073/pnas.261705699
- Marx, S. O. (1998). Coupled Gating Between Individual Skeletal Muscle Ca²⁺ Release Channels (Ryanodine Receptors). *Science*, 281, 818-821. doi: 10.1126/science.281.5378.818
- Marx, S. O., Gaburjakova, J., Gaburjakova, M., Henrikson, C., Ondrias, K., & Marks, A. R. (2001). Coupled Gating Between Cardiac Calcium Release Channels (Ryanodine Receptors). *Circulation Research*, 88, 1151-1158. doi: 10.1161/hh1101.091268
- McAllister, R. E., Noble, D., Tsien, R. W., & Haven, N. (1975). Reconstruction of the electrical activity of cardiac Purkinje fibres. *The Journal of physiology*, 251, 1-59.
- Meissner, G. (1994). Ryanodine receptor/Ca²⁺ release channels and their regulation by endogeneous effectors. *Annual Review of Physiology*, 56, 485-508.

- Nattel, S., Maguy, A., Bouter, S. L. E., & Yeh, Y.-h. (2007). Arrhythmogenic Ion-Channel Remodeling in the Heart : Heart Failure , Myocardial Infarction , and Atrial Fibrillation. *Physiological Reviews*, 87, 425- 456. doi: 10.1152/physrev.00014.2006.
- Nattel, S., Maguy, A., Le Bouter, S., & Yeh, Y. H. (2007). Arrhythmogenic ion-channel remodeling in the heart: heart failure, myocardial infarction, and atrial fibrillation. [Research Support, Non-U.S. Gov't Review]. *Physiol Rev*, 87(2), 425-456. doi: 10.1152/physrev.00014.2006
- Niggli, E., & Lederer, W. J. (1990). Voltage-Independent Calcium Release in Heart Muscle. *Science*, 250, 565-568.
- Noble, D., Garny, A., & Noble, P. J. (2012). How the Hodgkin-Huxley equations inspired the cardiac Physiome Project. *The Journal of physiology*. doi: 10.1113/jphysiol.2011.224238
- Noble, D., & Noble, S. J. (1984). A model of sino-atrial node electrical activity based on a modification of the DiFrancesco-Noble. *Proceedings of the Royal Society of London. Series B, Containing papers of a Biological character. Royal Society (Great Britain)*, 222, 295-304.
- Nygren, A., Fiset, C., Firek, L., Clark, J. W., Lindblad, D. S., Clark, R. B., & Giles, W. R. (1998). Mathematical model of an adult human atrial cell: the role of K⁺ currents in repolarization. *Circulation research*, 82, 63-81.
- Opie, L. H. (2004). *Heart Physiology: From cell to circulation*. (4rd edition ed.): Lippincott Williams & Wilkins.
- Orchard, C. H., Eisner, D. A., Allen, D. G., & Ringer, S. (1994). Sydney Ringer viewed in a new light. *Cardiovascular Research*, 28, 1765-1768.
- Page, E., McCallister, L. P., & Power, B. (1971). Stereological measurements of cardiac ultrastructures implicated in excitation-contraction coupling. *Proceedings of the National Academy of Sciences of the United States of America*, 68, 1465-1466.
- Pazoki, R., Wilde, A. a. M., & Bezzina, C. R. (2010). Genetic Basis of Ventricular Arrhythmias. *Current cardiovascular risk reports*, 4, 454-460. doi: 10.1007/s12170-010-0128-2

- Peskoff, A., & Langer, G. A. (1998). Calcium concentration and movement in the ventricular cardiac cell during an excitation-contraction cycle. *Biophysical journal*, 74, 153-174. doi: 10.1016/S0006-3495(98)77776-8
- Priebe, L., & Beuckelmann, D. J. (1998). Simulation Study of Cellular Electric Properties in Heart Failure. *Circulation Research*, 82, 1206-1223. doi: 10.1161/01.RES.82.11.1206
- Restrepo, J. G., & Karma, A. (2009). Spatiotemporal intracellular calcium dynamics during cardiac alternans. *Chaos*, 19, 1-15. doi: 10.1063/1.3207835
- Rice, J. J., Jafri, M. S., & Winslow, R. L. (1999). Modeling gain and gradedness of Ca^{2+} release in the functional unit of the cardiac diadic space. *Biophysical journal*, 77, 1871-1884.
- Richards, M. A., Clarke, J. D., Saravanan, P., Voigt, N., Dobrev, D., Eisner, D. A., . . . Dibb, K. M. (2011). Transverse (t-) tubules are a common feature in large mammalian atrial myocytes including human. *American journal of physiology. Heart and circulatory physiology*, 301, H1996-H2005. doi: 10.1152/ajpheart.00284.2011
- Rovetti, R., Cui, X., Garfinkel, A., Weiss, J. N., & Qu, Z. (2010). Spark-induced sparks as a mechanism of intracellular calcium alternans in cardiac myocytes. *Circulation research*, 106, 1582-1591. doi: 10.1161/CIRCRESAHA.109.213975
- Santana, L. F. F., Cheng, H., Gómez, A. M. M., Cannell, M. B. B., & Lederer, W. J. J. (1996). Relation between the sarcolemmal Ca^{2+} current and Ca^{2+} sparks and local control theories for cardiac excitation-contraction coupling. *Circulation research*, 78, 166-171.
- Savio-Galimberti, E., Frank, J., Inoue, M., Goldhaber, J. I., Cannell, M. B., Bridge, J. H., & Sachse, F. B. (2008). Novel features of the rabbit transverse tubular system revealed by quantitative analysis of three-dimensional reconstructions from confocal images. [Research Support, N.I.H., Extramural Research Support, Non-U.S. Gov't]. *Biophys J*, 95(4), 2053-2062. doi: 10.1529/biophysj.108.130617
- Schaub, M. C., & Heizmann, C. W. (2008). Calcium, troponin, calmodulin, S100 proteins: from myocardial basics to new therapeutic strategies. *Biochemical and biophysical research communications*, 369, 247-264. doi: 10.1016/j.bbrc.2007.10.082

- Schneider, M. F., & Chandler, W. K. (1973). Voltage dependent charge movement in skeletal muscle: a possible step in excitation-contraction coupling. *Nature*, 242, 244-247.
- Shannon, T. R., Wang, F., Puglisi, J., Weber, C., & Bers, D. M. (2004). A mathematical treatment of integrated Ca dynamics within the ventricular myocyte. *Biophysical journal*, 87, 3351-3371. doi: 10.1529/biophysj.104.047449
- Shiferaw, Y., Watanabe, M. A., Garfinkel, A., Weiss, J. N., & Karma, A. (2003). Model of intracellular calcium cycling in ventricular myocytes. *Biophysical journal*, 85, 3666-3686. doi: 10.1016/S0006-3495(03)74784-5
- Snyder, S. M., Palmer, B. M., & Moore, R. L. (2000). A mathematical model of cardiocyte Ca(2+) dynamics with a novel representation of sarcoplasmic reticular Ca(2+) control. *Biophysical journal*, 79, 94-115. doi: 10.1016/S0006-3495(00)76276-X
- Sobie, E. A., Dilly, K. W., dos Santos Cruz, J., Lederer, W. J., & Jafri, M. S. (2002). Termination of Cardiac Ca²⁺ Sparks: An Investigative Mathematical Model of Calcium-Induced Calcium Release. *Biophysical Journal*, 83, 59-78. doi: 10.1016/S0006-3495(02)75149-7
- Soeller, C., & Cannell, M. B. (1999). Examination of the Transverse Tubular System in Living Cardiac Rat Myocytes by 2-Photon Microscopy and Digital Image Processing Techniques. *Circulation Research*, 84, 266-275. doi: 10.1161/01.RES.84.3.266
- Stern, M. D. (1992). Theory of excitation-contraction coupling in cardiac muscle. *Biophysical journal*, 63, 497-517. doi: 10.1016/S0006-3495(92)81615-6
- Stern, M. D., Song, L.-s., Cheng, H., Sham, J. S. K. K., Yang, H. T., Boheler, K. R., & Ríos, E. (1999). Local control models of cardiac excitation-contraction coupling. A possible role for allosteric interactions between ryanodine receptors. *The Journal of general physiology*, 113, 469-489.
- ter Keurs, H. E. D., & Boyden, P. A. (2007). Calcium and Arrhythmogenesis. *Physiological reviews*, 87, 457-506. doi: 10.1152/physrev.00011.2006.
- Viswanathan, P. C., & Rudy, Y. (1999). Pause induced early afterdepolarizations in the long QT syndrome: a simulation study. *Cardiovascular research*, 42, 530-542.
- Wier, W. G., Egan, T. M., López-López, J. R., & Balke, C. W. (1994). Local control of excitation-contraction coupling in rat heart cells. *The Journal of physiology*, 474, 463-471.

- Williams, G. S. B., Chikando, A. C., Tuan, H.-T. M., Sobie, E. a., Lederer, W. J., & Jafri, M. S. (2011). Dynamics of Calcium Sparks and Calcium Leak in the Heart. *Biophysical journal*, 101, 1287-1296. doi: 10.1016/j.bpj.2011.07.021
- Williams, G. S. B., Huertas, M. a., Sobie, E. a., Jafri, M. S., & Smith, G. D. (2007). A probability density approach to modeling local control of calcium-induced calcium release in cardiac myocytes. *Biophysical journal*, 92, 2311-2328. doi: 10.1529/biophysj.106.099861
- Williams, G. S. B., Huertas, M. a., Sobie, E. a., Jafri, M. S., & Smith, G. D. (2008). Moment closure for local control models of calcium-induced calcium release in cardiac myocytes. *Biophysical journal*, 95, 1689-1703. doi: 10.1529/biophysj.107.125948
- Williams, G. S. B., Smith, G. D., Sobie, E. a., & Jafri, M. S. (2010). Models of cardiac excitation-contraction coupling in ventricular myocytes. *Mathematical biosciences*, 226, 1-15. doi: 10.1016/j.mbs.2010.03.005
- Winslow, R. L., Cortassa, S., O'Rourke, B., Hashambhoy, Y. L., Rice, J. J., & Greenstein, J. L. (2011). Integrative modeling of the cardiac ventricular myocyte. *Wiley interdisciplinary reviews. Systems biology and medicine*, 3, 392-413. doi: 10.1002/wsbm.122
- Winslow, R. L., Rice, J., Jafri, M. S., Marbán, E., & O'Rourke, B. (1999). Mechanisms of Altered Excitation-Contraction Coupling in canine tachycardia-induced heart failure, II: Model Studies. *Circulation Research*, 84, 571-586.

CHAPTER 2: ULTRA-FAST MARKOV-CHAIN MONTE CARLO ALGORITHM FOR CHANNEL GATING SIMULATION

Abstract

Mathematical modelling has been used as a powerful tool to represent the dynamics of a physical system, especially nonlinear systems. In mathematical physiology, one of the active research areas over the last fifty years has been the modeling excitation-contraction (EC) coupling in cardiac cells. The temporal dynamics of the system is represented by a set of differential equations, in which the changing of one or more dependent variables can tell how the cellular model behaves under different initial conditions. Many of the widely used computational models mainly use the deterministic approach, i.e. solving a set of ODEs with unknown variables are the concentrations of the species (e.g. $[Ca^{2+}]$) and gating variables (i.e. Hodgkin-Huxley-based models). These models, even though they seem to replicate some phenomenon, they fail to predict certain phenomena and often don't mechanistically explain the underlying cellular mechanism, e.g. high gain and gradedness of calcium release in excitation-contraction coupling. In addition, the elementary event of calcium release, Ca^{2+} sparks, is the result of the stochastic gating of individual calcium channels at which the small size of the channel cluster requires stochastic simulation.

The use of stochastic modelling, mainly Markov-Chain Monte Carlo (MCMC), though promising, face a rigid barrier of high computational demand, due to the state

space explosion and the massively huge number of computations. In this paper, a novel algorithm has been developed, which allows using Monte-Carlo simulation in an exact stochastic manner that is a thousand times faster than traditional methods. The method - Ultrafast Markov-Chain Monte Carlo (UMCMC) simulation - now opens a hope for studying the cellular event at tissue or whole-heart level, with the capability of incorporating the dynamics of ECC at the very detailed level.

Introduction

Cellular homeostasis is critical to the normal function of the cell (Carafoli, 1987; Dubyak, 2004). The ionic concentration of different chemical species between the intracellular and extracellular spaces, and in different cellular organelles are maintained by the opening and closing of associated ion channels. Among the different ion species, calcium is of particular importance that can determine the living or death of cells (Berridge, Bootman, & Roderick, 2003; Verkhratsky, 2007; Yu, Chang, & Tan, 2009). This is not only true for animal, but also for plants (Dodd, Kudla, & Sanders, 2010). Ryanodine receptors (RyR) and inositol triphosphate (IP3) are calcium channels located on the endoplasmic reticulum (ER) membrane; L-type calcium channels (LCC) are calcium channels located on the plasma sarcolemma. To study the calcium dynamics, the gating of ion channels are often modelled and simulated using an ensemble average approach in which the total currents can be approximated via the fraction of opening channels (Luo & Rudy, 1994; Shannon, Wang, Puglisi, Weber, & Bers, 2004).

$$I = N.P_o.i$$

with I is the whole-cell current, N is the total channels, i is the single-channel current and P_o is the opening probability at a given condition.

Since the discovery of calcium sparks (Cheng, Lederer, & Cannell, 1993), it's widely accepted that the elementary calcium release occurs at local sites in the cardiac myocytes. In cardiac ventricular myocytes, the micro domain of calcium release is a dyad subspace formed by a cluster of RyR2 (30-100 channels) on the terminal cristinae side and a smaller cluster of LCC on the T-tubular wall, in the case of cardiac myocyte, Figure

1. The dimension of this subspace is at the range of 10-15 nm height and 200-400 nm width. A similar phenomenon has also been found in other cell types, e.g. skeletal cells (Hollingworth, Peet, Chandler, & Baylor, 2001; Schneider & Klein, 1996) and smooth cells (Jaggar, Porter, Lederer, Nelson, & Jonathan, 2000; Nelson et al., 1995).

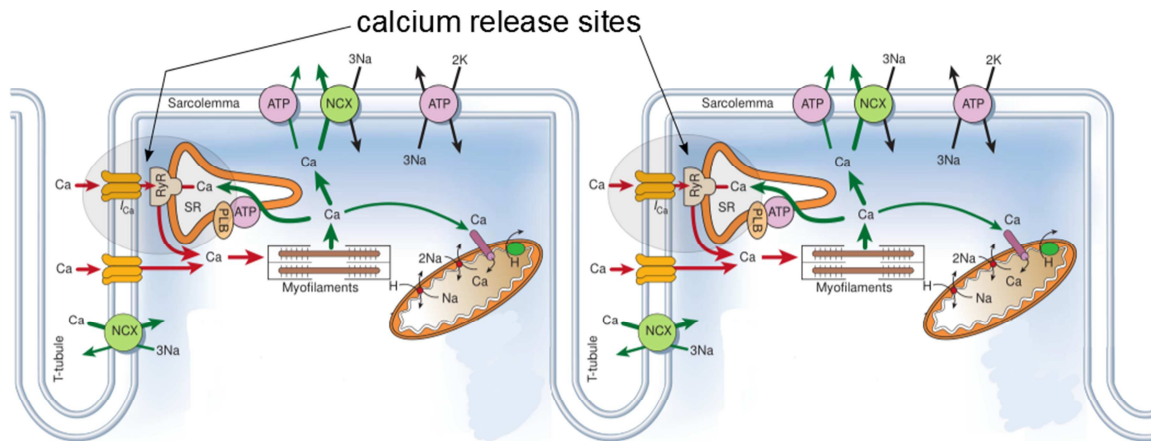


Figure 1. Calcium release sites (Adapted from (Donald M Bers, 2002))

Under the resting condition, without any electrical stimulus, spontaneous calcium sparks are observed (Cannell, Cheng, & Lederer, 1995; López-López, Shacklock, Balke, & Wier, 1994). This can be explained as the result of stochastic opening of one or more RyR2 which bring calcium concentration in the subspace higher. The higher calcium level facilitates other RyR2 channel opening via calcium-induced calcium release mechanism. Under calcium overload conditions where the mass of calcium releases are more frequent, these spontaneous sparks can become a calcium wave, which can lead to abnormal contraction of the cell (Cheng, Lederer, Lederer, & Cannell, 1996). Apart from

the observable calcium release, there is also a significant amount of hidden calcium leak which, if not being regulated properly, can cause an unbalanced in intracellular homeostasis (Kubalova et al., 2005; Lukyanenko, Viatchenko-Karpinski, Smirnov, Wiesner, & Györke, 2001; Tateishi et al., 2009). Calcium leak can link to several diseases, e.g. CPVT and Duchenne muscle dysfunction (Fauconnier et al., 2010; Lehnart et al., 2004). Several efforts have been made to explain this phenomenon using computational models (Hashambhoy, Greenstein, & Winslow, 2010; Eric A. Sobie, Dilly, dos Santos Cruz, Lederer, & Jafri, 2002; Eric a Sobie et al., 2006; Williams et al., 2011).

This raises the question of the predictive capability of existing computational models that are either deterministic and/or ignore the stochastic nature of calcium release. However, the major challenge when building a whole-cell model that possesses such features of stochastic calcium release is the high computational demand. In each ventricular myocyte, there are about 20,000 or more calcium release sites (Cheng et al., 1993). In cardiac myocyte, each release site is a heterogeneous cluster of RyR2s and LCCs. There are 30-300 RyR2s in a release site (Franzini-Armstrong, Protasi, & Ramesh, 1999). The RyR2:LCC ratio is 4:1 in guine pig, 5.6:1 in human and 8:1 in rat (Donald M. Bers & Stiffel, 1993). Due to the stochastic nature of Ca^{2+} release at each release site, the gating of channels should be modelled using a stochastic approach in which each channel can be modelled using a proper Markov-chain scheme. As channel gating is fast, a very small time-step is needed to guarantee numerical stability and accuracy of channel gating behavior (Keener, 2006). This paper introduces a novel algorithm for simulating the gating of these channels stochastically using any given Markov-model for RyR2 and

LCC, as shown in Figure 2. Sect. 1 introduces different approaches to use Markov-based model in a simulation. Sect.2 discusses the previous methods used for simulating gating of ion channels in cardiac cells. In Sect.3 and Sect. 4, we introduce the two different versions of the novel methods, called Ultra-fast Markov chain Monte-Carlo simulation.

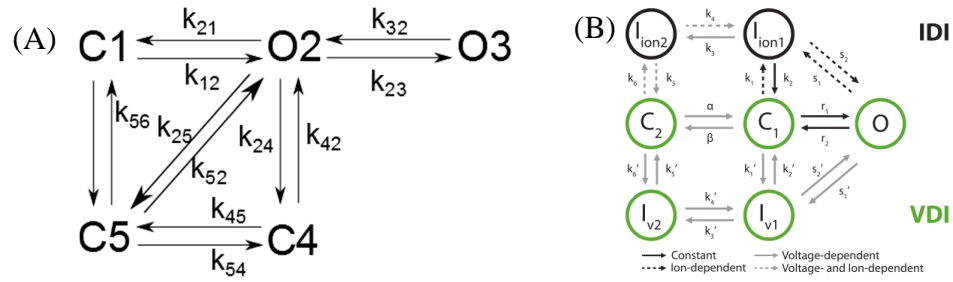


Figure 2. Markov-model of L-type Ca^{2+} channel (A) (Sun, Fan, Clark, & Palade, 2000), (B) (Morotti, Grandi, Summa, Ginsburg, & Bers, 2012)

Algorithm Development

Markov-Chain Monte Carlo (MCMC) simulations are widely used across many fields, including chemistry, finance, biology, ionic channel modeling, engineering ... to describe a dynamics system (Chib, 2001; Brooks and Brookst, 2010; Siekmann et al., 2011). A Markov model is a finite sequence of states, Figure 2, in which the transition from one state to another is a random process with Markov property. It means the process is memoryless; as the transition to the next state only depends on the present state, but not the past. Typically, the Markov chain is stationary or time-homogeneous. In such cases, the transition matrix \mathbf{P} is the same after each time step. However, in the case of channel gating, where the opening or close of ion channels depends not only on its intrinsic

property, but also the surrounding media, at which the change in ionic concentration or transmembrane voltage can enhance or inhibit its gating. Such process is time-inhomogeneous and the transition matrix needs to be updated after every step. This increases the computational cost of the simulation, even for a midsize system. Several methods have been developed to solve these types of stochastic systems including Stochastic Petri Nets, Stochastic Automata Networks, and Vectorized Gating.

Stochastic Petri Nets (SPNs) are isomorphism to Markov models which have been widely used to model a continuous time parallel systems (Molloy, 1982). There are two classes of nodes in a SPN: *places* (represented by circles) and *transition* (represent by rectangles). A directed *arc* connects a node on one place to a transition, and one transition to another place, as shown in Figure 3. It's a time-homogeneous system and is typically assumed the transition firing rate is an exponential distribution (Choi, Kulkarni, & Trivedi, 1994). A place in SPN contains a number of *tokens* (represented by dot or black-filled circle), where the state of a SPN is defined by the number of tokens in each place. So, it's a k -tuple $m = (\#(p_1), \#(p_2), \dots, \#(p_k))$ with $\#(p_i)$ is the number of tokens in place i , and k is the number of places. To model the stochastic nature of the system, the master equation is what gives stochastic Petri nets their name. Again, the major problem with chemical master equation is the high computational demands where a large set of pseudo-random numbers are generated, for all chemical reactions while only one is used.

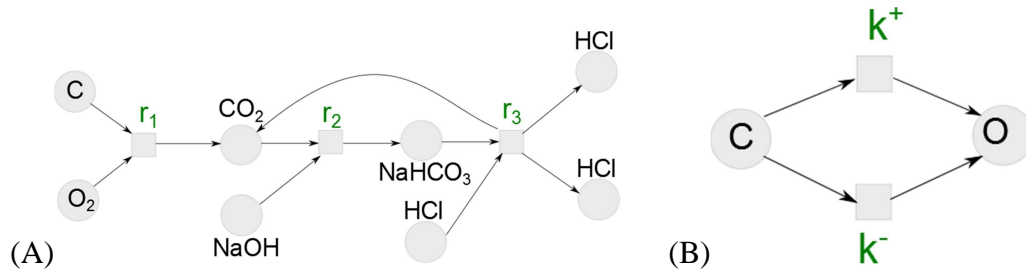


Figure 3. An example of a Petri Net for (A) a system of chemical reactions; (B) channel gating

SPNs focus on modelling local places, where the number of states is small (Lamprecht, Smith, & Kemper, 2009). In a Markov model, the states represents all the components in that model which thus can be used to model complex systems. To deal with state space explosion in Markov model, a modular approach called Stochastic Automata Network (SAN) which uses tensor product and tensor sum was developed (Plateau and Atif, 1991; Plateau and Stewart, 2000). SAN is a modular approach that allows modeling Markov-based system with a large state space using Kronecker product operation from local modular systems of smaller sizes (Langville & Stewart, 2004). The modules in SAN can be independent to each other or interacting to each other at a certain level. For example, based on the Markov model of a single channel, we have to build the Markov model for the system containing a number of channels in which the state is represented by a vector combining the states of individual channels. In a system that has more than one module, e.g. more than one types of channels (RyR and LCC in our case), Kronecker operations are used to generate the Markov model of this heterogeneous cluster. These Kronecker-based Markovian representations have been widely discussed in computer sciences (Benoit et al., 2004; Buchholz and Dayar, 2004; Buchholz and

Kemper, 2004), yet its applications, along with Petri Nets, to computational biology, especially cardiac cell modeling is still limited (Chin and Willsky, 1989; Schulz-Trieglaff, 2005; Lamprecht et al., 2009).

Smith and colleagues first applied and extended the method to channel gating based on the concept of vectorized gating (Smith, 2002). Despite the mathematical beauty of this method, the time-inhomogeneous nature at each calcium release site requires the transition rates of the system to be updated at every time step, which in turn requires the recalculation of tensor operators as well. This degrades the performance of the systems, or it requires a significant large amount of memory in keeping track of the large state space if tensor operators are avoided. The details of the method will be described below, and the improvement to resolve the practical limitations in the method, where the system is dynamic in the sense that the transition from one state to another need to be updated frequently.

Vectorized-gating of a continuous-time, discrete-state Markov chain

A continuous-time, discrete-state Markov chains (CTMC) is a stochastic process with a discrete state space Ω , with N states, as shown in Figure 4. Depending on the nature of the system, its state at time t can be represented by a single k -tuple vector that keeps the state index of individual components in the system, each component is also represented by a CTMC. The transition rates k_{ij} between two state S_i and S_j can be mapped to the probability for the state transition from S_i to S_j before time $(t + \Delta t)$. The dwell-time, or the time spent continuously in state S_i is a random variable with an

exponential distribution whose rate constant is equal to the sum of all transition rates exiting state S_i (Colquhoun & Hawkes, 1981).

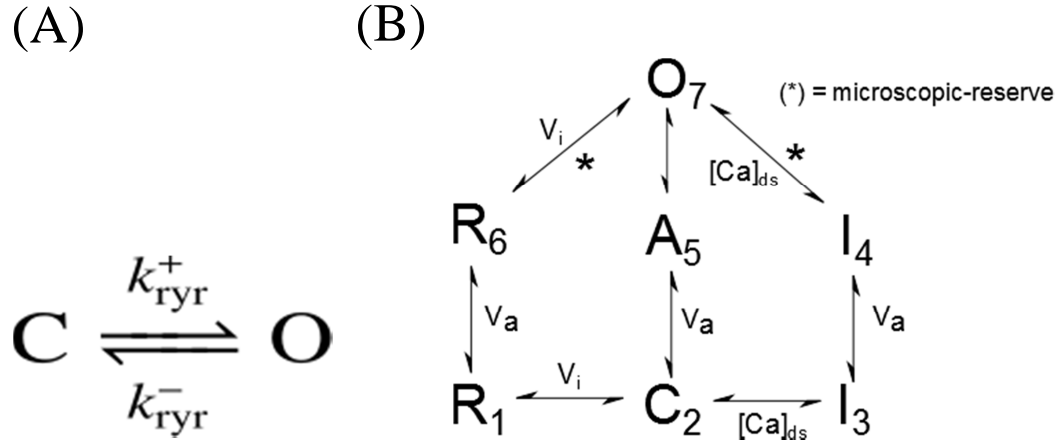


Figure 4. (A) A minimal 2-state model of RyR, (B) A 7-state model of LCC

A traditional approach is to generate two pseudo-random numbers, one to determine which is the next states and one to determine the dwell-time for the next transition to occur, based on the transition probability from the current state of a channel to the next possible states, Figure 5. In a cluster of many channels, an IF statement for each channel is used to determine the next state. This method is slow due to the sequential investigation of channel gating, the large amount of data is required to keep track of individual channel states, and the inefficient using of the pseudo-random numbers as many are generated but only one is really chosen.

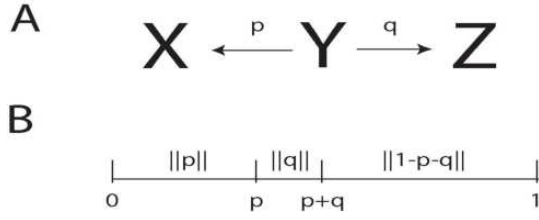


Figure 5. (A) A state diagram with Y is the current state, while X, Z are two potential future state. (B) A uniform pseudo-random number [0,1] determines the state transition

Mathematically, to model single channel gating, Q-matrix method is often used (Colquhoun, 1999; Colquhoun & Hawkes, 1994; David Colquhoun & Alan G Hawkes, 2009; David Colquhoun & Alan G. Hawkes, 2009). Consider a single channel of $m=2$ states, Figure 6, the matrix that represents the transition from one state to another

$Q=[q_{ij}]$ is coined the infinitesimal generator or Q-matrix: .

$$B_{2 \times 2} = \begin{bmatrix} X & c_{1,2} \cdot \phi \cdot f_1(C_{ds}) \\ c_{2,1} & X \end{bmatrix}$$

with $c_{1,2} = k^+$, $c_{2,1} = k^-$ are the two rate-constants. X represents the diagonal elements which are chosen in such a way that the row sum is always zero. Here, each off-diagonal element can be used to infer the probability per unit time transition from one state to another.

$$q_{ij} = \lim_{\Delta t \rightarrow 0} \frac{P(S(t + \Delta t) = j | S(t) = i)}{\Delta t}; i \neq j$$

If the time-step is chosen small enough, then the probability for state transition

$$P(S(t + \Delta t) = j | S(t) = i) = q_{ij} \times \Delta t$$

while the probability for state unchanged is

$$P(S(t + \Delta t) = i | S(t) = i) = 1 + \left(- \sum_{\forall j \neq i} q_{ij} \right) \times \Delta t = 1 + q_{ii} \times \Delta t$$

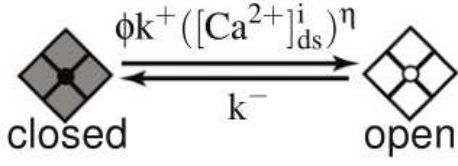


Figure 6. A two-state model of RyR (Williams et al., 2011)

Smith and colleagues applied this Q-matrix method for a single channel to a cluster of $m=2$ states RyR channels (Groff & Smith, 2008b; Nguyen, Mathias, & Smith, 2005) where the Q-matrix for the cluster of N identical and independent channels can be generated using Kronecker operator.

$$\mathbf{Q}^{(N)} = \bigoplus_{n=1}^N \mathbf{Q}^{(1)} = \sum_{n=1}^N \mathbf{I}^{(N-n)} \otimes \mathbf{Q}^{(1)} \otimes \mathbf{I}^{(n-1)}$$

with $\mathbf{I}^{(n)}$ is the identity matrix of size m^n . An example with $N=2$ is given below

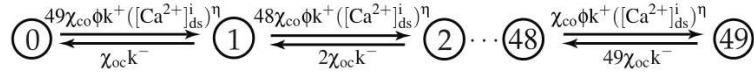
$$\mathbf{Q}^{(2)} = \mathbf{Q}^{(1)} \oplus \mathbf{Q}^{(1)} = \mathbf{Q}^{(1)} \otimes \mathbf{I}^{(1)} + \mathbf{I}^{(1)} \otimes \mathbf{Q}^{(1)}$$

with $\mathbf{Q}^{(1)}$ is the Q-matrix for the single channel, \oplus is the Kronecker sum and \otimes is the

Kronecker product (Langville & Stewart, 2004). The method is impractical in the case of large cluster and each channel has more than 2-state due to the memory expansion of state space and the high computational cost of evaluating the matrix every time due to the time-inhomogeneous of the system.

To reduce the number of state, the spatial arrangement of these ion channels can be ignored and one common assumption is that each channel experiences the same local calcium concentration that depends only on the number of open channels (i.e. mean-field

coupling) (Groff & Smith, 2008a, 2008b). Consider a cluster of 50 two-state RyR channels



Then the state-space is a set of vector, each one is a k -tuple ($k=2$), in which the i -th element tell how many channels in state S_i ($i=1..m$).

$$\text{SVS}_{\text{RyR}} = \begin{bmatrix} 49 & 0 \\ 48 & 1 \\ 47 & 2 \\ \cdots & \cdots \\ 0 & 49 \end{bmatrix}$$

This reduces the number of state from N^m to $\frac{(N+m-1)!}{N!(m-1)!}$. Using the vectorized-

computing of exact stochastic channel gating, the assumption changed from “one channel can change the state at a time” to “the total channels in the cluster that can change the state is maximum one. Here is the example of valid and invalid state transition for a cluster of 5 channel, each with 7-state

$$\begin{aligned} \text{VALID:} \quad & \text{SVS}_{\text{LCC}}(i) = [2 \quad 2 \quad 1 \quad 0 \quad 0 \quad 0 \quad 0] & (1) \\ \text{INVALID:} \quad & \text{SVS}_{\text{LCC}}(j) = [1 \quad 2 \quad 1 \quad 0 \quad 0 \quad 1 \quad 0] & (2) \\ \text{INVALID:} \quad & \text{SVS}_{\text{LCC}}(k) = [1 \quad 1 \quad 2 \quad 0 \quad 0 \quad 1 \quad 0] & (3) \\ \text{INVALID:} \quad & \text{SVS}_{\text{LCC}}(k) = [0 \quad 2 \quad 1 \quad 0 \quad 0 \quad 2 \quad 0] & (4) \end{aligned}$$

2

Using the schematic diagram of 7-state channel in Figure 4(B), there is no direct state transition from state (2) to state (6). So, the indirect state transition given below is not acceptable, even though there is only one channel changes the state. The method was

tested and showed only a very small difference compared to examining individual channels explicitly.

$$\text{SVS}_{\text{LCC}}(i) = \begin{bmatrix} 2 & 2 & 1 & 0 & 0 & 0 & 0 \end{bmatrix}$$

Indirect: (1) \rightarrow (6), (2) \rightarrow (1) :

$$\text{SVS}_{\text{LCC}}(k') = \begin{bmatrix} 2 & 1 & 1 & 0 & 0 & 1 & 0 \end{bmatrix}$$

INVALID: (2) \rightarrow (6)

To extend the Q-matrix method to a cluster, based on (Groff & Smith, 2008b; Williams et al., 2011), the Q-matrix for a single channel can be decomposed into component matrices so that the matrix elements are constant values.

$$B_{2 \times 2} = \underbrace{\begin{bmatrix} X & 0 \\ c_{2,1} & X \end{bmatrix}}_{B_1} + \phi \cdot f_1(C_{\text{ds}}) \underbrace{\begin{bmatrix} X & c_{1,2} \\ 0 & X \end{bmatrix}}_{B_2}$$

Similarly, the LCC cluster, for the model given in Figure 4(B), can be decomposed into matrices the same way

$$A_{7 \times 7} = \begin{bmatrix} X & c_{1,2} & 0 & 0 & 0 & c_{1,6} \cdot f(V_a) & 0 \\ c_{2,1} \cdot g(V_i) & X & c_{2,3} \cdot h(C_{\text{ds}}) & 0 & c_{2,5} \cdot f(V_a) & 0 & 0 \\ 0 & c_{3,2} & X & c_{3,4} \cdot f(V_a) & 0 & 0 & 0 \\ 0 & 0 & c_{4,3} & X & 0 & 0 & k_{4,7} \\ 0 & c_{5,2} & 0 & 0 & X & 0 & c_{5,7} \\ c_{6,1} & 0 & 0 & 0 & 0 & X & k_{6,7} \\ 0 & 0 & 0 & c_{7,4} \cdot h(C_{\text{ds}}) & c_{7,5} & c_{7,6} \cdot g(V_i) & X \end{bmatrix}$$

$$\mathbf{A}_{7 \times 7} = \mathbf{A}_1 + f(V_a) \cdot \mathbf{A}_2 + g(V_i) \cdot \mathbf{A}_3 + h([Ca]_{\text{ds}}) \cdot \mathbf{A}_4$$

The state of the heterogeneous cluster of RyR2 and LCC now can be represented by a k -tuple vector ($k = m_{\text{RyR}} \times m_{\text{LCC}}$) whose elements keep the number in each state.

When dealing with this heterogeneous cluster of RyR2 and LCC, there are two strategies to estimate the probability of state transition from one cluster state to another: (1) keep

component-matrices separated and use the Kronecker operator to calculate the heterogeneous Q-matrix at every step, (2) using Kronecker operator to build the component matrices at one time, and then estimate the transition rate at every step. There are pros and cons for each approach. The first method requires less memory, yet it uses Kronecker operators at every time step which take more time in computing. Consider the second approach, with the heterogeneous Q-matrix is

$\mathbf{Q} = K_{A_1} + f(V_a) \cdot K_{A_2} + g(V_i) \cdot K_{A_3} + h(C_{ds}) \cdot K_{A_4} + K_{B_1} + \phi \cdot f_1(C_{ds}) K_{B_2}$
with \mathbf{K}_{A_i} , \mathbf{K}_{B_i} represent the component matrix of the heterogeneous cluster that can be

generated from the corresponding component matrix of a single cluster. The size of each matrix is given by the formula

$$\frac{(N_{LCC} + m_{LCC} - 1)!}{N_{LCC}! (m_{LCC} - 1)!} \times \frac{(N_{RyR} + m_{RyR} - 1)!}{N_{RyR}! (m_{RyR} - 1)!}$$

Consider the case $N_{LCC} = 7; m_{LCC} = 7; N_{RyR} = 49; m_{RyR} = 2$. The size of the state space is $1716 \times 50 = 85,800$. A double-precision matrix of this size would requires ~ 7 (GB) of memory.

Ultra-fast Markov chain Monte-Carlo algorithm (version 1)

The first version of the UMC MC algorithm was developed based on the following remarks.

REMARK 1: The individual component matrices of the homogeneous / heterogeneous cluster are highly sparse: so each component matrix \mathbf{K} is now represented using two compact-form matrices \mathbf{cK} and \mathbf{iK} .

- $\mathbf{cK}[:,i] = \text{keep the rate constant of reachable states (i.e. non-zero)}$

- $iK[:,i]$ = keep the ‘true’ state-index of the corresponding reachable state

The compact-form matrix of a single cluster can be generated from the component matrices of a single channel using the method given in Appendix. Then, if there are two or more clusters, the compact-form matrix of the heterogeneous cluster can be generated from the compact-form matrix of individual clusters by combining the compact-form matrices between the clusters using the method given in the Appendix.

The question is how many columns for each compact-form component matrix cK ? Regardless of how big of the cluster, the nature of exact stochastic simulation requires that the reachable states is limited by the number of connection in the Markov-model of a single channel. Assuming that we can put one channel to each state ($N > m$), then this k -tuple vector is the state that has the most number of neighbors. This is equal to the total number of non-zero diagonal elements

```
numNeighbor = 0
DO ii = 1, nState
  numNeighbor += count (reachable_state(A(ii,:))
END DO
```

with *reachable_state()* is the function that returns the number of connection from state *ii*-th.

When $N < m$, if we sort the channel state in the order of descending number of neighbors; then the k -tuple vector of the state that has the most number of neighbors is the one that has at least one channel in as many channel index as possible in that order.

Thus, the pseudo-code for a more generalized approach is used

```
numNeighbor = 0
DO ii = 1, nState
  V(ii) = count (reachable_state(A(ii,:))
END DO
```

```
Vsorted = sort_descending(v)
numNeighbor = SUM(select_MIN(N,m)_largest_number(vsorted))
```

When a heterogeneous cluster is used: the number of columns is:

```
numNeighbors_RYR + numNeighbors_LCC
```

REMARK 2: Depending on the type of a problem, in our case, most of the time (90%) the channel doesn't change the state (Groff, DeRemigio, & Smith, 2009; Smith, 2002). So, to avoid unnecessary calculation, the diagonal values of the matrices are moved to the first column in each compact-form matrix.

- $\mathbf{cK}[:,1]$ = keep the rate constant of state-unchanged
- $\mathbf{iK}[:,1] = \mathbf{i}$

Given that s is the current state index of the heterogeneous cluster, then the transition rate for the first column is calculated as follows

$$\mathbf{cQ}(s, 1) = \mathbf{cK}_{A_1}(s, 1) + f(V_a) \cdot \mathbf{cK}_{A_2}(s, 1) + g(V_i) \cdot \mathbf{cK}_{A_3}(s, 1) + h(C_{ds}) \cdot \mathbf{cK}_{A_4}(s, 1) + \mathbf{cK}_{B_1}(s, 1) + \phi \cdot f_1(C_{ds}) \mathbf{cK}_{B_2}(s, 1)$$

REMARKS 3: If strategy one is used, instead of using two separate vectors, one to keep the index of the state in RyR2 cluster and the other one to keep the index of the state in LCC cluster, a single one can be used and the index of individual cluster-state can be determined using the formula

```
s = (LCCcluster_state-1) * size_RYR + RYRcluster_state
LCCcluster_state = (s-1)/size_RYR + 1
RYRcluster_state = s - (s-1)*size_RYR
```

with `size_RYR` is the number of state for the RyR cluster. This can be easily extended to multiple clusters.

REMARK 5: A state transition occurs when either a single LCC or a single RyR changes the state, but not both at each step. So, the transition rate can be extracted from a single (row,col) of one of the component matrices. The use of compact-form of matrix for Kronecker products/sums has been used in SAN networks (Langville & Stewart, 2004), however, it was limited to stationary Markov-models and the matrices need to be incompact before doing Kronecker product. The new method allows us to compute the new matrix for both stationary and non-stationary Markov-models, as well as the new matrix can be generated without incompacting - in essence for our specific case calculating Kronecker products of compact matrices.

Ultra-fast Markov chain Monte-Carlo algorithm (version 2)

The first version of the UMCMC method requires that the Q-matrix Markov-model is broken down into a number of components matrices in which the data elements having the same functional form of the transition rates are grouped into a single component matrix. Depending on the structure of the Markov-model, we may have a few or more number of component matrices. In some cases, the increasing in the number of component matrices can make the implementation of the algorithm difficult. In other words, a significant modification of the code is required to adopt a new model.

An example is the L-type Ca^{2+} channel model developed by (Sun et al., 2000). In this model, each state transition has its own functional form of either membrane voltage or calcium concentration. To resolve this problem, a second version of the UMCMC algorithm was developed. Instead of building the compact-form of the component

matrices that stores the rate constants, we only need to build the single compact-form matrix that keeps the number of channels for the state transition **cKfromto**[], and, for the case of non-stationary Markov-models, recalculate the Markov model at the single channel only. The performance is the same, yet the method is more generalized and can be applied to any Markov-model of channel gating scheme.

```
Krateconstant [] <- single channel matrix of rate constant
Ktransitionrate [] <- single channel matrix of transition rate
iK [] <- compact-form matrix of state-index
cKfromto [] <- compact-form matrix
StateSpaceVector [] <- each row is a k-tuple of state-vector
```

Consider the example of 5-state LCC developed by (Sun et al., 2000), we have

1LCC of 5-state					1LCC of 5-state				
StateSpaceVector[]					iK[:,0:numMaxNeighbors]				
1	0	0	0	0	2,	2,	5,	0,	0
0	1	0	0	0	4,	1,	3,	4,	5
0	0	1	0	0	1,	2,	0,	0,	0
0	0	0	1	0	2,	2,	5,	0,	0
0	0	0	0	1	3,	1,	2,	4,	0

Due to the small number of state in a Markov-scheme for a single channel, we only need 8-bits to keep the state index. Each element in the matrix **cKfromto**[] is 32-bit and is organized as

```
1LCC of 5-state
4-byte integer:
.....|.....|.....|.....
                    from      to
```

Here, only the lower 16-bits are used. This is more than enough, as a typical Markov-model of a single entity do not have more than 255 states. Example: The state 1

has two neighbors (2, and 5) which can be decoded as two values 258 and 261 in the matrix **cKfromto[]**.

Example: state [i=1] has 2 neighbors

```
cKfromto[1,1] = 258 = {from=1,to=1}
cKfromto[1,1] = 261 = {from=1,to=2}
```

1LCC of 5-state

```
cKfromto[]
0, 258, 261, 0, 0
0, 513, 515, 516, 517
0, 770, 0, 0, 0
0,1026,1029, 0, 0
0,1281,1282,1284, 0
```

The pseudo-code for the algorithm is given below

Algorithm

```
FOR ii=1,iK[s,0] //browser all neighbors
  detect_fromto(iK[s,ii],from,to)
  cQ[s,ii] = Ktransitionrate[from,to] * VectorStateSpace[s,from]
  compPdt[sfu] += cQ[s,ii]
ENDDO
compPdt[sfu] = - compPdt[sfu] // diagonal value (negative)
```

Implementation and Performance analysis

The first version of the algorithm was implemented in Fortran and then CUDA Fortran to run on C1060 GPU. Using a system of 10,000 release units, each one has 50 RyRs. For one second of simulation, the algorithm was compared with traditional Monte-Carlo simulation and Vectorized-gating method developed by Smith and colleagues implemented in MatLab.

Table 1. Performance comparison

Method	Original	MATLAB	Fortran	GPU
Runtime	11000 min	110 min	20 min	45 sec
Speedup	1x	100x	550x	14,667x

Running at the whole-cell level, the second version runs about 1.1x faster the first version of the code. The pros of the second version is that the amount of memory is smaller, and thus it can be used for significant larger systems, as well as it can be used with any Markov-model of the ion channels.

Appendix

Generate the compact-form matrix for a single cluster.

Consider a single component matrix **Ai** for LCC, the compact-form matrix is denoted as **cK_LAi**, and the index-matrix is **iK_LAi**

```
U_vector(size_L, mL) : the vector space, each row is a mL-  
tuple                                vector that represent the  
single state of                      the LCC-cluster  
cK_LAi(size_L, maxNeighbor_LAi)  
iK_LAi(size_L, maxNeighbor_LAi)  
  
DO ii = 1, size_L  
  kk  <- 1  
  sum <- 0  
  DO jj = 1, size_L  
    IF (valid_state_change(U_vector(ii,:),  
U_vector(jj,:)) THEN  
      stateFrom <- the state index that has a channel  
change  
      stateTo <- the state index that the channel jump  
to  
      cK_LAi(ii, ++kk) = U_vector(ii,stateFrom) *  
                          Ai(stateFrom, stateTo)  
      sum += cK_Lai(ii, kk)  
    ENDIF  
  ENDDO  
  cK_Lai(ii,1) = -sum  
  iK_LAi (ii,1) = ii  
ENDDO
```

Generate the compact-form matrix for the heterogeneous cluster

Here, no Kronecker operator is required to generate the matrix.

```
cK_L = compact matrix of single cluster LCC  
cK_R = compact matrix of single cluster RyR  
size_hete = size_LCC * size_RyR  
cK(size_hete, maxNeighbor); iK(size_hete, maxNeighbor)  
!!! LCC  
cK <- cK_L  
DO ii = 1, irow_LCC  
  DO kk = 1, maxnk
```

```

        IF (ABS(cK(ii,kk)) > 0) THEN
            cK((ii-1)*size_RYR + 1 : ii*size_RYR, kk) =
cK_L(ii,kk)
            idxK((ii-1)*size_RYR + 1 : ii*size_RYR, 0) =
idxK_L(ii,0)
            DO jj=1, size_RYR
                idxK((ii-1)*size_RYR + jj, kk) =
(idxK_L(ii,kk)-1)*size_RYR + jj
            ENDDO
        ENDIF
    ENDDO
ENDDO

!!! RyR:
cK <- cK_R
DO ii = 1, size_hete, size_RYR
    cK(ii:ii+size_RYR-1, 1:maxnkR) = cK_R(1:size_RYR,
1:maxnkR)
    idxK(ii:ii+size_RYR-1, 0) = idxK_R(1:size_RYR, 0)
ENDDO
DO ii = 1, size_RYR
    DO jj = 1, maxnkR
        IF (ABS(cK_R(ii,jj)) .GT. EPS) THEN
            DO kk = 1, Mbig, size_RYR
                idxK(kk+ii-1, jj) = kk-1 + idxK_R(ii,jj)
            ENDDO
        ENDIF
    ENDDO
ENDDO

```

Program structure

A Markov-model for the ion channel is passed into the program by an ASCII input file. An example of the input for L-type channel is given as follows:

```

# num states (the state can be resting, inactivated, close,
open)
6
# which state is open-state (00 =
closed/resting/inactivated, 01 = open)
00,01,01,00,00,00
# initial state for channels (closed state)
6
#####P_dhpr_T (permeability), 10^-6 L/sec

```

```

1.91213d-4
#rate transition
01,02,0.110d0
02,03,0.7d0
05,02,1.0d0
06,01,1.0d0
02,05,0.5d0
02,01,0.60d0
01,06,1.0d0
02,04,0.8d1

```

- The comment lines start with a # character
- The first non-comment line specifies the number of state in the Markov
- The next non-comment line is a vector, which either 00 or 01 value. It specifies whether the state of the corresponding index is conducting or not.
- The next non-comment line specifies the initial state for the model
- The next non-comment line specifies the whole-cell channel conductance or permeability
- The lines after that explain the transition rate constants in the format: *from, to, value*. Those not written heres means get value zero, i.e. no connection between the states

A function with the prototype given below is used to read-in this Markov

structure

```

read_LCC_Markov(LCC_Markov_filename, lcc_Krateconstant, mL,
iU_L,
lcc_initialstate, P_dhpr_T)

```

with

- LCC_Markov_filename: the name of the input file
- lcc_Krateconstant: the matrix for the Markov model

- mL : number of states for the single channel
- iU_L: the vector with 00 or 01
- lcc_initialstate: the initial state for each channel
- P_dhpr_T: the whole-cell channel permeability

The compact-form of the cluster will be defined by a function with the prototype

```
setup_LCC (lcc_Krateconstant, N_L, mL, iU_L, &
          lcc_stateFromTo, lcc_indxK, &
          U_Lo, irow_L, lcc_StateSpace, lcc_maxNumNeighbors)
with
```

- lcc_stateFromTo [irow_L, maxNumNeighbors]: keep track two state indices: *from* and *to*, at the single channel level corresponding to a cluster-state transition
- lcc_indxK [irow_L, maxNumNeighbors]: keep track the index of the cluster-state
- U_Lo [irow_L]: the vector keep the number of conducting channels in each cluster-state
- irow_L: the total number of cluster-state
- lcc_StateSpace [irow_L, mL]: the matrix with each row represent a cluster-state, i.e. each index of the vector tells how many channel in that state of the channel

When using CUDA-enabled GPU, a separate set of data are allocated on GPU.

```
REAL(KIND=dp), DIMENSION(:,:), ALLOCATABLE, device ::
```

```

        lcc_Ktransitionrate_dev, lcc_Krateconstant_dev,
        lcc_compK_dev
INTEGER, DIMENSION(:,:), ALLOCATABLE, device ::
        lcc_stateFromTo_dev, lcc_indxK_dev,
lcc_StateSpace_dev

```

Initially, the transition rates are calculated and copied to GPU

```

INCLUDE "Update_LCC_model.inc"
lcc_Ktransitionrate_dev = lcc_Ktransitionrate

```

During the course of the simulation, when there is a change in voltage or calcium concentration, the whole matrix will be recalculated and updated in the GPU. The code is designed so that another model can be used by replacing the content of “Update_LCC_model.inc” with a new one. The state transition rates at each release site are executed on GPU using the kernel *get_compPdt()*, from which the next time-step is calculated. Using the calculated time-step the next-states for all release sites are calculated in a different kernel *update_SFU()*.

```

CALL get_compPdt <<<gridSize, blockSize>>> ()
cuErr = cudaDeviceSynchronize()
min_Pdt = min_reduce_double_2host(compPdt_dev(1:NSFU),
NSFU, odata_d)
dtmax = -0.1d0/min_Pdt
dt = MAX(MIN(dtmax,dt_UB),dt_LB)

CALL update_SFU <<<gridSize, blockSize>>> &
        (X_r_dev((iinner-1)*NSFU+1:iinner*NSFU), &
        dt, Vm, dp_arg1, dp_arg2, Ca_myo, Ca_nsr)

<update bulk data where gating variables are updated>

```

REFERENCES

- Berridge, M. J., Bootman, M. D., & Roderick, H. L. (2003). Calcium signalling: dynamics, homeostasis and remodelling. *Nature reviews. Molecular cell biology*, 4, 517-529. doi: 10.1038/nrm1155
- Bers, D. M. (2002). Cardiac excitation-contraction coupling. *Nature*, 415, 198-205.
- Bers, D. M., & Stiffel, V. M. (1993). Ratio of ryanodine to dihydropyridine and skeletal muscle and implications receptors in cardiac for E-C coupling. *American Journal Of Physiology*, 264, C1587-C1593.
- Cannell, M. B., Cheng, H., & Lederer, W. J. (1995). The control of calcium release in heart muscle. *Science (New York, N.Y.)*, 268, 1045-1049.
- Carafoli, E. (1987). Intracellular calcium homeostasis. *Annual review of biochemistry*, 56, 395-433.
- Cheng, H., Lederer, M. R., Lederer, W. J., & Cannell, M. B. (1996). Calcium sparks and $[Ca^{2+}]_i$ waves in cardiac myocytes. *The American journal of physiology*, 270, C148-159.
- Cheng, H., Lederer, W. J. J., & Cannell, M. B. (1993). Calcium Sparks: Elementary Events Underlying Excitation-Contraction Coupling in Heart Muscle. *Science*, 262, 740-744.
- Choi, H., Kulkarni, V. G., & Trivedi, K. S. (1994). Markov regenerative stochastic Petri nets. *Performance Evaluation*, 20(1-3), 337-357.
- Practical analysis of single channel records 101-139 (1999).
- Colquhoun, D., & Hawkes, A. G. (1981). On the Stochastic Properties of Single Ion Channels. *Proceedings of the Royal Society of London. Series B, Biological Sciences*, 211, 205-235.
- The interpretation of single channel recordings 141-188 (1994).

- The principles of the stochastic interpretation of Ion-channel mechanisms 397-483 (Springer US 2009).
- A Q-matrix cookbook 589-633 (Springer US 2009).
- Dodd, A. N., Kudla, J., & Sanders, D. (2010). The language of calcium signaling. *Annual review of plant biology*, 61, 593-620. doi: 10.1146/annurev-arplant-070109-104628
- Dubyak, G. R. (2004). Ion homeostasis, channels, and transporters: an update on cellular mechanisms. *Advances in physiology education*, 28, 143-154. doi: 10.1152/advan.00046.2004
- Fauconnier, J., Thireau, J., Reiken, S., Cassan, C., Richard, S., Matecki, S., . . . Lacampagne, A. (2010). Leaky RyR2 trigger ventricular arrhythmias in Duchenne muscular dystrophy. *Proceedings of the National Academy of Sciences of the United States of America*, 107, 1559-1564. doi: 10.1073/pnas.0908540107
- Franzini-Armstrong, C., Protasi, F., & Ramesh, V. (1999). Shape, size, and distribution of Ca(2+) release units and couplons in skeletal and cardiac muscles. *Biophysical journal*, 77, 55. doi: 10.1016/S0006-3495(99)77000-1
- Groff, J. R., DeRemigio, H., & Smith, G. D. (2009). Markov chain models of ion channels and Ca²⁺ release sites. In L. C & Gabriel L (Eds.), *Stochastic Methods in Neuroscience* (pp. 29-64): Oxford University Press.
- Groff, J. R., & Smith, G. D. (2008a). Calcium-dependent inactivation and the dynamics of calcium puffs and sparks. *Journal of theoretical biology*, 253, 483-499. doi: 10.1016/j.jtbi.2008.03.026
- Groff, J. R., & Smith, G. D. (2008b). Ryanodine receptor allosteric coupling and the dynamics of calcium sparks. *Biophysical journal*, 95, 135-154. doi: 10.1529/biophysj.107.119982
- Hashambhoy, Y. L., Greenstein, J. L., & Winslow, R. L. (2010). Role of CaMKII in RyR leak, EC coupling and action potential duration: a computational model. *Journal of molecular and cellular cardiology*, 49, 617-624. doi: 10.1016/j.yjmcc.2010.07.011
- Hollingworth, S., Peet, J., Chandler, W. K., & Baylor, S. M. (2001). Calcium sparks in intact skeletal muscle fibers of the frog. *The Journal of general physiology*, 118, 653-678.

- Jaggard, J. H., Porter, V. a., Lederer, W. J., Nelson, M. T., & Jonathan, H. (2000). Calcium sparks in smooth muscle. *American journal of physiology. Cell physiology*, 278, C235-256.
- Keener, J. P. (2006). Stochastic calcium oscillations. *Mathematical medicine and biology : a journal of the IMA*, 23, 1-25. doi: 10.1093/imammb/dql002
- Kubalova, Z., Terentyev, D., Viatchenko-Karpinski, S., Nishijima, Y., Györke, I., Terentyeva, R., . . . Györke, S. (2005). Abnormal intrastore calcium signaling in chronic heart failure. *Proceedings of the National Academy of Sciences of the United States of America*, 102, 14104-14109. doi: 10.1073/pnas.0504298102
- Lamprecht, R., Smith, G. D., & Kemper, P. (2009). Stochastic Petri net models of Ca^{2+} signaling complexes and their analysis. *Natural Computing*, 10, 1045-1075. doi: 10.1007/s11047-009-9143-y
- Langville, A. N., & Stewart, W. J. (2004). The Kronecker product and stochastic automata networks. *Journal of Computational and Applied Mathematics*, 167, 429-447. doi: 10.1016/j.cam.2003.10.010
- Lehnart, S. E., Wehrens, X. H. T., Laitinen, P. J., Reiken, S. R., Deng, S.-X., Cheng, Z., . . . Marks, A. R. (2004). Sudden death in familial polymorphic ventricular tachycardia associated with calcium release channel (ryanodine receptor) leak. *Circulation*, 109, 3208-3214. doi: 10.1161/01.CIR.0000132472.98675.EC
- López-López, J. R., Shacklock, P. S., Balke, C. W., & Wier, W. G. (1994). Local, stochastic release of Ca^{2+} in voltage-clamped rat heart cells: visualization with confocal microscopy. *The Journal of physiology*, 480 (Pt 1, 21-29.
- Lukyanenko, V., Viatchenko-Karpinski, S., Smirnov, a., Wiesner, T. F., & Györke, S. (2001). Dynamic regulation of sarcoplasmic reticulum Ca^{2+} content and release by luminal Ca^{2+} -sensitive leak in rat ventricular myocytes. *Biophysical journal*, 81, 785-798. doi: 10.1016/S0006-3495(01)75741-4
- Luo, C. H., & Rudy, Y. (1994). A dynamic model of the cardiac ventricular action potential. I. Simulations of ionic currents and concentration changes. *Circulation research*, 74, 1071-1096.
- Morotti, S., Grandi, E., Summa, A., Ginsburg, K. S., & Bers, D. M. (2012). Theoretical study of L-type Ca^{2+} current inactivation kinetics during action potential repolarization and early afterdepolarizations. *The Journal of physiology*, 590, 4465-4481. doi: 10.1113/jphysiol.2012.231886

- Nelson, M. T., Cheng, H., Rubart, M., Santana, L. F., Bonev, a. D., Knot, H. J., & Lederer, W. J. (1995). Relaxation of arterial smooth muscle by calcium sparks. *Science (New York, N.Y.)*, 270, 633-637.
- Nguyen, V., Mathias, R., & Smith, G. D. (2005). A stochastic automata network descriptor for Markov chain models of instantaneously coupled intracellular Ca²⁺ channels. *Bulletin of mathematical biology*, 67, 393-432. doi: 10.1016/j.bulm.2004.08.010
- Schneider, M. F., & Klein, M. G. (1996). Sarcomeric calcium sparks activated by fiber depolarization and by cytosolic Ca²⁺ in skeletal muscle. *Cell calcium*, 20, 123-128.
- Shannon, T. R., Wang, F., Puglisi, J., Weber, C., & Bers, D. M. (2004). A mathematical treatment of integrated Ca dynamics within the ventricular myocyte. *Biophysical journal*, 87, 3351-3371. doi: 10.1529/biophysj.104.047449
- Smith, G. D. (2002). Modeling the stochastic gating of ion channels *Computational Cell Biology* (pp. 285-): Springer.
- Sobie, E. A., Dilly, K. W., dos Santos Cruz, J., Lederer, W. J., & Jafri, M. S. (2002). Termination of Cardiac Ca²⁺ Sparks: An Investigative Mathematical Model of Calcium-Induced Calcium Release. *Biophysical Journal*, 83, 59-78. doi: 10.1016/S0006-3495(02)75149-7
- Sobie, E. a., Guatimosim, S., Gómez-Viquez, L., Song, L.-S., Hartmann, H., Saleet Jafri, M., & Lederer, W. J. (2006). The Ca²⁺ leak paradox and rogue ryanodine receptors: SR Ca²⁺ efflux theory and practice. *Progress in biophysics and molecular biology*, 90, 172-185. doi: 10.1016/j.pbiomolbio.2005.06.010
- Sun, L., Fan, J. S., Clark, J. W., & Palade, P. T. (2000). A model of the L-type Ca²⁺ channel in rat ventricular myocytes: ion selectivity and inactivation mechanisms. *The Journal of physiology*, 529 Pt 1, 139-158.
- Tateishi, H., Yano, M., Mochizuki, M., Suetomi, T., Ono, M., Xu, X., . . . Matsuzaki, M. (2009). Defective domain-domain interactions within the ryanodine receptor as a critical cause of diastolic Ca²⁺ leak in failing hearts. *Cardiovascular research*, 81, 536-545. doi: 10.1093/cvr/cvn303
- Calcium and cell death 465-480 (Springer 2007).
- Williams, G. S. B., Chikando, A. C., Tuan, H.-T. M., Sobie, E. a., Lederer, W. J., & Jafri, M. S. (2011). Dynamics of Calcium Sparks and Calcium Leak in the Heart. *Biophysical journal*, 101, 1287-1296. doi: 10.1016/j.bpj.2011.07.021

Yu, J.-T., Chang, R. C.-C., & Tan, L. (2009). Calcium dysregulation in Alzheimer's disease: from mechanisms to therapeutic opportunities. *Progress in neurobiology*, 89, 240-255. doi: 10.1016/j.pneurobio.2009.07.009

CHAPTER 3: A LOCAL CONTROL RAT VENTRICULAR MYOCYTE YIELDS NOVEL UNDERSTANDING OF THE MECHANISM OF CARDIAC ARRHYTHMIA AND THE NUMBER OF CELLS AS A TRIGGER POINT

Abstract

In this chapter, a local-control model of rat ventricular myocyte is introduced. Local-control is the feature that excitation-contraction coupling is modulated locally at the release site level. This model features the fully stochastic gating of ion channels from 20,000 calcium release sites using the algorithm developed in the previous chapter. Each release site contains a cluster of 49 RyR channels and a smaller cluster of 7 L-type calcium channels in closed proximity to each other forming the dyadic subspace. The model can be used to explain the sarcoplasmic reticulum pump-leak balance in which the diastolic calcium leaks at rest can be fully accounted for by the visible and invisible leak of RyR channels, rather than another mechanism such as the back-flux of calcium via SERCA pump. The model also is used to explain, on both the local and cellular level, the mechanism by which alternans are generated by at high pacing stimulus. The single cell model is incorporated into a tissue model in which the individual cells are coupled to the four neighboring cells using electrical-coupling. The tissue model has provided some insights such as the number of cells, under different conditions, that is required to generate an ectopic heart beats i.e.sustained spontaneous voltage propagation across multiple cells. The numbers were 7 in 1D, 49 in 2D and 294 in 3D. This number is

greatly reduced in the case of trabecular tissues, due to the fact that the smaller size of the trabecular tissues reduces the electrotonic load.

Introduction

The ultimate goal of modelling cardiac cells is to reach an adequate quantitative understanding of the relationship between molecular functions, both at healthy and disease conditions, and the integrated behavior of the cell at tissue and whole-heart level. In the heart, the ventricular chambers are responsible for pumping blood to the lungs and rest of the body. Excitation-contraction coupling is tightly controlled by the action of different ions, such as Na^+ , K^+ , Ca^{2+} , which are coordinately transported into or extruded out of the cell via different ionic channels and carrier-like mechanisms known as pumps or exchangers. The changes in ionic concentration gradients lead to the change in transmembrane potential V_m . When the transmembrane potential depolarizes across a certain threshold, this results into a transient increase in an all-or-nothing process known as action potential (AP). Among the different ions, calcium is of particular importance as calcium regulates several signalling cascades (Berridge, Lipp, & Bootman, 2000; Bootman, Thomas, Tovey, Berridge, & Lipp, 2000); and the abnormal level of calcium has been implicated in several conditions of heart diseases (Sag et al., 2009; H. E. D. ter Keurs & Boyden, 2007; Vassalle & Lin, 2004; Viatchenko-Karpinski et al., 2004).

The mechanism of calcium-induced calcium release (CICR) has been widely accepted as the basic for the translation of electrical signals to the mechanical contractions in the cardiac myocytes during the process called excitation-contraction coupling (ECC) (Fabiato, 1983; Fabiato & Fabiato, 1975). During the cardiac AP, the calcium ions entering the cell via depolarization gated L-type calcium channels trigger the opening of closed-proximity RyR2 channels on the junctional SR membrane; with

both membranes forming a dyadic subspace of size 200-300nm in width and 10-15nm in height. The calcium signal is controlled not only temporally but also spatially, where the release occurring at these micro-domains known as calcium release can regulate the cellular events at the exact locations in the cell. At each release site, the calcium then diffuse to different parts of the cell to trigger other cellular signals, e.g. trigger the contractile machine by binding to the myofilaments (Wier, Egan, López-López, & Balke, 1994). This mechanism was thus coined local-control (Stern, 1990). At the end of the diastolic phase, calcium are sequestered back into the sarcoplasmic reticulum (SR) by the SERCA pump, or the mitochondria via the Ca^{2+} uniporters, and extruded out of the cell via $\text{Na}^+/\text{Ca}^{2+}$ exchanger (NCX) and plasma membrane Ca^{2+} ATP-ase (PMCA), Figure 1 (Donald M Bers, 2002). The elementary nature of Ca^{2+} signalling is important in understanding the underlying mechanism leading to cardiac diseases (Niggli & Egger, 2002).

In this chapter, we introduce an integrated local-control model of the rat ventricular myocytes. Compared to the model for the rat ventricular myocyte with 20,000 release sites developed by (Chikando, 2008), the model in this thesis has a number of advancements, some of which was introduced in (Williams et al., 2011) such as a newer spark model that fit better to experimental data and using a thermodynamics model for SERCA2a pump that only produces backflux of calcium under extreme conditions similar to experiment (Tran, Smith, Loiselle, & Crampin, 2009). Other changes include using (1) explicit buffer dynamics in the subspace, (2) a different L-type calcium channel that incorporate calcium-bound calmodulin dependent inactivation and updated

parameters based on newer experimental data from rat ventricular myocytes (Sun, Fan, Clark, & Palade, 2000). In addition, by using the novel computational method and GPU technology, it now allows us to do larger scale simulations that provide insights into calcium dynamics.

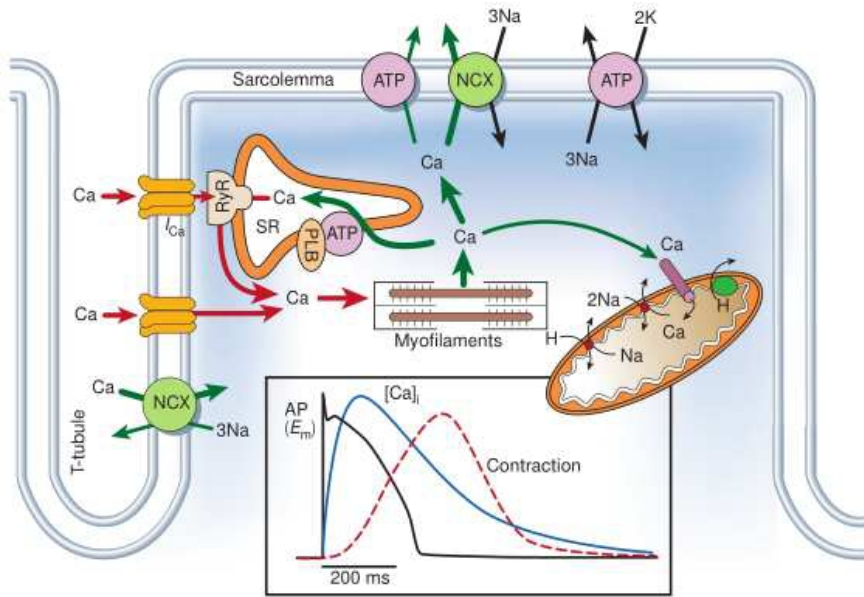


Figure 1. Calcium transport in the ventricular myocytes (Donald M Bers, 2002).

The current Ca^{2+} spark model was developed using the mean-field energetic coupling formulation (Jeffrey R Groff & Smith, 2008) which has been observed in biological systems (Stern et al., 1999). This spark model, which features both calcium-dependent from the jSR and from the myoplasmic side, can explain the robust mechanism of spark initiation and spark termination. The model has been used to explain the diastolic Ca^{2+} leak with how stochastic gating of RyR2s and a thermodynamic SERCA2a

model can balance SERCA-pump activity at the quiescent condition (Williams et al., 2011). Recently, (Liu, Lederer, & Sobie, 2012) have showed that dyad models with RyR gating without Ca^{2+} dependent inactivation produce more realistic Ca^{2+} spark results than those that assumed. By increasing SR buffer capacity, it increases Ca^{2+} spark which supports the idea that depletion of SR release play a dominant role in spark termination than Ca^{2+} dependent inactivation (Eric a Sobie & Lederer, 2012; Terentyev, 2002).

The whole-cell compartmental model was coded using the Ultra-fast Monte-Carlo algorithm introduced in the Chapter 2 for channel gating, with 20,000 CRUs per cell, and was simulated using Fermi CUDA-capable GPGPU. In the next section, the different components of the whole-cell rat ventricular model will be described.

Model development

The rat ventricular cell volume was chosen 25 pL to match to the number 20,000 CRUs per cell based on the estimation by (Cheng, Lederer, & Cannell, 1993). (Satoh, Delbridge, Blatter, & Bers, 1996) showed that the capacitance-volume ratio C_m/V_{cell} is significantly dependent on species and the development-stage. In rat, the ratio was 6.76 ± 0.62 pF/pL in 3-month old to 8.88 ± 1.14 pF/pL 6-month old. In the model, we chose $C_m/V_{\text{cell}} = 7.12$ pF/pL. The schematic diagram of the compartmental model of the rat ventricular myocyte with all the ionic currents is given in Figure 2.

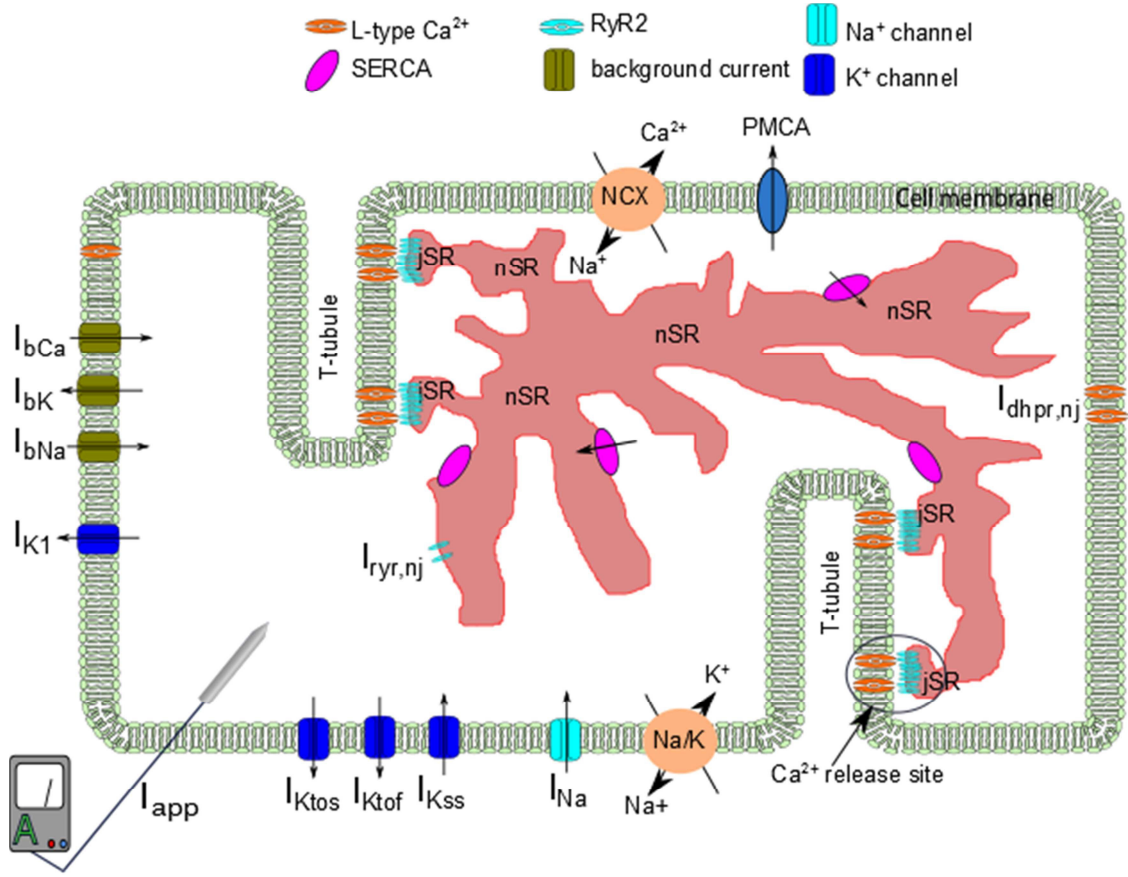


Figure 2. Schematic diagram of a ventricular cell that shows only 2 T-tubule branches

During AP, the dynamics of the membrane voltage V_m is governed by the equation

$$\frac{dV_m}{dt} = -\frac{10^3}{C_{sc}} \left(I_{dhpr}^T + I_{dhpr,nj} + I_{Na} + I_{NCX} + I_{NaK} + I_{pmca} + I_{K1} + I_{Kss} + I_{Ktof} + I_{Ktos} + I_{background} + I_{app} \right)$$

with N_{SFU} is the number of Ca^{2+} release sites, and

$$I_{dhpr}^T = \sum_{i=1}^{N_{SFU}} I_{dhpr}^{(i)}$$

$$I_{background} = I_{bCa} + I_{bNa} + I_{bK}$$

There is some evidence suggesting the existence of non-junctional DHPR (10-20%), located on the external sarcolemma and not forming the release sites with RyR2 (Brette, Leroy, Le Guennec, & Salle, 2006; Scriven, Dan, & Moore, 2000). Hence the contribution of calcium from a small fraction of DHPR $I_{dhpr,nj}$ (15%) was also added.

NOTE: The units: membrane potential and reversal potential are in miliVolt (mV), while other parameters are given in the form of *unit*-density, e.g. the specific membrane capacitance $C_{sc} = 1 \mu\text{F}/\text{cm}^2$, the ionic currents are given in $(\mu\text{A}/\text{cm}^2)$.

Calcium release site (CRU)

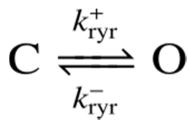
A calcium release site has a cluster of N_R RyR2 channels and N_L LCCs channels. At each calcium release site, rather than using the rapid buffering approximation or fixed buffering (Williams et al., 2011), dynamic calcium buffering is implemented for three different endogenous buffers: calmodulin (Calm - CALcium-MODULated proteIN), sarcolemmal (SL) buffer and sarcoplasmic reticulum (SR) buffer. The membrane buffers used here are similar to those used previously (Gregory D. Smith, Keizer, Stern, Lederer, & Cheng, 1998; Eric A. Sobie, Dilly, dos Santos Cruz, Lederer, & Jafri, 2002).

$$\begin{aligned}\frac{d[\text{Ca}]_{ds}^{(i)}}{dt} &= \frac{(J_{ryr}^{(i)} - J_{efflux}^{(i)} + J_{dhpr}^{(i)})}{\lambda_{ds}} - 2 \frac{d[\text{CaCM}]^{(i)}}{dt} - \frac{d[\text{CaSL}]^{(i)}}{dt} - \frac{d[\text{CaSR}]^{(i)}}{dt} \\ \frac{d[\text{CaCalm}]^{(i)}}{dt} &= k_{CM}^+ ([\text{Ca}]_{ds}^{(i)})^2 ([\text{CM}]_T - [\text{CaCalm}]_{ds}^{(i)}) - k_{CM}^- [\text{CaCalm}]_{ds}^{(i)} \\ \frac{d[\text{CaSL}]^{(i)}}{dt} &= k_{SL}^+ ([\text{Ca}]_{ds}^{(i)}) ([\text{SL}]_T - [\text{CaSL}]_{ds}^{(i)}) - k_{SL}^- [\text{CaSL}]_{ds}^{(i)} \\ \frac{d[\text{CaSR}]^{(i)}}{dt} &= k_{SR}^+ ([\text{Ca}]_{ds}^{(i)}) ([\text{SR}]_T - [\text{CaSR}]_{ds}^{(i)}) - k_{SR}^- [\text{CaSR}]_{ds}^{(i)}\end{aligned}$$

with (i) is an index indicating the i^{th} specific CRU out of the 20,000, $\lambda_{ds} = V_{ds} / V_{myo}$ is the volume fraction that scale the fluxes, defined based on myoplasmic volume, to the subspace volume compartment.

Ryanodine receptor type-2 model

In cardiac RyR2, Calm is widely accepted to have an inhibitory effect to the channels at all level of calcium concentration, though the effect is more pronounced at high level of $[Ca^{2+}]$. However, as pointed out by (Balshaw, Xu, Yamaguchi, Pasek, & Meissner, 2001), the time scale for association and dissociation from RyR2 is in the range of seconds to minutes, which makes the physiological role of Calm to RyR gating is unclear. Moreover, it was believed that CaCalm can play a facilitatory role in Ca^{2+} release termination, but not a critical factor (Sigalas, Bent, Kitmitto, O'Neill, & Sitsapasan, 2009; Xu & Meissner, 2004). Therefore, this is not included in our study. Instead, the minimal 2-state ryanodine receptor was used (Williams et al., 2011) that incorporates cytosolic calcium-dependent and luminal calcium dependent.



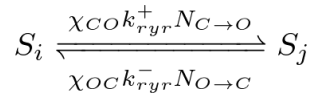
with the transition rates

$$k_{ryr}^+ = 12 \left([Ca^{2+}]_{ds}^{(i)} \right)^{2.2} \cdot \left(2.8 \times 10^{-4} [Ca^{2+}]_{jsr}^{(i)} + 0.02 \right)$$

$$k_{ryr}^- = 500$$

The RyR2 channels in each release site are modelled as a single cluster. Rather than keeping track of individual channel's state, the mean-field approach was used. The mean-field approach is based on the assumption that all channels in the cluster see the

same local calcium concentration in the dyadic subspace (Jeffrey R Groff & Smith, 2008). Thus, the individual channel's states are ignored, and only the number of channel in each states is important. In the case of RyR2, each cluster state is a vector of two components $S_i = (n_C, n_O)$ where n_C and n_O are the numbers of RyR2 in the closed state and open state, respectively $n_C + n_O = N_R$. The details of this are discussed in the previous chapter. To model the effect of FKBP12.6, the channels in the cluster are coupled together via allosteric coupling energies: $\epsilon_{OO}, \epsilon_{CC}$. At each release site, the transition between two cluster states S_i and S_j is represented as



where $N_{O \rightarrow C}(N_{C \rightarrow O})$ represents the number of channels in cluster state S_i (S_j) that can be switched from Open to Closed (Closed to Open). The coupling gating in the cluster is given by the formula

$$\begin{aligned}\chi_{CO} &= \exp\left(-\bar{a}_j \times 0.5 \times (N_{closed} \epsilon_{CC} - (N_{open} - 1) \epsilon_{OO})\right) \\ \chi_{OC} &= \exp\left(-\bar{a}_j \times 0.5 \times (N_{open} \epsilon_{OO} - (N_{closed} - 1) \epsilon_{CC})\right)\end{aligned}$$

with \bar{a}_j is the average allosteric connectivity for each RyR based on mean-field approach (Jeffrey R Groff & Smith, 2008). The variables N_{closed} and N_{open} represent the current number of non-conducting, and conducting channels in the cluster state S_i , respectively.

In the case of two-state RyR model, we have $N_{O \rightarrow C} = N_{open}$ and $N_{C \rightarrow O} = N_{closed}$.

The non-junctional or 'rogue' RyR is modelled deterministically using the formula

$$J_{ryr-nj} = P_{o,ryr-nj} \cdot v_{ryr,nj} ([Ca]_{nsr} - [Ca]_{myo})$$

$$v_{ryr-nj} = v_{ryr}^T \times [\text{fraction } nj - RyR]$$

$$\frac{dP_{o,ryr-nj}}{dt} = k_{ryr-nj}^+ (1 - P_{o,ryr-nj}) - k_{ryr-nj}^- P_{o,ryr-nj}$$

k_{ryr-nj}^+ has the same functional form like k_{ryr}^+ , except the subspace calcium $[Ca]_{ds}$ in the formula of is now replaced by $[Ca]_{myo}$. In our case, the fraction of nj-RyR is 5%.

L-type Ca^{2+} channel model

The 6-state L-type Ca^{2+} channel (LCC) model, Figure 3, is derived from 5-state LCC model for rat ventricle myocyte (Sun et al., 2000) with parameters adjusted for the new spark model. The original model was developed to work in the range of -30 mV + 30 mV of the transmembrane potential. As was suggested in their original paper, the 6-th state C6 was added to work with stronger depolarization (< -40 mV), so that all the channels stay in this state when the cell is at rest.

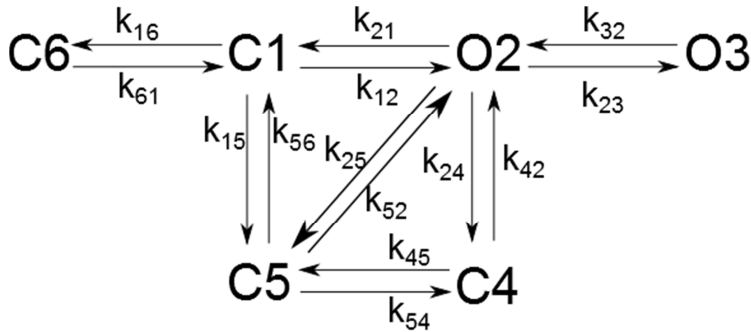


Figure 3. Schematic diagram of the model for the L-type calcium channel (DHPR channel), C4= Ca^{2+} -dependent inactivation, C5= V_m -dependent inactivation

The inactivation of the LCC was modelled via 2 separate pathways: VDI (voltage-dependent inactivation ($O2 \rightarrow C5$)) and CDI (Ca^{2+} -dependent inactivation ($O2 \rightarrow C4$)). At each release site, the Ca^{2+} level that controls the inactivation is the subspace calcium. The source of contributing calcium to this microdomain is the influx of calcium via LCC and the release of calcium from SR via RyR. The much higher level of calcium in this subspace, i.e. ~ 100 -fold compared to cytosolic bulk calcium, enhances the rate of inactivation of LCC and thereby preventing calcium overload.

The endogenous buffer Calm bound to Ca^{2+} (CaCalm) is the effector for Ca^{2+} -dependent inactivation (CDI) of L-type Ca^{2+} channel. The calcium-free CaM is called apo calmodulin (apo-Calm) with two homologous domains, known as lobes (Jurado, Chockalingam, & Jarrett, 2009). For each apo-Calm molecule, there are four different calcium binding sites: two at the E-F hand motifs of the N-terminal (N-lobe) and two at the E-F hand motifs of the C-terminal (C-lobe) of Calm (review: (Halling, Aracena-Parks, & Hamilton, 2005)). Depending on the lobe to which Ca^{2+} bind, the complex may induce different form of regulation on the same channel. In L-type Ca^{2+} channels (Cav1.2), CDI is triggered by the binding of two Ca^{2+} ions to the C-lobe of Calm; while in non-L-type Ca^{2+} channels, the inhibition comes from the binding of two Ca^{2+} ions to the N-lobe (Pitt et al., 2001; Tadross, Dick, & Yue, 2008; Van Petegem, Chatelain, & Minor, 2005). It means that to model CDI, two Ca^{2+} binding at C-lobe is necessary. The original Sun-2000 LCC model, which was developed based on earlier data (Qin, Olcese, Bransby, Lin, & Birnbaumer, 1999), used the Hill coefficient as 3. However, this was altered in this model, to follow the newer data that the simultaneous binding/unbinding of

two calcium ions at the low-affinity calcium binding sites (C-lobe) can trigger/remove CDI. In addition, the original model didn't incorporate the loss of calcium in the subspace due to binding to calmodulin. This is important as the level of free $[Ca]_{ds}$ control the gating of RyR2 channels. This was also corrected in our modified model.

It has been suggested that Calm tethers to a region of C-terminal between an EF and IQ domain of LCC (Ehlers, Augustine, & Field, 1999), with 2 different segments (A and C sequences) within the pre-IQ motif of LCC have been indicated to be critical for CDI (Fallon et al., 2009), and this tethering occurs at very low level of calcium concentration (20-100 nM) (Pitt et al., 2001). This is the range of resting calcium level, thus it is assumed that all Calm tethers to the channels all the time. So, the total $[Calm]$ is assumed fixed in the subspace, and calcium-dependent inactivation of LCC ($k_{2 \rightarrow 4}$) is modelled via calcium-Calmodulin (CaCalm) complex. In the model, similar to the experimental data, it is assumed that a single bound $Ca^{2+}/Calm$ complex is both necessary and sufficient for CDI (Mori, Erickson, & Yue, 2004). So the transition rate for CDI is formulated as $k_{24} = c_{24} [Ca^{2+}/Calm]$.

Not only Ca^{2+} , but also other ions can also permeate via LCC (P. Hess, Lansman, & Tsien, 1986). However, due to the large permeability of Ca^{2+} compared to other ions (e.g. $P_{Ca}/P_{Na} > 1000$), in this study, only Ca^{2+} current is modelled. Due to the nonlinearity in the I-V curve, and based on the assumption of independent permeation between ion species and constant-field theory, the Goldman-Hodkin-Katz (GHK) formalism was used (Goldman, 1943)

$$I_{dhpr}^{(i)} = N_{open,dhpr}^{(i)} \frac{P_{dhpr} z_{Ca}^2 V_m}{RT / F^2} \frac{[Ca^{2+}]_{ds}^{(i)} \exp\left(\frac{z_{Ca} V_m}{RT / F}\right) - \beta_0 / \beta_1 \cdot [Ca^{2+}]_o}{\exp\left(\frac{z_{Ca} V_m}{RT / F}\right) - 1}$$

with (i) represents the index of a release site ($N_{open,dhpr}^{(i)}$ is the number of opening DHP channels, $[Ca^{2+}]_{ds}^{(i)}$ is the calcium concentration in a dyadic subspace), $[Ca^{2+}]_o$ is the extracellular calcium concentration; P_{dhpr} is the single channel permeability; $z_{Ca}=2$ is the valence of Ca^{2+} ion; R is the universal gas constant, T is the temperature and F is the Faraday constant. The partition coefficients are $\beta_0 = 0.341$, $\beta_1 = 1$ in the case of Ca^{2+} channel (Lee & Tsien, 1984; Pitzer & Mayorga, 1973). NOTE: If $V_m = 0$, this formula is used instead

$$I_{dhpr}^{(i)} = N_{open,dhpr}^{(i)} P_{dhpr} z_{Ca} F ([Ca^{2+}]_{ds}^{(i)} - [Ca^{2+}]_o)$$

Even though the role of extracellular calcium was not investigated in this study, the model also took into account the effect of extracellular calcium $[Ca]_o$ on the model by modulating single channel current and shifting the half-activation voltage $V_{1/2}$.

$$V_{1/2} = -40.344 + 13.31 \times \exp(-[Ca]_o \times 10^{-3} / 0.053) + 31.65 \times \exp(-[Ca]_o \times 10^{-3} / 11.305) + 3$$

The equations for the LCC model is given in Table 8. The fraction of LCC channels in each state during a +10 (mV) voltage clamp is shown in Figure 4. State-2 and 3 are open states; while State-4 is calcium-dependent inactivation and State-5 is voltage-dependent inactivation.

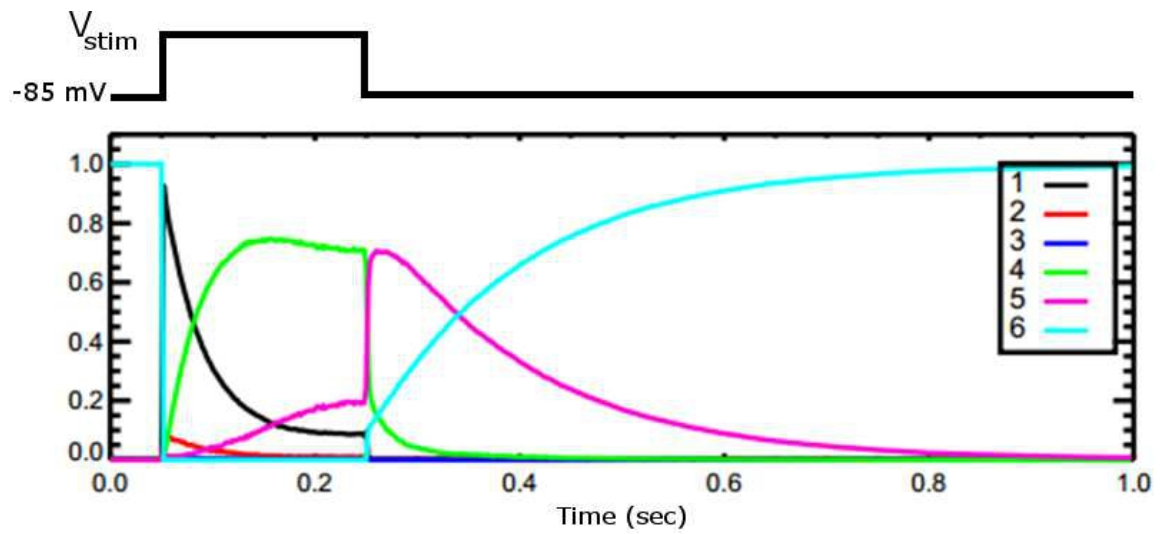


Figure 4. The fraction of LCC channels in different states during the voltage-clamp of $V_{stim} = +10$ mV for 200ms

Na⁺ channel model

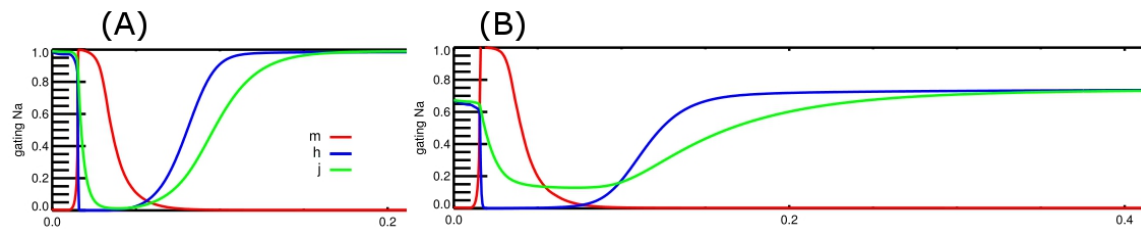


Figure 5. Dynamics of Na⁺ gating variables during an AP: (A) Luo-Rudy-94 model at 37°C for guinea pig, (B) Pandit et al.-2001 model at 23°C for rat.

The rapid inward Na⁺ current in the cardiac cells exhibits a bi-phasic time courses for recovery during inactivation and one activation gating variable (Brown, Lee, & Powell, 1981). Using Hodgkin-Huxley's approach, (Pandit, Clark, Giles, & Demir, 2001) proposed a modified Na⁺ model for rat ventricular myocyte, i.e. Pandit-01 Na⁺

model, at 22°C, Figure 5 (B). The Luo-Rudy Na model (C.-H. Luo & Rudy, 1991; C. H. Luo & Rudy, 1994) was derived based on pig ventricular myocyte data measured at 37°C (Gettes & Reuter, 1974), Figure 5 (A). Even though the Luo-Rudy Na⁺ model has widely been used in different models developed for various species, there are certain variations between species that need to be considered (Ulbricht, 2005).

The first consideration is to correctly simulate the upstroke velocity of the action potential. The gating variables in the Luo-Rudy whole-cell model for the guinea pig ventricular myocyte produce a very fast rate of depolarization, with $\max(dV/dt) \sim 400$ V/sec ($E_{Na}=54.4$ mV) (C.-H. Luo & Rudy, 1991; C. H. Luo & Rudy, 1994), while the experimental data from which the model was developed showed steady-state $\max(dV/dt)$ was ~ 300 V/sec (Gettes & Reuter, 1974). This maximum upstroke is smaller in rat and mice, compared to bigger species like human or guinea pig. (Brette & Orchard, 2006) measured this maximum rate in Wistar rat heart at 23°C, which gave ~ 150 - 190 (V/sec). By applying a minimum Q₁₀ of 1.23 (Colatsky, 1980; C.-H. Luo & Rudy, 1991), the maximum upstroke velocity in rat ventricular myocyte at 37°C is expected to be ~ 184 - 233 (V/sec). The Pandit-01 Na⁺ model produced a better approximation to the maximum rate of upstroke velocity of V_m in rat ventricular myocyte (i.e. 145 V/sec for the epicardial and 181 V/sec for the endocardial myocyte at room temperature 22°C).

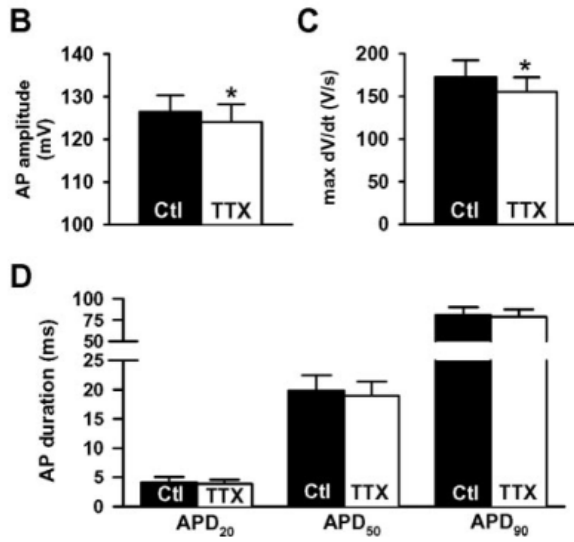


Figure 6. Experimental data from rat ventricular myocyte at 23°C (Brette & Orchard, 2006)

The second consideration is that the recovery of the steady-state inactivation h_{∞} for cardiac sodium current must match the experimental value, which is about 0.7-0.8 at -80 mV in rat and mice (Benndorf, Boldt, & Nilius, 1985; Brown et al., 1981). The value of h_{∞} in Pandit is 0.6; and the value in Luo-Rudy is 0.97. In terms of temperature dependence, the Q10 for recovery kinetics range from 1.7 to 2.3 for potential in the range -76 mV to -62 mV, and 1.5 to 1.8 for the potential in the range -84 mV to -65 mV (Gettes & Reuter, 1974).

A modified model was proposed to fit better to the experiment data for rat ventricular myocyte at 37°C, Figure 7. In this model, the value h_{∞} is 0.812 at -80mV, and, at the body temperature, the model gave maximum upstroke rate 213.8 ± 6.6 V/sec with the overshoot is 48.76 ± 1.09 (mV). The maximum current conductance is 8 mS/cm^2 which is in the range $3\text{-}25 \text{ mS/cm}^2$ (Brown et al., 1981; Drouhard & Roberge, 1987).

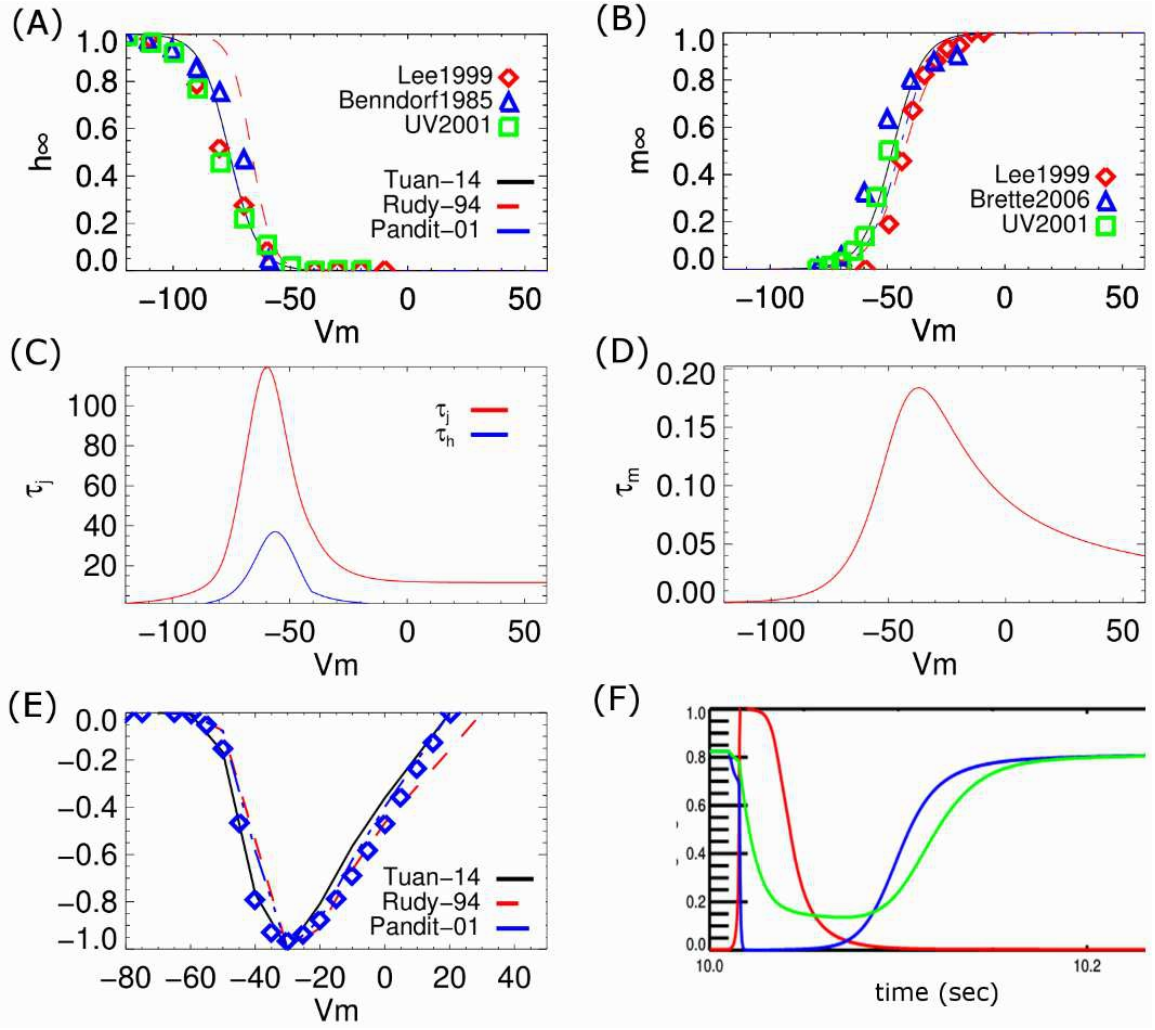


Figure 7. (A-B) gating variables; (C-D) time constants at different voltages. (E) I-V curve, (F) dynamics of gating variables of the proposed model during an AP

The whole-cell Na⁺ current was derived from the formula

$$I_{Na} = g_{Na} m_{Na} h_{Na}^3 j_{Na} (V_m - E_{Na})$$

with the ODE for gating variable follows the first-order differential equation (Hodgkin & Huxley, 1952)

$$\frac{dx_{Na}}{dt} = \frac{x_{\infty} - x_{Na}}{\tau_x}$$

where x represents the dimensionless gating variables, either m, h , or j , in the range between 0 and 1.0. The unit for the time constants is in seconds.

$$h_{\infty} = \frac{1}{1 + \exp((V_m + 76.1) / 6.07)}$$

$$j_{\infty} = h_{\infty}$$

$$m_{\infty} = \frac{1}{1 + \exp((V_m + 48) / -6.5)}$$

$$\tau_m = \frac{0.00136}{0.32(V_m + 47.13) / (1 - \exp(-0.1(V_m + 47.13))) + 0.08 \exp(-V_m / 11)}$$

- If $V_m \geq -40$

$$\tau_h = 0.0004537(1 + \exp((V_m + 10.66) / (-11.1)))$$

$$\tau_j = \frac{0.01163(1 + \exp(-0.1(V_m + 32)))}{\exp(-2.535 \times 10^{-7} V_m)}$$

- If $V_m < -40$

$$\tau_h = \frac{0.00349}{0.81 \exp((V_m + 80) / (-6.8)) + 3.56 \exp(0.079 V_m) + 3.1 \times 10^5 \exp(0.35 V_m)}$$

$$\tau_j = \frac{0.00349}{\frac{5(V_m + 37.78)}{1 + \exp(0.311(V_m + 79.23))} (-12714 \exp(0.2444 V_m) - 3.474 \times 10^{-5} \exp(-0.04391 V_m)) + \frac{0.1212 \exp(-0.01052 V_m)}{1 + \exp(-0.1378(V_m + 40.14))}}$$

$$h_{\infty} = \frac{0.135 \exp((V_m + 80) / (-6.8))}{0.135 \exp((V_m + 80) / (-6.8)) + 3.56 \exp(0.079 V_m) + 3.1 \times 10^5 \exp(0.35 V_m)}$$

$$j_{\infty} = \frac{\frac{V_m + 37.78}{1 + \exp(0.311(V_m + 79.23))} (-12714 \exp(0.2444 V_m) - 3.474 \times 10^{-5} \exp(-0.04391 V_m))}{\frac{V_m + 37.78}{1 + \exp(0.311(V_m + 79.23))} (-12714 \exp(0.2444 V_m) - 3.474 \times 10^{-5} \exp(-0.04391 V_m)) + \frac{0.1212 \exp(-0.01052 V_m)}{1 + \exp(-0.1378(V_m + 40.14))}}$$

K⁺ channel model

There are four different K⁺ currents, excluding the background current and the Na⁺/K⁺ exchanger. The formula for fast and slow transient outward currents (K_{tof}, K_{tos}, respectively) are based on developed for mouse (Bondarenko, Szigeti, Bett, Kim, & Rasmusson, 2004).

$$I_{K1} = g_{K1} \times \frac{[K]_o}{[K]_o + 210} \times \frac{(V_m - E_K - 1.73)}{1 + \exp(0.0896(V_m - E_K - 1.73))}$$

$$I_{Kss} = g_{Kss} \times a_{Kss} \times i_{Kss} (V_m - E_K)$$

$$I_{Ktof} = g_{Ktof} \times a_{Ktof} \times i_{Ktof} (V_m - E_K)$$

$$I_{Ktos} = g_{Ktos} \times a_{Ktos} \times i_{Ktos} (V_m - E_K)$$

$$\frac{da_{Kss}}{dt} = 10^3 \frac{1.0 / (1.0 + \exp(-(V_m + 22.5)/7.7)) - a_{Kss}}{0.13 + 0.393 \times \exp(-0.0862V_m)}$$

$$\frac{di_{Ktos}}{dt} = 0$$

$$\frac{da_{Ktof}}{dt} = 10^3 \times \left[\frac{0.18064 \exp((V_m + 30) \times 0.3577) \times (1 - a_{Ktof}) -}{0.3956 \exp(-(V_m + 30) \times 0.06237) \times a_{Ktof}} \right]$$

$$\frac{di_{Ktof}}{dt} = 10^3 \times \left[\frac{(0.000152 \exp(-(V_m + 13.5)/7))}{1 + 0.067083 \exp(-(V_m + 33.5)/7)} \times (1 - i_{Ktof}) - \left(\frac{0.00095 \exp((V_m + 33.5)/7)}{1 + 0.051335 \exp((V_m + 33.5)/7)} \right) \times i_{Ktof} \right]$$

$$\frac{da_{Ktos}}{dt} = 10^3 \frac{1.0 / (1.0 + \exp(-(V_m + 22.5)/7.7)) - a_{Ktos}}{2.058 + 0.493 \times \exp(-0.0629V_m)}$$

$$\frac{di_{Ktos}}{dt} = 10^3 \frac{1.0 / (1.0 + \exp((V_m + 45.20)/5.70)) - i_{Ktos}}{270.0 + 1050 / (1.0 + \exp((V_m + 45.20)/5.70))}$$

with $g_{K1} = 0.15$; $g_{Kss} = 0.0421$; $g_{Ktof} = 0.0798$; $g_{Ktos} = 0.00629$; $g_{bK} = 1.38e - 7$. The initial values are given in Table 6.

SL pumps/exchangers

The two extrusion pathways for calcium via SL are plasma-membrane $\text{Ca}^{2+}/\text{ATP}$ -ase (PMCA) and $\text{Na}^+/\text{Ca}^{2+}$ exchanger (NCX).

$$J_{ncx} = \frac{-A_m I_{ncx}}{FV_{myo}}$$

with A_m is the SL surface area and V_{myo} is the myoplasmic volume

The NCX is given by the formula

$$I_{ncx} = \overline{I_{ncx}} \frac{([Na]_i)^3 [Ca]_o \exp(\eta_{ncx} FV / (RT)) - ([Na]_o)^3 [Ca]_{myo} \exp((\eta_{ncx} - 1) FV / (RT))}{\left((K_{ncx, Na})^3 + ([Na]_o)^3 \right) (K_{ncx, Na} + [Ca]_o) (1 + k_{ncx}^{sat} \exp((\eta_{ncx} - 1) FV / (RT)))}$$

with $\overline{I_{ncx}}$ is the maximal NCX current. The parameters are given in Table 5.

$$I_{pmca} = \overline{I_{pmca}} \frac{([Ca^{2+}]_{myo})^{\eta_{pmca}}}{(K_{m, pmca})^{\eta_{pmca}} + ([Ca^{2+}]_{myo})^{\eta_{pmca}}}$$

In the case of sodium and potassium pumps, we have

$$I_{Na^+ / K^+} = \overline{I_{Na^+ / K^+}} \frac{1}{1 + 0.1245 \exp\left(-0.1 \left(V_m \frac{F}{RT}\right)\right) + 0.0365 \left(\frac{1}{7} \exp([Na]_o / 67300) - 1\right) \exp\left(-V_m \frac{F}{RT}\right)} \times \frac{1}{1 + \left(\frac{21000}{[Na]_i}\right)^{1.5} \frac{[K]_o}{[K]_o + 1500}}$$

Background currents

The background currents follow the linear Ohm-law

$$I_{bX} = g_X \times (V_m - E_X)$$

The three different background currents were used in the model

$$I_{bCa} = g_{bCa}(V_m - E_{Ca})$$

$$I_{bNa} = g_{bNa}(V_m - E_{Na})$$

$$I_{bK} = g_{bK}(V_m - E_K)$$

with the reversal potentials are derived from Nernst equation.

$$E_X = \frac{RT}{Fz_X} \ln \left(\frac{[X]_i}{[X]_o} \right)$$

with z_X is the valence of ion X.

SR pumps

The sarco(endo)plasmic reticulum Ca^{2+} -ATPase (SERCA) pump resequesters Ca^{2+} back to the SR/ER during each excitation-contraction cycle to facilitate muscle relaxation by pumping two calcium ions per ATP molecule hydrolyzed (Tada, Yamada, Kadoma, Inui, & Ohmori, 1982). In many computational models, Hill-based equations are used which assumed a single rate-limiting step (Balke, Egan, & Wier, 1994; Bassani, Bassani, & Bers, 1994; C. H. Luo & Rudy, 1994; Snyder, Palmer, & Moore, 2000). This phenomenological formula only works for certain set of experimental data, and doesn't explain the energetic behavior of the SERCA pump. Using the Hill-based equation, the resting steady-state calcium leak flux would be $\sim 1/5$ of the pump v_{\max} , which consume a large amount of ATP and eventually depleting the cell energetic phosphate (T R Shannon, Ginsburg, & Bers, 2000).

Another class of SERCA-pump model is the reversible model developed by Shannon and colleagues (T. R. Shannon & Bers, 1997; T. R. Shannon, Ginsburg, & Bers, 1998, 2002). In this type of model, it is assumed that a significant of Ca^{2+} leak at rest or during diastolic phase is accounted by the back-flux via SERCA pump. However, under

normal physiological condition, the back-flux is unfavored thermodynamically and thus has not been observed (Feher, 1984). Tran and co-workers developed a thermodynamic model of the SERCA pump (Tran et al., 2009). Figure 8 showed the comparison between the three common model formulations, at which the Tran-Crampin model showed that back-flux only occur at very high $[Ca^{2+}]_{sr}$. The 2-state reduced model of the Tran-Crampin model was chosen with parameters selected so that the maximum pumping rate per pump molecule, $\max(v_{serca})$, is 5 s^{-1} .

$$J_{serca} = 2 \times v_{serca} [\text{SERCA}]$$

$$v_{serca} = \frac{3.24873 \times 10^{12} (K_{myo})^2 + K_{myo} (9.17846 \times 10^6 - 11478.2 K_{sr}) - 0.329904 K_{sr}}{D_{cycle}}$$

$$D_{cycle} = 0.104217 + 17.923 K_{sr} + K_{myo} (1.75583 \times 10^6 + 7.61673 \times 10^6 K_{sr})$$

$$+ (K_{myo})^2 (6.08463 \times 10^{11} + 4.50544 \times 10^{11} K_{sr})$$

and

$$K_{myo} = \left(\frac{[Ca]_{myo}}{10^{-3} K_{d,myo}} \right)^2; K_{sr} = \left(\frac{[Ca]_{nsr}}{10^{-3} K_{d,sr}} \right)^2$$

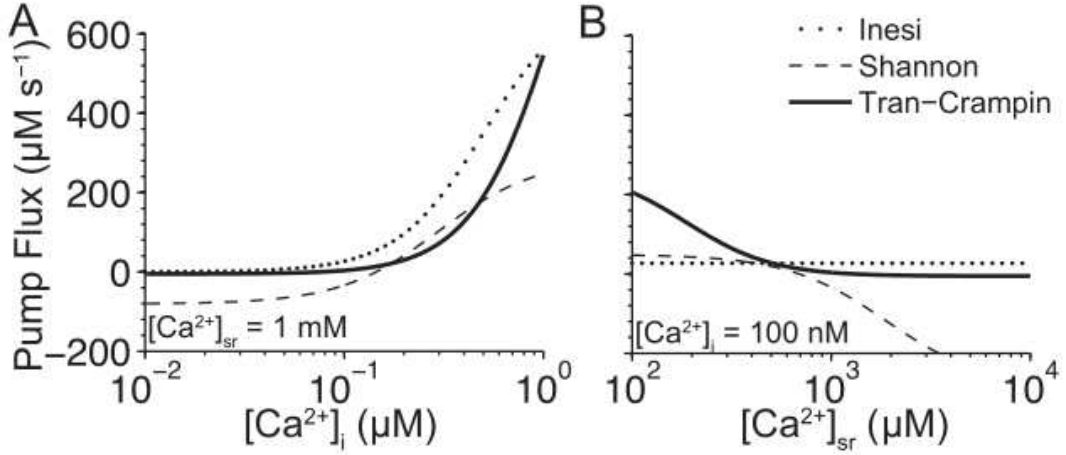


Figure 8. Comparison three common model formulation: Tran-Crampin (solid line), Shannon (dashed-line) and Inesi (dotted line), where SERCA2a pump flux vs. (A) $[Ca^{2+}]_i$ and (B) $[Ca^{2+}]_{sr}$ (Williams et al., 2011)

Calcium-bound to buffers

Three different endogenous buffers are used for the bulk myoplasm.

$$\frac{d[Ca/CaM]}{dt} = k_{CM}^+ ([Ca]_{myo})^2 ([CM]_T - [Ca/CaM]_{myo}) - k_{CM}^- [Ca/CaM]_{myo}$$

$$\frac{d[CaSR]}{dt} = k_{SR}^+ ([Ca]_{myo}) ([SR]_T - [CaSR]_{myo}) - k_{SR}^- [CaSR]_{myo}$$

$$\frac{d[CaTrpn]}{dt} = k_{Trpn}^+ ([Ca]_{myo}) ([Trpn]_T - [CaTrpn]_{myo}) - k_{Trpn}^- [CaTrpn]_{myo}$$

Numerical Methods

The system of ordinary differential equations comprising the model are solved using the explicit Euler method. The small time step (10 ns - 100 ns) which is required for numerical stability is also necessary to simulate the fast and stochastic gating of DHPR and RyR2 channels. So, it doesn't affect the performance when simulating the model with the stochastic gating of ionic channels.

Each release site is fed with a different sequence of pseudo-random numbers. These Monte-Carlo simulations are computed on Fermi-GPU cards, with pseudo-random numbers were derived from the Saru pseudo-random number generator “Saru PRNG” developed on GPU provided by Steve Worley (Afshar, Schmid, Pischevar, & Worley, 2013). Instead of using a fixed time-step, an adaptive time-step strategy is used. When the channel fires, a smaller time-step is selected; first to ensure numerical stability, second to limit maximum 10% of the CRUs having state changes to occur at a time (J.R. Groff, DeRemigio, & Smith, 2009; Gregory D Smith, 2002). Also, when tested, the two channels gating at the same time was 6% of the time. Thus, the chance that two channels change state at the same time was assumed not to happen

Dynamics of calcium sparks and calcium leak

The model predicts three possible mechanisms of the SR Ca^{2+} leak that are sufficient to account for balancing Ca^{2+} uptake via SERCA2a during the diastolic phase, which was published in (Williams et al., 2011). They are visible Ca^{2+} sparks (~120 sparks/cell/sec under quiescent), invisible Ca^{2+} leaks known as Ca^{2+} quarks (~4300 quarks/cell/sec under quiescent) and calcium leak via a small population of RyRs at a distance from the release sites, known as non-junctional RyR or ‘rogue’ RyR (Eric a Sobie et al., 2006). The so-called non-spark events or invisible Ca^{2+} quarks are the result of one or a few RyR channels opening whose signals cannot be detected using standard confocal imaging microscopies (Brochet, Xie, Yang, Cheng, & Lederer, 2011).

The visible leak i.e. 120 Ca^{2+} sparks per cell per second is in the physiological range (100-200 sparks/cell/s) and accounts for 75% of the leak. Part of the invisible leak

results from the stochastic gating of one or a few RyR2 channels, accounting for 25% of the leak. This yields a spark fidelity of $\sim 2.8\%$ which is the ability a single calcium release to trigger the Ca^{2+} spark. The total quiescent leak rate was $\sim 1.2 \mu\text{mol}/(\text{L cyt.})/\text{sec}$ which is in the range $0.5 \mu\text{M}$ - $5 \mu\text{M}$ (D. M. Bers, 2014). The Ca^{2+} spark peak was $\sim 100.1 \mu\text{M}$, Figure 9, which is in agreement with the estimate that due to the small subspace, the elevation of free calcium can be two orders of magnitude larger than the resting value (Cheng et al., 1993). The plateau in the spark profile of free calcium explains the energy coupling effect between the closed and open channels, before the Ca^{2+} spark is completely terminated. Similar to the study of (Williams et al., 2011), the effect of IP_3R has not been incorporated in this model study. Thus, the involvement of other leak pathways like via IP_3 -receptors (IP_3R) has not been excluded, though the functional role of IP_3R at rest has not been confirmed. As shown in Figure 9(D), the higher frequency of $[\text{Ca}^{2+}/\text{Calm}]$ elevation in the quiescent cell model provided the evidence of non-spark events where calcium release via the opening of one or a few RyRs bind to calmodulin buffer, as well as SR and SL buffers.

The termination of Ca^{2+} sparks, as explained in the model, is the combination of luminal calcium depletion, which reduce the driving force for the Ca^{2+} flux; the stochastic closing of the channels, which affect the adjacent ones via the allosteric coupling. Clearly, this predates the concept of pernicious attrition in which the smaller Ca^{2+} flux at each RyR2 due to local luminal calcium depletion devastates inter-RyR2 CICR (Gillespie & Fill, 2013). In fact, the idea the reduced Ca^{2+} flux through the RyR2s

in the diad are insufficient to sustain CICR as suggested in pernicious attrition has been suggested previously (Jafri Rice Winslow 1998, Rice Jafri Winslow –gain-gradedness).

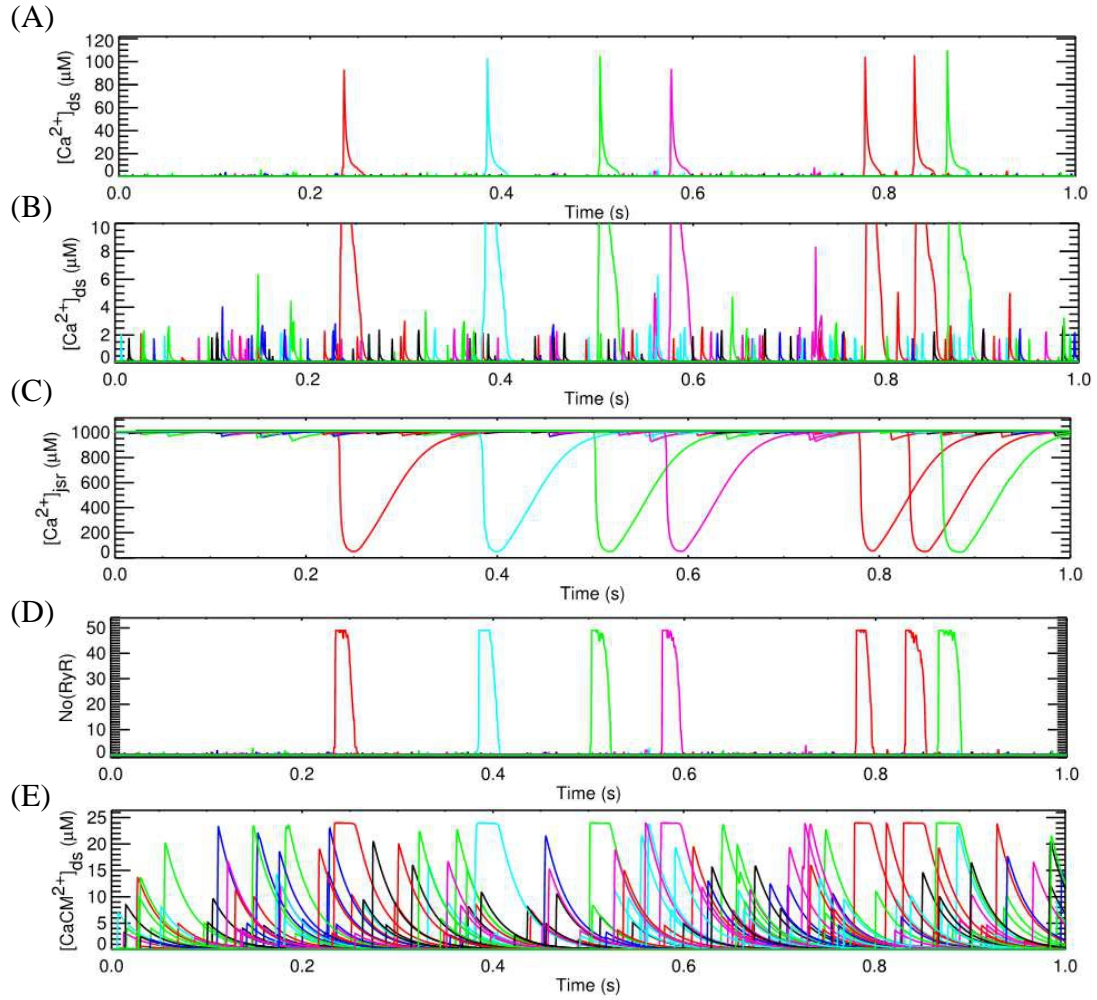


Figure 9. Calcium in the subspaces during (A) Ca^{2+} sparks and (B) Ca^{2+} quarks, (C) Dynamics of jSR Ca^{2+} release, (D) Number of RyR openings, (E) Ca^{2+} -bound calmodulin complex

The model formulation used in the reduced 2-state thermodynamically-based SERCA model is balanced with the Ca^{2+} leak, without a non-physiological back-flux. This, in essence fully account for the homeostatic leak without the need to invoke additional mechanisms or components that have not been found experimentally. This strongly implies that the mechanistic representation of the integrative model here is a useful tool to study pathophysiological conditions that may be implicated from subcellular signalling events.

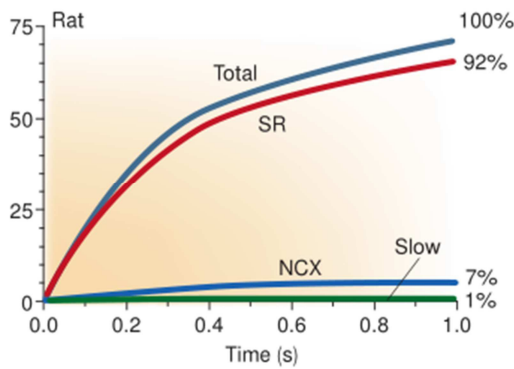


Figure 10. Quantitative Ca^{2+} fluxes during excitation-contraction coupling. The integrated fluxes during twitch relaxation in rat ventricular myocytes (Donald M Bers, 2002)

Dynamics of calcium during a twitch-relaxation cycle

To emulate the excitation-contraction of the cell, a stimulus current $I_{\text{stim}} = -6.5189 \mu\text{A}/\text{cm}^2$ was given during 5.0 ms second (Pandit et al., 2001). As transmembrane potential depolarize, it triggers the opening of LCCs; and the influx of calcium via these voltage-gated channels trigger the much higher release of Ca^{2+} from the SR. As calcium

is heavily buffered in the myocyte, it was estimated that $>100 \mu\text{M}$ is required to raise $[\text{Ca}^{2+}]_i$ from diastolic level $\sim 0.1 \mu\text{M}$ to peak $\sim 1 \mu\text{M}$ (D. M. Bers, 2000). This includes mainly the influx calcium via LCC and the release of calcium via RyR2. Among them, steady-state I_{caL} influx during a twitch was estimated about $13.4 \pm 0.7 \mu\text{mol} /$ (nonmitochondrial cell volume) (Delbridge et al., 1997) which is about $10.3 \pm 0.5 \mu\text{M}$ assuming 35% of cell is mitochondria and 50% is cytosolic volume.

In our model, the ratio of SR calcium release over the influx of calcium during a twitch is 10.017 ± 0.34 . It means that, on average, the SR-release contributes about 90.07% and calcium influx contributes 9.03%. This approximates the value 92% of SR contribution estimated for rat ventricular myocytes given in Figure 10 (D. M. Bers, 2000; Donald M Bers, 2002). Our model produced a total extrusion of calcium of about $11.5 \mu\text{M}/\text{cell}/\text{s}$. Among this, $\sim 1 \mu\text{M}$ is extruded by the PMCA and $\sim 10.5 \mu\text{M}$ is extruded by the NCX. This is in agreement with the value given above by (Delbridge et al., 1997). The ionic currents during a twitch-relaxation cycle is given in Figure 11. In our current model, the contribution from the background current is still significant, which is about $4 \mu\text{M}/\text{cell}/\text{s}$. The physiological role of this background calcium current is not clear, and we think that a better NCX model can help removing this from the model.

During the diastolic phase, we can see an increase in the spark rate. The model showed ~ 2.3 -fold increase in the spark rate compared to quiescent spark rate at rest. This is similar to what we observed in experiments. Along with this, the quark rate increase even higher, ~ 3.1 -fold. The long trace of calcium dynamics and action potential (AP)

during 1 Hz current-injected stimulus is given in Figure 12, with APD20 \sim 10.69 (ms), APD50 \sim 22.57 (ms) and APD90 \sim 78.3 (ms).

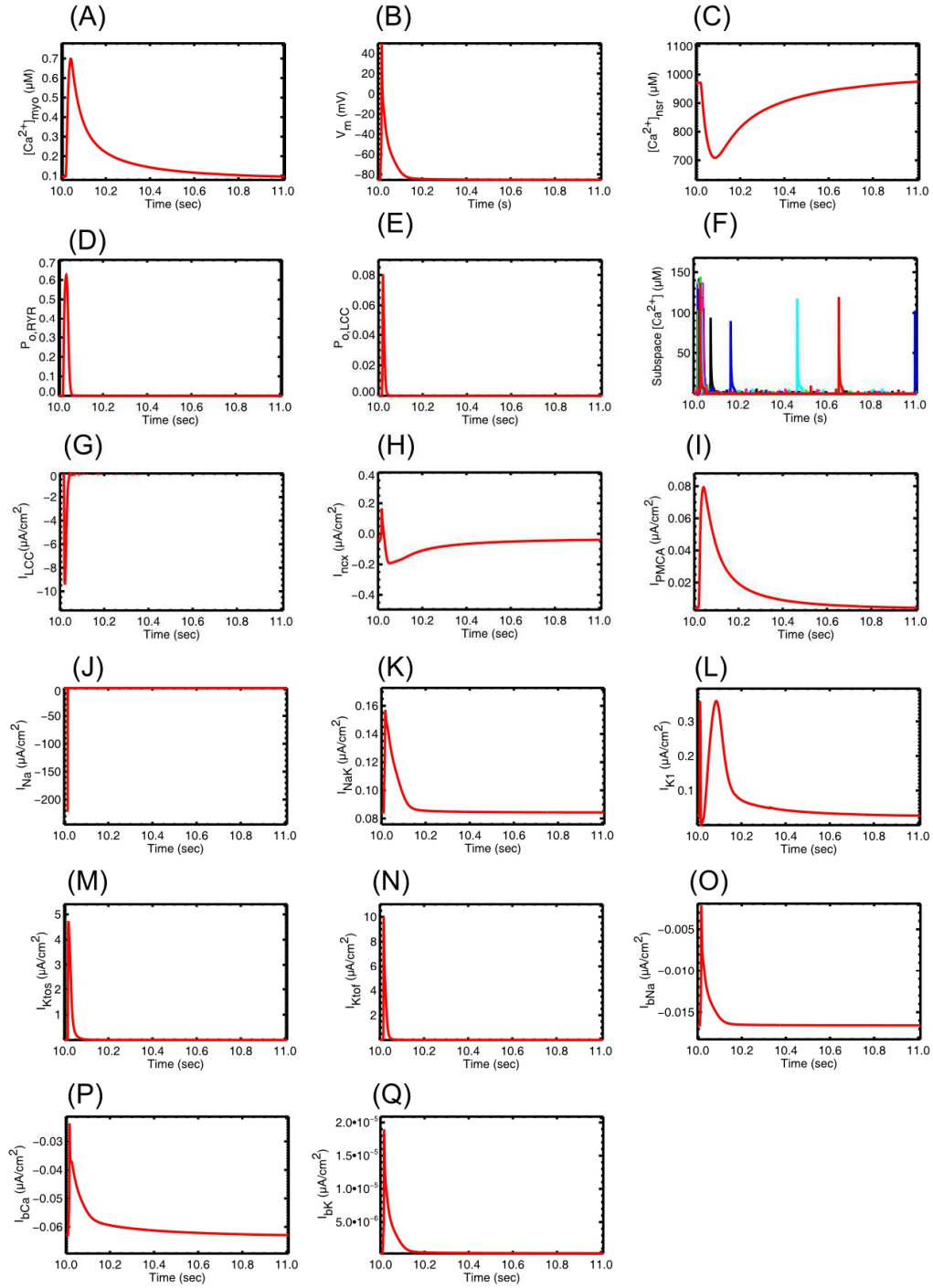


Figure 11. (A) $[Ca]_{myo}$, (B) Action potential (AP), (C) $[Ca]_{nsr}$, (D) opening probability of RyR, (E) opening probability of LCC, (F) subspace free $[Ca]_{ds}$, (G) L-type current density; (H) NCX current density; (I) PMCA current density; (J) Na^+ current density; (K) Na/K exchanger current density; (L) K1 current density; (M) slow

component of transient-outward K^+ current, (N) fast-component of transient-outward K^+ current, (O,P,Q) background currents.

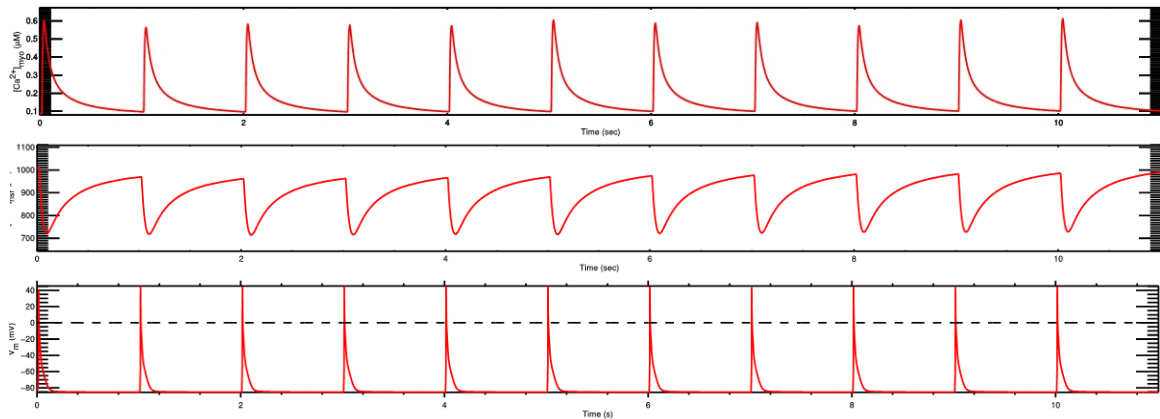


Figure 12. A long trace of calcium dynamics in the (A) myoplasm, (B) network SR, and (C) AP

T-tubule remodelling and Heart failure

The T-tubule networks, Figure 2, serve as a link between the fast membrane depolarization and the uniform global transient of calcium in the cell. The evidence that T-tubule propagates the action potential (AP) inside the ventricular myocyte was recorded using intracellular voltage imaging (Bu, Adams, Berbari, & Rubart, 2009; Endo, 1964). The influx of calcium via the LCC triggers the SR Ca^{2+} release via RyR gating channels. In a normal ventricular myocyte, the voltage-gated calcium channel links with the calcium-gating channel RyR2 on the SR membrane via a dyadic subspace with ~12 nm wide (Franzini-Armstrong, Protasi, & Ramesh, 1998, 1999; Hayashi et al., 2009). In rat, about 75% of dyads are in the T-tubule network (Page & Surdyk-Droske, 1979). In addition, cells devoid of T-tubule system has showed slow intracellular calcium transient

(Haddock et al., 1999). Thus, the functional role of T-tubule networks is believed to synchronize calcium releases from individual calcium release sites (L S Song, Sham, Stern, Lakatta, & Cheng, 1998).

T-tubule alterations (dilation, and loss of T-tubules) were first observed in failing hearts by electron microscopy (EM), e.g. higher T-tubule surface area given the total sarcolemma area to cell volume remains constant in rat pressure overload hypertrophy (Page & McCallister, 1973) or loss of T-tubules in degenerating cells (Maron, Ferrans, & Roberts, 1975). Later on, using laser scanning confocal microscopy, researchers were able to quantify the significant loss in T-tubule density in failing canine heart (He et al., 2001).

Abnormal spatial organization of the T-tubule networks was hypothesized as a mechanism of intracellular Ca^{2+} dyssynchrony through ‘orphaning’ of RyR2 (L. S. Song et al., 2006). The T-tubule remodelling may disrupt the functional co-localization (Bito, Heinzel, Biesmans, Antoons, & Sipido, 2008), as shown in Figure 13 (Polakova & Sobie, 2013). Regional loss of T-tubules was also found to associate with delayed, dyssynchronous Ca^{2+} transient in heart failure in adult ventricular myocytes (Guo, Zhang, Wei, Chen, & Song, 2013; Kemi et al., 2011; van Oort et al., 2011; Wei et al., 2010; Wu et al., 2011). Today, the major common characteristics of T-tubule alterations are: (1) loss of T-tubule (reduction in T-tubule density), (2) disruption of the orderly arrayed T-tubule network, (3) a decrease in transverse direction and increase in longitudinal direction, (4) an increase in T-tubule diameter (Guo et al., 2013).

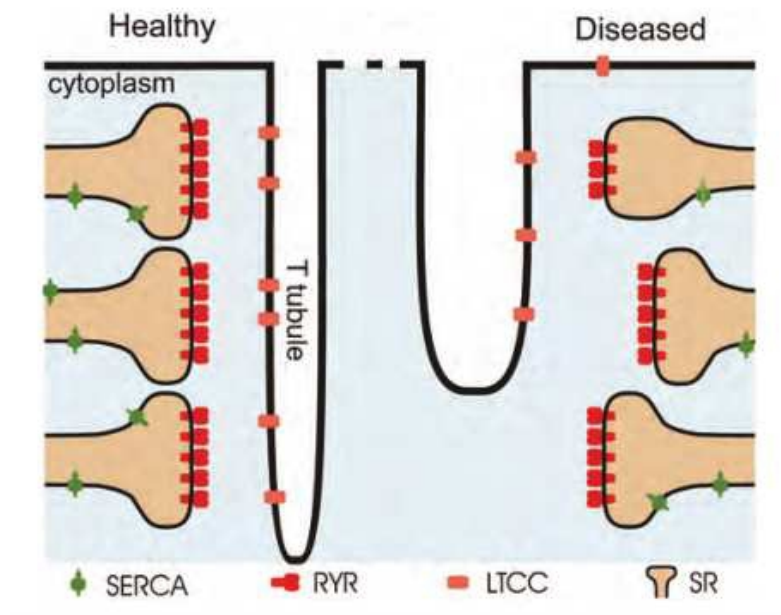


Figure 13. A schematic diagram of dyadic junctions in healthy and diseased cardiac cells (adopted from (Polakova & Sobie, 2013))

Using stimulated emission depletion (STED) microscopy, Wagner et al. was able to show T-tubule remodelling during early HF development (SHAM vs. 4-week (4pMI) and 8-week (8pMI) post-myocardial infarction hearts) (Wagner et al., 2012). The higher resolution of STED provided a better quantification of T-tubule diameters and their enlargement during MI, Table 1. Interestingly, in contrast to previous results about regional loss, the authors found a significantly increase in the total network length, both at 4pMI and 8pMI. In particular, the nearly 2-fold increase in triple junctions, which was only detectable using STED. Therefore, the authors suggested a more complicated scenario than previously thought, which now include T-tubule network length, complexity, proliferate membrane remodelling processes during early HF. The fracturing

in network sarcomere misalignment at 8pMI suggested severe disorganization with loss of local T-tubule association with junctional SR at striations, which is consistent with other studies at relative late stage of HF.

Table 1. Comparison of measured T-tubule at less than 3 μm from the surface between using confocal vs STED mode (* $p < 0.001$).

Imaging mode	Diameter X (nm)	Diameter Y (nm)	Area (1000 nm^2)	Circumference (nm)
Confocal	273.1 ± 2.7	266.1 ± 2.1	57.2 ± 0.7	945.3 ± 6.7
STED	206.0 ± 3.5 *	194.6 ± 2.7 *	31.8 ± 0.7 *	708.6 ± 9.8 *

The data in (Wagner et al., 2012) suggest heterogeneous changes of individual TT components as well as RyR2 clusters and CRUs. The findings are consistent with and extend the previously described RyR2 “orphaning” (L. S. Song et al., 2006) and further show decreased Jph2 levels previously established as mechanism of increased CRU spacing at TT junctions (van Oort et al., 2011). Here, computational modeling of changes in HF and through heterogeneous T-tubule reorganization and RyR2 orphaning was used to uncover the local mechanism of delayed subcellular Ca^{2+} release and action potential prolongation. The fully stochastic model features 20,000 independent calcium release sites, including Ca^{2+} spark behavior, and reproduce the systolic $[\text{Ca}^{2+}]_i$ transient throughout a propagated action potential activating L-type Ca^{2+} channels (LCC) at the surface membrane and at TTs. The LCC current elevates $[\text{Ca}^{2+}]_i$ locally in the “subspace”

compartment between the TT and terminal SR membrane, which is greatly amplified when RyR2 clusters are activated by locally elevated subspace $[Ca^{2+}]_i$ as occurs during CICR.

This whole-cell model examines the changes in local calcium concentration in HF by implementing previously established changes in ion transport proteins: fast and slow K^+ currents (I_{to} and I_{K1}) were reduced by 20%; NCX protein expression was increased by 100% (Hasenfuss et al., 1999); SR Ca^{2+} ATPase (SERCA2a) protein was decreased by 30% (Meyer et al., 1995); and RyR2 Ca^{2+} sensitivity was increased by 50% to mimic increased activity from chronic hyperphosphorylation (Lehnart et al., 2005). The results from an earlier version of the model were published elsewhere (Wagner et al., 2012). As shown in Figure 14, I_K plays a major role in AP prolongation which may provoke arrhythmogenic, delayed afterdepolarization.

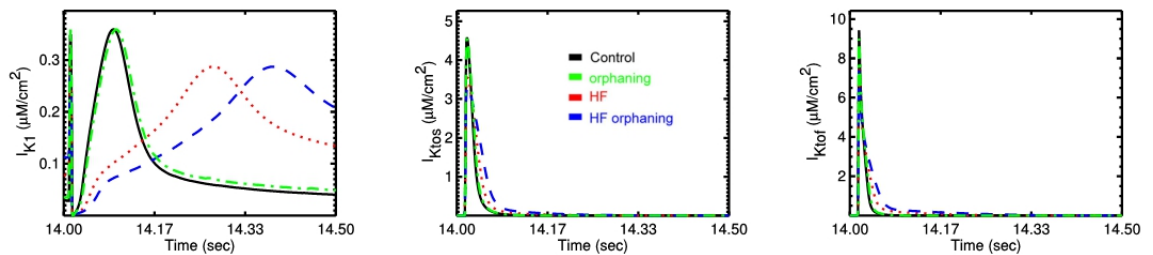


Figure 14. Dynamics change of Potassium currents during HF

Heterogeneous TT changes were investigated through increased spacing between TTs and RyR2 clusters at CRUs of only 25% of TT junctions (whereas 75% of CRU nanodomains remained unchanged), consistent with our data and earlier studies (L. S. Song et al., 2006). Orphaning of RyR2 clusters during HF due to T-tubule remodelling was implemented for 25% CaRUs through 30-fold increases in the subspace volume; whereas 75% of CaRUs remains unchanged. The increase in subspace volume emulates the uncoupling between LCC and RyR2 during an AP. In failing hearts, the spontaneous calcium leak increases which may imply an increase in opening rate constants. The delayed subcellular Ca^{2+} release and AP prolongation showed in the simulation result confirmed that the RyR cluster reorganization may contribute to electric and contractile dysfunction.

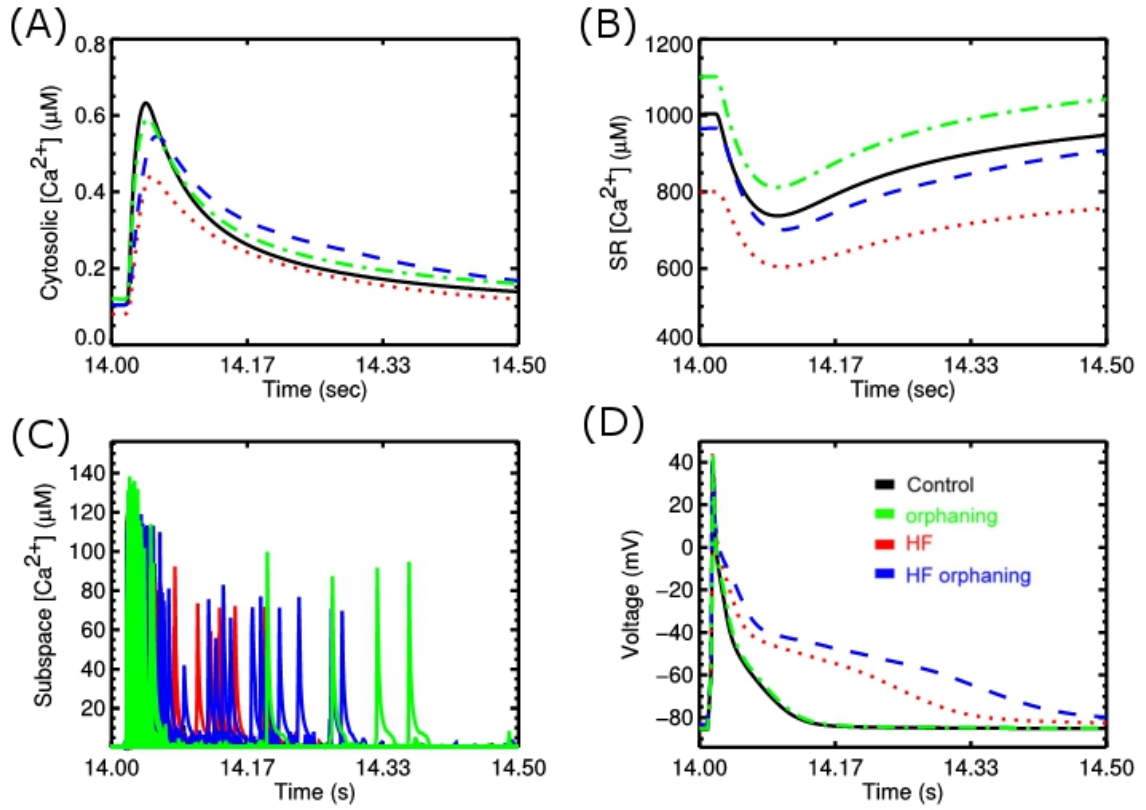


Figure 15. (A) Cytosolic $[Ca^{2+}]$, (B) SR $[Ca^{2+}]$, (C), subspace $[Ca^{2+}]_{ds}$, (D) AP

Under steady-state pacing conditions (1 Hz), the CRU model readily reproduced AP prolongation in HF, which was further worsened by additional RyR2 orphaning, whereas isolated RyR2 orphaning (without any HF changes) at 25% of CRUs caused only minimal AP prolongation (Figure 15.D). In HF, AP prolongation was paralleled by a delayed cytosolic $[Ca^{2+}]_i$ transient, and additional RyR2 orphaning clearly aggravated the $[Ca^{2+}]_i$ transient delay and decay (Figure 15. A). Importantly, the CRU model reproduced decreased SR Ca^{2+} load, a hallmark of E-C coupling pathophysiology in HF, which was blunted by RyR2 orphaning (Figure 15. B – dotted red line). Unexpectedly, combined

RyR2 orphaning with HF normalized SR $[Ca^{2+}]$ load in diastole (Figure 15. B – dashed blue line). Furthermore, in HF depletion of diastolic SR $[Ca^{2+}]$ load resulted in an increased late L-type Ca^{2+} current (LCC) due to decreased Ca^{2+} dependent inactivation, further increased by RyR2 orphaning in HF (Figure 16. A), and late Ca^{2+} leak components, Figure 15. C and Figure 16Figure 16 (C).

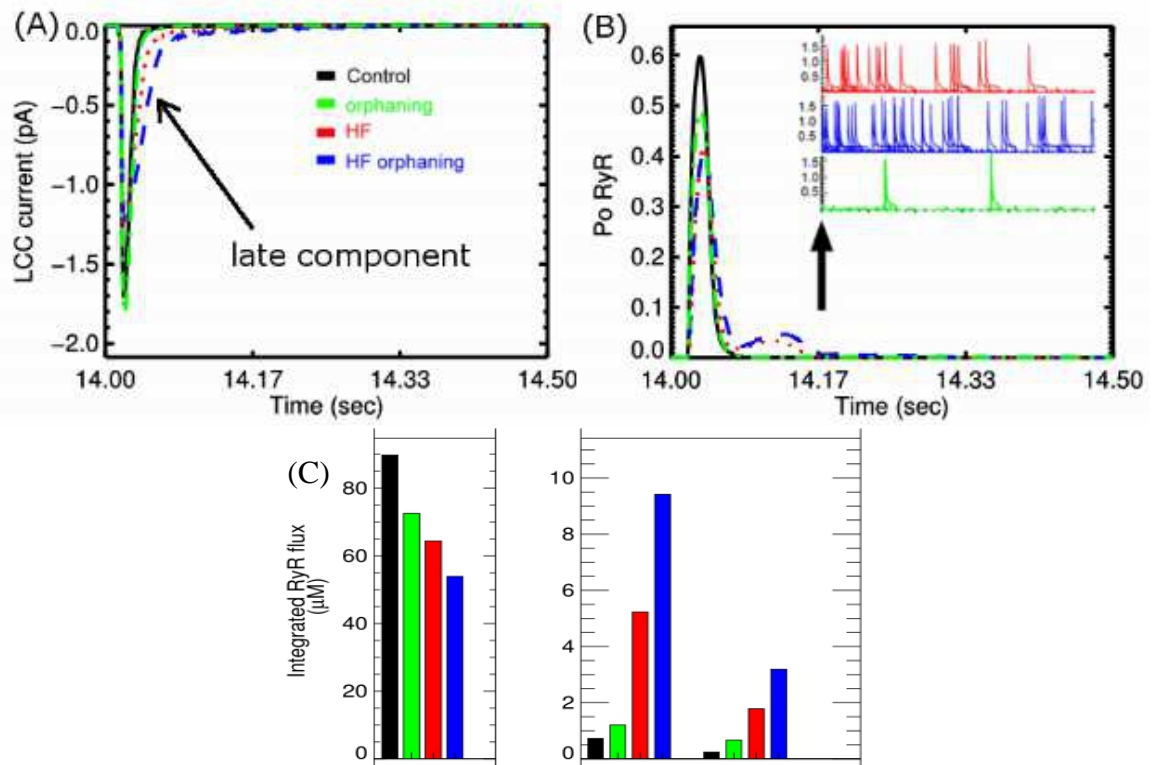


Figure 16. (A) LCC current, (B) Probability of RyR opening, (C) Integrated RyR Ca^{2+} flux during diastole and systole

Calciums alternans

The alternating strong and weak beats in left ventricle is known as *pulsus alternans* or mechanical alternans which was first described in the 19th century by Traube (Traube, 1872). Another type is electrical alternans (or T-wave alternans) which describe the beat-to-beat variation in direction, amplitude, and duration of any components in an ECG waveform (J. M. Smith, Clancy, Valeri, Ruskin, & Cohen, 1988). The two are distinguished, yet they may both coexist (Lewis, 1911; Surawicz & Fisch, 1992). Using ECG, T-wave alternans (beat-to-beat alternation in the amplitude of the T-wave, ST segments or U-wave) can be observed and is considered as a useful indicator for assessing sudden cardiac death (SCD) (Estes et al., 1997; Narayan, 2006; Pastore, Girouard, Laurita, Akar, & Rosenbaum, 1999; Rosenbaum et al., 1994).

The mechanisms producing pulsus alternans fall into 2 categories: hemodynamic or contractile (Euler, 1999). For the first category, the hemodynamic mechanism (with the change in pressure, volume) is explained by the Frank-Starling relationship which describes an intrinsic property of the myocardium by which an increase in the end-diastolic volume causes a greater stroke volume and systolic pressure in the next beat. For the second category (with the change in inotropic state or heart rate), the mechanism for the alternation in the contractility may be explained by the variation in AP duration (APD).

Pulsus alternans is associated with different pathophysiological conditions, e.g. aortic stenosis, tachycardia, ischemia, acidosis and hypertrophic cardiomyopathy (Edwards & Cohen, 2003). Other tested conditions that may lead to cellular or subcellular

alternans include, but not limited to: decrease RyR P_o to increase the variability of Ca^{2+} transient between the different area of the cell (Diaz, Eisner, & O'Neill, 2002), metabolic deficiencies, e.g. acidosis (Orchard, McCall, Kirby, & Boyett, 1991) and/or abnormal calcium handling (Surawicz & Fisch, 1992).

The pulses alternans may lead to pulseless activity (Weiss et al., 2006), i.e. when there is an electrical activity, but the heart either does not contract, or the contraction is not strong enough to produce an sufficient cardiac output to generate a pulse. This pulseless condition is life-threatening due to the loss of blood supply to the brain, causing the patients unconsciousness or stop breathing, leading to cardiac arrest. Pulsus alternans is a systolic phenomenon in left ventricular myocytes with alternation in contractility, but non-significant changes in relaxation and diastolic function (O. M. Hess, Surber, Ritter, & Krayenbuehl, 1984).

It has been suggested that modified intracellular calcium cycling play a role in occurrence of mechanical and electrical alternans (Diaz, O'Neill, & Eisner, 2004; Kihara & Morgan, 1991; Lab & Lee, 1990; Xie, Sato, Garfinkel, Qu, & Weiss, 2008). Thus, calcium alternans is associated with T-wave alternans and pulsus alternans. Calcium alternans is a beat-to-beat variation in intracellular Ca^{2+} transient amplitude. Typically, calcium alternans occurs at high heart rates, yet the frequency threshold varies by different conditions such as ischemia or ionic disturbances that disturb the bidirectional coupling between the membrane potential and intracellular calcium. This has been identified as a potential precursor to the dangerous reentrant arrhythmias and SCD; yet the mechanism is not well understood (Gaeta & Christini, 2012). Current computational

models are unable to recreate this phenomenon; unless certain modifications to the ionic currents were made (Fox, McHarg, & Gilmour, 2002; Tao et al., 2008).

Using the computational model developed above, we aimed to test the following:

(1) Does the model generate alternans at high pacing rate, a condition that has been widely observed in experiments? (2) If so, what is the mechanism of calcium alternans observed in the model? (3) How do other factors, e.g. temperature and $[Na^+]_i$, affect the generation of alternans? To the best of our knowledge, this is the first study of its kind using a stochastic computational model with a fully stochastic 20,000 CRUs to investigate the underlying mechanism of cellular cardiac alternans.

At high pacing rate, both the $[Ca^{2+}]_i$ and $[Ca^{2+}]_{SR}$ has not been recovered back to the normal diastolic level is depicted in Figure 17. During higher pacing frequencies, here we tested from 1 Hz to 8 Hz, the diastolic cytosolic calcium at the time of the next trigger remains at a high level than that at a lower pacing frequency. As a result, the subspace calcium remains high which likely affect the gating of L-type calcium channels due to Ca^{2+} -dependent inactivation. Besides, the lower SR Ca^{2+} level along with the higher $[Ca^{2+}]_{ds}$ in turns affect the gating of RyR2 in an opposite way. Lower $[Ca^{2+}]_{SR}$ reduces the opening probability of RyR2, while higher $[Ca^{2+}]_{ds}$ enhances the opening probability of RyR2. This bidirectional effect is believed to a factor contributing to forming the alternations in RyR2 opening probability.

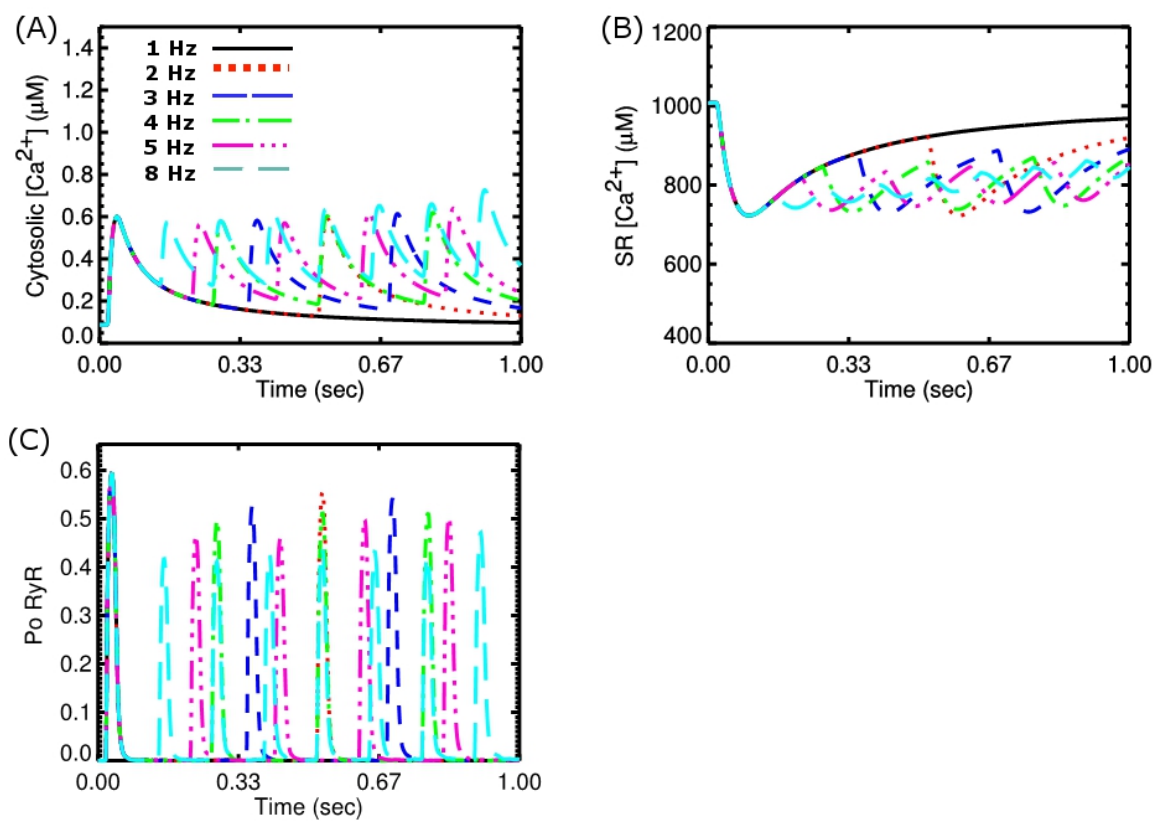


Figure 17. (A) Cytosolic calcium, (B) SR $[Ca^{2+}]$, (C) P_o of RyR2

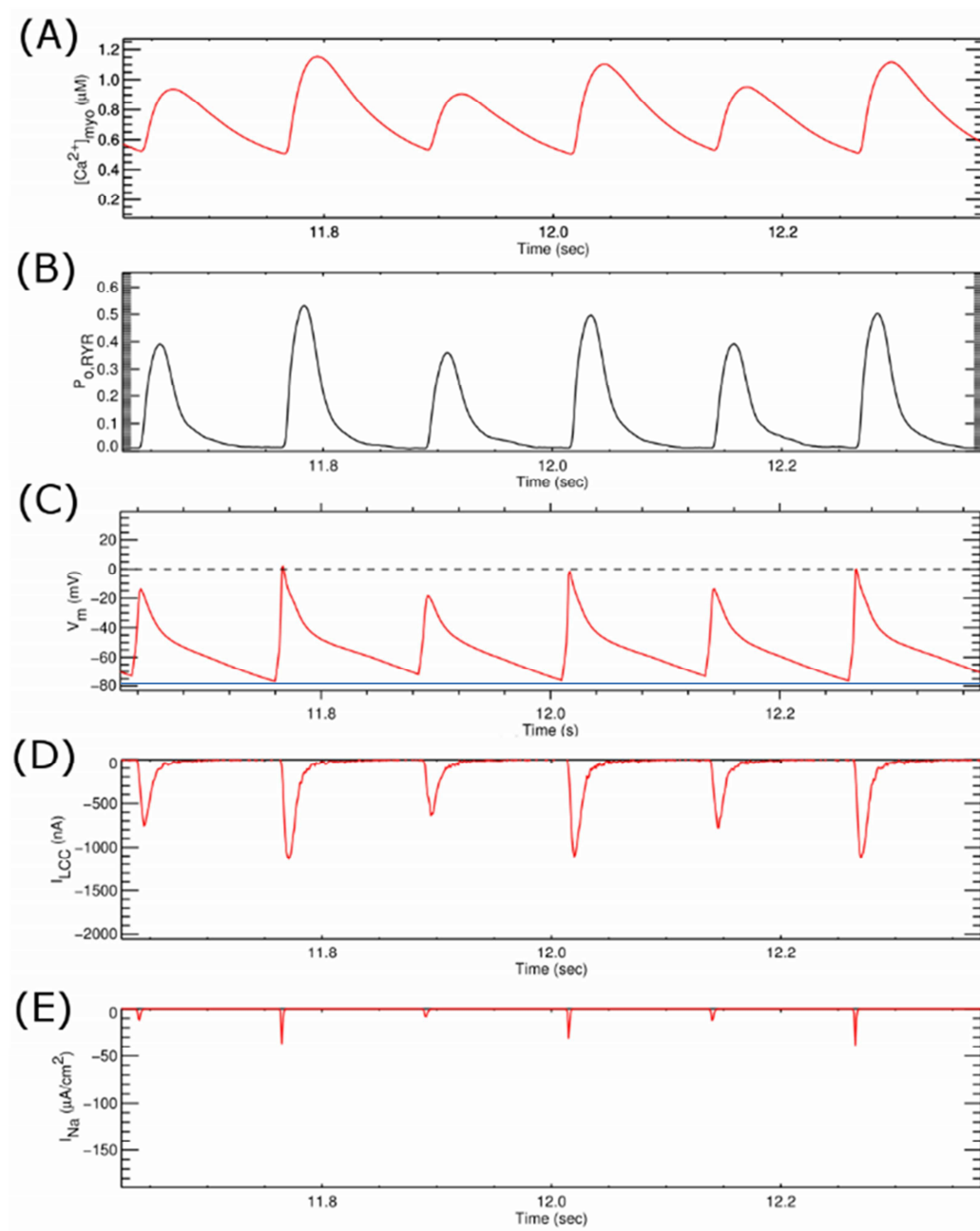


Figure 18. Calcium alternans at 8Hz: (A) Cytosolic calcium, (B) $P_0(RyR2)$, (C) V_m , (D) I_{CaL} , (E) I_{Na}

As shown in Figure 18, calcium alternans in the model, observed at 8 Hz, is in sync with voltage alternans which is termed concordant alternans. During calcium alternans at high pacing rate, we see the change in I_{Na} , I_{CaL} , SR $[Ca^{2+}]$ levels, V_m and APD. This multifactorial change makes it harder to infer the cellular origin of voltage and calcium alternans. Using our advanced stochastic model, we now are able to investigate these changes at individual calcium release sites.

Due to one or many of the above factors, at high frequency, a certain fraction of CRUs firing in the current beat will not be able to fire in the next beat. We tested by analyzing beat-to-beat changes of CRU's states. CRUs are grouped into either Activated or Inactivated at each beat. Then, there are 4 groups: Act-Act, Act-Inact, Inact-Act, and Inact-Inact. As showed in Figure 19, when there is alternans, there is a significant change in Act-Inact (blue group) or Inact-Act (yellow group). In the transition from beat-1 to beat-2, there is a large fraction of CRUs changing from Inactivated to Activated (green), and also a large fraction of CRUs which are Activated in beat-1 continue to Activate in beat-2 (red) – the beat that has a strong contraction. This is interesting, as we want to know what is the driving force that keep the CRUs activated in the beat-(i) continue to activate in beat-(i+1), as shown in Figure 20, and what make more CRUs firing in the large beat than in the small beat.

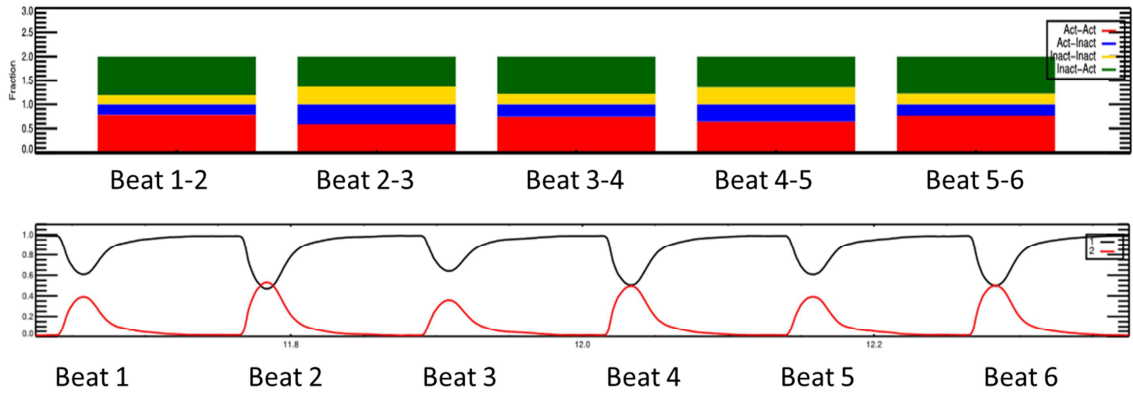


Figure 19. (A) beat-to-beat variation in CRU's states where we examine Act-Act (the fraction of CRU that Activate in beat- i , and continue to Activate in beat- $(i+1)$), similarly with Act-Inact, Inact-Inact, and Inact-Act, **(B)** The probability of RyR opening at each beat (red = open, black = closed)

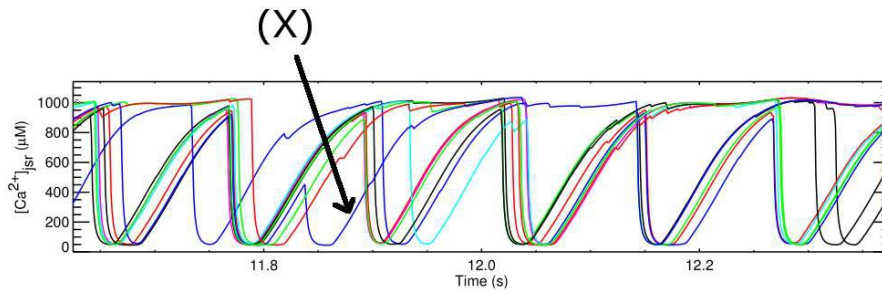


Figure 20. An example that show a CRU that fires at two contiguous beats, e.g. (X) marks the release sites that is Act-Act

The high diastolic calcium at high frequency can be explained by the shortened diastolic phase, thus Na^+/Ca^{2+} exchanger and SERCA pump don't have enough time to bring cytosolic calcium back to the normal resting level. Along with this, we can see a significant increase in basal Ca^{2+} /Calm level, e.g. at 8 Hz compared with 1 Hz as shown in Figure 21. This implies the strong Ca^{2+} -dependent inactivation of L-type Ca^{2+} channels

during high stimulus rate. During calcium alternans, we also see alternations in I_{CaL} current and opening probability of RyR. The reduction in I_{Na} current which reduced the action potential magnitude contributed a huge effect in reducing the number of L-type channels opening that opens the gateway for alternans, Figure 18. This is in agreement with the result in which a small depolarizing potential can induce alternans (Diaz et al., 2004), and to confirm the hypothesis that SR Ca^{2+} release is graded with the beat-to-beat alternation in I_{CaL} (Altamirano & Bers, 2007a, 2007b). The simultaneous alternation of calcium (Ca-ALT) and voltage (Vm-ALT) alternans was also observed in isolated guinea pig (Wan et al., 2012). However, in their model study, the Vm-ALT is the alternation in AP duration (APD), without any alternation in voltage overshoot where they hypothesized the balance between I_{NCX}/I_{Ca} plays the role. We suspect that using guinea pig, the BCL is large that doesn't affect the Na current. Thus, the mechanism we found here is different.

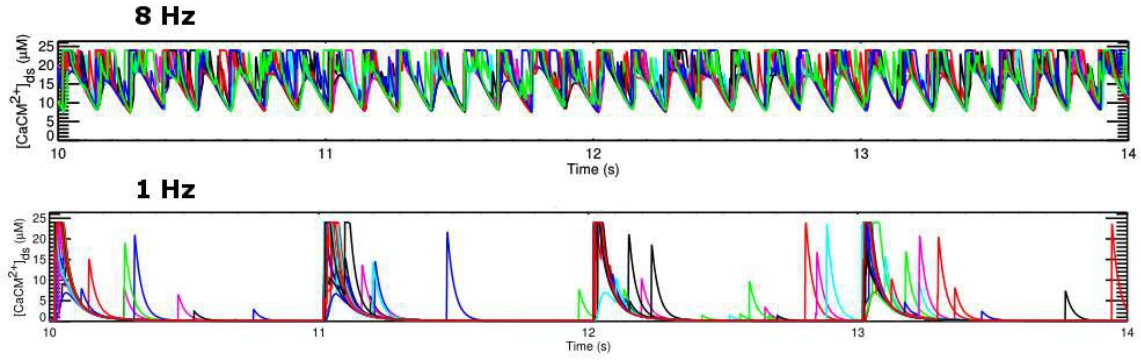


Figure 21. Ca^{2+} /CaM complex at the subspace during 8Hz and 1Hz pacing frequency

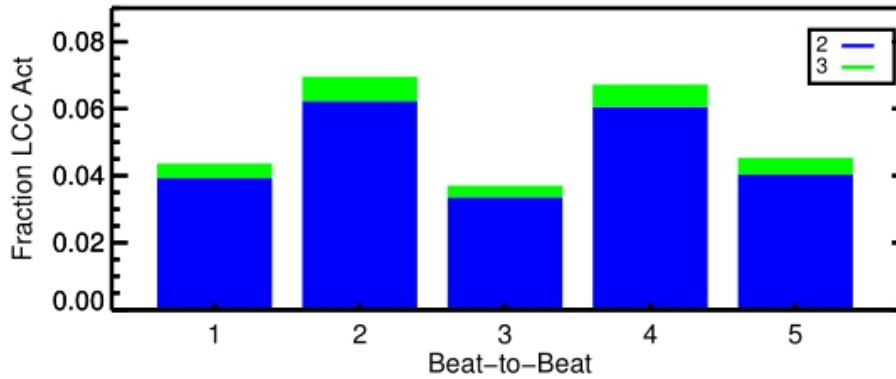


Figure 22. LCC opening (S_2 and S_3) at each beat

With the current model, it enables us to investigate the states of L-type Ca^{2+} channels at the release sites that activate during each beat. During Ca^{2+} alternans, the model reflects an alternation in the fraction of channels in the open states (S_2 and S_3) at the activated CRUs, Figure 22. We then investigate what is the difference between LCCs from the activated CRUs and those from the inactivated CRUs, by dissecting the fraction of channels in each state before each stimulus for different groups of CRUs. Table 2 and

Table 3 showed the fraction of L-type Ca^{2+} channels (LCCs) in each states, given that these LCCs are from two separate groups of CRU: activated and inactivated, respectively, in each beat. As we can see here, LCCs from inactivated CRUs has more channels in Ca^{2+} -dependent inactivation and V_m -dependent inactivation. The small number here is significant given the fact that in the model, the peak $\text{Po}(\text{LCC}) = 8\%$ during a normal AP. This is because each CRU has 7 channels, and typically, only one LCC opening is enough to trigger the CRU, and not all CRUs are opened during an AP.

Table 2. The fraction of LCCs (from the CRUs which are **Activated**) in each state at the beginning of the stimulus at each beat [S2 = open, S3 = open, S4 = Ca^{2+} -dependent inactivation, S5 = V_m -dependent inactivation]

	Beat 1	Beat 2	Beat 3	Beat 4	Beat 5
S1	0.000227842	0.00000	0.00000	0.00000	0.00000
S2	0.00000	0.00000	0.00000	0.00000	5.58690e-05
S3	5.69606e-05	0.00000	0.00000	0.00000	0.00000
S4	0.0516632	0.0436445	0.0576588	0.0433101	0.0510643
S5	0.0901686	0.0789605	0.0902382	0.0809587	0.0855355
S6	0.857883	0.877395	0.852103	0.875731	0.863344

Table 3. The fraction of LCCs (from the CRUs which are **Inactivated**) in each state at the beginning of the stimulus at each beat [S2 = open, S3 = open, S4 = Ca^{2+} -dependent inactivation, S5 = V_m -dependent inactivation]

	Beat 1	Beat 2	Beat 3	Beat 4	Beat 5
S1	9.57488e-05	0.000165920	0.00000	0.00000	0.00000
S2	0.00000	0.00000	0.00000	0.00000	0.00000
S3	0.00000	0.00000	0.00000	0.00000	0.00000
S4	0.0570663	0.0545877	0.0629136	0.0527631	0.0577171
S5	0.0968020	0.0930811	0.102621	0.0892122	0.0983071
S6	0.846036	0.852165	0.834466	0.858025	0.843976

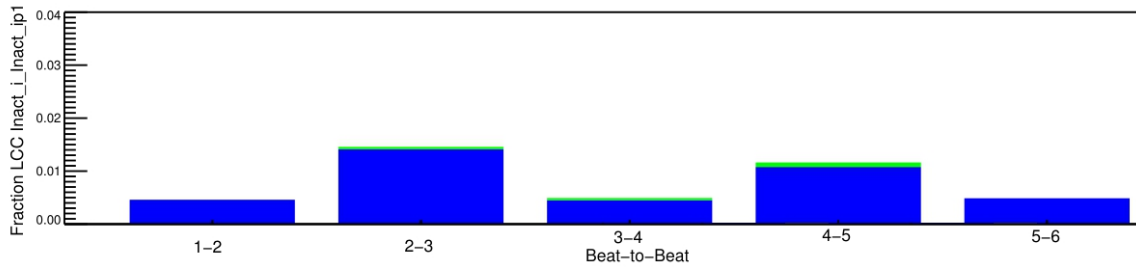


Figure 23. The fraction of LCCs in the opening states at the beginning of the stimulus from Inact-Inact CRUs

Given the fact that the CRUs are inactivated during an AP, the question is at these inactivated release sites, whether the LCCs are opened or not? By looking at CRUs that are inactivated in beat-(i) and continue to inactivated at beat-(i+1), as shown in Figure 23, interestingly, there are some CRUs which have opening LCCs, yet RyR2 are not opened. This only can be seen in a stochastic model. The result suggested that there are some other factors that may control to the opening of RyRs, other than the influx of LCC. This can be the stochastic nature of RyR gating, the diastolic SR $[Ca^{2+}]$ level or both. In the current model, RyR refractoriness has not been incorporated.

One factor that may leads to the alternans is the recovery of junctional SR Ca^{2+} , the direct source of calcium release during CRU activations. Some studies found that the cellular alternans has been related to the amount of SR Ca^{2+} release, when high external $[Ca^{2+}]$ is used (5 mM) and no high frequency stimulation (Diaz et al., 2004), and was explained by the stability vs. instability in the regulation of SR $[Ca^{2+}]$ (Eisner, Diaz, Li, O'Neill, & Trafford, 2005; Sipido, 2004). In another study, loaded the rabbit ventricular myocytes with Fluo-4 and Fluo-5N, (Picht, DeSantiago, Blatter, & Bers, 2006) found that

Ca^{2+} alternans occurs with SR $[\text{Ca}^{2+}]$ alternations in about 50% of the cases, and can also occur without significant diastolic SR $[\text{Ca}^{2+}]$ alterations in about 20% of the cases, Figure 24. The authors explained the smaller SR $[\text{Ca}^{2+}]$ release, for the same diastolic $[\text{Ca}^{2+}]$ level by the slow SR Ca^{2+} release responsiveness, i.e. RyR refractoriness (Picht et al., 2006; Shkryl, Maxwell, Domeier, & Blatter, 2012). In addition, these studies didn't found I_{CaL} alternate during alternans. The species that these studies did are large animal (rabbit) in which the pacing rate is small. We suspect that the longer BCL in their model allow enough time for LCC to recover, thus it doesn't disturb the I_{CaL} current. So, the mechanism that we found in the model for rat ventricular myocyte is different. However, we still don't know the role of $[\text{Ca}^{2+}]_{\text{jSR}}$.

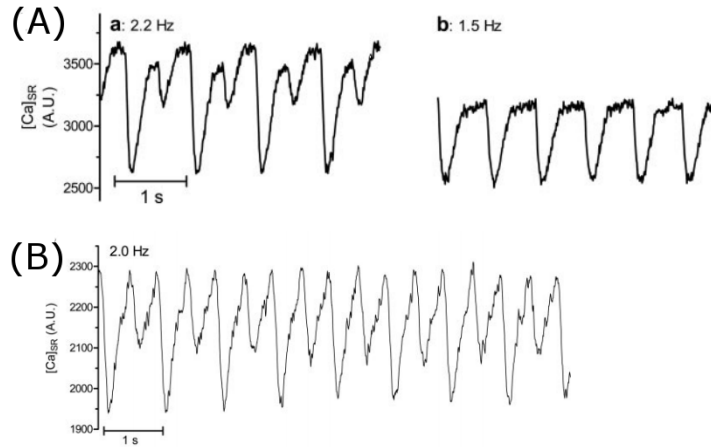


Figure 24. From rabbit ventricular myocyte: (A)a. alternans with alternation in diastolic SR $[\text{Ca}^{2+}]$ at 2.2Hz, (A)b. no alternans at 1.5Hz, (B) alternans without alternation in diastolic SR $[\text{Ca}^{2+}]$ at 2Hz (Picht et al., 2006)

At high frequency, $[\text{Ca}^{2+}]_{\text{jSR}}$ may not have enough time to fully recover, thus diastolic $[\text{Ca}^{2+}]_{\text{jSR}}$ may affect the opening probability of RyR2 whose gating is modelled

with lumenal calcium dependency. We splits the CRUs at each beat in two groups: those that are activated (Act) and those are not (Inact), and investigated two things: (1) the values of $[Ca]_{jSR}$ at these release sites, right at before the next beat to start, (2) the nadir of $[Ca]_{SR}$ during calcium release. Interestingly, the effect of $[Ca^{2+}]_{jSR}$ difference at the CRUs between the two groups are more prominent than $[Ca^{2+}]_{SR}$, Figure 25. As shown in the figure, the larger SR $[Ca^{2+}]$ comes with a larger release. We can see that the ensemble $[Ca^{2+}]_{SR}$ is not an indicator of alternans formation. If we look at the nadir $[Ca^{2+}]_{SR}$, the result show a similar small beat-to-beat alternation, in agreement with the study of (Diaz et al., 2004). At the normal quiescent condition, in our previous study, the activation of a CRU is the result of 8-10 RyR2 opening (Williams et al., 2011). During field-stimulus simulation with high pacing, this number reduces to 5, where Ca^{2+} alternans is observed, Figure 26. During the large beat, there can be upto 80% of CRUs activated, though the peak of activation is slower, e.g. 60%. The data also suggest that more recruitment of CRUs during large beat.

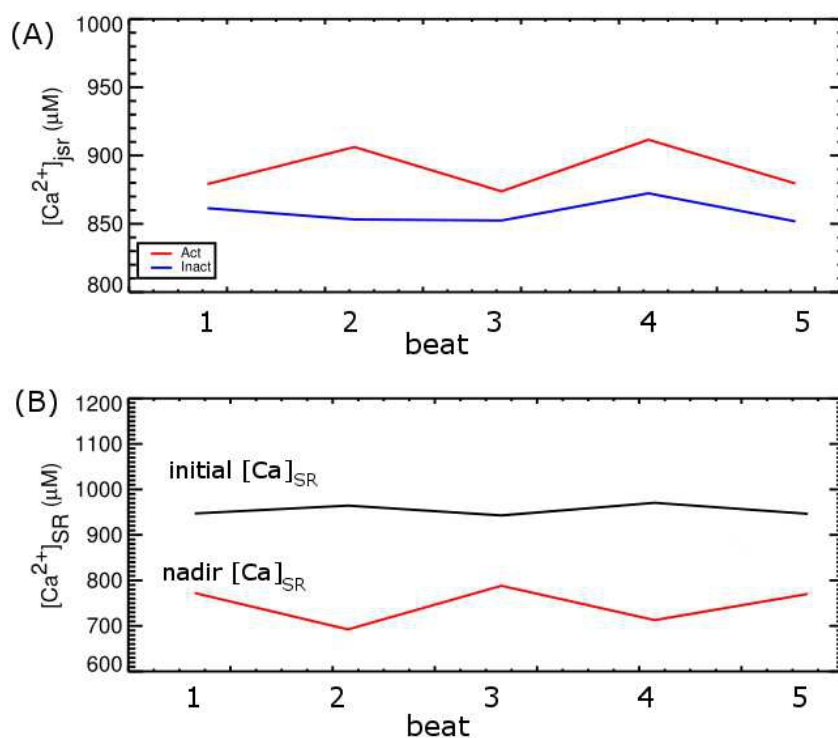


Figure 25. (A) The diastolic $[Ca^{2+}]_{SR}$ right before the stimulus from CRUs in two groups: **red** = Act, **blue** = Inactivate. (B) The upper black line shows the average $[Ca^{2+}]_{SR}$ level right before the I_{stim} is applied, and the lower **red** line shows the nadir of average $[Ca^{2+}]_{SR}$ level at the corresponding beat.

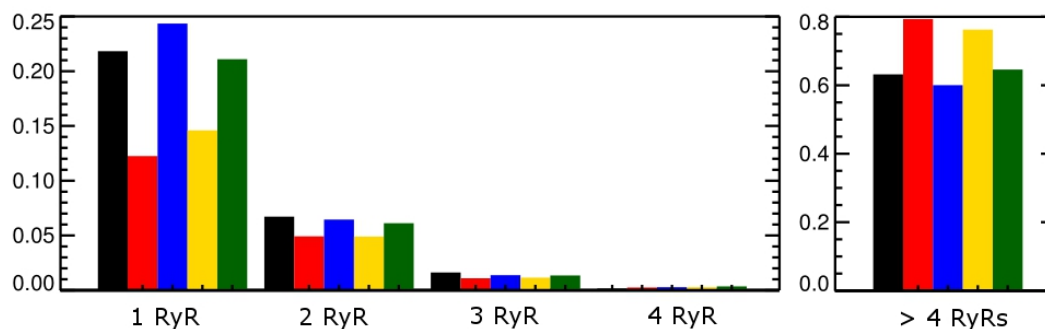


Figure 26. The fraction of CRUs that has 1 or more RyR openings during each beat (black = beat-1, red = beat-2, blue = beat-3, yellow=beat-4, green=beat-5)

We then tested the model with other scenarios that may facilitate the formation of cardiac alternans. These hypotheses involve high level of $[Na^+]_i$ that may affect Na^+/Ca^{2+} exchanger activity (NCX). The normal function of NCX is to extrude one calcium out and bring three sodium in. At high level of $[Na^+]_i$, it may fail to extrude calcium, thus maintaining a high diastolic cytosolic $[Ca^{2+}]$. In other words, increasing Na^+ lead to more reverse mode NCX, Figure 31 (C), leading to more $[Ca^{2+}]_i$ and $[Ca^{2+}]_{SR}$ loaded. In the normal high pacing simulation of our model, alternans were observed at $[Na^+]_i$ at ~ 12 mM. We tested the effect of high sodium concentration by fixing the sodium level with $[Na^+]_i = 15$ mM. Under this condition, alternans were also observed, Figure 27, yet the levels of cytosolic calcium, at both basal and peak, are higher. Compared to the normal 8 Hz condition, the diastolic $[Ca^{2+}]_i$ increase from $0.5 \mu M$ to $0.6 \mu M$, and increase $[Ca^{2+}]_{nSR} \sim 1.1$ mM from 1.05 mM, Figure 30. However, at $[Na^+]_i = 20$ mM, it reduces alternans, Figure 31. This is quite interesting. What we observe from the model is that both $[Ca^{2+}]_{myo}$ and $[Ca^{2+}]_{SR}$ have reached to a level high enough to trigger sufficient RyR2 activation per beat. This also affects the V_m depolarization, i.e. V_m is positive enough, Figure 31, making I_{Na} becoming more regular. This shows the complicated relationship between different gating channels, as well as the ionic concentration that involves, in that when a single one go extreme, it may affect the whole system dramatically and in an unpredictable way (Eisner et al., 2005).

We then tested with NCX upregulation. The high expression level of NCX brings SR calcium down, along with cytosolic $[Ca^{2+}]$ and thus reduce alternan amplitude, Figure 28. When NCX is downregulated to 50%, it also generates alternans. However,

the effect of calcium alternation is smaller, Figure 29 (B). We can see the clearly difference in the basal level of $[Ca^{2+}]_i$ which is quite high and closed to the value we see when $[Na^+]_i = 20$ mM. In other words, reducing NCX expression 50% yield the result lie in between $[Na^+]_i = 15$ mM and $[Na^+]_i = 20$ mM. It again confirms that there is a range of changes that can be critical for the arrhythmogenesis to occur. When the temperature is reduced ($23^{\circ}C$), the alternans become more prominent, Figure 32. In this test case, the simulation was done using the Na^+ model developed by (Pandit et al., 2001). This is in agreement with many other experiments that low-temperature increases the likelihood of alternans development (G. L. Aistrup et al., 2006; Pastore et al., 1999; Rubenstein & Lipsius, 1995), and we anticipated that Na^+ current plays an important role here.

In conclusion, we presented here the first study using stochastic computational model to study the cellular mechanism underlying cardiac alternans in rat ventricular myocyte. The model helps to explain a modest role of $[Ca^{2+}]_{jSR}$ in forming alternans, while it's suggested that disturbing I_{Na} , I_{CaL} and membrane potential plays a dominant role in the forming of pulsus alternans. In addition to this, the model was able to reproduce results at conditions that has been known for alternans like lowering the temperature, high $[Na^+]_i$ or reducing alternans amplitude by up/down regulation of NCX. The limitation of the model is the inability to investigate the spatial effect on the generation of cardiac alternans, i.e. subcellular Ca^{2+} alternans or calcium waves in alternans. This will be the next step in our study with a full-scale spatio-temporal model of the cardiac ventricular myocyte to investigate subcellular Ca^{2+} alternans (Gary L

Aistrup, Shiferaw, Kapur, Kadish, & Wasserstrom, 2009; Blatter et al., 2002; Kockskamper & Blatter, 2002).

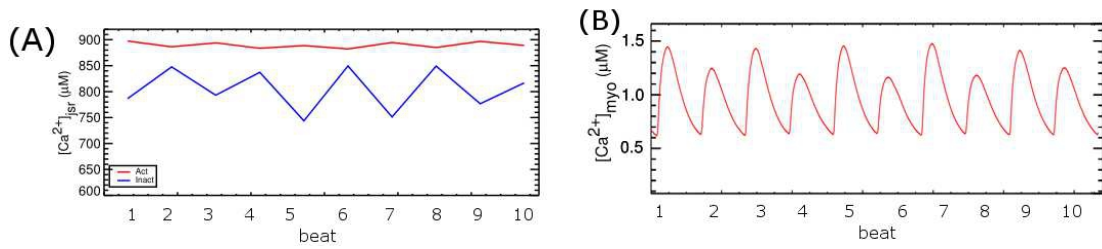


Figure 27. 8Hz pacing with $[Na^+]_i = 15mM$: (A) The average of $[Ca^{2+}]_{SR}$ right before the stimulus from CRUs in two groups: red = Act, blue = Inactivate, and the nadir value. (C) calcium transient

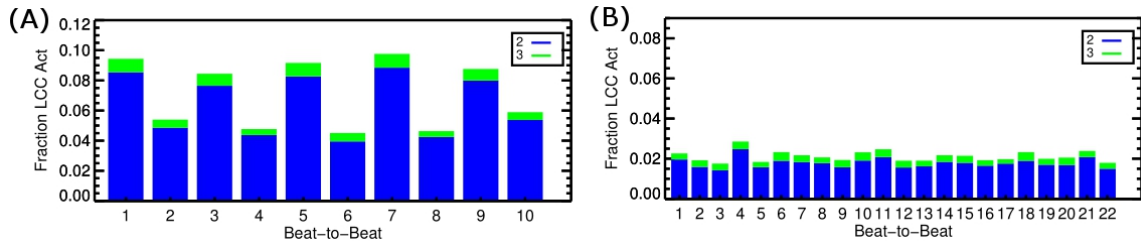


Figure 28. LCC opening (S2,S3) when (A) $[Na^+]_i = 15mM$, (B) NCX expression 1.5x increase

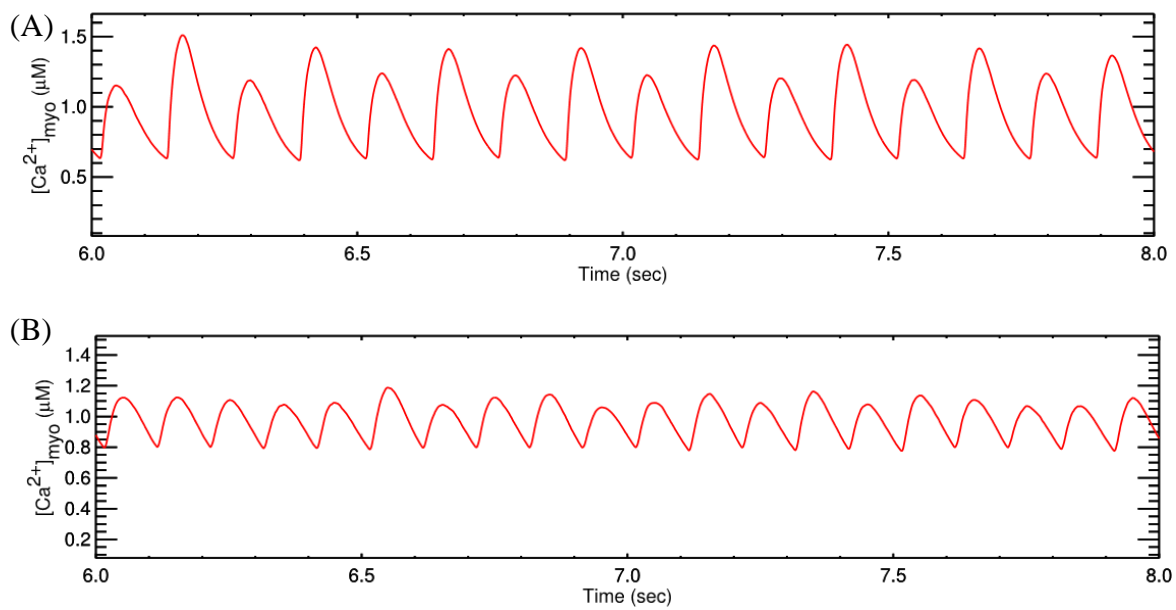


Figure 29. Calcium transient in (A) 8Hz and $[Na]_i = 15mM$; (B) 8Hz and NCX downregulated 0.5x

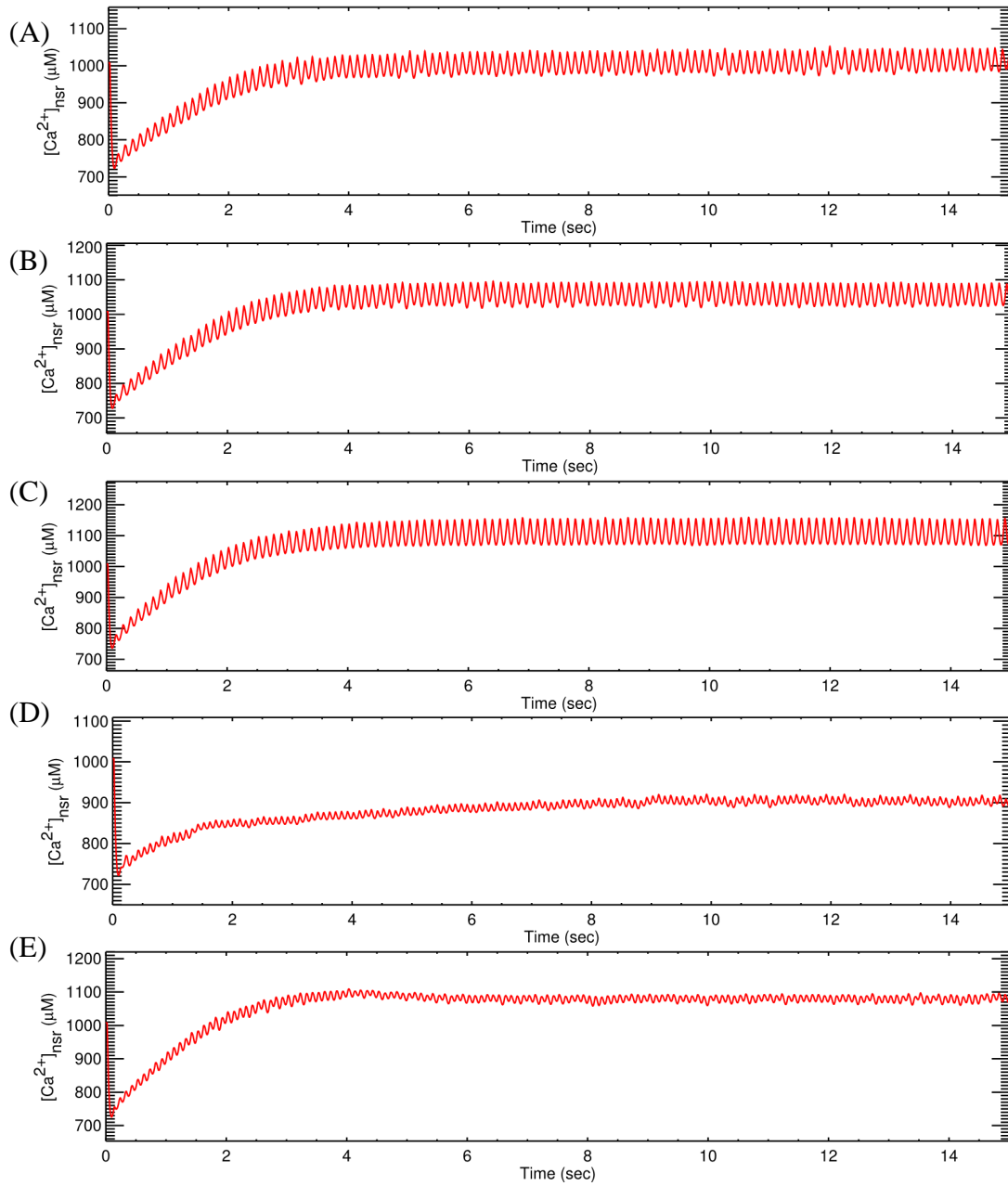


Figure 30. SR $[Ca^{2+}]$ at (A) 8Hz pacing rate, (B) 8Hz pacing rate + $[Na^+]_i = 15mM$, (C) 8Hz pacing rate + $[Na^+]_i = 20mM$, (D) 8Hz pacing and NCX upregulated 1.5-fold, (E) 8Hz pacing and NCX downregulated 0.5-fold

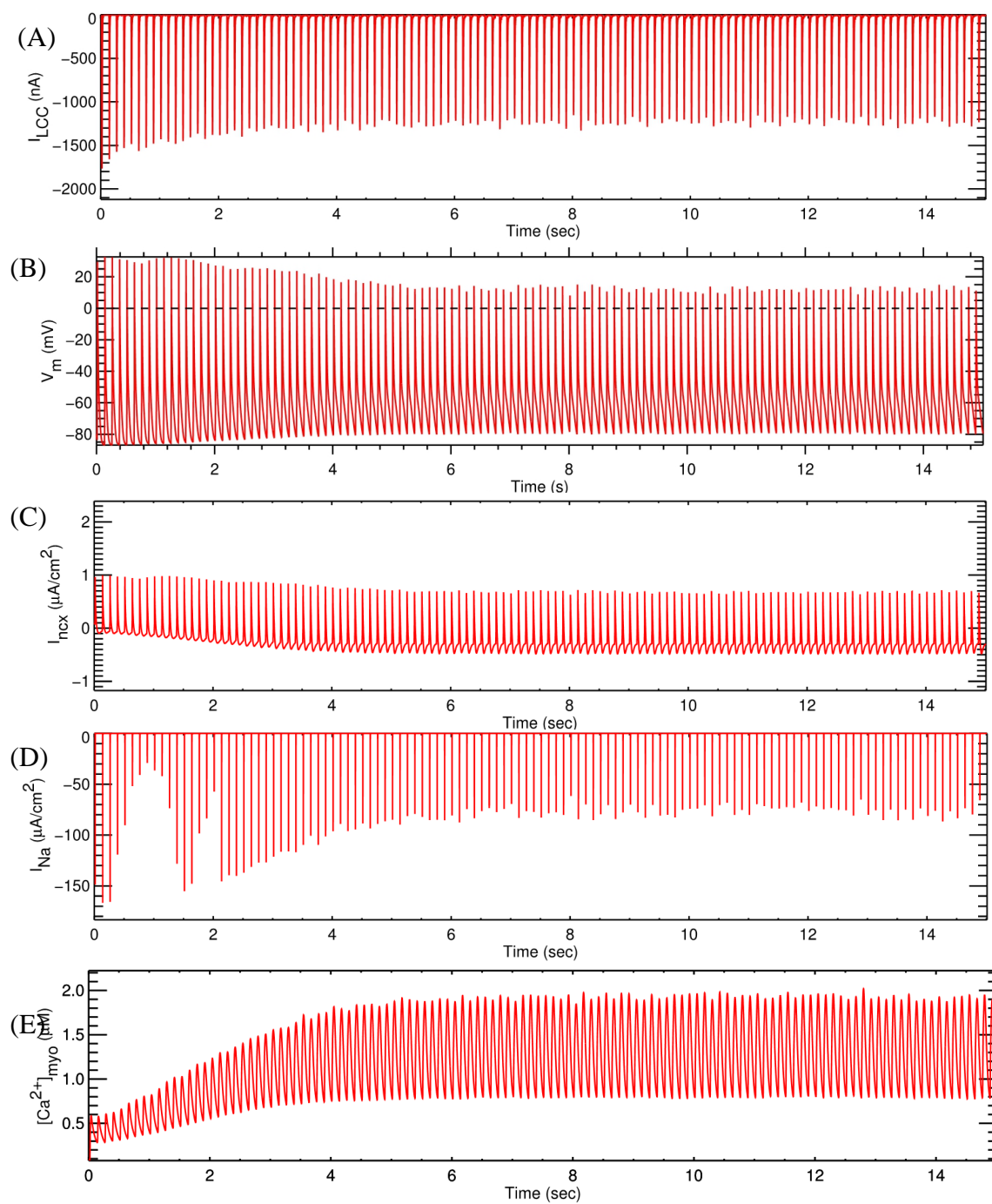


Figure 31. At $[Na^+]_i = 20mM$ and 8Hz

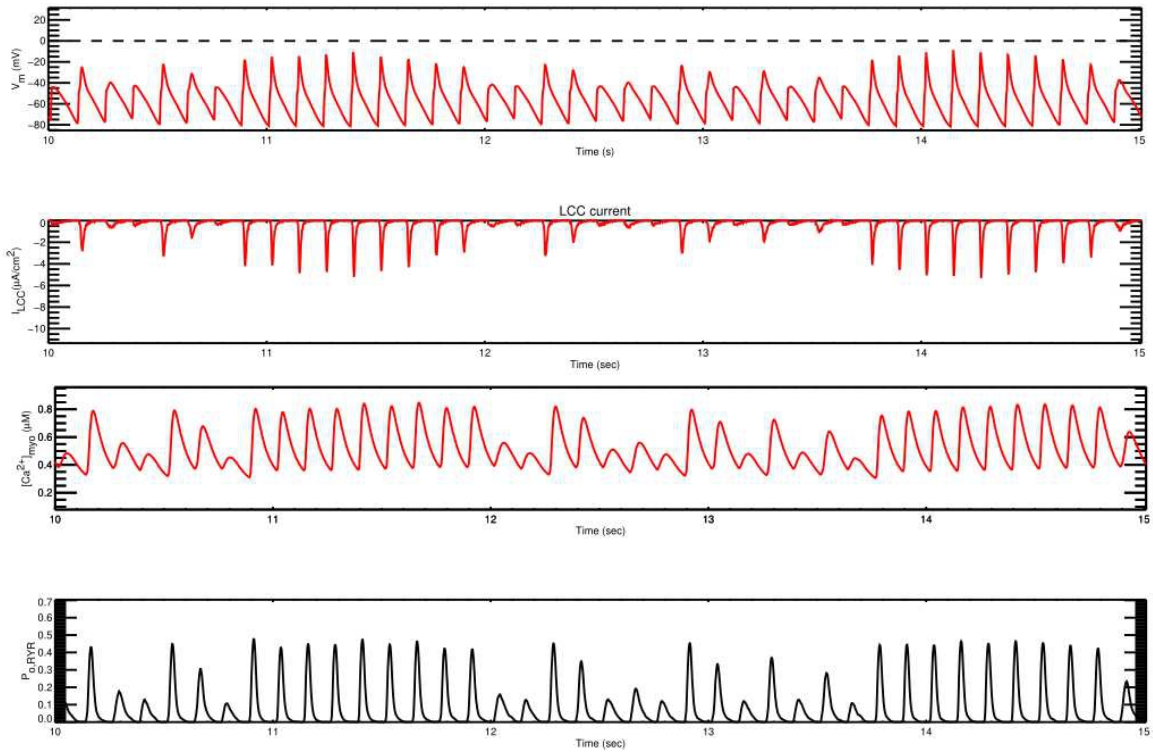


Figure 32. Alternans at high pacing rate (8Hz) using Na^+ stochastic modelled at 23°C , (A) action potential, (B) I_{CaL} current; (C) cytosolic calcium, (D) opening probability of whole-cell ryanodine receptors

How many cells to trigger a sustained electrical response

Even though Ca^{2+} sparks are often local elevation of Ca^{2+} in a restricted space, under pathological conditions, multiple Ca^{2+} sparks can combine to form Ca^{2+} waves. These propagating elevations of $[\text{Ca}^{2+}]_i$ can activate inward NCX current (I_{NCX}) that contribute to early after-depolarization (EADs) and delayed after-depolarizations (DADs). However, how cellular currents lead to full depolarization of the myocardium and how they initiate extra systoles is still not fully understood. Some earlier studies that have investigated this question suggested that, in 3-dimensional tissue, as many as about ~700,000 cells must undergo such behavior to initiate a propagating action potential or an

arrhythmia (Y. Xie, D. Sato, A. Garfinkel, Z. Qu, & J. N. Weiss, 2010). Using the mechanistic computational model developed above, we present the results of our study which explores how many cells must be entrained to initiate arrhythmogenic depolarizations. A similar protocol was used to compare the result.

The two primary ways for cells to communicate are electrical synapse and chemical synapse. However, in muscle cells and cardiac cells, electrical synapse is the major way for cell communication. Two cardiac cells are connected via the gap junctions which behave like ion channels to form a relatively nonselective, low-resistance pore through which electrical current or chemical species can flow (Keener & Sneyd, 2009). In adult ventricles, gap junctions are mainly found in the intercalated disk between cells (Jongsma & Wilders, 2000). Thus, anisotropic coupling is assumed in that the coupling at two cell ends is stronger than the other sides. In a tissue setting, a single cell may have end-to-end with many cells, average 11.3 neighbors, i.e. 5.3 on the sides and 6.0 at the ends (Hoyt, Cohen, & Saffitz, 1989; Humphrey & McCulloch, 2003; Peters & Wit, 1998). In the current simulation, it's assumed that each has 4 neighbors in 2D and 6 neighbors in 3D, yet the conductance between cells reflects the coupling strengths at each direction. This is a reasonable assumption, particularly in the case of trabeculae where the small size limits the number of cell connections. In addition, to emulate the effect of a larger number of neighbors, a smaller, yet longer stimulus was used; so that the loss in electrical signal from one cell to neighboring cells is larger. Even in this case, the increase in the number of cell is still much smaller than the value reported.

The model presented here suggests that only small number cells must activate in order to trigger an arrhythmogenic propagating action potential. These conditions were examined in 1-D, 2-D, and 3-D taking into account heart geometry, Figure 33 and Figure 34. The finding that only a small number of cells are required to trigger an arrhythmia provides a plausible mechanism by which cardiac arrhythmias might occur.

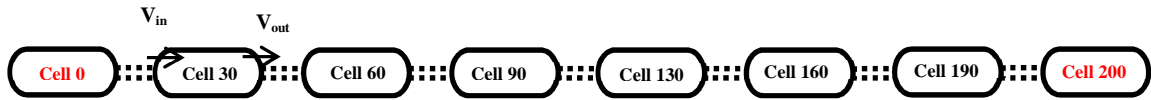


Figure 33 Schematic of a 1-D tissue, cells are coupled by the gap junction conductance g_{gap} . Stimulus is applied to cells on the left side.

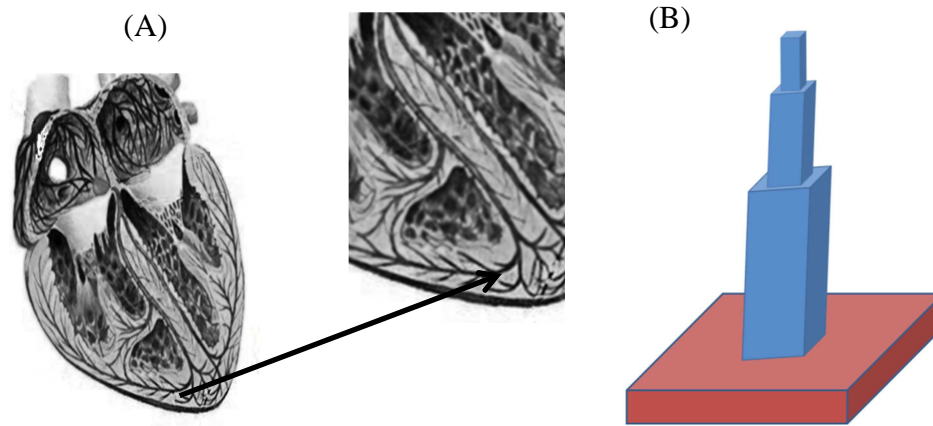


Figure 34. (A) The heart has many fine structures such as Purkinje fibers and trabeculae (lining the chambers of the heart) that are in effect 1-D structure or small-size 3D structure that extend from the atrioventricular. (A) The schematic diagram of a trabeculae that interface with the heart wall.

In 1D, using $G_{gap} = 2500 \text{ nS}$, the number of cell required to trigger a sustained electrical propagation is 7. In 2D tissue, for anisotropic gap conductance, we reduced the gap junction conductance three fold along side direction. For the propagation of AP in 2D tissue the number of AP cells increased to 49 cells which is about 140 times smaller than what previously has been reported, i.e. 6940 cells in 2D. For the 3D with the anisotropy gap conductance the cell needed for the propagating AP are only 294 cells compare to about 700000 cells previously reported (Yuanfang Xie, Daisuke Sato, Alan Garfinkel, Zhilin Qu, & James N. Weiss, 2010).

We also investigated the response of the cells in the tissue when we applied an instantaneous and gradual current injection by keeping the same current mass of the stimulus. In case of a gradual stimulus we have injected current of $-6.51890 \mu\text{A}/\text{cm}^2$ for 5 msec which make total mass of the stimulus to $-32.5945 \mu\text{A}/\text{cm}^2$, while for the instantaneous case a stimulus of $-16.29725 \mu\text{A}/\text{cm}^2$ for only 2 msec is applied. In instantaneous case, the number of cell to produce propagating AP reduce in 2D and 3D since the cells in tissue are coupled by gap junction conductance G_{gap} so if we inject current gradually then there is sink to the neighboring cells and the cell lose stimulus which make it hard for the injected cell to depolarize on the other hand if we inject a large amount of current in the form of a flash then there is a less sink to the unstimulated cells in the tissue. The relationship between instantaneous and gradual current injection is shown in Table 4.

Table 4 Number of Myocytes with the instantaneous and gradual current injection in 1D, 2D and 3D tissue.

Protocol	1D	2D	3D
Gradual	7	49	294
Instantaneous	5	36	100

The heart has many fine structures such as Purkinje fibers and trabeculae (lining the chambers of the heart) that are in effect 1-D structure as shown in Figure 34 (A) and there is a possibility that depolarization can trigger AP with the minimum number of cells if it start in trabecular or Purkinje fibers. Even couple hundred of cells seems a large number to generate an arrhythmia so by taking into account the site of initiation we simulated trabeculae that interface with the heart wall Figure 7 B. A previous study confirmed that arrhythmias occurred frequently in trabeculae (H. E. D. J. ter Keurs et al., 2006). In this simulation we concluded that initiation site does play a role in triggering AP and we were able to reduce the number of cells to 32 for triggering arrhythmic by gradual current injection compare to 292 and if we inject current instantaneously then the number of cells reduce to 20 from 100.

Supplemental data

Table 5. Constant data and whole-cell level data

Variables	Value	Unit
Faraday constant (F)	9.6485d4	C/mol
Universal gas constant (R)	8.314d3	mJ/(mol.K)
Temperature (T)	310	K
[Na] _o	1.4d5	μM
[Ca] _o	1.8d3	μM
[K] _o	5.4d3	μM
Cell volume (V _{cell})	25.0	pL
Myoplasmic volume (V _{myo})	12.5	pL
Network SR volume (V _{nsr})	0.762d0	pL
Junctional SR volume (V _{jsr} ^T)	1.25d-1	pL
Subspace volume (V _{ds} ^T)	1.55d-2	pL
Concentration [SERCA]	300	μM
K _{d,myo}	900	μM
K _{d,sr}	2150	μM
RyR release rate (v _{ryr} ^T)	56.4279	1/sec
Percent nj-RyR	0.5	Unitless
Transfer rate from subspace to bulk myoplasm (v _{efflux} ^T)	300	1/sec
Refill rate from nSR to jSR (v _{refill} ^T)	2.4	1/sec
NCX maximum current density ($\overline{I_{ncx}}$)	520	μA/μF
K _{d,ncxNa}	8750	
K _{d,ncxCa}	1380	
PMCA maximum current density ($\overline{I_{pmca}}$)	0.12	μA/μF
K _{d,pmca}	0.5	
Na/K maximum current density ($\overline{I_{Na/K}}$)	0.88	μA/μF

Table 6. Initial values

Variables	Value	Unit
m_{Na}	0.0015d0	Unitless
h_{Na}	0.9849d0	Unitless
j_{Na}	0.9849d0	Unitless
a_{Kss}	0.0021d0	Unitless
in_{Kss}	1.d0	Unitless
a_{Ktof}	0.0021d0	Unitless
in_{Ktof}	1.d0	Unitless
a_{Ktos}	2.9871d-04	Unitless
in_{Ktos}	0.9994d0	Unitless
$[Ca]_{myo}$	0.08769	μM
$[Ca]_{nsr}$	1.00737d3	μM
$[Na]_i$	1.02d4	μM
$[K]_i$	1.4372d5	μM

Table 7. Calcium buffers

Variables	Value	Unit
General buffer in myoplasm	1.23d2	μM
Kd	0.96	μM
General buffer in jSR (e.g. Calsequestrin)	1.4d4	μM
Kd	6.38d2	μM
High-affinity Troponin C	1.40d2	μM
kon	2.37	$1/(\mu M.s)$
koff	3.2d-2	1/s
Calmodulin	2.4d1	μM
kon	3.0d1	$1/(\mu M.s)$
koff	7.14d1	1/s
SL buffer	250	μM
kon	115	$1/(\mu M.s)$
koff	1000	1/s
SR buffer	47	μM
kon	115	$1/(\mu M.s)$
koff	100	1/s

Table 8. Parameters for L-type Ca^{2+} channel model

P_{O_2}	$= \frac{-1}{1 + e^{(V-V_{1/2})/S}} + 1$
$V_{1/2}$	$= -40.344 + 13.31 \times e^{(-[\text{Ca}]_o/53.0)} + 31.65 \times e^{-[\text{Ca}]_o/11305} + 3$
S	$= (0.632 + 0.368 \times e^{(-[\text{Ca}]_o/10^3 - 0.1)/0.784}) \times (-3.792/(1 + e^{([\text{Ca}]_o/10^3 - 0.0469)/0.011} + 6.395)) + 2.7$
$\tau_{P_{O_2}}$	$= 0.00025 + 0.00305 \times e^{-0.0045 \times (V+7)^2} + 0.00105 \times e^{-0.002 \times (V-18)^2}$
att	$= 130 + \frac{-129}{1 + e^{(Vm-60)/8}} + \frac{0.76}{1 + e^{(Vm-5)/3.14}}$
inh _{Ca}	$= 0.89 + \frac{-0.888}{1 + e^{(Vm-43.066)/2.289}} \times \left(1.004 + \frac{-1.199}{1 + e^{([\text{Ca}]_o/10^3 - 0.259)/0.164}} \right)$
$k_{1,5}$	$= \frac{k_{5,1}k_{1,2}k_{2,5}}{k_{5,2}k_{2,1}}$
$k_{5,4}$	$= \frac{k_{4,5}k_{5,2}k_{2,4}}{k_{4,2}k_{2,5}}$
P_{dhpr}	$= P_{\text{dhpr},([\text{Ca}]_o=1.8\text{mM})} \left(1 + \frac{-1}{1 + e^{([\text{Ca}]_o/1000 - 0.08)/0.00159}} \right)$
$k_{1,2}$	$= 0.115 \times P_{O_2}/\tau_{P_{O_2}}$
$k_{2,1}$	$= 0.6 \times (1 - 0.155 \times P_{O_2})/\tau_{P_{O_2}} \times \text{att}$
$k_{2,3}$	$= 0.7 \times \left(987.3 + \frac{-902.53}{1 + e^{(V-51.23)/6.785}} \right)$
$k_{3,2}$	$= 500$
$k_{2,5}$	$= 0.5 \times \left(32 + \frac{-18.465}{1 + e^{(V-30)/5.746}} \right) * (1 - \text{inh}_{\text{Ca}})$
$k_{5,2}$	$= 1.0 \times \left(5.05 + \frac{-5.03}{1 + e^{(V-30)/0.787}} \right) + (0.95 + \frac{-0.93}{1 + e^{(Vm+40)/0.787}})$
$k_{2,4}$	$= 8 \times [\text{CaCM}]$
$k_{4,2}$	$= 1$
$k_{5,1}$	$= 6.9$
$k_{4,5}$	$= 600$
$k_{4,2}$	$= 1$
$k_{3,2}$	$= 500$

$$k_{6,1} = 1 \times \left(0.0022 + \frac{2998.978}{1 + e^{-(V_m + 42) * 0.71428}} \right)$$

$$k_{1,6} = 1 \times \left(3000 - \frac{2998.978}{1 + e^{-(V_m + 45) * 0.6667}} \right)$$

Table 9. Fluxes' parameters

	Value	Unit
Variables		
Volume fraction: λ_{ds}	V_{ds} / V_{myo}	Unitless
Volume fraction: λ_{jsr}	V_{jsr} / V_{myo}	Unitless
Volume fraction: λ_{nsr}	V_{nsr} / V_{myo}	Unitless

REFERENCES

- Afshar, Y., Schmid, F., Pischevar, A., & Worley, S. (2013). Exploiting seeding of random number generators for efficient domain decomposition parallelization of dissipative particle dynamics. *Computer Physics Communications, 184*, 1119–1128.
- Aistrup, G. L., Kelly, J. E., Kapur, S., Kowalczyk, M., Sysman-Wolpin, I., Kadish, A. H., & Wasserstrom, J. A. (2006). Pacing-induced heterogeneities in intracellular Ca^{2+} signaling, cardiac alternans, and ventricular arrhythmias in intact rat heart. [In Vitro Research Support, Non-U.S. Gov't]. *Circ Res, 99*(7), e65-73. doi: 10.1161/01.RES.0000244087.36230.bf
- Aistrup, G. L., Shiferaw, Y., Kapur, S., Kadish, A. H., & Wasserstrom, J. A. (2009). Mechanisms underlying the formation and dynamics of subcellular calcium alternans in the intact rat heart. *Circulation research, 104*, 639-649. doi: 10.1161/CIRCRESAHA.108.181909
- Altamirano, J., & Bers, D. M. (2007a). Effect of intracellular Ca^{2+} and action potential duration on L-type Ca^{2+} channel inactivation and recovery from inactivation in rabbit cardiac myocytes. [Research Support, N.I.H., Extramural]. *Am J Physiol Heart Circ Physiol, 293*(1), H563-573. doi: 10.1152/ajpheart.00469.2006
- Altamirano, J., & Bers, D. M. (2007b). Voltage dependence of cardiac excitation-contraction coupling: unitary Ca^{2+} current amplitude and open channel probability. [Research Support, N.I.H., Extramural]. *Circ Res, 101*(6), 590-597. doi: 10.1161/CIRCRESAHA.107.152322
- Balke, C. W., Egan, T. M., & Wier, W. G. (1994). Processes that remove calcium from the cytoplasm during excitation-contraction coupling in intact rat heart cells. *Physiology, 474*, 447-462.
- Balshaw, D. M., Xu, L., Yamaguchi, N., Pasek, D. A., & Meissner, G. (2001). Calmodulin binding and inhibition of cardiac muscle calcium release channel (ryanodine receptor). [Research Support, Non-U.S. Gov't]

- Research Support, U.S. Gov't, P.H.S.]. *J Biol Chem*, 276(23), 20144-20153. doi: 10.1074/jbc.M010771200
- Bassani, J. W., Bassani, R. a., & Bers, D. M. (1994). Relaxation in rabbit and rat cardiac cells: species-dependent differences in cellular mechanisms. *The Journal of physiology*, 476, 279-293.
- Benndorf, K., Boldt, W., & Nilius, B. (1985). Sodium current in single myocardial mouse cells. *Pflugers Arch*, 404(2), 190-196.
- Berridge, M. J., Lipp, P., & Bootman, M. D. (2000). The versatility and universality of Calcium signalling. *Nature reviews. Molecular cell biology*, 1, 11-21.
- Bers, D. M. (2000). Calcium Fluxes Involved in Control of Cardiac Myocyte Contraction. *Circulation Research*, 87, 275-281. doi: 10.1161/01.RES.87.4.275
- Bers, D. M. (2002). Cardiac excitation-contraction coupling. *Nature*, 415, 198-205.
- Bers, D. M. (2014). Cardiac sarcoplasmic reticulum calcium leak: basis and roles in cardiac dysfunction. *Annu Rev Physiol*, 76, 107-127. doi: 10.1146/annurev-physiol-020911-153308
- Bito, V., Heinzel, F. R., Biesmans, L., Antoons, G., & Sipido, K. R. (2008). Crosstalk between L-type Ca²⁺ channels and the sarcoplasmic reticulum: alterations during cardiac remodelling. [Research Support, Non-U.S. Gov't Review]. *Cardiovasc Res*, 77(2), 315-324. doi: 10.1093/cvr/cvm063
- Blatter, L. a., Kockskamper, J., Sheehan, K. a., Zima, a. V., Huser, J., & Lipsius, S. L. (2002). Local calcium gradients during excitation-contraction coupling and alternans in atrial myocytes. *The Journal of Physiology*, 546, 19-31. doi: 10.1113/jphysiol.2002.025239
- Bondarenko, V. E., Szigeti, G. P., Bett, G. C. L., Kim, S.-J., & Rasmusson, R. L. (2004). Computer model of action potential of mouse ventricular myocytes. *American journal of physiology. Heart and circulatory physiology*, 287, H1378-1403. doi: 10.1152/ajpheart.00185.2003
- Bootman, M. D., Thomas, D., Tovey, S. C., Berridge, M. J., & Lipp, P. (2000). Nuclear calcium signalling. *Cellular and molecular life sciences : CMLS*, 57, 371-378.
- Brette, F., Leroy, J., Le Guennec, J. Y., & Salle, L. (2006). Ca²⁺ currents in cardiac myocytes: Old story, new insights. [Research Support, Non-U.S. Gov't Review]. *Prog Biophys Mol Biol*, 91(1-2), 1-82. doi: 10.1016/j.pbiomolbio.2005.01.001

- Brette, F., & Orchard, C. H. (2006). No apparent requirement for neuronal sodium channels in excitation-contraction coupling in rat ventricular myocytes. [Research Support, Non-U.S. Gov't]. *Circ Res*, 98(5), 667-674. doi: 10.1161/01.RES.0000209963.02720.70
- Brochet, D. X. P., Xie, W., Yang, D., Cheng, H., & Lederer, W. J. (2011). Quarky calcium release in the heart. *Circulation research*, 108, 210-218. doi: 10.1161/CIRCRESAHA.110.231258
- Brown, A. M., Lee, K. S., & Powell, T. (1981). Sodium current in single rat heart muscle cells. *J. Physiol.*, 479-500.
- Bu, G., Adams, H., Berbari, E. J., & Rubart, M. (2009). Uniform action potential repolarization within the sarcolemma of in situ ventricular cardiomyocytes. [In Vitro Research Support, N.I.H., Extramural Research Support, Non-U.S. Gov't]. *Biophys J*, 96(6), 2532-2546. doi: 10.1016/j.bpj.2008.12.3896
- Cheng, H., Lederer, W. J. J., & Cannell, M. B. (1993). Calcium Sparks: Elementary Events Underlying Excitation-Contraction Coupling in Heart Muscle. *Science*, 262, 740-744.
- Chikando, A. C. (2008). A Computational Study of Excitation-Contraction Coupling: Mechanisms of Sarcoplasmic Reticulum Calcium Leak and the Role of Mitochondria in Myoplasmic Calcium Regulation (pp. 187).
- Colatsky, T. J. (1980). Voltage clamp measurements of sodium channel properties in rabbit cardiac Purkinje fibres. [In Vitro Research Support, U.S. Gov't, P.H.S.]. *J Physiol*, 305, 215-234.
- Delbridge, L. M., Satoh, H., Yuan, W., Bassani, J. W., Qi, M., Ginsburg, K. S., . . . Bers, D. M. (1997). Cardiac myocyte volume, Ca²⁺ fluxes, and sarcoplasmic reticulum loading in pressure-overload hypertrophy. [Research Support, Non-U.S. Gov't Research Support, U.S. Gov't, P.H.S.]. *Am J Physiol*, 272(5 Pt 2), H2425-2435.
- Diaz, M. E., Eisner, D. A., & O'Neill, S. C. (2002). Depressed ryanodine receptor activity increases variability and duration of the systolic Ca²⁺ transient in rat ventricular myocytes. [Research Support, Non-U.S. Gov't]. *Circ Res*, 91(7), 585-593.

- Diaz, M. E., O'Neill, S. C., & Eisner, D. A. (2004). Sarcoplasmic reticulum calcium content fluctuation is the key to cardiac alternans. [Research Support, Non-U.S. Gov't]. *Circ Res*, 94(5), 650-656. doi: 10.1161/01.RES.0000119923.64774.72
- Drouhard, J. P., & Roberge, F. A. (1987). Revised formulation of the Hodgkin-Huxley representation of the sodium current in cardiac cells. [Research Support, Non-U.S. Gov't]. *Comput Biomed Res*, 20(4), 333-350.
- Edwards, P., & Cohen, G. I. (2003). Both diastolic and systolic function alternate in pulsus alternans: a case report and review. [Case Reports]. *J Am Soc Echocardiogr*, 16(6), 695-697.
- Ehlers, M. D., Augustine, G. J., & Field, R. O. (1999). Calmodulin at the channel gate. *Nature*, 399, 105-107.
- Eisner, D. A., Diaz, M. E., Li, Y., O'Neill, S. C., & Trafford, A. W. (2005). Stability and instability of regulation of intracellular calcium. [Review]. *Exp Physiol*, 90(1), 3-12. doi: 10.1113/expphysiol.2004.029231
- Endo, M. (1964). Entry of a Dye into the Sarcotubular System of Muscle. *Nature*, 202, 1115-1116.
- Estes, N. A., 3rd, Michaud, G., Zipes, D. P., El-Sherif, N., Venditti, F. J., Rosenbaum, D. S., . . . Cohen, R. J. (1997). Electrical alternans during rest and exercise as predictors of vulnerability to ventricular arrhythmias. [Clinical Trial Multicenter Study Research Support, U.S. Gov't, Non-P.H.S.]. *Am J Cardiol*, 80(10), 1314-1318.
- Euler, D. E. (1999). Cardiac alternans: mechanisms and pathophysiological significance. [Review]. *Cardiovasc Res*, 42(3), 583-590.
- Fabiato, A. (1983). Calcium-induced release of calcium from the cardiac sarcoplasmic reticulum. *American journal of physiology. Cell physiology*, 245, C1-C14. doi: 10.1016/0022-2828(92)90114-F
- Fabiato, A., & Fabiato, F. (1975). Contractions induced by a calcium-triggered release of calcium from the sarcoplasmic reticulum of single skinned cardiac cells. *Journal of Physiology*, 249, 469-495.
- Fallon, J. L., Baker, M. R., Xiong, L., Loy, R. E., Yang, G., Dirksen, R. T., . . . Quiocho, F. A. (2009). Crystal structure of dimeric cardiac L-type calcium channel regulatory domains bridged by Ca²⁺* calmodulins. [Research Support, N.I.H., Extramural

- Research Support, Non-U.S. Gov't]. *Proc Natl Acad Sci U S A*, 106(13), 5135-5140. doi: 10.1073/pnas.0807487106
- Feher, J. J. (1984). Unidirectional calcium and nucleotide fluxes in sarcoplasmic reticulum. I. Interpretation of flux ratios for different reaction schemes. [Research Support, Non-U.S. Gov't]. *Biophys J*, 45(6), 1125-1133. doi: 10.1016/S0006-3495(84)84260-5
- Fox, J. J., McHarg, J. L., & Gilmour, R. F. (2002). Ionic mechanism of electrical alternans. *American journal of physiology. Heart and circulatory physiology*, 282, H516-530. doi: 10.1152/ajpheart.00612.2001
- Franzini-Armstrong, C., Protasi, F., & Ramesh, V. (1998). Comparative Ultrastructure of Ca²⁺ release units in skeletal and cardiac muscle. *Annals of the New York Academy of Sciences*, 853, 20-30.
- Franzini-Armstrong, C., Protasi, F., & Ramesh, V. (1999). Shape, size, and distribution of Ca(2+) release units and couplons in skeletal and cardiac muscles. *Biophysical journal*, 77, 55. doi: 10.1016/S0006-3495(99)77000-1
- Gaeta, S. A., & Christini, D. J. (2012). Non-linear dynamics of cardiac alternans: subcellular to tissue-level mechanisms of arrhythmia. *Front Physiol*, 3, 157. doi: 10.3389/fphys.2012.00157
- Gettes, L. S., & Reuter, H. (1974). Slow recovery from inactivation of inward currents in mammalian myocardial fibres. [In Vitro]. *J Physiol*, 240(3), 703-724.
- Gillespie, D., & Fill, M. (2013). Pernicious attrition and inter-RyR2 CICR current control in cardiac muscle. [Research Support, N.I.H., Extramural Review]. *J Mol Cell Cardiol*, 58, 53-58. doi: 10.1016/j.yjmcc.2013.01.011
- Goldman, D. E. (1943). Potential, Impedance, and rectification in membranes. *The Journal of General Physiology*, 27, 37-60.
- Groff, J. R., DeRemigio, H., & Smith, G. D. (2009). Markov chain models of ion channels and Ca²⁺ release sites. In L. C & Gabriel L (Eds.), *Stochastic Methods in Neuroscience* (pp. 29-64): Oxford University Press.
- Groff, J. R., & Smith, G. D. (2008). Ryanodine receptor allosteric coupling and the dynamics of calcium sparks. *Biophysical journal*, 95, 135-154. doi: 10.1529/biophysj.107.119982
- Guo, A., Zhang, C., Wei, S., Chen, B., & Song, L. S. (2013). Emerging mechanisms of T-tubule remodelling in heart failure. [Research Support, N.I.H., Extramural

Research Support, Non-U.S. Gov't

Review]. *Cardiovasc Res*, 98(2), 204-215. doi: 10.1093/cvr/cvt020

Haddock, P. S., Coetzee, W. A., Cho, E., Porter, L., Katoh, H., Bers, D. M., . . . Artman, M. (1999). Subcellular $[Ca^{2+}]_i$ gradients during excitation-contraction coupling in newborn rabbit ventricular myocytes. [Research Support, Non-U.S. Gov't

Research Support, U.S. Gov't, P.H.S.]. *Circ Res*, 85(5), 415-427.

Halling, D. B., Aracena-Parks, P., & Hamilton, S. L. (2005). Regulation of voltage-gated Ca^{2+} channels by calmodulin. [Review]. *Sci STKE*, 2005(315), re15. doi: 10.1126/stke.3152005re15

Hasenfuss, G., Schillinger, W., Lehnart, S. E., Preuss, M., Pieske, B., Maier, L. S., . . . Just, H. (1999). Relationship between Na^{+} - Ca^{2+} -exchanger protein levels and diastolic function of failing human myocardium. [Comparative Study

In Vitro

Research Support, Non-U.S. Gov't]. *Circulation*, 99(5), 641-648.

Hayashi, T., Martone, M. E., Yu, Z., Thor, A., Doi, M., Holst, M. J., . . . Hoshijima, M. (2009). Three-dimensional electron microscopy reveals new details of membrane systems for Ca^{2+} signaling in the heart. *Journal of cell science*, 122, 1005-1013. doi: 10.1242/jcs.028175

He, J., Conklin, M. W., Foell, J. D., Wolff, M. R., Haworth, R. A., Coronado, R., & Kamp, T. J. (2001). Reduction in density of transverse tubules and L-type Ca^{2+} channels in canine tachycardia-induced heart failure. [Research Support, U.S. Gov't, P.H.S.]. *Cardiovasc Res*, 49(2), 298-307.

Hess, O. M., Surber, E. P., Ritter, M., & Krayenbuehl, H. P. (1984). Pulsus alternans: its influence on systolic and diastolic function in aortic valve disease. [Research Support, Non-U.S. Gov't]. *J Am Coll Cardiol*, 4(1), 1-7.

Hess, P., Lansman, J. B., & Tsien, R. W. (1986). Calcium channel selectivity for divalent and monovalent cations. Voltage and concentration dependence of single channel current in ventricular heart cells. *The Journal of general physiology*, 88, 293-319.

Hodgkin, A. L., & Huxley, A. F. (1952). A quantitative description of membrane current and its application to conduction and excitation in nerve. *Journal of Physiology*, 117, 25-71.

- Hoyt, R. H., Cohen, M. L., & Saffitz, J. E. (1989). Distribution and three-dimensional structure of intercellular junctions in canine myocardium. *Circulation Research*, 64, 563-574. doi: 10.1161/01.RES.64.3.563
- Humphrey, J. D., & McCulloch, A. D. (2003). The Cardiovascular System - Anatomy, Physiology, and Cell Biology. In G. A. Holzapfel & R. W. Ogden (Eds.), *Biomechanics of Soft Tissue in Cardiovascular Systems* (pp. 3): SpringerWien Newyork.
- Jongsma, H. J., & Wilders, R. (2000). Gap junctions in cardiovascular disease. [Research Support, Non-U.S. Gov't Review]. *Circ Res*, 86(12), 1193-1197.
- Jurado, L. A., Chockalingam, P. S., & Jarrett, H. W. (2009). Apocalmodulin. *Physiological Reviews*, 79, 661-682.
- Keener, J. P., & Sneyd, J. (2009). Chapter 8. Cellular Communication *Mathematical Physiology: I: Cellular Physiology* (Vol. 2): Springer.
- Kemi, O. J., Hoydal, M. A., Macquaide, N., Haram, P. M., Koch, L. G., Britton, S. L., . . . Wisloff, U. (2011). The effect of exercise training on transverse tubules in normal, remodeled, and reverse remodeled hearts. [Research Support, N.I.H., Extramural Research Support, Non-U.S. Gov't]. *J Cell Physiol*, 226(9), 2235-2243. doi: 10.1002/jcp.22559
- Kihara, Y., & Morgan, J. P. (1991). Abnormal Ca^{2+} handling is the primary cause of mechanical alternans: study in ferret ventricular muscles. [Research Support, Non-U.S. Gov't Research Support, U.S. Gov't, P.H.S.]. *Am J Physiol*, 261(6 Pt 2), H1746-1755.
- Kockskamper, J., & Blatter, L. a. (2002). Subcellular Ca^{2+} alternans represents a novel mechanism for the generation of arrhythmogenic Ca^{2+} waves in cat atrial myocytes. *The Journal of Physiology*, 545, 65-79. doi: 10.1113/jphysiol.2002.025502
- Lab, M. J., & Lee, J. A. (1990). Changes in intracellular calcium during mechanical alternans in isolated ferret ventricular muscle. [In Vitro Research Support, Non-U.S. Gov't

Research Support, U.S. Gov't, P.H.S.]. *Circ Res*, 66(3), 585-595.

Lee, K. S., & Tsien, R. W. (1984). High selectivity of calcium channels in single dialysed heart cells of the guinea-pig. [In Vitro

Research Support, Non-U.S. Gov't

Research Support, U.S. Gov't, P.H.S.]. *J Physiol*, 354, 253-272.

Lehnart, S. E., Wehrens, X. H. T., Reiken, S., Warrier, S., Andriy, E., Harvey, R. D., . . . Marks, R. (2005). Phosphodiesterase 4D deficiency in the Ryanodine-Receptor Complex Promotes Heart Failure and Arrhythmias. *Cell*, 123, 25-35. doi: 10.1016/j.cell.2005.07.030.Phosphodiesterase

Lewis, T. (1911). Notes upon alternation of the heart. *Q J Med.*, 4, 141-144.

Liu, O. Z., Lederer, W. J., & Sobie, E. A. (2012). Does the Goldilocks Principle apply to calcium release restitution in heart cells? [Comment

Editorial

Research Support, N.I.H., Extramural

Research Support, Non-U.S. Gov't]. *J Mol Cell Cardiol*, 52(1), 3-6. doi: 10.1016/j.yjmcc.2011.10.014

Luo, C.-H., & Rudy, Y. (1991). A Model of the Ventricular Cardiac Action Potential. Depolarization, repolarization, and their interaction. *Circulation Research*, 68, 1501-1526. doi: 10.1161/01.RES.68.6.1501

Luo, C. H., & Rudy, Y. (1994). A dynamic model of the cardiac ventricular action potential. I. Simulations of ionic currents and concentration changes. *Circulation research*, 74, 1071-1096.

Maron, B. J., Ferrans, V. J., & Roberts, W. C. (1975). Ultrastructural features of degenerated cardiac muscle cells in patients with cardiac hypertrophy. *Am J Pathol*, 79(3), 387-434.

Meyer, M., Schillinger, W., Pieske, B., Holubarsch, C., Heilmann, C., Posival, H., . . . et al. (1995). Alterations of sarcoplasmic reticulum proteins in failing human dilated cardiomyopathy. [Research Support, Non-U.S. Gov't]. *Circulation*, 92(4), 778-784.

Mori, M. X., Erickson, M. G., & Yue, D. T. (2004). Functional stoichiometry and local enrichment of calmodulin interacting with Ca²⁺ channels. [Research Support, U.S. Gov't, P.H.S.]. *Science*, 304(5669), 432-435. doi: 10.1126/science.1093490

- Narayan, S. M. (2006). T-wave alternans and the susceptibility to ventricular arrhythmias. *Journal of the American College of Cardiology*, 47, 269-281. doi: 10.1016/j.jacc.2005.08.066
- Niggli, E., & Egger, M. (2002). Calcium quarks. *Frontiers in Biocience*, 7, 1288-1297.
- Orchard, C. H., McCall, E., Kirby, M. S., & Boyett, M. R. (1991). Mechanical alternans during acidosis in ferret heart muscle. [Research Support, Non-U.S. Gov't]. *Circ Res*, 68(1), 69-76.
- Page, E., & McCallister, L. P. (1973). Quantitative electron microscopic description of heart muscle cells. Application to normal, hypertrophied and thyroxin-stimulated hearts. *Am J Cardiol*, 31(2), 172-181.
- Page, E., & Surdyk-Droske, M. (1979). Distribution, surface density, and membrane area of diadic junctional contacts between plasma membrane and terminal cisterns in mammalian ventricle. [Research Support, U.S. Gov't, P.H.S.]. *Circ Res*, 45(2), 260-267.
- Pandit, S. V., Clark, R. B., Giles, W. R., & Demir, S. S. (2001). A mathematical model of action potential heterogeneity in adult rat left ventricular myocytes. *Biophysical journal*, 81, 3029-3051. doi: 10.1016/S0006-3495(01)75943-7
- Pastore, J. M., Girouard, S. D., Laurita, K. R., Akar, F. G., & Rosenbaum, D. S. (1999). Mechanism linking T-wave alternans to the genesis of cardiac fibrillation. [Research Support, Non-U.S. Gov't
Research Support, U.S. Gov't, Non-P.H.S.]
- Research Support, U.S. Gov't, P.H.S.]. *Circulation*, 99(10), 1385-1394.
- Peters, N. S., & Wit, a. L. (1998). Myocardial Architecture and Ventricular Arrhythmogenesis. *Circulation*, 97, 1746-1754. doi: 10.1161/01.CIR.97.17.1746
- Picht, E., DeSantiago, J., Blatter, L. A., & Bers, D. M. (2006). Cardiac alternans do not rely on diastolic sarcoplasmic reticulum calcium content fluctuations. [Research Support, N.I.H., Extramural
Research Support, Non-U.S. Gov't]. *Circ Res*, 99(7), 740-748. doi: 10.1161/01.RES.0000244002.88813.91
- Pitt, G. S., Zühlke, R. D., Hudmon, a., Schulman, H., Reuter, H., & Tsien, R. W. (2001). Molecular basis of calmodulin tethering and Ca²⁺-dependent inactivation of L-type Ca²⁺ channels. *The Journal of biological chemistry*, 276, 30794-30802. doi: 10.1074/jbc.M104959200

- Pitzer, K. S., & Mayorga, G. (1973). Thermodynamics of electrolytes. II. Activity and osmotic coefficients for strong electrolytes with one or both ions univalent. *Journal of Physical Chemistry*, 77, 2300-2308.
- Polakova, E., & Sobie, E. A. (2013). Alterations in T-tubule and dyad structure in heart disease: challenges and opportunities for computational analyses. [Research Support, N.I.H., Extramural Review]. *Cardiovasc Res*, 98(2), 233-239. doi: 10.1093/cvr/cvt026
- Qin, N., Olcese, R., Bransby, M., Lin, T., & Birnbaumer, L. (1999). Ca²⁺-induced inhibition of the cardiac Ca²⁺ channel depends on calmodulin. *Proceedings of the National Academy of Sciences of the United States of America*, 96, 2435-2438.
- Rosenbaum, D. S., Jackson, L. E., Smith, J. M., Garan, H., Ruskin, J. N., & Cohen, R. J. (1994). Electrical alternans and vulnerability to ventricular arrhythmias. [Research Support, Non-U.S. Gov't Research Support, U.S. Gov't, P.H.S.]. *N Engl J Med*, 330(4), 235-241. doi: 10.1056/NEJM199401273300402
- Rubenstein, D. S., & Lipsius, S. L. (1995). Premature beats elicit a phase reversal of mechanoelectrical alternans in cat ventricular myocytes. A possible mechanism for reentrant arrhythmias. [Research Support, U.S. Gov't, P.H.S.]. *Circulation*, 91(1), 201-214.
- Sag, C. M., Wadsack, D. P., Grefe, C., Neumann, K., Opiela, M.-k., Backs, J., . . . Maier, L. S. (2009). Calcium/Calmodulin-Dependent Protein Kinase II Contributes to Cardiac Arrhythmogenesis in Heart Failure. *Circ Heart Fail.*, 2, 664-675. doi: 10.1161/CIRCHEARTFAILURE.109.865279.Calcium/Calmodulin-Dependent
- Satoh, H., Delbridge, L. M., Blatter, L. A., & Bers, D. M. (1996). Surface:volume relationship in cardiac myocytes studied with confocal microscopy and membrane capacitance measurements: species-dependence and developmental effects. *Biophysical journal*, 70, 1494-1504. doi: 10.1016/S0006-3495(96)79711-4
- Scriven, D. R., Dan, P., & Moore, E. D. (2000). Distribution of proteins implicated in excitation-contraction coupling in rat ventricular myocytes. [In Vitro Research Support, Non-U.S. Gov't]. *Biophys J*, 79(5), 2682-2691. doi: 10.1016/S0006-3495(00)76506-4
- Shannon, T. R., & Bers, D. M. (1997). Assessment of intra-SR free [Ca] and buffering in rat heart. *Biophys J*, 73(3), 1524-1531. doi: 10.1016/S0006-3495(97)78184-0

- Shannon, T. R., Ginsburg, K. S., & Bers, D. M. (1998). Reverse mode of the sarcoplasmic reticulum Ca pump limits sarcoplasmic reticulum Ca uptake in permeabilized and voltage-clamped myocytes. [In Vitro]. *Ann N Y Acad Sci*, 853, 350-352.
- Shannon, T. R., Ginsburg, K. S., & Bers, D. M. (2000). Reverse mode of the sarcoplasmic reticulum calcium pump and load-dependent cytosolic calcium decline in voltage-clamped cardiac ventricular myocytes. *Biophysical journal*, 78, 322-333. doi: 10.1016/S0006-3495(00)76595-7
- Shannon, T. R., Ginsburg, K. S., & Bers, D. M. (2002). Quantitative assessment of the SR Ca²⁺ leak-load relationship. [Research Support, Non-U.S. Gov't Research Support, U.S. Gov't, P.H.S.]. *Circ Res*, 91(7), 594-600.
- Shkryl, V. M., Maxwell, J. T., Domeier, T. L., & Blatter, L. A. (2012). Refractoriness of sarcoplasmic reticulum Ca²⁺ release determines Ca²⁺ alternans in atrial myocytes. [Research Support, N.I.H., Extramural Research Support, Non-U.S. Gov't]. *Am J Physiol Heart Circ Physiol*, 302(11), H2310-2320. doi: 10.1152/ajpheart.00079.2012
- Sigalas, C., Bent, S., Kitmitto, A., O'Neill, S., & Sitsapesan, R. (2009). Ca(2+)-calmodulin can activate and inactivate cardiac ryanodine receptors. [In Vitro Research Support, Non-U.S. Gov't]. *Br J Pharmacol*, 156(5), 794-806. doi: 10.1111/j.1476-5381.2008.00092.x
- Sipido, K. R. (2004). Understanding cardiac alternans: the answer lies in the Ca²⁺ store. [Comment Editorial]. *Circ Res*, 94(5), 570-572. doi: 10.1161/01.RES.0000124606.14903.6F
- Smith, G. D. (2002). Modeling the stochastic gating of ion channels *Computational Cell Biology* (pp. 285-): Springer.
- Smith, G. D., Keizer, J. E., Stern, M. D., Lederer, W. J., & Cheng, H. (1998). A simple numerical model of calcium spark formation and detection in cardiac myocytes. *Biophysical journal*, 75, 15-32. doi: 10.1016/S0006-3495(98)77491-0
- Smith, J. M., Clancy, E. A., Valeri, C. R., Ruskin, J. N., & Cohen, R. J. (1988). Electrical alternans and cardiac electrical instability. [Research Support, U.S. Gov't, Non-P.H.S.]. *Circulation*, 77(1), 110-121.
- Snyder, S. M., Palmer, B. M., & Moore, R. L. (2000). A mathematical model of cardiocyte Ca(2+) dynamics with a novel representation of sarcoplasmic reticular

- Ca(2+) control. *Biophysical journal*, 79, 94-115. doi: 10.1016/S0006-3495(00)76276-X
- Sobie, E. A., Dilly, K. W., dos Santos Cruz, J., Lederer, W. J., & Jafri, M. S. (2002). Termination of Cardiac Ca²⁺ Sparks: An Investigative Mathematical Model of Calcium-Induced Calcium Release. *Biophysical Journal*, 83, 59-78. doi: 10.1016/S0006-3495(02)75149-7
- Sobie, E. a., Guatimosim, S., Gómez-Viquez, L., Song, L.-S., Hartmann, H., Saleet Jafri, M., & Lederer, W. J. (2006). The Ca²⁺ leak paradox and rogue ryanodine receptors: SR Ca²⁺ efflux theory and practice. *Progress in biophysics and molecular biology*, 90, 172-185. doi: 10.1016/j.pbiomolbio.2005.06.010
- Sobie, E. a., & Lederer, W. J. (2012). Dynamic local changes in sarcoplasmic reticulum calcium: physiological and pathophysiological roles. *Journal of molecular and cellular cardiology*, 52, 304-311. doi: 10.1016/j.yjmcc.2011.06.024
- Song, L. S., Sham, J. S., Stern, M. D., Lakatta, E. G., & Cheng, H. (1998). Direct measurement of SR release flux by tracking 'Ca²⁺ spikes' in rat cardiac myocytes. *The Journal of physiology*, 512 (Pt 3, 677-691.
- Song, L. S., Sobie, E. A., McCulle, S., Lederer, W. J., Balke, C. W., & Cheng, H. (2006). Orphaned ryanodine receptors in the failing heart. [Research Support, N.I.H., Extramural
Research Support, Non-U.S. Gov't]. *Proc Natl Acad Sci U S A*, 103(11), 4305-4310. doi: 10.1073/pnas.0509324103
- Stern, M. D. (1990). Theory of excitation-contraction coupling in cardiac muscle. 497-517.
- Stern, M. D., Song, L.-s., Cheng, H., Sham, J. S. K. K., Yang, H. T., Boheler, K. R., & Ríos, E. (1999). Local control models of cardiac excitation-contraction coupling. A possible role for allosteric interactions between ryanodine receptors. *The Journal of general physiology*, 113, 469-489.
- Sun, L., Fan, J. S., Clark, J. W., & Palade, P. T. (2000). A model of the L-type Ca²⁺ channel in rat ventricular myocytes: ion selectivity and inactivation mechanisms. *The Journal of physiology*, 529 Pt 1, 139-158.
- Surawicz, B., & Fisch, C. (1992). Cardiac alternans: diverse mechanisms and clinical manifestations. [Review]. *J Am Coll Cardiol*, 20(2), 483-499.

- Tada, M., Yamada, M., Kadoma, M., Inui, M., & Ohmori, F. (1982). Calcium transport by cardiac sarcoplasmic reticulum and phosphorylation of phospholamban. [Research Support, Non-U.S. Gov't Review]. *Mol Cell Biochem*, 46(2), 73-95.
- Tadross, M. R., Dick, I. E., & Yue, D. T. (2008). Mechanism of local and global Ca^{2+} sensing by calmodulin in complex with a Ca^{2+} channel. *Cell*, 133, 1228-1240. doi: 10.1016/j.cell.2008.05.025
- Tao, T., O'Neill, S. C., Diaz, M. E., Li, Y. T., Eisner, D. a., & Zhang, H. (2008). Alternans of cardiac calcium cycling in a cluster of ryanodine receptors: a simulation study. *American journal of physiology. Heart and circulatory physiology*, 295, H598-609. doi: 10.1152/ajpheart.01086.2007
- ter Keurs, H. E. D., & Boyden, P. A. (2007). Calcium and Arrhythmogenesis. *Physiological reviews*, 87, 457-506. doi: 10.1152/physrev.00011.2006.
- ter Keurs, H. E. D. J., Wakayama, Y., Sugai, Y., Price, G., Kagaya, Y., Boyden, P. a., . . . Stuyvers, B. D. M. (2006). Role of sarcomere mechanics and Ca^{2+} overload in Ca^{2+} waves and arrhythmias in rat cardiac muscle. *Annals of the New York Academy of Sciences*, 1080, 248-267. doi: 10.1196/annals.1380.020
- Terentyev, D. (2002). Luminal Ca^{2+} Controls Termination and Refractory Behavior of Ca^{2+} -Induced Ca^{2+} Release in Cardiac Myocytes. *Circulation Research*, 91, 414-420. doi: 10.1161/01.RES.0000032490.04207.BD
- Tran, K., Smith, N. P., Loiselle, D. S., & Crampin, E. J. (2009). A Thermodynamic Model of the Cardiac Sarcoplasmic/ Endoplasmic Ca^{2+} (SERCA) Pump. *Biophysical journal*, 96, 2029-2042. doi: 10.1016/j.bpj.2008.11.045
- Traube, L. (1872). Ein Fall von Pulsus Bigeminus nebst Bemerkungen uber die Leberschwellungen bei Klappenfehlern and uber acute Leberatrophie. . *Berlin Klin Wochenschr*, 9, 185–188.
- Ulbricht, W. (2005). Sodium channel inactivation: molecular determinants and modulation. [Review]. *Physiol Rev*, 85(4), 1271-1301. doi: 10.1152/physrev.00024.2004
- van Oort, R. J., Garbino, A., Wang, W., Dixit, S. S., Landstrom, A. P., Gaur, N., . . . Wehrens, X. H. (2011). Disrupted junctional membrane complexes and hyperactive ryanodine receptors after acute junctophilin knockdown in mice. [Comparative Study]. *Circulation*, 123(9), 979-988. doi: 10.1161/CIRCULATIONAHA.110.006437

- Van Petegem, F., Chatelain, F. C., & Minor, D. L., Jr. (2005). Insights into voltage-gated calcium channel regulation from the structure of the CaV1.2 IQ domain-Ca²⁺/calmodulin complex. [Research Support, N.I.H., Extramural Research Support, Non-U.S. Gov't]. *Nat Struct Mol Biol*, 12(12), 1108-1115. doi: 10.1038/nsmb1027
- Vassalle, M., & Lin, C.-I. (2004). Calcium overload and cardiac function. *Journal of biomedical science*, 11, 542-565. doi: 10.1159/000079666
- Viatchenko-Karpinski, S., Terentyev, D., Györke, I., Terentyeva, R., Volpe, P., Priori, S. G., . . . Györke, S. (2004). Abnormal calcium signaling and sudden cardiac death associated with mutation of calsequestrin. *Circulation research*, 94, 471-477. doi: 10.1161/01.RES.0000115944.10681.EB
- Wagner, E., Lauterbach, M. a., Kohl, T., Westphal, V., Williams, G. S. B., Steinbrecher, J. H., . . . Lehnart, S. E. (2012). Stimulated emission depletion live-cell super-resolution imaging shows proliferative remodeling of T-tubule membrane structures after myocardial infarction. *Circulation research*, 111, 402-414. doi: 10.1161/CIRCRESAHA.112.274530
- Wan, X., Cutler, M., Song, Z., Karma, A., Matsuda, T., Baba, A., & Rosenbaum, D. S. (2012). New experimental evidence for mechanism of arrhythmogenic membrane potential alternans based on balance of electrogenic I(NCX)/I(Ca) currents. *Heart Rhythm*, 9(10), 1698-1705. doi: 10.1016/j.hrthm.2012.06.031
- Wei, S., Guo, A., Chen, B., Kutschke, W., Xie, Y. P., Zimmerman, K., . . . Song, L. S. (2010). T-tubule remodeling during transition from hypertrophy to heart failure. [Comparative Study Research Support, N.I.H., Extramural Research Support, Non-U.S. Gov't]. *Circ Res*, 107(4), 520-531. doi: 10.1161/CIRCRESAHA.109.212324
- Weiss, J. N., Karma, A., Shiferaw, Y., Chen, P.-S., Garfinkel, A., & Qu, Z. (2006). From pulsus to pulseless: the saga of cardiac alternans. *Circulation research*, 98, 1244-1253. doi: 10.1161/01.RES.0000224540.97431.f0
- Wier, W. G., Egan, T. M., López-López, J. R., & Balke, C. W. (1994). Local control of excitation-contraction coupling in rat heart cells. *The Journal of physiology*, 474, 463-471.

- Williams, G. S. B., Chikando, A. C., Tuan, H.-T. M., Sobie, E. a., Lederer, W. J., & Jafri, M. S. (2011). Dynamics of Calcium Sparks and Calcium Leak in the Heart. *Biophysical journal*, 101, 1287-1296. doi: 10.1016/j.bpj.2011.07.021
- Wu, C. Y., Jia, Z., Wang, W., Ballou, L. M., Jiang, Y. P., Chen, B., . . . Lin, R. Z. (2011). PI3Ks maintain the structural integrity of T-tubules in cardiac myocytes. [Research Support, N.I.H., Extramural
- Research Support, Non-U.S. Gov't
- Research Support, U.S. Gov't, Non-P.H.S.]. *PloS one*, 6(9), e24404. doi: 10.1371/journal.pone.0024404
- Xie, L. H., Sato, D., Garfinkel, A., Qu, Z., & Weiss, J. N. (2008). Intracellular Ca alternans: coordinated regulation by sarcoplasmic reticulum release, uptake, and leak. [Research Support, N.I.H., Extramural
- Research Support, Non-U.S. Gov't]. *Biophys J*, 95(6), 3100-3110. doi: 10.1529/biophysj.108.130955
- Xie, Y., Sato, D., Garfinkel, A., Qu, Z., & Weiss, J. N. (2010). So little source, so much sink: requirements for afterdepolarizations to propagate in tissue. [Research Support, N.I.H., Extramural
- Research Support, Non-U.S. Gov't]. *Biophys J*, 99(5), 1408-1415. doi: 10.1016/j.bpj.2010.06.042
- Xie, Y., Sato, D., Garfinkel, A., Qu, Z., & Weiss, J. N. (2010). So Little Source, So Much Sink: Requirements for Afterdepolarizations to Propagate in Tissue. *Biophysical Journal*, 99, 1408-1415. doi: 10.1016/j.bpj.2010.06.042
- Xu, L., & Meissner, G. (2004). Mechanism of calmodulin inhibition of cardiac sarcoplasmic reticulum Ca²⁺ release channel (ryanodine receptor). [Research Support, U.S. Gov't, P.H.S.]. *Biophys J*, 86(2), 797-804. doi: 10.1016/S0006-3495(04)74155-7

CHAPTER 4: FUNCTIONAL CONSEQUENCE OF RYR CLUSTER FRAGMENTATION AND REDISTRIBUTION IN PERSISTENT ATRIAL FIBRILLATION

Abstract

Atrial fibrillation (AF) is the most common cardiac arrhythmia. In chronic atrial fibrillation (AF), abnormalities in Ca^{2+} release from ryanodine receptor type 2 (RyR2) have been implicated as a major factor contributing to arrhythmia and contractile dysfunction. Our collaborators have used STED microscopy (STimulated Emission Depletion) to examine RyR clusters in fixed atrial myocytes from sheep with persistent AF (N=6) and control (Ctrl, N=6) animals. In parallel experiments, Ca^{2+} sparks were measured in live permeabilized myocytes, with AF has >50% higher frequency in sparks and there was a higher prevalence of macrosparks. The average cluster sizes, 15 RyRs, were not different between AF and Ctrl. However, the distance between the clusters were reduced in AF. In addition, the relation to RyR organization and SR Ca^{2+} release remains unknown. A computational 3D model of the CRU put together in a subcellular region with 10,800 CRUs showed that an increased fragmentation led to higher spark frequency, increased TTP and duration similar to that seen in AF. The model suggested RyR clusters of 150nm apart of each other can be grouped as functional Ca^{2+} release units (CRU). In AF, using this criteria, these units exhibit increases fragmentation, with more clusters per

CRU. Also, in AF, there were more RyR clusters in between Z-lines. The presence of RyRs between Z-lines can increase the occurrence of macrosparks in AF.

Introduction

Atrial fibrillation (AF) was first recognized by (Mackenzie, 1914). Nowadays, it is the most common arrhythmia ((CDC), 2006). The normal rhythmic cycle of the heart is triggered by the electrical signal received from the sinoatrial (SA) node, followed by atrial contraction, and then ventricular activation. However, under AF, this normal electrical signaling pathway is disturbed that weaken the pumping activity, as shown in Figure 1 (Wakili, Voigt, Kaab, Dobrev, & Nattel, 2011). Even though AF is not life threatening, the resultant loss of atrial contraction leads to atrial thrombi (the blood clot formed by blood residing in the atrial); embolization and stroke are major causes of morbidity and mortality. In particular, AF causes 15% of all strokes; and patients with AF has 50% higher risk in mortality in male, and 200% higher risk in female, compared to patients without AF (Troughton & Crozier, 2013). Depending on how long of an AF, it can be classified into 3 types: paroxymal AF (in which the abnormal heart rate starts and stops by itself within a day to a week), persistent AF (in which the abnormal heart rate goes on more than a week, which may need medical treatment to stop or it can stop by itself), and permanent AF (the normal heart rate can not be restored with treatment).

In established persistent AF, antiarrhythmic drug therapies are ineffective, as is catheter ablation (Heidbuchel et al., 2013). Thus, further understanding of the cellular processes involved in the generation and maintenance of AF may help to identify novel targets for antiarrhythmic treatment (Dobrev, Carlsson, & Nattel, 2012). Recently, evidence has emerged for a major role of dysregulation of the ryanodine receptor (RyR) function and Ca^{2+} release from the sarcoplasmic reticulum (SR) where AF is associated

with increased spontaneous calcium release (Hove-Madsen et al., 2004). An increase in RyR activity, attributed to an upregulation of Ca^{2+} /Calm-dependent protein kinase II (CaMKII) was reported in patients with chronic and persistent AF (Neef et al., 2010). This can lead to an increased propensity for spontaneous Ca^{2+} waves and subsequent activation of $\text{Na}^+/\text{Ca}^{2+}$ exchanger (NCX). An upregulation of NCX was also reported and this, coupled with the spontaneous release led to membrane depolarization and delayed afterdepolarizations (Voigt et al., 2012). This agrees with the observation of an earlier study by Hove-Madsen and co-workers (Hove-Madsen et al., 2004) showing an increased frequency of spontaneous Ca^{2+} waves and sparks in patients with AF. At the molecular level, changes in RyR phosphorylation have been emphasized but few studies reported changes in expression (Ohkusa et al., 1999) and no data on the organization of RyR.

Data from animal models similarly highlight a role for RyR in AF, though the number of studies in chronic and persistent AF is limited. In the dog with heart failure and in dogs with chronic AF, abnormal Ca^{2+} release has been reported as well as increase in phosphorylation (Neef et al., 2010; Zhao et al., 2007). A recent study in the sheep with persistent AF highlighted RyR and T-tubule re-organization but also found RyR expression was reduced, although confocal immunofluorescence imaging revealed no change in RyR distribution and overall density (Zhao et al., 2007). This hints at an underlying remodeling of RyR ultrastructural organization; however no data currently exists as this would be undetectable by conventional microscopy methods.

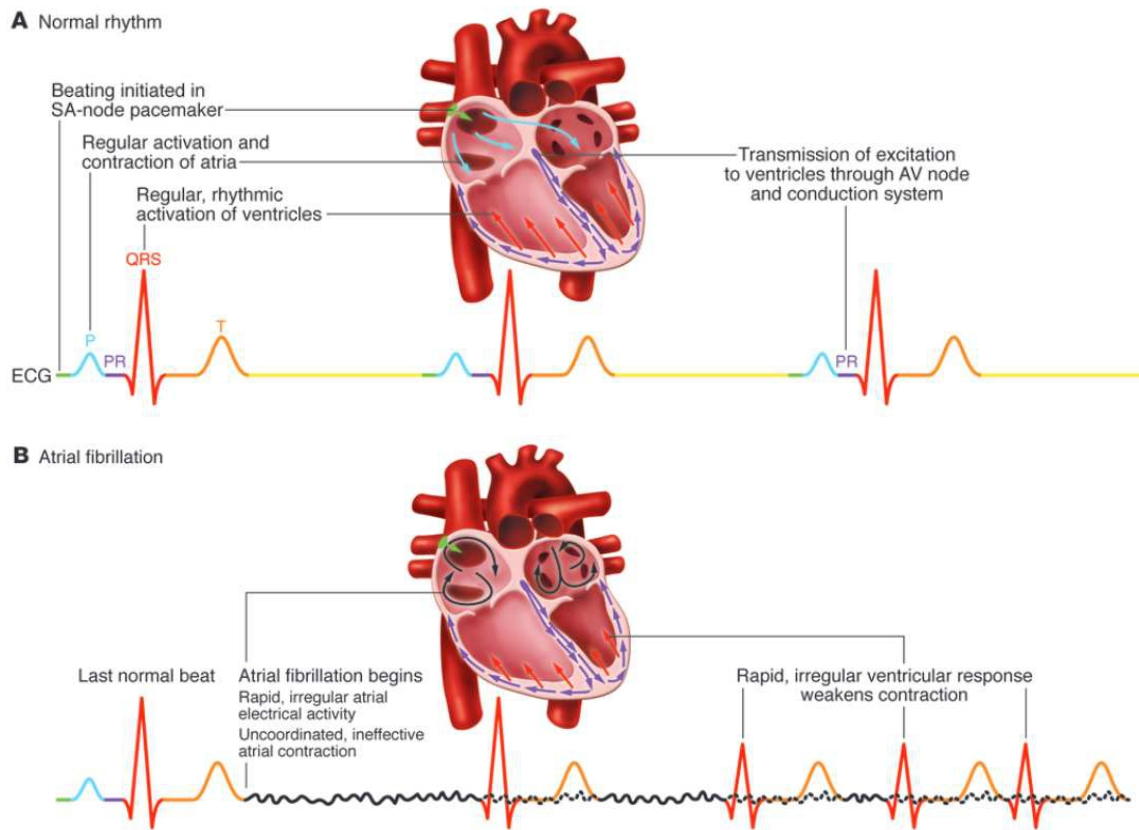


Figure 1. Schematic diagrams that show ECG recordings with (A) a normal sinus rhythm, and (B) an AF. The rapid and irregular AF activation is showed on ECG as an undulating baseline (the dotted lines show the continuous activity of atrial activation during QRS and T wave phases). During AF, ventricular activations (QRS complex) are driven by fibrillating atria which weaken the cardiac contraction efficiency and causing clinical symptoms (adapted from (Wakili et al., 2011))

RyR clusters have previously been studied using electron microscopy of freeze fracture and thin slice preparations of skeletal and cardiac tissue. From these measurements, RyR clusters were considered as contiguous crystalline arrays. Recently, new methods have been developed to allow the measurement of intracellular structures below the resolution limits of traditional fluorescence microscopy (David Baddeley et al., 2009; Betzig et al., 2006; Huang, Wang, Bates, & Zhuang, 2008). These super resolution

microscopy methods have recently been applied to the study of peripheral RyR clusters in ventricular cardiac myocytes (Baddeley, Jayasinghe, Cremer, Cannell, & Soeller, 2009).

These have shown RyR clusters have a more fragmented organization than previously thought, with small and large sub-clusters grouped together in “supercluster” formations (David Baddeley et al., 2009) which may act together to release Ca^{2+} as observed as a Ca^{2+} spark (Heping Cheng & Lederer, 2008); this unit is termed a calcium release unit (CRU) (Franzini-Armstrong, Protasi, & Ramesh, 1998, 1999), which in the case of atrial cells as studied here are frequently not coupled with the sarcolemma nor the T-tubule networks.

Computational modeling has recently revealed RyR cluster behavior may relate to their size. Small clusters are proposed to have lower levels of allosteric regulation via coupled gating and so fire more readily, contributing more to diastolic release (Sobie et al., 2006). Similarly, preferential inhibition of small RyR clusters has highlighted their involvement in the initiation of spontaneous Ca^{2+} waves (MacQuaide, Ramay, Sobie, & Smith, 2010). It was hypothesized that small clusters would act to relay Ca^{2+} release to neighboring clusters and that this was particularly important in gaining critical mass for the initiation of a Ca^{2+} wave. It is conceivable that abnormal fragmentation of RyR clusters may assist in the process of inter-cluster activation which initiates Ca^{2+} waves, but so far this has not been studied.

Our collaborators, Niall *et al.* (manuscript in preparation) carried out super-resolution measurements of RyR, to explore cluster size, shape and fragmentation, whereby we define functional calcium release units (CRUs) as a group of clusters within

150 nm distance of each other, allowing cluster-cluster interaction. In the same cells, they measured subcellular Ca^{2+} release to assess the functional changes which occur in AF. In the present study, using the data from our collaborators who have investigated alterations in RyR cluster morphology in an established sheep model of persistent AF (Anne et al., 2007; Lenaerts et al., 2009; Willems et al., 2001), we developed a computational modeling to predict the impact of the altered organization of RyR clusters and CRUs on Ca^{2+} release, comparing predictions to observations of spark properties.

Computational modelling

A spatial model with dimensions $58 \times 20 \times 18 \mu\text{m}$ was developed to describe a subcellular region of the permeabilized sheep atrial myocyte. The model has dynamics equations for myoplasmic calcium $[\text{Ca}^{2+}]_{\text{myo}}$, $[\text{Ca}^{2+}]_{\text{nsr}}$, $[\text{Ca}^{2+}]_{\text{jsr}}^i$, where i denotes the i^{th} release site as well as stationary endogenous calcium buffers and mobile dyes (free and Ca^{2+} -bound EGTA and , free and Ca^{2+} -bound Ca^{2+} indicator dye) . Each release site consist of a cluster of a varying number of ryanodine receptors (RyR2) as specified in the figure legends,. The calcium release sites distributed spatially with uniform distances of $1.8 \mu\text{m}$ along x-direction and $0.8 \mu\text{m}$ along the transversal direction (y- and z- axis). This allows the hypercube to accommodate 10,800 calcium release units (CRUs) within. The model of calcium dynamics for the ventricular myocyte developed previously by these authors (Wagner et al., 2012; Williams et al., 2011) was modified to simulate an atrial myocyte with the following changes:

- 1) RyR2s sense the calcium from the local cytosolic calcium instead of the subspace calcium

- 2) RyR2 coupling was adjusted to reproduce the atrial spark rates at the experiment condition

The sarcoplasmic reticulum (SR) and cytosol are homogeneously distributed throughout the cell with each occupying a specific fraction of volume in each grid point. In other words, at each grid-point, the volume is partitioned into myoplasmic volume and network SR volume. The calcium release sites are located at specific sites in the myocyte as specified in the figure legends. In the atrial myocyte, a large fraction of calcium release sites are not closely apposed to a T-tubule and hence do not have a junctional subspace as is the case with ventricular myocytes. Thus, when the channel opens, the calcium flows directly into the local myoplasmic volume of the neighboring grid-points. Depending on the cluster size of RyR2, the junctional SR (jSR) spreads an area of either 100nm x 100nm (6 RyR2s) or 200nm x 200nm (25 RyR2s), for example. Figure 2 showed a release site spreading two grid-points.

At the Ca^{2+} release site, calcium is released into the myoplasm from the jSR via the RyR (J_{ryr}). A stochastic model for the calcium release site in the sheep atrial cell was developed using the formulation of RyR channel gating derived from Williams et al (Williams et al., 2011). When the jSR that is not apposed to the T-tubule spans more than one grid point, calcium release via RyR2 channels on the jSR is distributed to the one or more myoplasmic volumes of the nearby grid points, depending upon the size of the RyR2 cluster and the jSR, as shown in Figure 2. Also, the calcium in the junctional SR is refilled by calcium from the nearby network SR grid points. In order to capture the idea that the opening of RyR2 channels will activate adjacent RyR2 channels, the mean-field

approach RyR2 assumes the channels sense the calcium of highest concentration in the corresponding cytosolic grid point that links to jSR. When varying the number of RyRs in a cluster, the size of the jSR was modified accordingly and the coupling energy between channels in the cluster were also modified using mean-field approach (Groff & Smith, 2008). It's important to notice that the subspace is not being used, instead, Ca^{2+} release via RyR2 flow directly into the adjacent myoplasmic volumes.

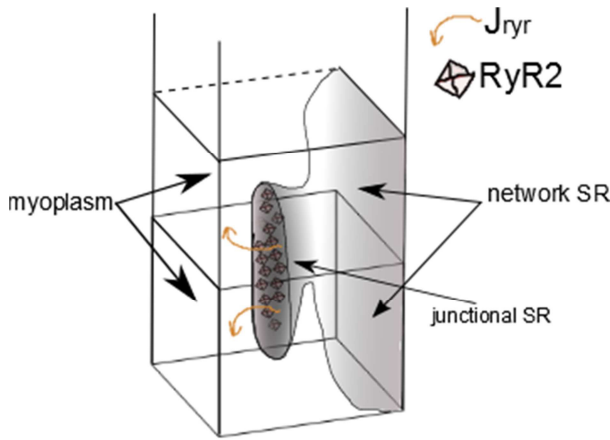


Figure 2. Schematic diagram of a release site (with 25 RyRs) that sense calcium from 2 voxels of size 100nm x 100nm

The elevated calcium is removed from the myoplasm and sequestered in the nSR (network SR) by the sarcoplasmic/endoplasmic reticulum Ca^{2+} -ATPase (J_{serca}). The SERCA pumps are modelled uniformly distributed across all the grid-points as they are located in the network SR. Similarly, the intrinsic SR buffers are assumed to be uniformly distributed as well. SERCA pumps are modelled using a thermodynamics 2-

state model developed by (Tran, Smith, Loiselle, & Crampin, 2009) with the equation for two-state reduced model from (Williams et al., 2011).

$$J_{serca} = 2 \times v_{serca} [\text{SERCA}]$$

$$v_{serca} = \frac{3.24873 \times 10^{12} (K_{myo})^2 + K_{myo} (9.17846 \times 10^6 - 11478.2 K_{sr}) - 0.329904 K_{sr}}{D_{cycle}}$$

$$D_{cycle} = 0.104217 + 17.923 K_{sr} + K_{myo} (1.75583 \times 10^6 + 7.61673 \times 10^6 K_{sr}) + (K_{myo})^2 (6.08463 \times 10^{11} + 4.50544 \times 10^{11} K_{sr})$$

and

$$K_{myo} = \left(\frac{[\text{Ca}]_{myo}}{10^{-3} K_{d,myo}} \right)^2; K_{sr} = \left(\frac{[\text{Ca}]_{nsr}}{10^{-3} K_{d,sr}} \right)^2$$

In the myoplasm calcium is buffered by the endogeneous buffers [calmodulin (Calm), troponin-C (Trpn-C), SL, SR membrane buffers] or exogeneous buffers [EGTA (EGTA) or Fluo-3 (F)] with the kinetics based on (Loughrey, MacEachern, Cooper, & Smith, 2003)

$$J_{buffer} = J_{CaTrpn} + J_{CaCalm} + J_{CaSR} + J_{CaEGTA} + J_{CaF} + J_{CaSL}$$

with CaTrpn = calcium-bound to troponin, CaCalm = calcium-bound calmodulin, CaSR = calcium-bound to SR buffer, CaEGTA = calcium-bound to EGTA, CaF = calcium-bound to Fluo-3. Of these, calmodulin, the SL, SR membrane buffers and troponin are assumed to be stationary and are described by the following ordinary differential equations:

$$\begin{aligned}
\frac{d[\text{CaCalm}]}{dt} &= J_{\text{CaM}} = k_{\text{CM}}^+ ([\text{Ca}]_{\text{myo}})([\text{Calm}]_T - [\text{CaCalm}]_{\text{myo}}) - k_{\text{CM}}^- [\text{CaCalm}]_{\text{myo}} \\
\frac{d[\text{CaSR}]}{dt} &= J_{\text{CaSR}} = k_{\text{SR}}^+ ([\text{Ca}]_{\text{myo}})([\text{SR}]_T - [\text{CaSR}]_{\text{myo}}) - k_{\text{SR}}^- [\text{CaSR}]_{\text{myo}} \\
\frac{d[\text{CaSL}]}{dt} &= J_{\text{CaSL}} = k_{\text{SL}}^+ ([\text{Ca}]_{\text{myo}})([\text{SL}]_T - [\text{CaSL}]_{\text{myo}}) - k_{\text{SL}}^- [\text{CaSL}]_{\text{myo}} \\
\frac{d[\text{CaTrpn}]}{dt} &= J_{\text{Trpn}} = k_{\text{Trpn}}^+ ([\text{Ca}]_{\text{myo}})([\text{Trpn}]_T - [\text{CaTrpn}]_{\text{myo}}) - k_{\text{Trpn}}^- [\text{CaTrpn}]_{\text{myo}}
\end{aligned}$$

The exogenous buffers EGTA and Fluo-3 are mobile buffers and are describe by the following differential equations:

$$\begin{aligned}
\frac{\partial [\text{CaF}]_{\text{myo}}}{\partial t} &= J_{\text{CaF}} + \nabla^2 [\text{CaF}]_{\text{myo}} \\
\frac{\partial [\text{F}]_{\text{myo}}}{\partial t} &= -J_{\text{CaF}} + \nabla^2 [\text{F}]_{\text{myo}} \\
\frac{\partial [\text{CaEGTA}]_{\text{myo}}}{\partial t} &= J_{\text{CaEGTA}} + \nabla^2 [\text{CaEGTA}]_{\text{myo}} \\
\frac{\partial [\text{EGTA}]_{\text{myo}}}{\partial t} &= -J_{\text{CaEGTA}} + \nabla^2 [\text{EGTA}]_{\text{myo}}
\end{aligned}$$

where the fluxes are

$$\begin{aligned}
J_{\text{CaF}} &= k_F^+ ([\text{Ca}]_{\text{myo}})([\text{F}] - k_F^- [\text{CaF}]) \\
J_{\text{CaEGTA}} &= k_{\text{EGTA}}^+ ([\text{Ca}]_{\text{myo}})([\text{EGTA}] - k_{\text{EGTA}}^- [\text{CaEGTA}])
\end{aligned}$$

Free calcium and mobile buffers passively diffuse from one grid point to the neighboring ones following Fickian diffusion laws. Combined with the above fluxes the following partial differential equations describe these model variables:

$$\begin{aligned}
\frac{\partial [\text{Ca}^{2+}]_{\text{myo}}}{\partial t} &= J_{\text{ryr}} - J_{\text{buffer}} - J_{\text{serca}} + \nabla^2 [\text{Ca}^{2+}]_{\text{myo}} \\
\frac{\partial [\text{Ca}^{2+}]_{\text{nsr}}}{\partial t} &= J_{\text{serca}} + J_{\text{refill}} + \nabla^2 [\text{Ca}^{2+}]_{\text{nsr}}
\end{aligned}$$

The calcium in the jSR is replenished from the nSR by a diffusive flux (J_{refill}) which has been described by (Williams et al., 2011). Even though Ca^{2+} release via RyR2 from the jSR can spread more than one grid-point, the jSR is treated as a single volume. Thus the changes in $[Ca^{2+}]_{jSR}$ at the i -th release site is described by the following ordinary differential equation:

$$\frac{\partial [Ca^{2+}]_{jSR}^i}{\partial t} = \beta_{jSR} (J_{refill} - J_{ryr}) / \lambda_{jSR}$$

with fast buffering is assumed in the jSR, and $\lambda_{jSR} = V_{jSR} / V_{myo}$ is the volume fraction.

$$\beta_{jSR} = 1d0 / (1d0 + (B_{jSR}^T \times Km_{jSR}) / ((Km_{jSR} + [Ca^{2+}]_{jSR}^i)^2))$$

The parameters for the model are given in Table 1, which are based on values from permeabilized cell conditions. RyR channel gating was solved using our Ultrafast Monte Carlo method. The partial differential equations were solved using the explicit Euler method. The reaction part represents the creating and consuming of the corresponding species within each grid-point. Simulations were run on HP Z800 workstation with a NVIDIA C2050 GPU using CUDA Fortran (Portland Compiler Group). The statistics was collected based on 384 independent simulations. The rectangular-solid shaped region 100 nm grid size in each dimension and is solved using the finite-difference method. Dynamics equations for calcium in each of these compartments are developed. Channel gating for each channel cluster is gated to optimize efficiency using our Ultrafast Monte Carlo algorithm.

Table 1. Parameters in the model

Parameter	Definition	Value
V_{cell}	Cell volume	39.83(pL)
V_{myo}	Myoplasmic volume	55% * V_{cell}
V_{nsr}	Network SR volume	3.2% * V_{cell}
V_{jsr}	Junctional SR volume	0.5% * V_{cell}
$D_{\text{myo}}(x,y,z)$	Free cytosolic calcium diffusion	220 $\mu\text{m}^2/\text{sec}$
$D_{\text{nsr}}(x,y,z)$	Free SR calicum diffusion	60 $\mu\text{m}^2/\text{sec}$
$D_{\text{dye}}(x,y,z)$	Fluorescence and Calcium-bound fluorescence diffusion	80 $\mu\text{m}^2/\text{sec}$
F_T	Total fluorescence (Fluo-4)	50 μM
K_{on}	Binding constant for fluorescence	80 $\mu\text{M}^{-1}.\text{sec}^{-1}$
K_{off}	Unbinding constant for fluorescence	72 sec^{-1}
i_{Irr}	Single RyR channel current	0.22 pA
E_{cc}	Change in free energy between closed RYR pairs	-0.872 $k_B T$
E_{oo}	Change in free energy between open RYR pairs	-1.15 $k_B T$
k_B	Boltzmann constant	1.381x10 ⁻²³ J/K
T	Temperature	295.15 K
EGTA	Total EGTA	350 μM
$K_{\text{on_EGTA}}$	Binding constant for EGTA	49.8 $\mu\text{M}^{-1}.\text{sec}^{-1}$
$K_{\text{off_EGTA}}$	Unbinding constant for EGTA	2.72 sec^{-1}
$D_{\text{EGTA}}(x,y,z)$	Diffusion constant of EGTA and calcium-bound EGTA	200 $\mu\text{m}^2/\text{sec}$
$[\text{Ca}_i]$	Cytosolic calcium concentration	0.15 μM
$[\text{Ca}_{\text{sr}}]$	SR calcium concentration	1.2 mM
B_{myoT}	Total myoplasmic buffer concentration	Ctrl: 3.703026e2 (μM)
		AF: 2.424742e2 (μM)
$K_{\text{m,myo}}$	Disassociation constant of myoplasm buffer	Ctrl: 1.1900 (μM)
		AF: 1.310 (μM)
Calmodulin	The dynamics buffers with $K_d=2.38 \mu\text{M}$ ($k^+=30 \mu\text{M}^{-1}.\text{s}^{-1}$, $k^-=71.4 \text{s}^{-1}$)	24 μM
B_{SR}	The SR buffer with $K_d=0.86 \mu\text{M}$ ($k^+=115 \mu\text{M}^{-1}.\text{s}^{-1}$, $k^-=100 \text{s}^{-1}$)	47 μM
A_{pump}	Concentration of SERCA pump	220 μM
$K_{\text{p,myo}}$	The binding affinity of cytosolic calcium to SERCA	850 μM

$K_{p,nsr}$	The binding affinity of SR calcium to SERCA	1,900 μ M
-------------	---	---------------

Results

RyR cluster size and Ca^{2+} spark frequency

Using STED imaging, Niall *et al.* was able to see a 4-6x improvement over conventional laser-scanning confocal microscope was observed. This gives a potential resolution of 1-2 individual RyR tetramers in the focal plane. The method to estimate cluster size is demonstrated in Figure 3. Figure 3.B shows a typical myocyte imaged using conventional confocal microscopy. Figure 3.C shows a confocal image of a 3-sarcomere wide region, with RyRs clearly visible along the Z-lines. Progressive improvements in resolution are evident in the STED (D) and then deconvolved STED images (E). After deconvolution, reliable automated thresholding was then possible (F). Figure 3.G shows the typical image of the clusters of contiguous RyRs that are resolved by this method. Here, 10 individual clusters could be resolved, with highly variable size and shape. These images were used as a mask and the approximate RyR number which could fit into each detected cluster was calculated using a grid of RyR sized units (30 x 30 nm) (Figure 3.H). This was assumed as a good approximation, given the limits of resolution, but had limited utility in the measurement of clusters with less than 2 RyRs. Since some uncertainty underlies this quantification, the number of RyRs will be stated as approximate.

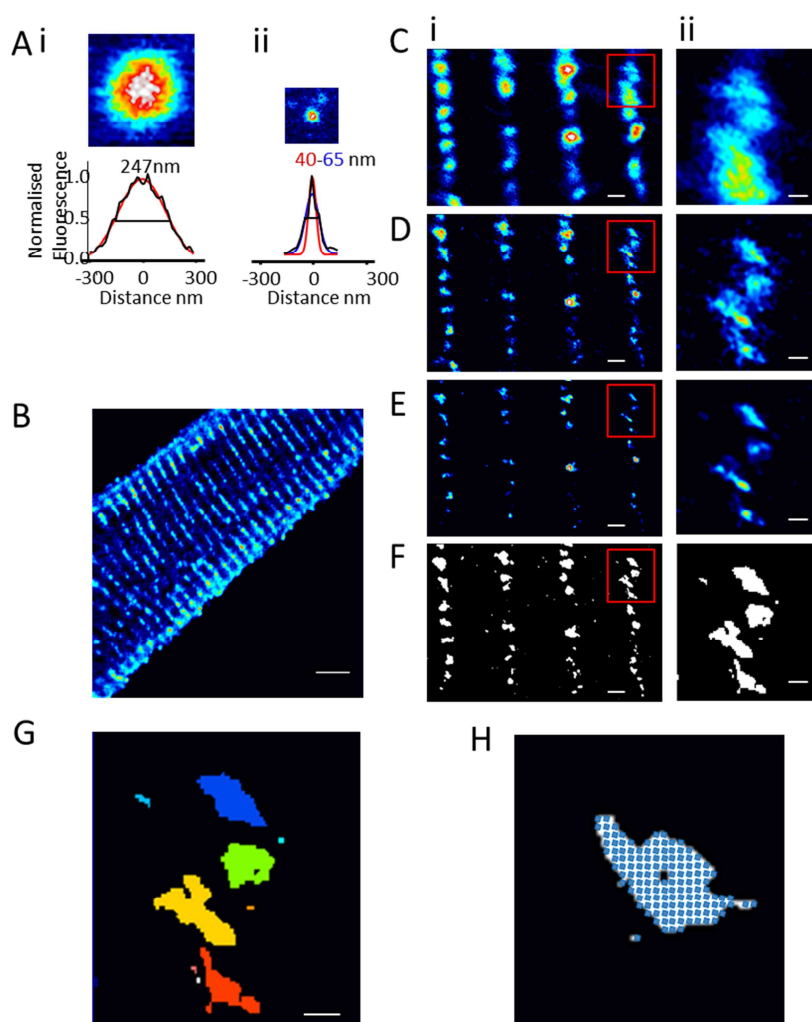


Figure 3. Deconvolved STED microscopy resolves RyR sub-cluster formations in atrial myocytes. A. Images show average of the same 3 fluorescent beads aligned on their peaks from confocal (i) and STED (ii) recordings. B. RyR antibody labelling in an atrial myocyte visualized using confocal microscopy. Allowing a ~4-6x improvement in resolution. The much reduced Gaussian half maximal fit, with 2 possible fits has been reported before (5). This may allow further improvements the resolution of closely packed clusters of proteins. C-F Optical and software-based methods used to allow sub-cluster resolution (region outlined in red is shown in ii). C. A confocal image the sub-region used in subsequent imaging steps. D. The STED image of this region shows a marked improvement in resolution. E Deconvolution of the image in (D) allows further improvements in image, with reduced noise and more defined edges of each sub-cluster. F. RyR clusters are segmented using the Otsu thresholding method to allow further quantification of their size and shape. G. Here, the colors delineate the 10 RyR clusters detected in Fii. H. Illustration of RyR cluster size quantification. A grid of single RyRs (blue squares) are superimposed on the thresholded image to count the number of RyRs which would fit. (extract from Niall's study)

Based on the measurement above, we tested the frequency of Ca^{2+} sparks at different cluster sizes. Modeling reveals an increased spark probability in more fragmented CRUs. Simulation of clusters of 5, 25 and 49 RyRs showed an inverse relationship between cluster size and spark frequency. Spark frequency was ~ 20x higher in 5 RyR clusters than those with 49 RyRs. The probability of such small RyR clusters within a CRU to trigger larger (25 RyR) neighboring clusters (P_{trigger}) was further investigated (Figure 4). Small clusters were set to open simultaneously, with subsequent Ca^{2+} diffusion to the larger cluster, activating release. The probability of the large central cluster being triggered by varying the number of small peripheral clusters is plotted in Figure 4. Bi. This predicts a very steep dependence of P_{trigger} on the number of small peripheral RyR clusters. Reducing buffering to the same extent as observed experimentally then had a notable effect, increasing P_{trigger} by 17.4% and 31.4% in the 2 and 3 small cluster simulations.

The changes with AF which were found experimentally, i.e. more small clusters and increased fragmentation within CRUs, can be approximated by simulating an increase from between 2 and 3 satellite RyR clusters. This together with the changes in buffering resulted in a ~ 130% increase in P_{trigger} . Since the observed experimental increase in satellites was approximately half of this, the 75% increase in spark frequency observed experimentally is in good agreement with this. In reality, not all satellites would be triggered simultaneously or would be exactly 100 nm away, so this should be an upper limit of this effect. A high variation in cluster distance was evident in the STED data, so asynchronous activation of satellite clusters would be more likely. Even given both of

these caveats, it is clear that higher CRU fragmentation and reduced buffering would both facilitate intra-cluster interaction, leading to an increased spontaneous CRU activation rate, observed experimentally as an increase in spark rate. This is in agreement with the previous studies (Sobie et al., 2006; Williams et al., 2011), which proves that with RyR cluster fragmentation, the probability of RyR firing increase significantly.

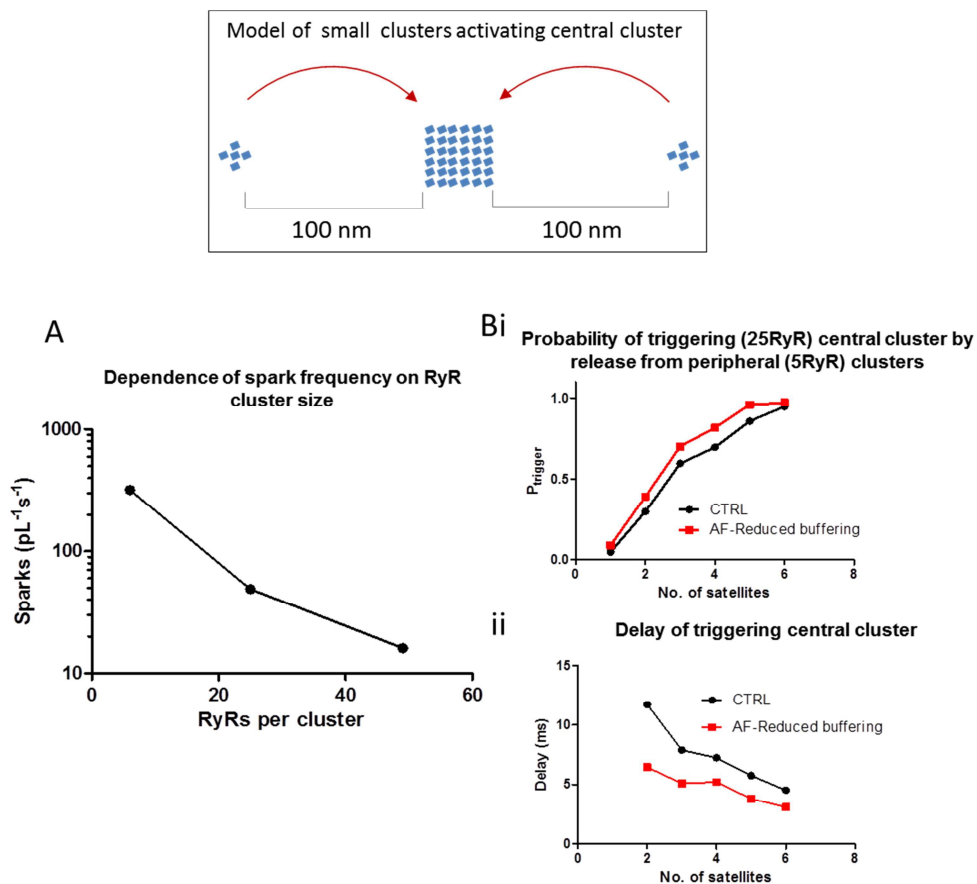


Figure 4. Computational modeling of intraCRU activation: Activation of large clusters by release from small RyR clusters. Insert shows release from small RyR within the CRU which can activate the larger RyR cluster. The small clusters are triggers simultaneously and the central cluster is activated by the diffusion of released Ca^{2+} . Red arrows depict the sequence of activation. Distance shown is edge-to-edge. A. Simulation of spark frequency of clusters with 5, 25 and 49 RyRs, revealing an order of magnitude increased frequency from smaller

clusters. B. The probability (i) and delay(ii) of triggering release from a 25 RyR cluster by varying numbers small clusters placed 100 nm away which are triggered simultaneously.

Functional RyR cluster

Due to the fragmentation in the RyR arrangement, it is important to know whether these small RyR2 clusters can function as a whole functional Ca^{2+} release site. A model of main cluster activating smaller cluster was created, Figure 5. In this first simulation, the ability of one small RyR cluster (5RyRs) to be triggered by a larger neighboring cluster (49 RyR) was simulated. A pseudo linescan image, without addition of photon and instrumentation noise (Figure 5. Ai) and the $[\text{Ca}^{2+}]_{\text{free}}$ profiles (Figure 5. Aii) highlight a mild asymmetry on the left hand side of the image due to the opening of the neighboring RyR. This can be further quantified in the profiles of fluorescence (Figure 5. Bi) and total Ca^{2+} (Figure 5. Bii). Effects on FWHM or FDHM were not evident; only a slight (<5%) increase in width could be seen, but as this occurs after the peak of the main release has been reached, it would be undetectable by traditional spark analysis, especially given the relatively high levels of noise present in cellular recordings. The relationship in Figure 5. Ci shows open probability (P_o) of the small clusters as a function of their distance from the main cluster. This shows a relatively steep drop at ~150 nm from 0.937 to 0.315 indicating that small clusters at distances ≥ 150 nm, are unlikely to be influenced by RyR release from the main cluster. The delay in activation of the small clusters was negligible (<2 ms) for distances ≤ 150 nm. The inclusion of the reduced cytosolic buffer observed in AF had little effect in any of these simulations.

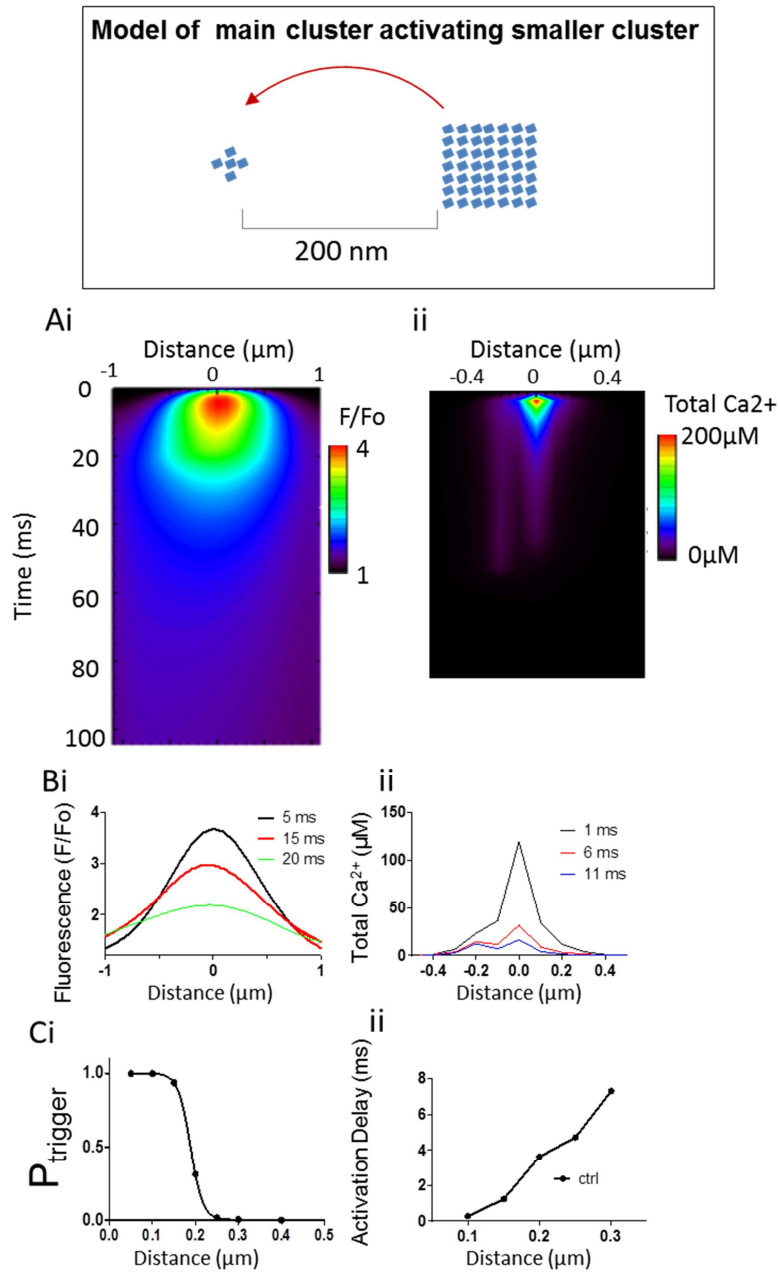


Figure 5. Computational modeling of intraCRU activation: Activation of small cluster by release from large RyR clusters. Insert shows release from one large RyR within the CRU which can activate the smaller RyR cluster. The small cluster is activated by the diffusion of released Ca^{2+} from the larger cluster. Red arrows depict the sequence of activation. A. Waterfall plot of F/F_0 and (B) total Ca^{2+} signals from 2 the release sites depicted in the inset; The 49 RyR is 200 nm edge-to-edge away from the 5 RyR cluster. A smaller, more prolonged release from the small cluster is visible, after activation by Ca^{2+} released from the main cluster. B Plots show spatial profiles of fluorescence (i) and total Ca^{2+} released (ii). Cluster interaction is only evident on the free Ca^{2+} plot at -0.1 and -0.2 distances, however this is not visible on the simulated linescan F/F_0 image. C. (i) The relationship between the probability of triggering release from a small cluster (P_{trigger}) vs. distance from a larger site and the

corresponding delay of activation (ii). This shows a high likelihood of activation and <2 ms delay if small clusters are ≤ 150 nm away from a larger one.

Modeling sarcomeric Ca^{2+} propagation.

One notable functional difference was the appearance of propagating release events or macrosparks in the AF cells. Previous modeling work has shown sarcomere shortening can greatly increase the probability of this type of propagating release (Izu, Means, Shadid, Chen-izu, & Balke, 2006). No such shortening was observed in the current study; however functional consequence were expected of the prevalence of shortened separation in sections of the sarcomere and more frequent RyR clusters which were away from the z-line in AF myocytes.

Simulation of 2 CRUs with varying separation as shown in the inset in Figure 6. Two clusters with 25 RyRs was moved 400-700 nm edge-to-edge, with 3 smaller subclusters with 5 RyRs 100 nm apart. To mimic the average number of subclusters observed in AF cells. With this configuration, the probability of propagation between the two CRUs was 100% when 400 nm apart. A sharp transition was observed when the central clusters were moved further than 500 nm apart, and when moved 700 nm apart, no propagation possible.

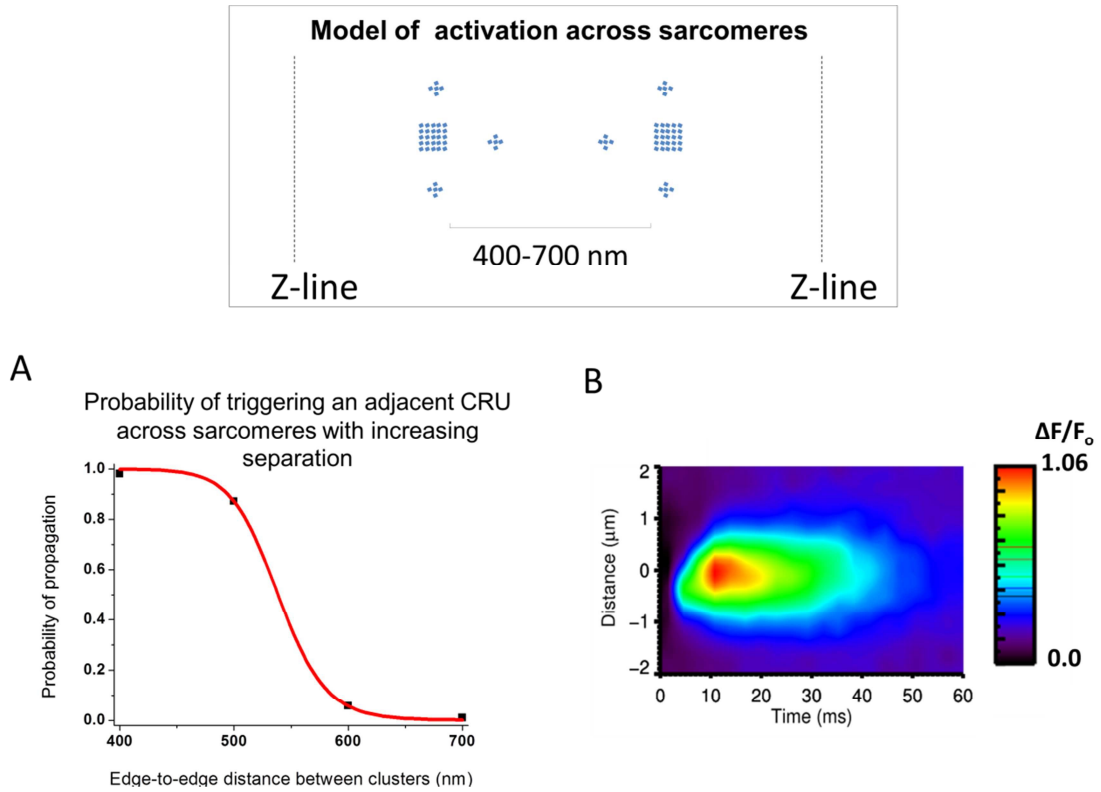


Figure 6. Simulation of neighboring CRU activation during a macrospark. Inset shows schematic of model. 2 CRUs with one central 25 RyR cluster and 3 subclusters with 5 RyR. Edge to edge distance from the large cluster was varied from 400-700 nm. A. The resultant probability of propagation between adjacent clusters, mimicking the effect of altering the longitudinal separation between CRUs and macrospark formation. B. Simulated linescan image of a typical macrospark event. Two CRUs were placed 400 nm apart; The central release site from one site was triggered, releasing Ca^{2+} . This then diffused to raise Ca^{2+} local to the neighboring site triggering its release.

Discussion

In the current study we have quantified RyR clusters and their organization in atrial cells. The computational models developed was used to explain the probability of RyR clusters interaction and was used to quantify a functional Ca^{2+} release units. The STED data from our collaborators show evidence for remodeling of RyR cluster reorganization within the CRUs in persistent AF. We demonstrate the impact of this

nanoscale remodeling on unitary Ca^{2+} signaling in AF, through simulation that support experimental finding. RyR clusters in atrial cells are highly variable in size and have a second order organization into super-clusters that most likely represent functional CRUs.

Previous modeling and experimental data have suggested that small individual RyR clusters could underlie non-spark-mediated loss of Ca^{2+} in the regulation of SR content (Sobie et al., 2006; Williams et al., 2011; Zima, Bovo, Bers, & Blatter, 2010) and that they participate in the initiation of spontaneous Ca^{2+} waves (MacQuaide et al., 2010). The current modeling and experimental data indicate that the presence of more small RyR clusters within CRUs contributes to the generation of Ca^{2+} sparks, leading to the observed increase in Ca^{2+} spark rate in AF compared with Ctrl. Primarily this is due to smaller clusters within the functional group opening (>20x) more often than larger clusters. When these cluster openings synchronize, they can trigger release from clusters close by. In AF, this fragmented CRU geometry is more prevalent, given that the mean number of clusters per CRU increases from 3 to ~3.5. This could explain the increased spark frequency observed. This configuration with more small clusters per CRU may be the reason for repetitive or hyperactive spark sites previously described (H Cheng et al., 1999; Parker & Wier, 1997; Wang et al., 2002). Similarly, sarcomeres with CRUs in close proximity were more common, bridging the sarcomeric separation, allowing propagation. Modeling demonstrated that this bridging of the sarcomere could explain the higher macrospark frequency observed.

Prolonged or slow sparks have been described recently in a murine model of heart failure and were proposed to occur due to more subdivision in each CRU (Louch et al.,

2013). The current study finds structural and functional measurements which agree with the mechanism proposed and highlight its relevance to remodeling in cardiac disease. Dysregulation of Ca^{2+} release, observed as increased spark activity and Ca^{2+} waves has been demonstrated in patients with AF (Hove-Madsen et al., 2004; Neef et al., 2010; Voigt et al., 2012), and altered regulation of the RyR was observed as a major contributing factor in the generation of arrhythmia. Mostly these changes have been attributed to secondary modification of RyR function through CaMKII-dependent phosphorylation, while oxidation or nitrosylation, described in heart failure, may also be present (Neef et al., 2010; Vest et al., 2005). The current study demonstrates that remodeling at the nanoscale level may be an additional factor in the arrhythmogenic behavior observed.

In addition, at elevated pacing rates, the increased open probability due to ultrastructural changes may induce a positive feedback loop of CaMKII activation in the vicinity of increased release activity. Conversely, additional phosphorylation or oxidation processes would sensitize the fragmented clusters to prevailing Ca^{2+} . Since smaller RyR clusters are proposed to be more sensitive to phosphorylation processes (Sobie et al., 2006), it is likely that indeed organization at the nanoscale level and functional modifications will interact in facilitating abnormal Ca^{2+} release in AF.

In AF, remodeling of CRUs is evident as fragmented CRUs, with more clusters in close proximity. This leads to more inter-cluster interaction, which is further potentiated by the reduced Ca^{2+} buffering observed. This process leads to an overactive diastolic Ca^{2+} release with increased chance of propagating events leading to a reduced contractile

reserve and increased likelihood of spontaneously triggered membrane depolarization. Further computer modeling and experimental study is needed to uncover the involvement of this process in the generation of arrhythmias. Similarly, whether this form of remodeling occurs in other pathological hypertrophic models is currently unknown.

The data further indicate that reduced cytosolic buffering would allow more of the released Ca^{2+} to remain free to diffuse, allowing activation of adjacent CRUs. This form of inter-CRU recruitment may play an important role in the recruitment of adjacent sites in physiological Ca^{2+} waves, which occur as part of the E-C coupling process in the atria of larger mammals, with a sparse t-tubule system (Dibb et al., 2009). In persistent AF, this would infer an increase in the effective gain of the Ca^{2+} release system. This effective increase in gain and reduced cellular buffering may partially compensate for the reduced L-type current and reduced t-tubule density observed, but may have detrimental effects by inducing spontaneous Ca^{2+} waves which may generate DADs, especially when NCX activity is increased (Voigt et al., 2012) as is the case here (Lenaerts et al., 2009).

Future modeling could include the structural data described here, in a global model of AF Ca^{2+} handling including the observed increases in NCX activity and reduced number of RyR clusters in the vicinity of sarcolemma, given the reduction in the TATS with AF (Landstrom et al., 2011; Lenaerts et al., 2009).

REFERENCES

- (CDC), C. F. D. C. a. P. (2006).
http://www.cdc.gov/dhdsdp/data_statistics/fact_sheets/fs_atrial_fibrillation.htm
 Retrieved May, 07, 2012
- Anne, W., Willems, R., Holemans, P., Beckers, F., Roskams, T., Lenaerts, I., . . . Heidbuchel, H. (2007). Self-terminating AF depends on electrical remodeling while persistent AF depends on additional structural changes in a rapid atrially paced sheep model. [Research Support, Non-U.S. Gov't]. *J Mol Cell Cardiol*, 43(2), 148-158. doi: 10.1016/j.yjmcc.2007.05.010
- Baddeley, D., Jayasinghe, I. D., Cremer, C., Cannell, M. B., & Soeller, C. (2009). Light-induced dark states of organic fluochromes enable 30 nm resolution imaging in standard media. [Letter
 Research Support, Non-U.S. Gov't]. *Biophys J*, 96(2), L22-24. doi: 10.1016/j.bpj.2008.11.002
- Baddeley, D., Jayasinghe, I. D., Lam, L., Rossberger, S., Cannell, M. B., & Soeller, C. (2009). Optical single-channel resolution imaging of the ryanodine receptor distribution in rat cardiac myocytes. *Proceedings of the National Academy of Sciences of the United States of America*, 106, 22275-22280. doi: 10.1073/pnas.0908971106
- Betzig, E., Patterson, G. H., Sougrat, R., Lindwasser, O. W., Olenych, S., Bonifacino, J. S., . . . Hess, H. F. (2006). Imaging intracellular fluorescent proteins at nanometer resolution. [Research Support, N.I.H., Extramural]. *Science*, 313(5793), 1642-1645. doi: 10.1126/science.1127344
- Cheng, H., & Lederer, W. J. (2008). Calcium sparks. *Physiological reviews*, 88, 1491-1545. doi: 10.1152/physrev.00030.2007
- Cheng, H., Song, L. S., Shirokova, N., González, a., Lakatta, E. G., Ríos, E., & Stern, M. D. (1999). Amplitude distribution of calcium sparks in confocal images: theory and studies with an automatic detection method. *Biophysical journal*, 76, 606-617. doi: 10.1016/S0006-3495(99)77229-2
- Dibb, K. M., Clarke, J. D., Horn, M. A., Richards, M. A., Graham, H. K., Eisner, D. A., & Trafford, A. W. (2009). Characterization of an extensive transverse tubular

- network in sheep atrial myocytes and its depletion in heart failure. [Research Support, Non-U.S. Gov't]. *Circ Heart Fail*, 2(5), 482-489. doi: 10.1161/CIRCHEARTFAILURE.109.852228
- Dobrev, D., Carlsson, L., & Nattel, S. (2012). Novel molecular targets for atrial fibrillation therapy. [Research Support, Non-U.S. Gov't Review]. *Nat Rev Drug Discov*, 11(4), 275-291. doi: 10.1038/nrd3682
- Franzini-Armstrong, C., Protasi, F., & Ramesh, V. (1998). Comparative Ultrastructure of Ca²⁺ release units in skeletal and cardiac muscle. *Annals of the New York Academy of Sciences*, 853, 20-30.
- Franzini-Armstrong, C., Protasi, F., & Ramesh, V. (1999). Shape, size, and distribution of Ca(2+) release units and couplons in skeletal and cardiac muscles. *Biophysical journal*, 77, 55. doi: 10.1016/S0006-3495(99)77000-1
- Groff, J. R., & Smith, G. D. (2008). Ryanodine receptor allosteric coupling and the dynamics of calcium sparks. *Biophysical journal*, 95, 135-154. doi: 10.1529/biophysj.107.119982
- Heidbuchel, H., Verhamme, P., Alings, M., Antz, M., Hacke, W., Oldgren, J., . . . Kirchhof, P. (2013). EHRA practical guide on the use of new oral anticoagulants in patients with non-valvular atrial fibrillation: executive summary. [Practice Guideline Research Support, Non-U.S. Gov't]. *Eur Heart J*, 34(27), 2094-2106. doi: 10.1093/eurheartj/eh134
- Hove-Madsen, L., Llach, A., Bayes-Genís, A., Roura, S., Rodriguez Font, E., Arís, A., & Cinca, J. (2004). Atrial fibrillation is associated with increased spontaneous calcium release from the sarcoplasmic reticulum in human atrial myocytes. *Circulation*, 110, 1358-1363. doi: 10.1161/01.CIR.0000141296.59876.87
- Huang, B., Wang, W., Bates, M., & Zhuang, X. (2008). Three-dimensional super-resolution imaging by stochastic optical reconstruction microscopy. [Research Support, N.I.H., Extramural Research Support, Non-U.S. Gov't]. *Science*, 319(5864), 810-813. doi: 10.1126/science.1153529
- Izu, L. T., Means, S. A., Shadid, J. N., Chen-izu, Y., & Balke, C. W. (2006). Interplay of ryanodine receptor distribution and calcium dynamics. *Biophysical journal*, 91, 95-112. doi: 10.1529/biophysj.105.077214

- Landstrom, A. P., Kellen, C. A., Dixit, S. S., van Oort, R. J., Garbino, A., Weisleder, N., . . . Ackerman, M. J. (2011). Junctophilin-2 expression silencing causes cardiocyte hypertrophy and abnormal intracellular calcium-handling. [Research Support, N.I.H., Extramural Research Support, Non-U.S. Gov't]. *Circ Heart Fail*, 4(2), 214-223. doi: 10.1161/CIRCHEARTFAILURE.110.958694
- Lenaerts, I., Bito, V., Heinzl, F. R., Driesen, R. B., Holemans, P., D'Hooge, J., . . . Willems, R. (2009). Ultrastructural and functional remodeling of the coupling between Ca²⁺ influx and sarcoplasmic reticulum Ca²⁺ release in right atrial myocytes from experimental persistent atrial fibrillation. [Research Support, Non-U.S. Gov't]. *Circ Res*, 105(9), 876-885. doi: 10.1161/CIRCRESAHA.109.206276
- Louch, W. E., Hake, J., Mørk, H. K., Hougen, K., Skrbic, B., Ursu, D., . . . Sejersted, O. M. (2013). Slow Ca²⁺ sparks de-synchronize Ca²⁺ release in failing cardiomyocytes: evidence for altered configuration of Ca²⁺ release units? *Journal of molecular and cellular cardiology*, 58, 41-52. doi: 10.1016/j.yjmcc.2013.01.014
- Loughrey, C. M., MacEachern, K. E., Cooper, J., & Smith, G. L. (2003). Measurement of the dissociation constant of Fluo-3 for Ca²⁺ in isolated rabbit cardiomyocytes using Ca²⁺ wave characteristics. *Cell Calcium*, 34, 1-9. doi: 10.1016/S0143-4160(03)00012-5
- Mackenzie, J. (1914). *Diseases of the Heart* (3rd ed.). London, UK: Oxford Medical Publications.
- MacQuaide, N., Ramay, H. R., Sobie, E. A., & Smith, G. L. (2010). Differential sensitivity of Ca(2)+ wave and Ca(2)+ spark events to ruthenium red in isolated permeabilised rabbit cardiomyocytes. [Research Support, N.I.H., Extramural Research Support, Non-U.S. Gov't]. *J Physiol*, 588(Pt 23), 4731-4742. doi: 10.1113/jphysiol.2010.193375
- Neef, S., Dybkova, N., Sossalla, S., Ort, K. R., Fluschnik, N., Neumann, K., . . . Maier, L. S. (2010). CaMKII-dependent diastolic SR Ca²⁺ leak and elevated diastolic Ca²⁺ levels in right atrial myocardium of patients with atrial fibrillation. [Research Support, Non-U.S. Gov't]. *Circ Res*, 106(6), 1134-1144. doi: 10.1161/CIRCRESAHA.109.203836
- Ohkusa, T., Ueyama, T., Yamada, J., Yano, M., Fujumura, Y., Esato, K., & Matsuzaki, M. (1999). Alterations in cardiac sarcoplasmic reticulum Ca²⁺ regulatory proteins in the atrial tissue of patients with chronic atrial fibrillation. *Journal of the American College of Cardiology*, 34, 255-263.

- Parker, I., & Wier, W. G. (1997). Variability in frequency and characteristics of Ca^{2+} sparks at different release sites in rat ventricular myocytes. [In Vitro Research Support, U.S. Gov't, P.H.S.]. *J Physiol*, 505 (Pt 2), 337-344.
- Sobie, E. a., Guatimosim, S., Gómez-Viquez, L., Song, L.-S., Hartmann, H., Saleet Jafri, M., & Lederer, W. J. (2006). The Ca^{2+} leak paradox and rogue ryanodine receptors: SR Ca^{2+} efflux theory and practice. *Progress in biophysics and molecular biology*, 90, 172-185. doi: 10.1016/j.pbiomolbio.2005.06.010
- Tran, K., Smith, N. P., Loiselle, D. S., & Crampin, E. J. (2009). A Thermodynamic Model of the Cardiac Sarcoplasmic/ Endoplasmic Ca^{2+} (SERCA) Pump. *Biophysical journal*, 96, 2029-2042. doi: 10.1016/j.bpj.2008.11.045
- Troughton, R. W., & Crozier, I. (2013). Fine Tuning Risk Stratification for Atrial Fibrillation. *Journal of the American College of Cardiology*. doi: 10.1016/j.jacc.2013.02.066
- Vest, J. A., Wehrens, X. H., Reiken, S. R., Lehnart, S. E., Dobrev, D., Chandra, P., . . . Marks, A. R. (2005). Defective cardiac ryanodine receptor regulation during atrial fibrillation. [Research Support, Non-U.S. Gov't Research Support, U.S. Gov't, P.H.S.]. *Circulation*, 111(16), 2025-2032. doi: 10.1161/01.CIR.0000162461.67140.4C
- Voigt, N., Li, N., Wang, Q., Wang, W., Trafford, A. W., Abu-Taha, I., . . . Dobrev, D. (2012). Enhanced sarcoplasmic reticulum Ca^{2+} leak and increased Na^{+} - Ca^{2+} exchanger function underlie delayed afterdepolarizations in patients with chronic atrial fibrillation. [Research Support, N.I.H., Extramural Research Support, Non-U.S. Gov't]. *Circulation*, 125(17), 2059-2070. doi: 10.1161/CIRCULATIONAHA.111.067306
- Wagner, E., Lauterbach, M. a., Kohl, T., Westphal, V., Williams, G. S. B., Steinbrecher, J. H., . . . Lehnart, S. E. (2012). Stimulated emission depletion live-cell super-resolution imaging shows proliferative remodeling of T-tubule membrane structures after myocardial infarction. *Circulation research*, 111, 402-414. doi: 10.1161/CIRCRESAHA.112.274530
- Wakili, R., Voigt, N., Kaab, S., Dobrev, D., & Nattel, S. (2011). Recent advances in the molecular pathophysiology of atrial fibrillation. [Research Support, Non-U.S. Gov't Review]. *J Clin Invest*, 121(8), 2955-2968. doi: 10.1172/JCI46315

- Wang, S. Q., Song, L. S., Xu, L., Meissner, G., Lakatta, E. G., Rios, E., . . . Cheng, H. (2002). Thermodynamically irreversible gating of ryanodine receptors in situ revealed by stereotyped duration of release in Ca(2+) sparks. *Biophys J*, 83(1), 242-251. doi: 10.1016/S0006-3495(02)75165-5
- Willems, R., Sipido, K. R., Holemans, P., Ector, H., Van de Werf, F., & Heidbuchel, H. (2001). Different patterns of angiotensin II and atrial natriuretic peptide secretion in a sheep model of atrial fibrillation. [Research Support, Non-U.S. Gov't]. *J Cardiovasc Electrophysiol*, 12(12), 1387-1392.
- Williams, G. S. B., Chikando, A. C., Tuan, H.-T. M., Sobie, E. a., Lederer, W. J., & Jafri, M. S. (2011). Dynamics of Calcium Sparks and Calcium Leak in the Heart. *Biophysical journal*, 101, 1287-1296. doi: 10.1016/j.bpj.2011.07.021
- Zhao, Z. H., Zhang, H. C., Xu, Y., Zhang, P., Li, X. B., Liu, Y. S., & Guo, J. H. (2007). Inositol-1,4,5-trisphosphate and ryanodine-dependent Ca²⁺ signaling in a chronic dog model of atrial fibrillation. [Research Support, Non-U.S. Gov't]. *Cardiology*, 107(4), 269-276. doi: 10.1159/000095517
- Zima, A. V., Bovo, E., Bers, D. M., & Blatter, L. A. (2010). Ca(2)+ spark-dependent and -independent sarcoplasmic reticulum Ca(2)+ leak in normal and failing rabbit ventricular myocytes. [Research Support, Non-U.S. Gov't]. *J Physiol*, 588(Pt 23), 4743-4757. doi: 10.1113/jphysiol.2010.197913

CHAPTER 5: TEMPORO-SPATIAL MODEL OF CARDIAC CELLS TO STUDY Ca^{2+} WAVES INDUCED BY SR Ca^{2+} OVERLOAD

Abstract

Calcium plays a central role in the excitation and contraction of cardiac myocytes. Experiments have indicated that calcium release is stochastic and regulated locally suggesting the possibility of spatially heterogeneous calcium levels in the cells. This spatial heterogeneity might be important mediating different signalling pathways. During more than 50 years of computational cell biology, the computational models have been advanced to incorporate more ionic currents, going from deterministic models to stochastic models. However, the study of the spatial role of calcium ions has been limited due to the computational expense of using a three-dimensional stochastic computational model. In this chapter, we introduce the first three-dimensional stochastic computational model for rat ventricular myocyte at the whole-cell level that incorporate detailed calcium dynamics, with (1) non-uniform release site placement, (2) non-uniform membrane ionic currents and membrane buffers, (3) stochastic calcium-leak dynamics. The model will be used to study spark-induced spark and spark-induced Ca^{2+} wave under calcium overload at the closed-cell condition. This is considered important as Ca^{2+} waves are regarded as arrhythmogenic substrates.

Introduction

Cytoplasmic calcium waves were first observed in medaka eggs when activated by sperms using light-emitting protein aequorin with the speed of about $10\text{-}30\text{ }\mu\text{m}^2/\text{s}$ at 20°C (Ridgway, Gilkey et al. 1977). Other experiments discovered that increasing certain hormones can induce frequent, periodic calcium oscillations in isolated hepatocytes, which brings calcium resting level 200 nM to about $600\text{ nM} - 1\text{ }\mu\text{M}$ with oscillation period varying from a few seconds to a few minutes depending upon the agonist concentration (Woods, Cuthbertson et al. 1986; Woods, Cuthbertson et al. 1987). It was later confirmed that inositol-1,4,5-triphosphate (IP3R) plays the important role as inducing calcium release (Berridge 1993; Ramos-Franco, Fill et al. 1998).

Ca^{2+} waves in cardiac myocytes has not been observed under physiological condition, but during diastole if the cell is overloaded with calcium (Orchard, Eisner et al. 1983; Wier, Cannell et al. 1987; Wier and Blatter 1991). In cardiac cells, calcium is released in the form of calcium sparks at discrete microdomains known as calcium release sites of size $\sim 300\text{ nm}$ in width and $\sim 12\text{ nm}$ in height (Cheng, Lederer et al. 1993). The large size of the cardiac cell ($\sim 120\text{ }\mu\text{m}$ in length, $\sim 20\text{ }\mu\text{m}$ in width and $\sim 15\text{ }\mu\text{m}$ in depth) allow calcium signals to propagate as Ca^{2+} waves. The link between calcium sparks and calcium waves have been documented before and has been implicated in the origin of cardiac arrhythmias (Cheng, Lederer et al. 1996; Wier, ter Keurs et al. 1997; Lukyanenko and Gyorke 1999). During Ca^{2+} alternans, a wave-like Ca^{2+} release were observed during systole in ventricular myocytes by triggering the cells with a small stimulus (Diaz, Eisner et al. 2002; Diaz, O'Neill et al. 2004). However, the mechanism and conditions under which calcium sparks can form a propagating calcium wave is still under investigation. The relation between Ca^{2+} sparks and Ca^{2+} waves is complicated by the cell

structure, asymmetric spatial distribution of RyR clusters, anisotropic diffusion of Ca^{2+} , Ca^{2+} sensitivity of CRUs, etc.

The nature and properties of calcium sparks have been intriguing problems in the field for more than twenty-four years (Cheng, Lederer et al. 1993; Shen, Wang et al. 2004; Wang, Stern et al. 2004; Niggli and Shirokova 2007; Cheng and Lederer 2008). Among them, there is a major unresolved problem between the Full Width at Half-Maximal concentration (FWHM) of experimentally recorded Ca^{2+} sparks (which is about 1.8-2.2 μm) and pseudo-line scan generated Ca^{2+} spark from computational modelling (which is about 1.1-1.6 μm) (Pratusevich and Balke 1996; Smith, Keizer et al. 1998; Izu, Mauban et al. 2001; Sobie, Dilly et al. 2002; Koh, Srinivasan et al. 2006; Hake, Edwards et al. 2012; Laver, Kong et al. 2013). Izu and co-workers developed a 3D model with spherical geometry using FASCIMILE (AEA Technologies, Harwell, UK) for studying Ca^{2+} sparks. In their model, in order to reproduce FWHM $\sim 2 \mu\text{m}$, they created a supercluster with 4 CRUs at 0.4 μm apart and a very large release of Ca^{2+} was assumed, i.e. from 2 pA to 5-10 pA for each CRU (Izu, Mauban et al. 2001). A recent 3D model developed using FASCIMILE by Kong and co-workers can only produce FWHM of 1.2 μm (Kong, Laver et al. 2013).

Even though Ca^{2+} wave has not been observed under the physiological condition, the occurrence of Ca^{2+} wave under SR Ca^{2+} overload condition underlie arrhythmias. The mechanism and condition leading to Ca^{2+} wave are still unclear. Early deterministic or stochastic models assumed very high Ca^{2+} sensitivity threshold for Ca^{2+} release in order to see Ca^{2+} wave, e.g. 1.2 μM (Backx, de Tombe et al. 1989) or $K_{\text{Ca}} < 1.5 \mu\text{M}$ (Keizer and Smith 1998; Keizer, Smith et al. 1998). Using a more realistic Ca^{2+} sensitivity ($K_{\text{Ca}} = 15 \mu\text{M}$), Izu and co-workers estimated $P_{\text{o,trigger}}$ depending on the distance d and the rate and total mass of the source Ca^{2+}

release, though the CRU model requires large Ca^{2+} release (Izu, Wier et al. 2001). Using a more realistic model of CRU, Ramay and co-workers created a 3D model to study Ca^{2+} wave, with a T-tubule of 200 μm as a diffusion barrier (Ramay, Jafri et al. 2010). They found that local increase in $[\text{Ca}^{2+}]_{\text{SR}}$, if occurs, is not the result of Ca^{2+} diffusion in the SR but the diffusion of Ca^{2+} from the cytosol that are uptaken by the SERCA at the next release site. Thus, the sensitization of RyR can only occur with the diffusion of SR Ca^{2+} is very slow.

In 2010, a 2D model to study spark-induced spark was created by Rovetti and co-workers (Rovetti, Cui et al. 2010). The model didn't look into the condition leading Ca^{2+} wave. In addition, their model wasn't able to produce a proper spark model, i.e. the peak $[\text{Ca}^{2+}]_i < 10 \mu\text{M}$, while an estimated level should be around 100 μM (Cheng, Lederer et al. 1993). A recently developed 3D model for the rabbit ventricular myocyte by Nivala and co-workers (Nivala, de Lange et al. 2012) extended the previous model by Rovetti *et al.* to 3D with 100x20x10 CRUs. In their model, they assumed (1) fast buffering, (2) the transmembrane voltage sense the calcium everywhere, (3) underestimate the role of SERCA pump by using the simple Hill equation, (4) no flux into the subspace calcium and the calcium in the dyadic subspace at equilibrium state all the time, (5) assuming Ca^{2+} -dependent inactivation, which make the model cannot reproduce Ca^{2+} spark. The current model overcomes all of these drawbacks.

For atrial cells, due to the lack of the transverse T-tubule system, the physiological activation of the contraction process requires the propagation of Ca^{2+} in the form of Ca^{2+} waves from the sarcolemma to the interior of the cell (Berlin 1995; Kockskamper, Sheehan et al. 2001). Thul and co-workers developed a 3D model in which the stochastic nature of Ca^{2+} release was simply modelled using a threshold model in which a random variable is generated to determine whether Ca^{2+} is released or not (Thul, Coombes et al. 2012).

At whole-cell level, Shiferaw and colleagues (Shiferaw and Karma 2006) split the cells into subregions that each represented an individual sarcomere and combined them into 1D chain of these identical subregions to approximate the myocyte. Li and co-workers (Li, Lancaster et al. 2007) developed the first detailed model by describing the cell as a cylinder with space step 200 nm, with cell volume 20.1 pL and modelling the release of calcium as a point source. Thus, they were unable to investigate the stochastic nature of calcium release which is important to the triggering of calcium waves (Soeller, Jayasinghe et al. 2009).

In Section I, we introduce the 3D spatiotemporal model of the rat ventricular myocyte. Section II focuses on the computational methodology that we used in model development. The major contribution of this chapter is two-fold: it investigates the probabilities and conditions for spark-induced spark to occur, and the probabilities and conditions for spark-induced wave to occur.

Model development

Due to the high computational demands, efforts to model spatial effect of Ca^{2+} have been limited to a few CRUs (Ramay, Jafri et al. 2010) or in 1D (Backx, de Tombe et al. 1989), in 2D (Lipp and Niggli 1993), or in 3D with a coarser resolution (Restrepo, Weiss et al. 2008; Restrepo and Karma 2009; Nivala, de Lange et al. 2012). In the realm of 3D modelling, several factors have been missed such as the spatial distribution of CRUs, the balancing of leak/load at a physiological range, the complicated structure of T-tubule network.

In our study, the detailed 3D model of the rat is developed that takes into accounts detailed structures of calcium release sites and physiological parameters based on current experimental data. The rat ventricular myocyte is modeled as a rectangular solid with the dimension $120 \times 20.8 \times 10 \mu\text{m}^3$ so that the total cell volume is 24.96(pL) which falls into the

experimentally observed range (Satoh, Delbridge et al. 1996; Delbridge, Satoh et al. 1997), and is consistent to the cell volume with 20,000 CRUs (Cheng, Lederer et al. 1993). To capture the local effect of calcium release, the rectangular cell is divided into grid points of size $0.2 \times 0.2 \times 0.2 \mu\text{m}^3$, Figure 1 which yields a total of 3,120,000 grid points.

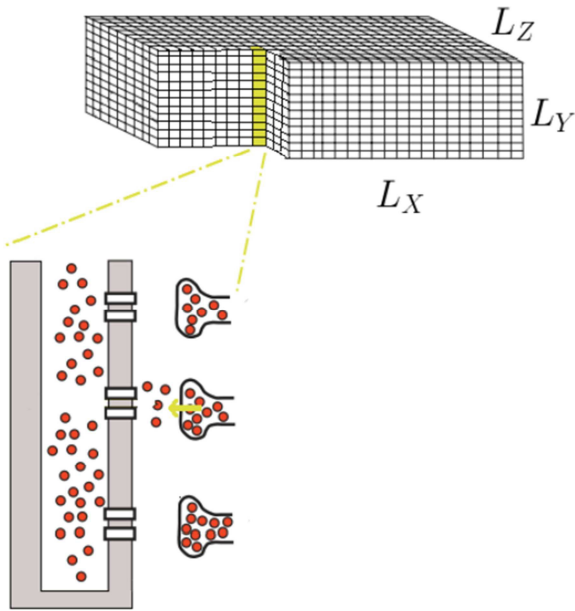


Figure 1. A schematic diagram of ventricular myocyte modeled as a hypercube

The traditional electrophysiological approach of using total membrane capacitance to estimate the surface area and as an indirect index of cell volume is considered not accurate due to the variation in degree of membrane folding. Even though there are differences in cell volumes and the capacitance-volume ratios between species, data derived from optical cell sections obtained with laser scanning confocal microscopy (LSCM) showed a surprisingly constant membrane capacitance-to-cell volume ratio for each species across a wide range of cell volume using Sprague-Dawley rats (with volumes ranging from 23 *pL* to 63 *pL*) (Delbridge, Satoh et al.

1997). In rats, the capacitance-volume ratio is quite high 8.42 pF/pL ; even though the value is age-dependent (with about 6.76 pF/pL in 3-month-old rat, and 8.88 pF/pL in 6-month-old rat). A similar number (8.43 pF/pL) was measured in Wistar rat (with cell volume 23.6 pL and capacitance 200 pF) (Swift, Stromme et al. 2006). This is much underestimated by other rat models, i.e. 6.25 pF/pL (Pandit, Clark et al. 2001; Padmala and Demir 2003).

Sarcolemma(SL) and T-tubule membrane

Given the specific capacitance of cell membrane is fairly constant among different cell types and species, $C_{sc} \approx 1 \mu\text{F} / \text{cm}^2$, the total membrane surface area was given as $A_m = 2.00 \times 10^{-4} \text{ cm}^2$ and the equivalent whole-cell membrane capacitance in the model is 200 pF . The sarcolemmal membrane includes the surface membrane and the membrane in the T-tubular system. Depending on the cell types, the thickness of the plasma membrane of a single cell is typically in the range a few to tens of nanometer (Andersen and Koeppe 2007); thus it can be easily fit into a single grid point of the size used in the model. If we assume that the surface membrane at each grid point is 1.12-times the area for one side of the grid point, and using the total sarcolemma area above, it requires 445,000 grid points. The total number of grid points for the external surface membrane takes only 195,200 grid points, which means than more than half of the membrane (i.e. 56%) belongs to the T-tubular system.

The fraction of total surface membrane area that forms the T-tubules has been known to be species-dependent (Bers 2001). In rat, early measurement showed that it's about 33% (Page 1978; Stewart and Page 1978) in which about 20-50% of the T-tubular membrane is part of the junctional complex with the junctional-SR (Page and Surdyk-droske 1979). Measurements of cell capacitance following formamide-induced detubulation using electron microscopy suggest a similar value (32%) (Kawai, Hussain et al. 1999). However, recent data using optical

measurements showed that the fraction of folded membrane forming the T-tubular system is much higher (about 65%) in rat (Soeller and Cannell 1999; Brette and Orchard 2003). Based on the development-stage dependent volume-ratio data by (Satoh, Delbridge et al. 1996), the T-tubule fractions would be in the range 50% to 65% (Pasek, Brette et al. 2008). Thus, the value of 56% in the model is in the range. The discrepancy between the capacitance reduction and detubulation measurement can be explained by incomplete detubulation, structural distortions during the preparation of tissue for electron microscopy and even the smaller specific capacitance ($0.56 \mu F/cm^2$) in the T-tubule due to high cholesterol level as suggested by (Pasek, Brette et al. 2008).

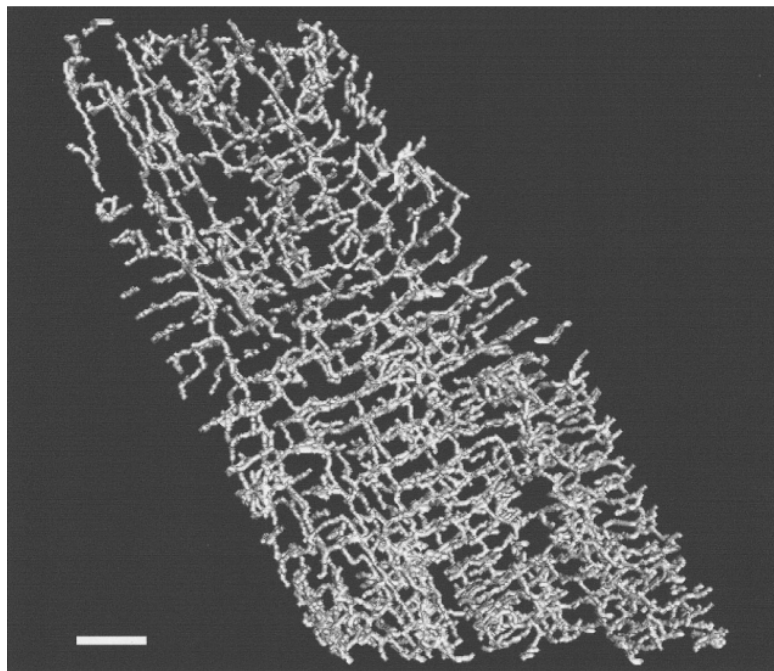


Figure 2. Three-dimensional skeleton of the TATS system in rat ventricular myocytes reconstructed from fluorescence micrograph [from (Soeller and Cannell 1999)]

In addition, the recent data showed that even though the T-tubules leave the surface membrane at the Z-lines, only about 60% of the tubular volume occurs near the Z-line, Figure 2. Using our model, the number of grid points along the Z-line contains the T-tubule is ~151,000, which means the number of longitudinal grid points forming the branching T-tubules is ~101,000 (or 40.6%). This is closed to the value (40%) estimated experimentally in rat (Soeller and Cannell 1999; Brette and Orchard 2003). Due to the fact that the membrane folds not only in transverse direction but also axial direction, we call it transverse-axial tubular system (TATS or T-Ax) as suggested by (Forbes, Hawkey et al. 1984) or sarcolemmal Z rete (ZRE) (Soeller and Cannell 1999). The TATs is also referred to as the sarcolemmal tubule network (Bers 2001). There are several studies suggesting that disruption or loss of the TATS is linked to several cardiac diseases, and that the understanding the connection between them is crucial to drug development (Heinzel, Bito et al. 2008; Lyon, MacLeod et al. 2009; Wei, Guo et al. 2010; Wagner, Lauterbach et al. 2012; Guo, Zhang et al. 2013; Polakova and Sobie 2013). This emphasizes the importance of developing a spatiotemporal model for the ventricular myocyte that incorporates the detailed structure of the TATS to improve our understanding of its function.

In summary, the external sarcolemmal membrane spans the 6 surfaces of the rectangular solid. The TATS is composed of two parts. The T-tubular part is assumed to span along the y-axis of the cell, co-localizing at the calcium release site placements, Figure 2. The longitudinal part of the TATS is added to the network forming 40.6% of the membrane folding.

Calcium release site

Similar to Chapter 3, the dynamics of calcium and calcium-calmodulin (CaCalm) complex at each release site is given by the equations

$$\begin{aligned} \frac{d[\text{Ca}]_{ds}^{(i)}}{dt} &= \frac{(J_{\text{ryr}}^{(i)} - J_{\text{efflux}}^{(i)} + J_{\text{dhprr}}^{(i)})}{\lambda_{ds}} - 2 \frac{d[\text{CaCalm}]^{(i)}}{dt} - \frac{d[\text{CaSL}]^{(i)}}{dt} - \frac{d[\text{CaSR}]^{(i)}}{dt} \\ \frac{d[\text{CaCalm}]^{(i)}}{dt} &= k_{\text{Calm}}^+ ([\text{Ca}]_{ds}^{(i)})^2 ([\text{Calm}]_T - [\text{CaCalm}]_{ds}^{(i)}) - k_{\text{Calm}}^- [\text{CaCalm}]_{ds}^{(i)} \\ \frac{d[\text{CaSL}]^{(i)}}{dt} &= k_{\text{SL}}^+ ([\text{Ca}]_{ds}^{(i)}) ([\text{SL}]_T - [\text{CaSL}]_{ds}^{(i)}) - k_{\text{SL}}^- [\text{CaSL}]_{ds}^{(i)} \\ \frac{d[\text{CaSR}]^{(i)}}{dt} &= k_{\text{SR}}^+ ([\text{Ca}]_{ds}^{(i)}) ([\text{SR}]_T - [\text{CaSR}]_{ds}^{(i)}) - k_{\text{SR}}^- [\text{CaSR}]_{ds}^{(i)} \end{aligned}$$

where i represents the index of the calcium release sites ($i=1..20000$). J_{ryr} is the flux of calcium release via RyR2 channels. J_{efflux} is the flux of calcium from the dyadic subspace (ds) into the cytosol. In order to take into account the volume different between the cellular compartment, the volume ratio $\lambda_{ds} = V_{ds} / V_{\text{myo}}$ was incorporated into the fluxes.

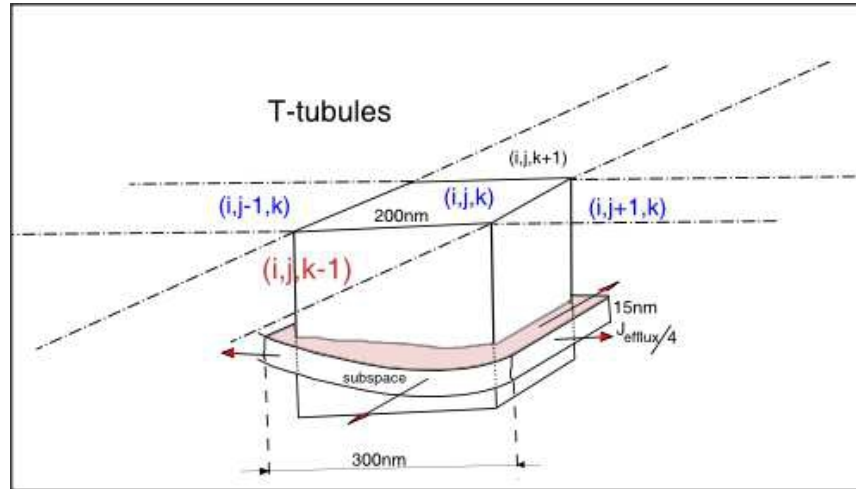


Figure 3. The schematic diagram of a single dyad spreading into multiple grid points

Spatial placement of CRUs

For L-type calcium channels, detubulation reduces the calcium current (I_{Ca}) current by 87%, suggesting a smaller fraction on the surface membrane (Kawai, Hussain et al. 1999). This was incorporated in the model by using 13% of CRU on the surface membrane. There are two strategies for placing CRUs: (1) uniformly along each dimension at a given distance, or (2)

nonuniformly based on the given distribution of nearest distance along the T-tubule. The first case, a typical assumption is $1.8\ \mu\text{m}$ along x and $0.8\ \mu\text{m}$ along the transversal direction. In the second case, an algorithm was developed to place CRUs based on the distribution between adjacent CRUs along each T-tubule measured previously, Figure 4 (Chen-izu, Mcculle et al. 2006). An example of the generated CRU locations on a given depth value is shown in Figure 5.

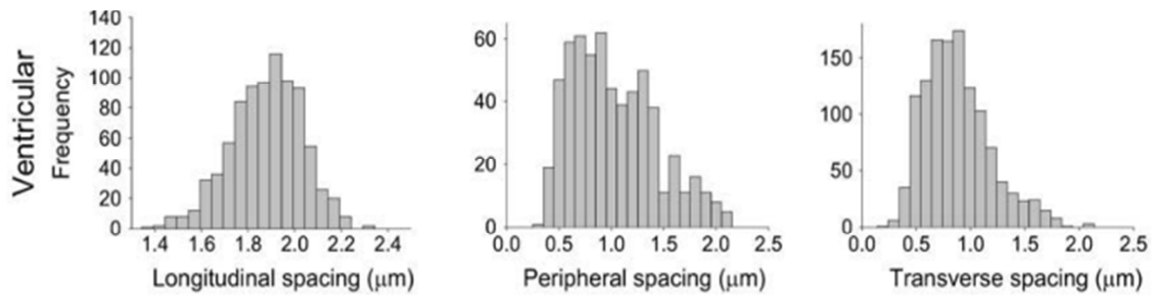


Figure 4. Distribution of nearest neighbor distance of CRUs along different directions

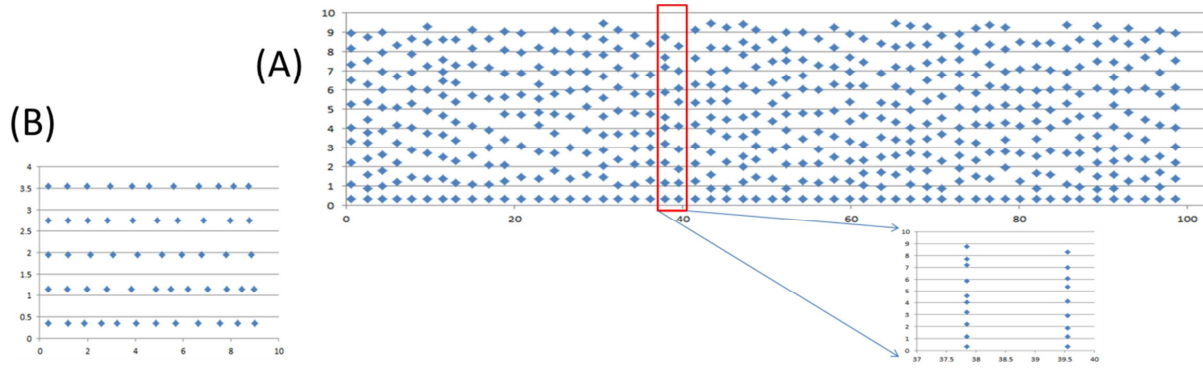


Figure 5. The placement of calcium release sites (A) at one z-depth, (B) at one Z-disc. The inset in (A) shows the CRUs on two T-tubule at two adjacent Z-discs. The distribution of inter-CRU distance is derived based on the experimental data.

Spatial placement of $\text{Na}^+/\text{Ca}^{2+}$ exchangers, SERCA pump, SR and SL buffers

$\text{Na}^+/\text{Ca}^{2+}$ exchanger (NCX) is the major route for Ca^{2+} extrusion. The distribution of NCX was unclear, measured with immunofluorescence and/or immunoelectron microscopy, with both even distribution between external membrane surface and the T-tubules in rat and guinea pig (Kieval, Bloch et al. 1992) and higher distribution in the T-tubular system in guinea pig (Frank, Mottino et al. 1992). In another study for rat ventricular myocyte, NCX distributed largely in the T-tubule yet NCX has not been observed in the dyad (Scriven, Dan et al. 2000). In a more recent study, by measuring the rise in extracellular calcium, (Yang, Pascarel et al. 2002) showed that the detubulated cell has a smaller rise which suggested a higher distribution of NCX in T-tubules in rat, yet they could not quantify the change. Using formamide-induced detubulation, (Despa, Brette et al. 2003) estimated NCX to be 3-3.5-fold more concentrated in the T-tubules. However, in these studies, the decrease in cell surface area in detubulated cells is in the range 25%-32%. Therefore, we focus on modelling NCX with 3x higher in the T-tubules than in the external sarcolemma.

The transport of Ca^{2+} from the cytosol of the cardiomyocyte to the lumen of the sarcoplasmic reticulum (SR) is the major mechanism of removing Ca^{2+} , therefore, it plays a major role in contraction-relaxation cycle of the myocardium. There are different isoforms of SERCA pump that have been found in cardiac myocytes; with some are species-specific. In rat cardiac myocytes, SERCA2a is the major cardiac isoform; while the level of SERCA2b is small. In mice, unlike SERCA2b which has a preferential localization around the T-tubules, SERCA2a is distributed transversely and longitudinally in the SR membrane (Greene, Lalli et al. 2000; Periasamy and Huke 2001). Using immunostaining of rat ventricular myocyte with anti-SERCA2a primary antibody, it shows a uniform striated patterns where the brightest regions on the image are the Z-lines of the sarcomeres, Figure 6. (Smith, Keizer et al. 1998) modelled this

using a hypothetical function that has a bell-shaped with the peak at the Z-line. (Drago, Colyer et al. 1998) also found the presence of SERCA2a in the perinuclear region of the cardiac cell, yet the signal is weaker than that in the Z-lines. It's also noted that phospholamban (PLB) interact directly with SERCA2a to inhibit the uptake of Ca^{2+} back to the SR. Phosphorylation of PLB, which relieves the inhibition of PLB on SERCA2a, can occur at two sites: Ser16 (PLB-16P) and Thr17 (PLB-17P), via cAMP-dependent kinases (PKA) and Ca^{2+} /Calm-dependent kinase (CaMKII). Thus, the subcellular distribution of PLB-16P and PLB-17P can be of functional significance. (Drago, Colyer et al. 1998) found that PLB-16B has a higher density at the Z-lines and perinuclear region; while PLB-17 is stronger at the Z-lines, in the intercalated disk region, and also the external surface membrane. In essence, PLB-17 is found mainly in the region of important to the EC-coupling. However, here we only focus on SERCA2a. The role of PLB will be a part of future studies.

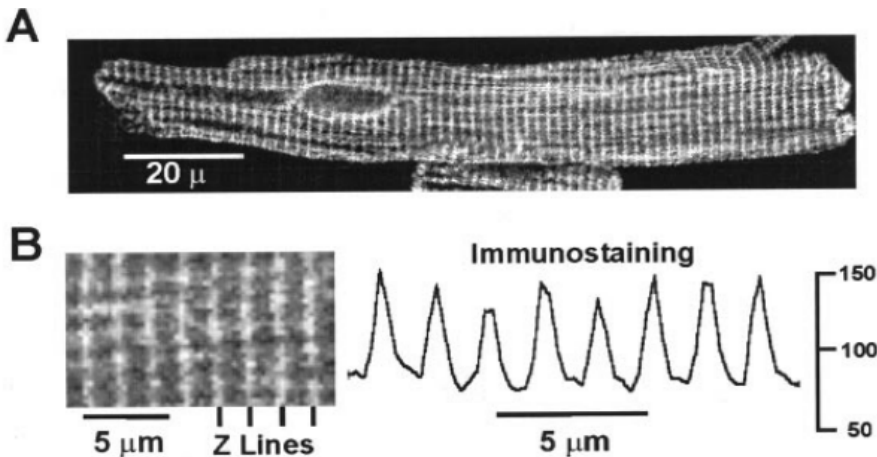


Figure 6. (A) A single rat ventricular myocyte stained with anti-SERCA2a primary antibody, (B) enlarged view of eight sarcomere in panel A, and the plot of immunofluorescence distribution (adapted from (Smith, Keizer et al. 1998))

In addition to calmodulin and Troponin, SR and SL also play an important role as Ca^{2+} buffers. The membranes near the Z-line have a greater Ca^{2+} buffering capacity than those close to the M-line (Hake, Edwards et al. 2012). Thus, in our model, 90% of the SR and SL buffers are assumed near the Z-line.

Diffusion of ions

The diffusion of Ca^{2+} in aqueous solution of physiological ionic strength was estimated about 700-800 $\mu\text{m}^2/\text{s}$ (Wang 1953). Kushmerick and Podolsky estimated the diffusion coefficient in muscle is 50x slower than in aqueous solution, i.e. $D_{\text{Cafree}} = 14 \mu\text{m}^2/\text{s}$ (Kushmerick and Podolsky 1969). However, recent data suggested the diffusion in cytosol of free (unbuffered) Ca^{2+} is only 2-2.5x (Smith, Keizer et al. 1998), with the value 400 $\mu\text{m}^2/\text{s}$ in smooth muscle cells (Kargacin and Fay 1991) and 223 $\mu\text{m}^2/\text{s}$ from *Xenopus laevis* oocytes (Allbritton, Meyer et al. 1992). Other studies used $D_{\text{Cafree}} = 300 \mu\text{m}^2/\text{s}$ (Ramay, Jafri et al. 2010; Nivala, de Lange et al. 2012; Kong, Laver et al. 2013). The diffusion constant $D_{\text{Cafree}} = 270 \mu\text{m}^2/\text{s}$ being used in the model is in the range.

Using FRAP (fluorescence recovery after bleach) of intra-SR Ca^{2+} indicator Fluo-5N, Wu and Bers estimated the diffusion of Ca^{2+} in the SR of rabbit cardiac myocyte about 60 $\mu\text{m}^2/\text{s}$ (Wu and Bers 2006). However, another study estimated a much smaller value 8-9 $\mu\text{m}^2/\text{s}$ in rat and guinea pig myocytes (Swietach, Spitzer et al. 2008). Swietach and co-workers suggested that the slow diffusion for Ca^{2+} in the SR helps to explain the long recovery time for $[\text{Ca}^{2+}]_{\text{SR}}$ within 100-200 ms. Also, the authors suggested that the high value measured by Wu and Bers didn't consider the SR Ca^{2+} leak during measurement. A recent study by Picht and co-workers that supported the previous result in Bers' group and rejected that claim (Picht, Zima et al. 2011). A study by Sobie and Lederer supported the results of Bers' group in that their simulation data can

reproduce simulation results with $D_{\text{Casr}} = 60 \mu\text{m}^2/\text{s}$, rather than with $D_{\text{Casr}} = 20 \mu\text{m}^2/\text{s}$ (Sobie and Lederer 2012). To explain the slow recovery during Ca^{2+} sparks, e.g. 161 ms by (Zima, Picht et al. 2008), given the fast diffusion of Ca^{2+} in the SR, one possible hypothesis is that the duration of SR Ca^{2+} release, time-to-blink nadir, is longer than time-to-spark peak (Brochet, Yang et al. 2005; Sobie and Lederer 2012). The authors suggested some irregularities in the structure of the RyR cluster, e.g. involving rogue RyRs.

Another factor for the long recovery time that we suggests is not only the sharp depletion of $[\text{Ca}^{2+}]$ in the jSR compared to the network SR, but also the partial depletion of $[\text{Ca}^{2+}]$ in the neighboring nSR grid points. The released Ca^{2+} includes not only the free calcium but also the calcium that bind to CSQ. The amount of Ca^{2+} bind to CSQ in cardiac muscle was estimated about 50% (Bers 2001); though this value is likely to vary with species and experimental conditions. Terentyev and co-workers applied an acute, 3-fold reduction in CSQ2 in quiescent rat and found about 2-fold decrease in SR Ca^{2+} ; without change in free intra-SR $[\text{Ca}^{2+}]$, which suggested 70% of Ca^{2+} was bound to CSQ2 (Terentyev, Viatchenko-Karpinski et al. 2003; Kubalova, Gyorke et al. 2004). Given the depletion of $[\text{Ca}^{2+}]_{\text{jSR}}$ from 1000 μM to $\sim 100 \mu\text{M}$ during a Ca^{2+} spark as suggested by a previous version of our current model (Sobie, Dilly et al. 2002) and a recent study (Hake, Edwards et al. 2012), and the binding constant between CSQ and Ca^{2+} is about 400 μM , a significant amount of Ca^{2+} unbinding from CSQ is released. In addition, we also observe a significant Ca^{2+} reduction in the neighboring nSR ($\sim 500 \mu\text{M}$). Thus, the recovery time for $[\text{Ca}^{2+}]_{\text{jSR}}$ should be long enough to provide an enough amount of Ca^{2+} to refill the free $[\text{Ca}^{2+}]_{\text{jSR}}$, to neighboring nSR, including Ca^{2+} to bind to [CSQ]. This, not including the possible rate-limiting effect between the jSR and nSR due to geometrical structure, can be

used to explain the long recovery time, given the diffusion constant of $[Ca^{2+}]_{SR}$ at $60 \mu m^2/s$.

Thus, in the model, we choose $D_{Casr} = 60 \mu m^2/s$.

The diffusion of Fluo-3 as $90 \mu m^2/s$ was used. This is in agreement with latest measurement (Michailova, DelPrincipe et al. 2002) that is almost 5-fold larger than what has been measured earlier in skeletal muscle (Harkins, Kurebayashi et al. 1993). The role of ATP mobility and its serving as a Ca^{2+} buffer has not been considered in the model (Baylor and Hollingworth 1998). Based on molecular weight, calmodulin (Calm) is expected to diffuse with about an order of magnitude lower than that of calcium. Even though other studies have modelled it as a mobile buffer with a small diffusion constant: $20-40 \mu m^2/s$, calmodulin is modelled as a stationary buffer in our model.

Model formulation in spatial cell

At each grid point, the model contains the concentrations of the chemical species in the myoplasm, and in the network SR. Each grid point contains a myoplasmic fraction and SR fraction. In the myoplasmic volume part of a grid point, the chemical species are calcium, calcium bound to fluorescent indicator dye and other calcium-bound buffers. Depending upon the location of the grid point, ie if it resides at the external SL or the T-tubule, there can be other species, e.g. SL buffer. Due to the fast diffusion rate of the membrane potential V_m , it is assumed that the transmembrane potential V_m is spatially uniform distributed across the cell. The dynamics of transmembrane potential is derived from the ionic currents in the form

$$\frac{dV_m}{dt} = -\frac{1}{C_{sc}} \left(\sum_{i=ion} I_i \right) + I_{app} \quad (\text{Eq. 1})$$

with I_{app} is the stimulus current and

$$\sum_{i=ion} I_i = I_{Na} + \frac{I_{dhpr}^T}{A_m} + I_{K1} + I_{Kss} + I_{Ktof} + I_{Ktos} + \overline{I_{NCX}} + I_{Na/K} + \overline{I_{pmca}} + I_{bNa} + \overline{I_{bCa}} + I_{bK}$$

where

$$I_{dhpr}^T = \sum_{i=indexCRU} I_{dhpr}^{(i)}$$

$$\overline{I_{NCX}} = \frac{\sum_{i=1}^{\#grids-as-membrane} I_{NCX}^{(i)}}{\#grids-as-membrane}$$

$$\overline{I_{bCa}} = \frac{\sum_{i=1}^{\#grids-as-membrane} I_{bCa}^{(i)}}{\#grids-as-membrane}$$

$$\overline{I_{pmca}} = \frac{\sum_{i=1}^{\#grids-as-membrane} I_{pmca}^{(i)}}{\#grids-as-membrane}$$

The formulas for these currents (e.g. sodium current, potassium current) are the same as the ones being used in the compartmental model. In the current model, only the spatial distribution of calcium and calcium-bound species are considered. In the myoplasm calcium is buffered by the endogeneous buffers [calmodulin (Calm), troponin-C (Trpn), SL, SR membrane buffers] or exogeneous buffers [Fluo-3 (F)] with the kinetics based on (Loughrey, MacEachern et al. 2003)

$$J_{buffer} = J_{CaTrpn} + J_{CaCM} + J_{CaSR} + J_{CaF} + J_{CaSL}$$

with CaTrpn = calcium-bound to troponin, CaCalm = calcium-bound calmodulin, CaSR = calcium-bound to SR buffer, CaF = calcium-bound to Fluo-3. Of these, calmodulin, the SL, SR membrane buffers and troponin are assumed to be stationary and are described by the following ordinary differential equations:

$$\begin{aligned}
\frac{d[\text{CaCalm}]}{dt} &= J_{\text{Calm}} = k_{\text{Calm}}^+ ([\text{Ca}]_{\text{myo}})([\text{Calm}]_T - [\text{CaCalm}]_{\text{myo}}) - k_{\text{Calm}}^- [\text{CaCalm}]_{\text{myo}} \\
\frac{d[\text{CaSR}]}{dt} &= J_{\text{CaSR}} = k_{\text{SR}}^+ ([\text{Ca}]_{\text{myo}})([\text{SR}]_T - [\text{CaSR}]_{\text{myo}}) - k_{\text{SR}}^- [\text{CaSR}]_{\text{myo}} \\
\frac{d[\text{CaSL}]}{dt} &= J_{\text{CaSL}} = k_{\text{SL}}^+ ([\text{Ca}]_{\text{myo}})([\text{SL}]_T - [\text{CaSL}]_{\text{myo}}) - k_{\text{SL}}^- [\text{CaSL}]_{\text{myo}} \\
\frac{d[\text{CaTrpn}]}{dt} &= J_{\text{Trpn}} = k_{\text{Trpn}}^+ ([\text{Ca}]_{\text{myo}})([\text{Trpn}]_T - [\text{CaTrpn}]_{\text{myo}}) - k_{\text{Trpn}}^- [\text{CaTrpn}]_{\text{myo}}
\end{aligned}$$

The exogenous buffer Fluo-3 are mobile buffers and are describe by the following differential equations:

$$\begin{aligned}
\frac{\partial [\text{CaF}]_{\text{myo}}}{\partial t} &= J_{\text{CaF}} + \nabla^2 [\text{CaF}]_{\text{myo}} \\
\frac{\partial [F]_{\text{myo}}}{\partial t} &= -J_{\text{CaF}} + \nabla^2 [F]_{\text{myo}}
\end{aligned}$$

where the fluxes are

$$J_{\text{CaF}} = k_F^+ ([\text{Ca}]_{\text{myo}})[F] - k_F^- [\text{CaF}]$$

Free calcium and mobile buffers passively diffuse from one grid point to the neighboring ones following Fickian diffusion laws. Combined with the above fluxes the following partial differential equations describe these model variables:

$$\begin{aligned}
\frac{\partial [\text{Ca}^{2+}]_{\text{myo}}}{\partial t} &= J_{\text{ryr}} - J_{\text{buffer}} - J_{\text{serca}} + \nabla^2 [\text{Ca}^{2+}]_{\text{myo}} \\
\frac{\partial [\text{Ca}^{2+}]_{\text{nsr}}}{\partial t} &= J_{\text{serca}} + J_{\text{refill}} + \nabla^2 [\text{Ca}^{2+}]_{\text{nsr}}
\end{aligned}$$

The calcium in the jSR is replenished from the nSR by a diffusive flux (J_{refill}) which has been described by (Williams, Chikando et al. 2011). Even though Ca^{2+} release via RyR2 from the jSR can spread more than one grid-point, the jSR is treated as a single volume. Thus the changes in $[\text{Ca}^{2+}]_{\text{jSR}}$ at the i -th release site is described by the following ordinary differential equation:

$$\frac{\partial [Ca^{2+}]_{jsr}^i}{\partial t} = \beta_{jsr} (J_{refill} - J_{ryr}) / \lambda_{jsr}$$

with fast buffering is assumed in the jSR, and $\lambda_{jsr} = V_{jsr} / V_{myo}$ is the volume fraction.

$$\beta_{jsr} = 1 / (1 + (B_{jsr}^T \times Km_{jsr}) / ((Km_{jsr} + [Ca^{2+}]_{jsr}^i)^2))$$

Computational methods

The model is fully stochastic in terms of channel gating of RyRs and LCCs. The program was mainly written in Fortran and CUDA Fortran, using CUDA programming toolkit to run on Nvidia Fermi GPU, with some parts were written in C++. The Euler method was used to solve the partial-differential equations (PDEs) of diffusion-reaction, and other ordinary differential equations (ODEs). The adaptive time-step ranging from 10 nanoseconds to 1 microsecond was used. When there is some activity, due to channel gating, the time-step will be reduced for numerical stability. The units in the systems are: transmembrane potential - mV , membrane currents - $\mu A/cm^2$, the ionic concentration - μM (defined based on the corresponding volume), time - second (s). In spatial model, the forward difference in time and central difference in space derivatives yields

$$\frac{u_{i,j,k}^{t+\Delta t} - u_{i,j,k}^t}{\Delta t} = f(u_{i,j,k}^t, t) + D_x \left(\frac{u_{i+1,j,k}^t - 2u_{i,j,k}^t + u_{i-1,j,k}^t}{(\Delta x)^2} \right) + D_y \left(\frac{u_{i,j+1,k}^t - 2u_{i,j,k}^t + u_{i,j-1,k}^t}{(\Delta y)^2} \right) + D_z \left(\frac{u_{i,j,k+1}^t - 2u_{i,j,k}^t + u_{i,j,k-1}^t}{(\Delta z)^2} \right)$$

$$\frac{u_{ijk}^{p+1} - u_{ijk}^p}{\Delta t} = f(u^p, t) + D \left(\frac{u_{i+1,j,k}^p - 2u_{ijk}^p + u_{i-1,j,k}^p}{(\Delta x)^2} + \frac{u_{i,j+1,k}^p - 2u_{ijk}^p + u_{i,j-1,k}^p}{(\Delta y)^2} + \frac{u_{i,j,k+1}^p - 2u_{ijk}^p + u_{i,j,k-1}^p}{(\Delta z)^2} \right)$$

where u represents the species concentration in a single grid point.

$$u_{ijk}^{p+1} = u_{ijk}^p + \Delta t \left\{ f(u, t) + D \left(\frac{u_{i+1,j,k}^p - 2u_{ijk}^p + u_{i-1,j,k}^p}{(\Delta x)^2} + \frac{u_{i,j+1,k}^p - 2u_{ijk}^p + u_{i,j-1,k}^p}{(\Delta y)^2} + \frac{u_{i,j,k+1}^p - 2u_{ijk}^p + u_{i,j,k-1}^p}{(\Delta z)^2} \right) \right\}$$

For a single cell, the Neumann boundary condition is used, i.e. no flux

$$\begin{aligned}
u_{0,j,k}^p &= u_{1,j,k}^p \text{ and } u_{X+1,j,k}^p = u_{X,j,k}^p \\
u_{i,0,k}^p &= u_{i,1,k}^p \text{ and } u_{i,Y+1,k}^p = u_{i,Y,k}^p \\
u_{i,j,0}^p &= u_{i,j,1}^p \text{ and } u_{i,j,Z+1}^p = u_{i,j,Z}^p
\end{aligned}$$

To handle the extremely large data generated by the 3D model, the HDF5 (Heirarchical Data Format) library is used (HDF-group 2014), where the data exported in a compressed format that can be extracted later for further data analysis. The IDL language (Data Visualization Software, 2014) was used to perform all data visualization and data analysis. In this study of calcium waves, the two ions (K^+ , Na^+) are kept constant during the course of the simulation. Similarly, the corresponding currents are modeled as uniform too (Yang, Pascarel et al. 2002).

In the 3D model, several 3D data arrays need to be created, e.g. data for cytosolic calcium, myoplasmic calcium, calcium-bound to fluorescence, free fluorescence. However, there are certain data that are not ‘everywhere’ but are only present at a certain number of grid points only. Many of them are species that reside on the sarcolemma membranes, e.g. SL buffer, ionic channels (K^+ , Na^+ , LCC) and pumps/exchangers (NCX, PMCA, Na^+/K^+). To save memory and also to enhance the performance, a single 3D data array called **grid point data** is used. Each element of this array is a 32-bit value, where we splitt them into groups of 4 bits. Each group of bits tells us some information about that grid-point.

- Bit 0-3: index to the array that tells NCX distribution
- Bit 4-7: index to the array that tells SERCA distribution
- Bit 8-11: index to the array that tells SR buffer distribution
- Bit 12-15: index to the array that tells Troponin-C distribution
- Bit 16-19: index to the array that tells the grid-type (MEMBRANE, INNER-GRIDPOINT, OUTER-GRIDPOINT, NUCLEUS, MITO). Currently, we only

use MEMBRANE (both SL and T-tubule) and INNER-GRIDPOINT and OUTER-GRIDPOINT (stencil gridpoint).

- Bit 20-31: reserved (future use)

This significantly reduces the memory usage, from six 3D arrays, now we only need the same number of 1D arrays of a few data elements, and a single 3D array. In the current study, only channels, buffers related to Ca^{2+} are modelled spatially. The arrays that tells the SL buffer distribution, SR buffer distribution, NCX distribution contains just one (in the case of uniform distribution), or two (in the case we have high and low distribution) data elements. The value in each array represents the concentration of the corresponding species in each grid point. This is important due to the limited memory on CUDA-capable GPUs, and also to reduce the overhead of memory access, where reading data from global memory is very expensive compared to reading data on constant memory of much smaller sizes as bit-operations are very fast.

Results

Ca^{2+} transient

A pseudo line-scan image along the longitudinal direction during the Ca^{2+} transient is shown in Figure 7. The current model allows us to investigate the level of Ca^{2+} directly without using Ca^{2+} -bound fluorescent intensities. Even though the value F/F_0 is in agreement with experimental data, comparing the result between using back-calculation formula given by (Cheng, Lederer et al. 1993), the peak of free Ca^{2+} is about 3x higher than the value estimated. It means that the calculated calcium from experiment underestimated the amount of level free calcium in the cell. This emphasizes the functional role of local Ca^{2+} near the Ca^{2+} release site (at the z-line) in the cell due to the restricted space can regulate different cellular signals.

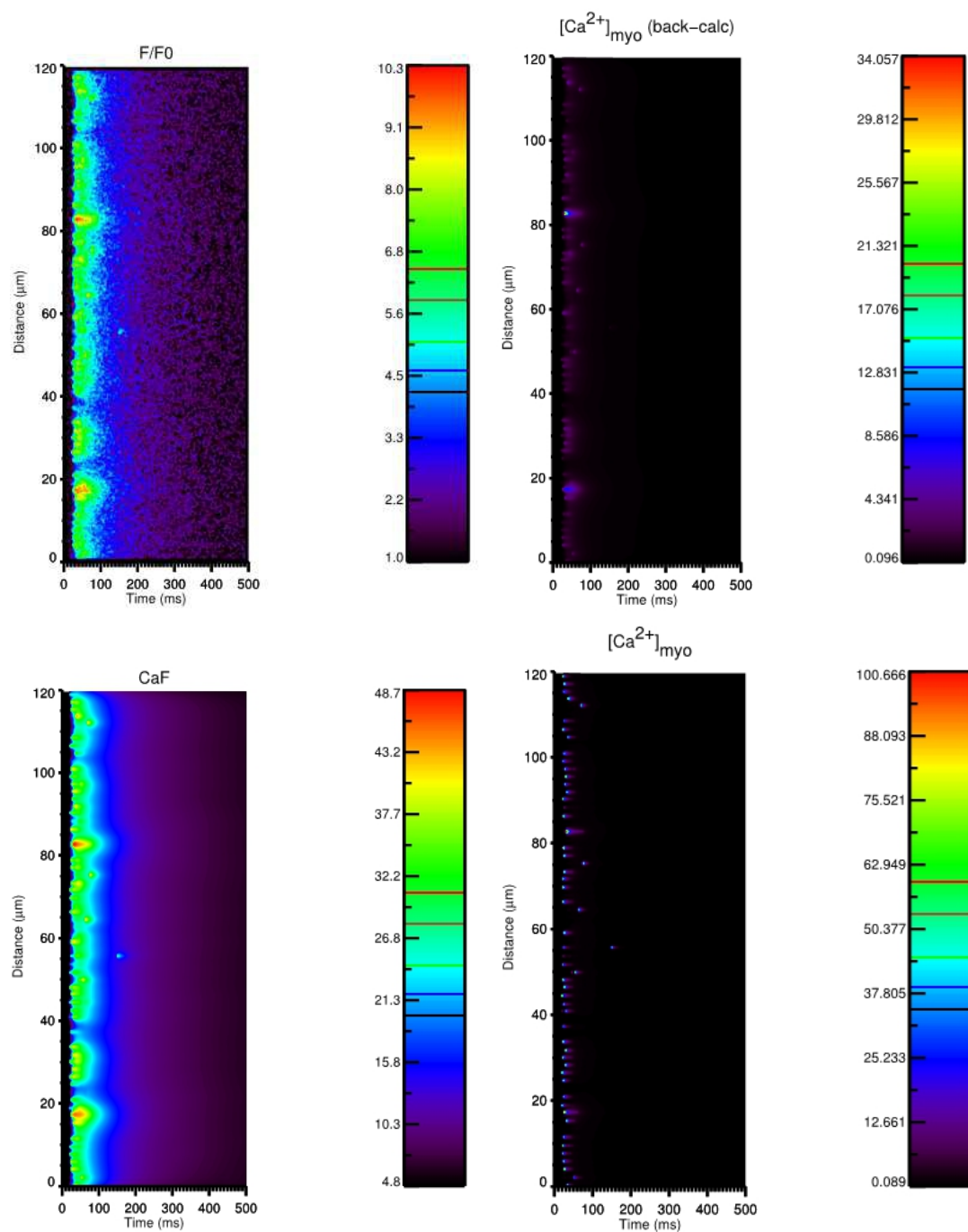


Figure 7. Calcium transient during an action potential (AP)

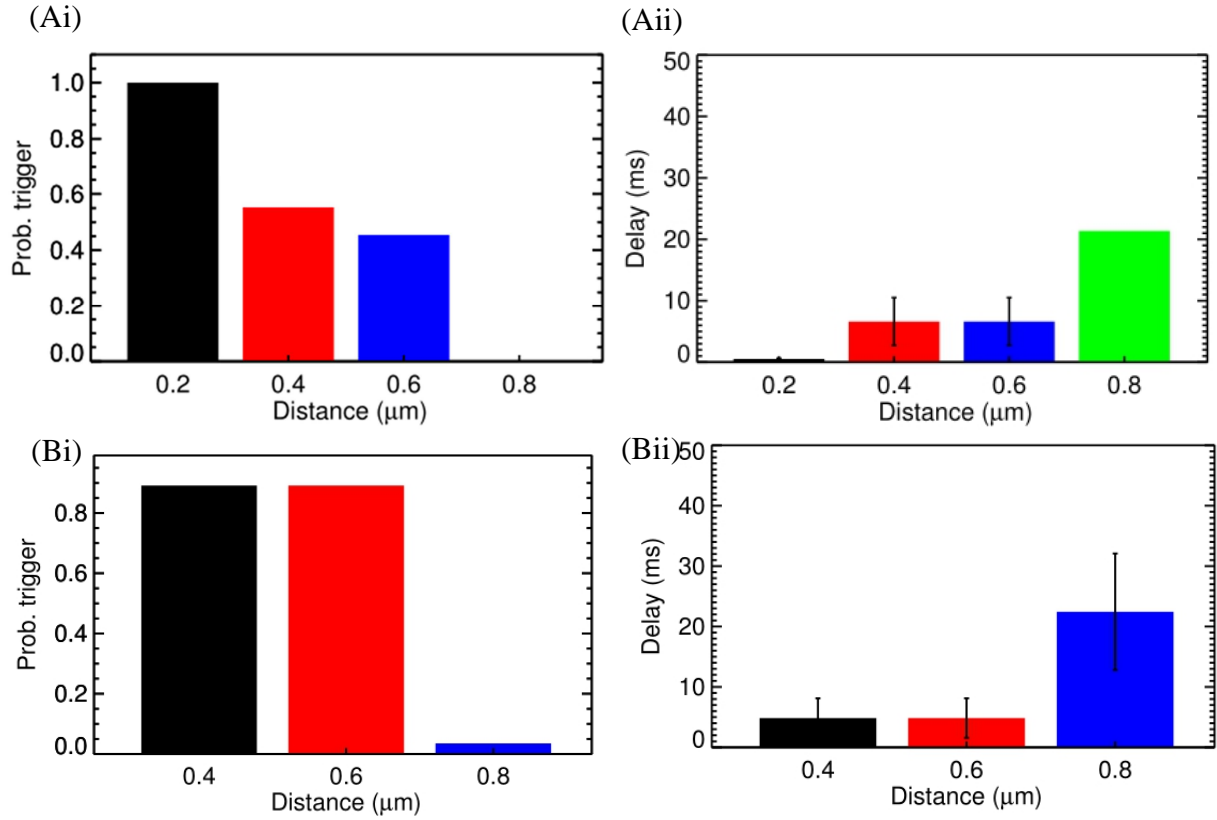


Figure 8. Using different distances between the two CRUs, (i) shows the probability of one CRU to trigger the neighboring one, and (2) shows the delay of the activation. (A) The normal condition at diastolic phase is used ($[Ca^{2+}]_{myo} = 0.096 \mu M$, and $[Ca^{2+}]_{nsr} = 1.02 mM$), (B) The high cytosolic calcium ($[Ca^{2+}]_{myo} = 0.4 \mu M$, and $[Ca^{2+}]_{nsr} = 1.02 mM$)

Ca^{2+} spark-induced Ca^{2+} sparks

We first look into the role of different factors, e.g. $[Ca^{2+}]_{myo}$, $[Ca^{2+}]_{SR}$, CRU distances in spark triggering. The result was collected based on 1,416 test cases. Under normal condition, we can see a sharp transition when the CRU distance goes beyond $0.6 \mu m$, Figure 8, with the $P_{o,trigger}$ for CRU at $0.8 \mu m$ is only 0.14% and the delay in time is 21 ms on average. This is in agreement with experimental data where Ca^{2+} sparks are local release of calcium that span a restricted space, without affecting the neighboring sites (Cheng, Lederer et al. 1993). The increase of cytosolic calcium, to $0.1564 \mu M$, brings the $P_{o, trigger}$ for the CRU at $0.6 \mu m$ distance from 45.40% to 58.41%. However, at $[Ca^{2+}]_{myo} = 0.4 \mu M$, it significantly increase the $P_{o,trigger}$ which is

now 89.12% for CRU at 0.6 μm apart and is 3.56% for the CRU at 0.8 μm apart. Along with that, we see a reduction in the delay time, which reduces from 6.6 ms for the CRU at 0.6 μm apart in Figure 8(A), to 4.8 ms for the CRU at 0.6 μm apart in Figure 8(B). A similar result can be achieved when increasing $[\text{Ca}^{2+}]_{\text{sr}}$, Figure 9.

To induce higher SR calcium, (Lukyanenko, Viatchenko-Karpinski et al. 2001) applied anti-phospholamban (APL) antibodies. The result showed that calcium sparks increase from ~ 4 events/100 μm only to ~ 7 events/100 μm and remains at this level during the course of the experiment. Using $[\text{Ca}^{2+}]_o = 10 \text{ mM}$, a 4-fold increase in Ca^{2+} spark was observed (Cheng, Lederer et al. 1996). In the cardiac cell, calsequestrin (CSQ) is the direct regulator to RyR gating from the luminal side, and Ca^{2+} bind to this protein to perform the regulation function. Even though CSQ can exist in multiple forms (monomers, dimers and multimers), monomer plays the regulatory function in RyR (Qin, Valle et al. 2008); while the role of multimers in RyR2 regulation has not been confirmed other than serving as Ca^{2+} buffers (review: (Gyorke, Stevens et al. 2009)).

During Ca^{2+} overload, a significant amount of SR loaded Ca^{2+} are bound to CSQ in oligomer forms. In the current model, luminal dependency is modelled as a function of $[\text{Ca}^{2+}]_{\text{jSR}}$, not $[\text{Ca}^{2+}/\text{CSQ}]$. Also, we haven't included the multiple forms of CSQ, i.e. dimers and multimers, which can function as Ca^{2+} buffers to hold more SR Ca^{2+} during Ca^{2+} overload. With a fixed amount of CSQ at the jSR, we suggest that when $[\text{Ca}^{2+}]_{\text{jSR}}$ exceed a certain amount, the dependency on $[\text{Ca}^{2+}]_{\text{jSR}}$ saturates. Thus, the luminal function is revised to match the spark frequency from the experimental results at Ca^{2+} overload condition, while also to allow a higher $[\text{Ca}^{2+}]_{\text{SR}}$ that can trigger Ca^{2+} wave. The luminal function is changed from

$$\Theta = k_0 \times [\text{Ca}^{2+}]_{\text{jSR}} + k_1$$

to

$$\Theta = k_0 \times \min(Ca_{max}, [Ca^{2+}]_{jSR}) + k_1$$

with $Ca_{max} = 1.13$ mM. The saturation value $[Ca^{2+}]_{SR} = 1.13$ mM was selected to be in agreement with the previous experiment.

Interesting, we don't see much different in $P_{o,trigger}$ between the two cases, as shown in

Table 1. It means that the $P_{o,trigger}$ is strongly influenced by the Ca^{2+} diffused from the neighboring release site. Even though the mobility of calmodulin has not been incorporated in the model, the slow diffusion constant ($\sim 20 \mu m^2/s$) compared to the diffusion of free calcium ($\sim 270 \mu m^2/s$) is expected not to affect much to the result. Based on the measurement of (Chen-izu, Mcculle et al. 2006), Figure 4(C), a significant number of transversal CRUs with the nearest neighbors fall into this the $0.7 \mu m$ range (21%), which may allow multiple CRUs to be activated on the same Z-disc.

Table 1. Po,trigger when $[Ca^{2+}]_{myo}=0.156 \mu M$, and $[Ca^{2+}]_{sr}=1.3mM$. The latter case assumes luminal Ca^{2+} sensitivity saturate at 1.13 mM

CRU dist. \ RyR sense	0.6	0.8	1.0
$[Ca^{2+}]_{sr,max} = 1.13 \text{ mM}$	93.22%	1.27%	0.8%
$[Ca^{2+}]_{sr,max} = 1.3 \text{ mM}$	95.48%	1.55%	1%

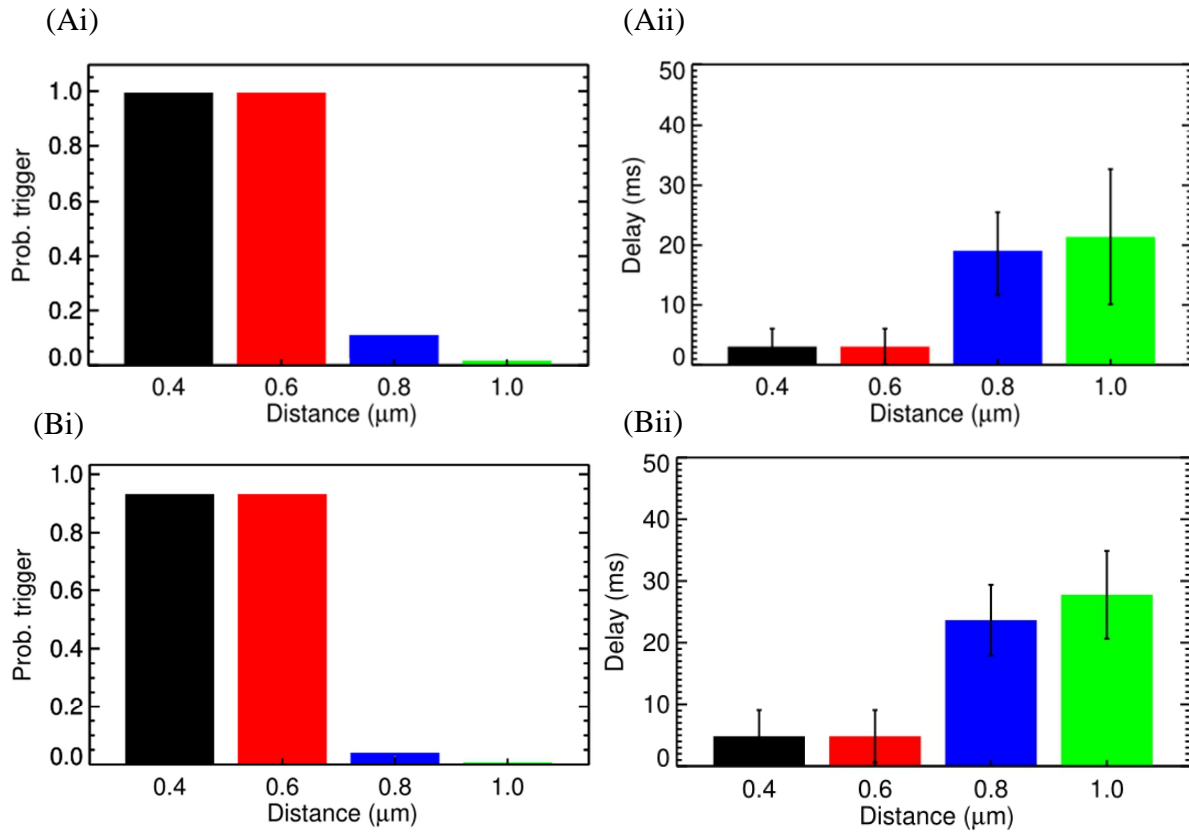


Figure 9. Using different distances between the two CRUs, (i) shows the probability of one CRU to trigger the neighboring one, and (2) shows the delay of the activation. The overload condition (A) ($[Ca^{2+}]_{myo} = 0.156 \mu M$, and $[Ca^{2+}]_{nsr} = 1.70 \text{ mM}$), and (B) ($[Ca^{2+}]_{myo} = 0.156 \mu M$, and $[Ca^{2+}]_{nsr} = 1.30 \text{ mM}$)

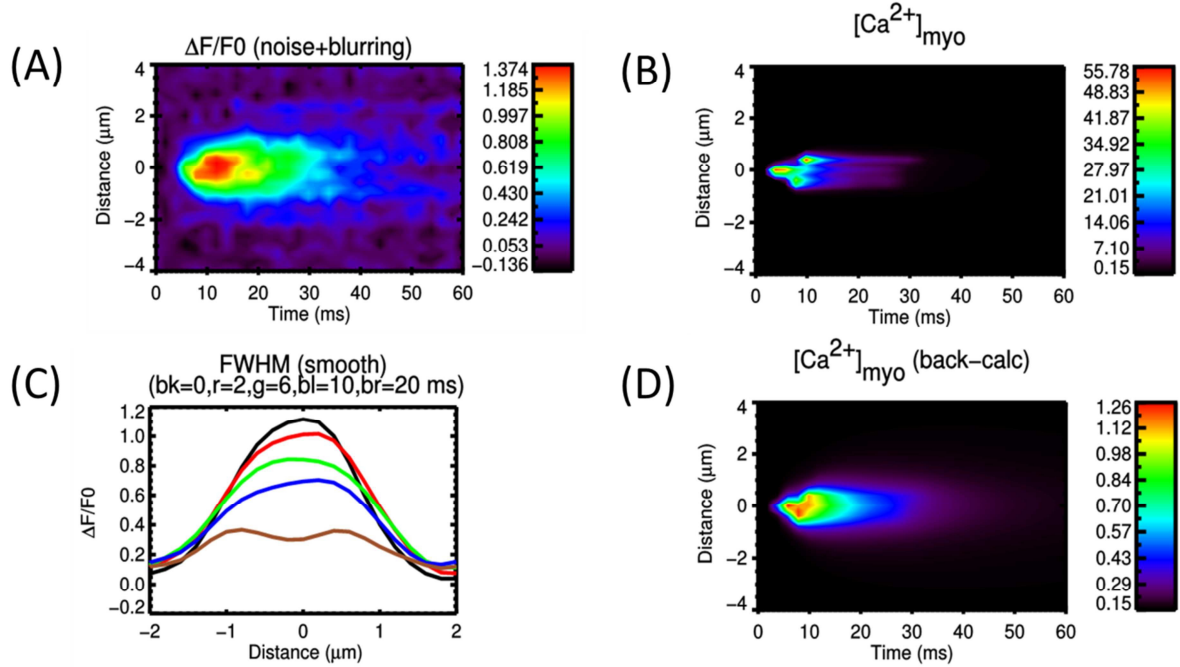


Figure 10. (A) A simulated calcium sparks, (B) Free calcium shows the underlying structure of release site (the delayed activation of the two satellite clusters are invisible under fluorescence profile), (C) The profile of a calcium spark giving FWHM=1.85 μm (each color represents the snapshot at different time point after the peak (e.g. bk=0 means black line at 0ms delayed)); (D) The free calcium profile using back-calculation method agrees with experimental estimates, however, it underestimates the real free myoplasmic calcium amplitude.

Given the newer experimental data using high resolution imaging, there are several experimental studies that showed RyR2s are organized in subclusters that can function as a single functional CRUs (Brochet, Yang et al. 2005; Baddeley, Jayasinghe et al. 2009; Brochet and Lederer 2014; Macquaide, Tuan et al. 2014). In this study, by using a big cluster with 36 RyR2 and two smaller satellite clusters of 15 RyR2 and at 0.150 μm apart, we were able to demonstrated the realistic FWHM = 1.85 μm , Figure 10. We then investigate the role of these satellite cluster in spark-induce spark triggering. Here, each CRU is modeled with 3 satellite cluster of size 10 RyR2s at 0.2 μm apart. As shown in Figure 11, the satellite clusters help boosting the chance for spark-induced sparks. Compared to the result in Figure 9(B), the CRU can now trigger a neighboring CRU at a further distance, with a higher probability for the ones at

the same distances as being used the earlier case. This is in agreement with the study by (MacQuaide, Ramay et al. 2010) in which they suggested that blocking small, non-spark producing clusters of RyR using ruthenium red (RuR) are important to the process of Ca^{2+} wave propagation.

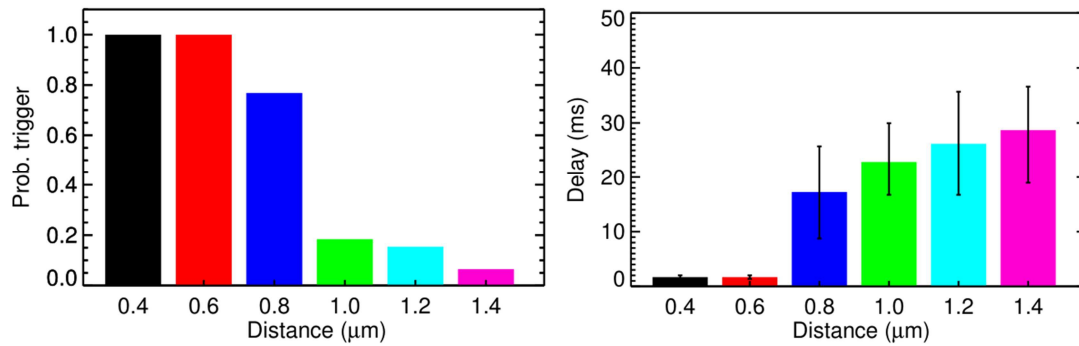


Figure 11. Using different distances, (i) shows the probability of one CRU to trigger the neighboring one, and (2) shows the delay of the activation. The overload condition (B) ($[\text{Ca}^{2+}]_{\text{myo}} = 0.156 \mu\text{M}$, and $[\text{Ca}^{2+}]_{\text{nsr}} = 1.30 \text{ mM}$) where each CRU has 3 satellite clusters of 10 RyRs each at distance $0.2 \mu\text{m}$.

There are two factors that may contribute to this increase in spark-induced spark activity. The first is the amplification of the Ca^{2+} signal by the opening of RyR2 from these satellite clusters. Also, it has been suggested that cluster of smaller sizes tend to open more often due to the weak allosteric coupling between the channels (Sobie, Guatimosim et al. 2006; Williams, Chikando et al. 2011). Thus, we suggested that the high opening activity of these satellite is the second factor that contribute to this rise in spark-induced-spark phenomenon. The overall effect is quite critical as we can see now a CRU can activate another one at a farther distance, forming the so-called macros-sparks that has been observed in other experiments (Cheng, Lederer et al. 1996; Parker, Zang et al. 1996; Cheng and Lederer 2008; Shah, Sikkell et al. 2012).

Ca²⁺ waves

In the study by Cheng and co-workers (Cheng, Lederer et al. 1996), increasing extracellular [Ca²⁺] from 1 mM to 10 mM elicited a 4-fold increase in Ca²⁺ sparks, with spark amplitude and spark size increased 4.1-fold and 1.7-fold accordingly. These macro Ca²⁺ sparks also served as the sites of wave initiation (65%), indicating that the macrosparks may represent aborted waves involving propagation between release sites. Our study, in agreement with these studies, also suggests that the Ca²⁺ spark observed is the result of calcium release not from a single one but multiple CRUs, and thus the mass of Ca²⁺ release from multiple CRUs is considered strong enough to trigger the wave in most cases.

The general mechanism for Ca²⁺ wave propagation is the fire-diffuse-fire model (Keizer and Smith 1998; Keizer, Smith et al. 1998) with the estimated wave velocity was 67 $\mu\text{m/s}$ with CRUs at $d = 2.0 \mu\text{m}$ apart. For the Ca²⁺ wave to sustain, we believe that there are two important factors: first the diffusing Ca²⁺ from one Z-line should be able to activate the CRU in the next Z-line and then calcium release from this CRU should be able to activate the neighboring ones in the same Z-line of it, and the process repeats. Given the shorter nearest neighbor distances for CRU on the same Z-line, in Figure 4, the CRUs on the same Z-line should be activated first during a Ca²⁺ wave initiation. This is in agreement with the prediction that a single spark is unlikely to trigger a spark at the next Z-line (Parker, Zang et al. 1996; Izu, Wier et al. 2001).

The previous section already provided us the $P_{o,\text{trigger}}$ at which a Ca²⁺-spark from one CRU can induce the activation of the neighboring CRU in the same Z-line under different conditions of [Ca²⁺]_{myo}, [Ca²⁺]_{nsr}, the distance and the role of satellite RyR2. We now investigate the second factor contributing wave formation along the longitudinal direction at which the distance between the CRUs are much longer 1.4 – 2.2 μm , Figure 4. The question is under what

condition that this can happen? This is determined by two factors: the number of activated CRUs on one Z-line and the mass of Ca^{2+} release, i.e. the level of Ca^{2+} overload.

We then created a simulation setting by putting a few CRUs on the same Z-line and another CRU at the other end of the sarcomere, and assuming that the CRUs on one Z-line are activated. Instead of modelling the activation of a single CRU, in this case, we created a model at which a few ‘black’ CRUs are activated, and we analyze the $P_{o,trigger}$ of the ‘blue’ CRU, Figure 12.

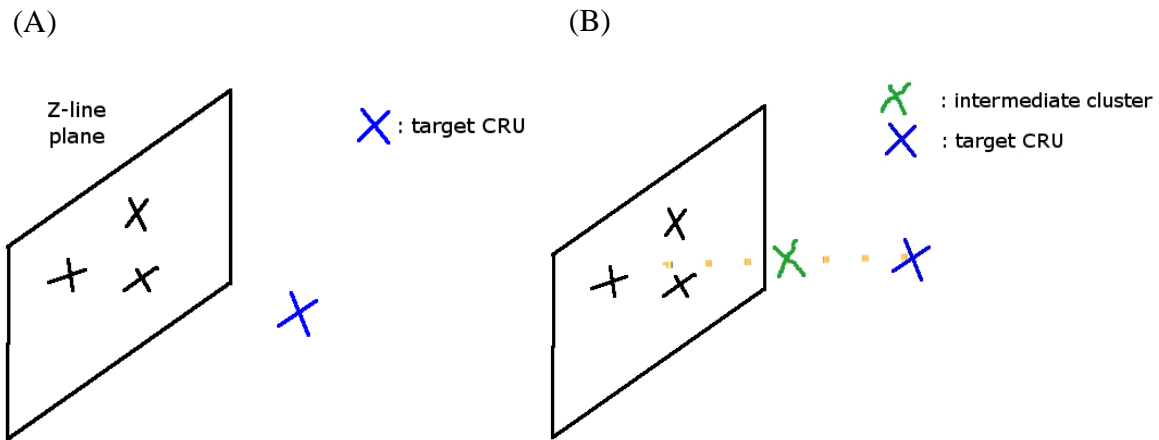


Figure 12. Simulation setting to study spark-induced waves (X = CRU location). Black X = the activated CRU, Blue X = the CRU to be activated by diffusing Ca^{2+} , Green X = intermediate RyR cluster

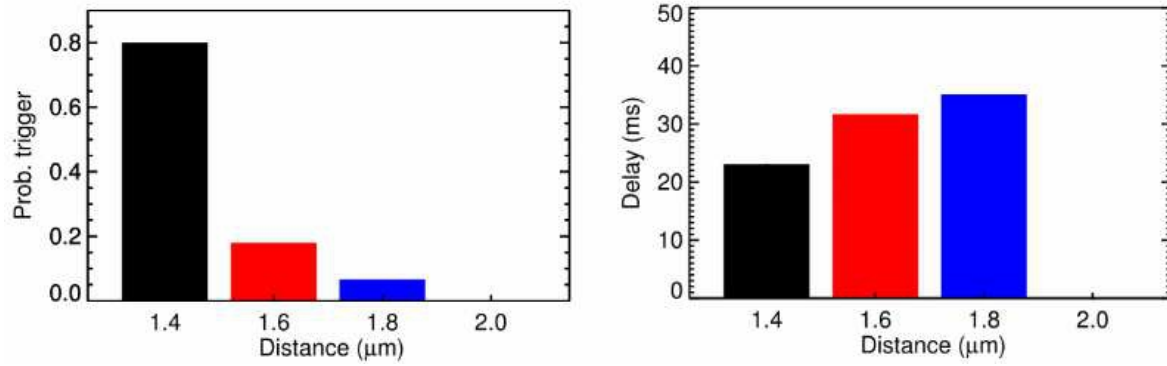


Figure 13. The $P_{o,trigger}$ of Ca^{2+} release from 9 activated CRUs on one Z-line on the CRU at different distance, and the time delay for the activation

We tested with $[Ca^{2+}]_{sr} = 1.3$ mM with 9 activated CRUs; however the signal is not strong enough. Given the spatial resolution of confocal microscope is 10x larger than the size of a junctional SR (0.06 fL vs. 0.008 fL), it's practically impossible to accurately detect the level of Ca^{2+} in the jSR. In addition, fluo-5N, the dye being used to estimate $[Ca^{2+}]_{jSR}$ has the Ca^{2+} affinity ~ 400 μM , which is 2-3x smaller than the diastolic level of $[Ca^{2+}]_{SR}$. Thus, estimating the level of $[Ca^{2+}]_{SR}$ overload is currently impossible (Ramay, Jafri et al. 2010). To estimate the total $[Ca^{2+}]_{SR}$ during a Ca^{2+} overload, it requires detailed modelling of CSQ in multiple forms which is not available in the current model. Therefore, we focus on the number of activated sites. Nevertheless, we were able to see a full and repetitive Ca^{2+} wave with $[Ca^{2+}]_{SR}=1.7$ mM and $[Ca^{2+}]_{myo} = 0.156$ μM .

Izu and co-workers used 5-7 supercluster (Izu, Wier et al. 2001). Each super-CRU releases 10-20 pA, compared to the typical 3 pA current (Cheng, Lederer et al. 1993; Blatter, Huser et al. 1997). This maps to the number of 15-27 CRUs being fired at the same times to achieve the wave velocity 126 $\mu m/s$. In our model, 7-9 CRUs is enough to trigger a Ca^{2+} wave. Thus, the spark model in our system is considered more viable to happen. In addition, they used

a two dimensional space which clearly enhance the calcium propagation compared to 3D. The general condition to test is $[Ca^{2+}]_{myo} = 0.156 \mu M$, $[Ca^{2+}]_{sr} = 1.7 mM$, and the statistics were collected based on 144 trial cases.

We calculated the propagation velocity as shown in the case of spark-induced spark, when the source of Ca^{2+} is from a single release site, the velocity is 30-45 $\mu m/s$. Using 9 activated CRUs, the wave velocity in the simulation setting, as shown in Figure 12, is 63.6 $\mu m/s$ at 1.4 μm apart and then reduced to 48.4 $\mu m/s$ at 1.8 μm apart. Another simulation setting was created where one intermediate clusters of RyRs was added, Figure 12(B). When an intermediate RyR cluster was added, at 0.6 μm apart, not only the probability for triggering, $P_{o,trigger}$, increases but also the wave speed is 74 $\mu m/s$ (for Z-line 2.0 μm apart) and 100 $\mu m/s$ (for Z-line 1.8 μm apart). This suggested that the wave velocity is strongly dependent on the mass of calcium release, i.e. the number of activated CRUs on one Z-line and the distance to the CRU in the next Z-line, and the important role of intermediate RyR clusters.

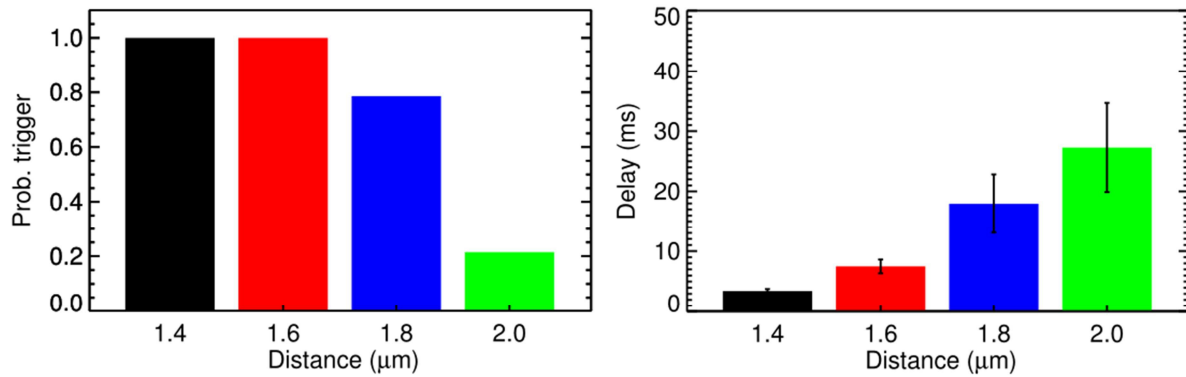


Figure 14. The $P_{o,trigger}$ of Ca^{2+} release from 9 activated CRUs on one Z-line, with 1 intermediate RyR cluster in the middle, on the CRU at the next Z-line of different distance, and the time delay for the activation

The results presented strengthen the positive amplitude-velocity relationship that has been suggested by experiments (Trafford, Lipp et al. 1995; Smith and O'Neill 2001). The estimated wave velocities vary significantly from different studies. The early estimation of wave velocity in cardiac myocytes was 100 $\mu\text{m/s}$ (Jaffe 1991). Recently, by testing different diffusion constants of calcium, (Swietach, Spitzer et al. 2010) estimated the value around 78 $\mu\text{m/s}$. Experimental data by (MacQuaide, Ramay et al. 2010) in rabbit ventricular myocyte suggested the range 102.2 ± 4.19 $\mu\text{m/s}$. In other experiments for rat, the authors have showed that the wave speed strongly depend on the amount of calcium overload and temperature (Kort, Capogrossi et al. 1985) (review: (Stuyvers, Boyden et al. 2000)). In particular, using $[\text{Ca}^{2+}]_o$ from 2 mM to 15 mM, the wave speed increases from 33 $\mu\text{m/s}$ to 87 $\mu\text{m/s}$; while at $[\text{Ca}^{2+}] = 3$ mM, the wave speed was 33 $\mu\text{m/s}$ at 23°C and 74 ± 19 $\mu\text{m/s}$ at 30°C. Another experiment in rat has confirmed the diversity in spatiotemporal properties of Ca^{2+} waves which is modulated by the Ca^{2+} -loading state (Kaneko, Tanaka et al. 2000) with different wave velocities: 84 ± 16 $\mu\text{m/s}$ and 116 ± 29.4 $\mu\text{m/s}$. This is in agreement with our results that the wave speed varies with the mass calcium release that elevate basal level of $[\text{Ca}^{2+}]_i$. In addition, we showed the important role of off-Z-lines CRUs in wave propagation. A whole-cell simulation of Ca^{2+} wave is given in Figure 15 and Figure 18, and the experiment is shown in Figure 16.

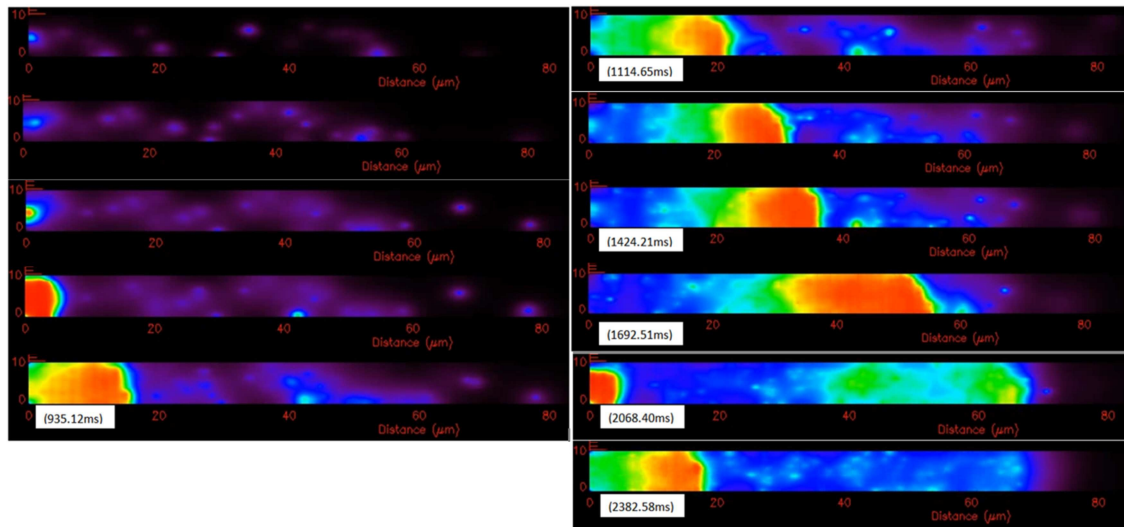


Figure 15. Calcium overload ($[Ca]_{nsr}=1.7mM$, $[Ca]_i=0.15\mu M$), this computational model of the rat ventricular myocyte can reproduce a repetitive sustained calcium wave which typically initiates at one end of the cell. The initiation site typically occurs where release sites are closer together or at a boundary.

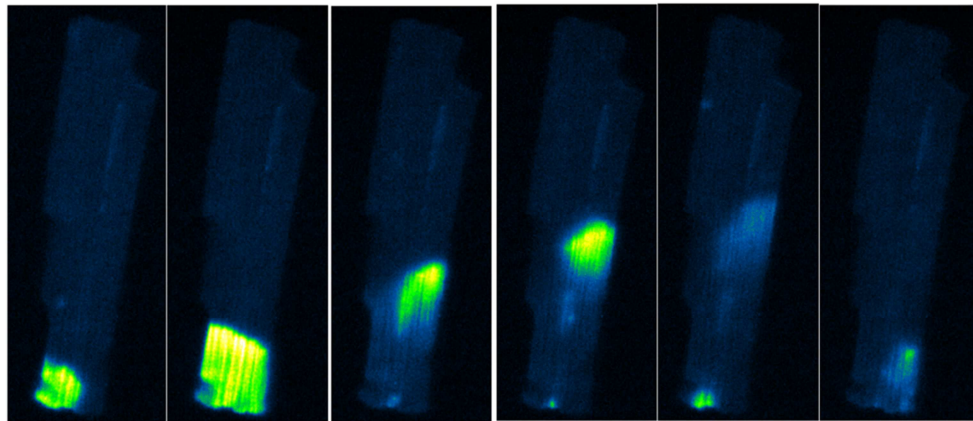


Figure 16. Calcium waves under $[Ca]_o = 5mM$ overload condition, the repetitive waves occur at a particular sites for each cell. This suggest there is a more density of release sites surrounding that region that allows mass calcium release is high enough to trigger the wave. Some waves can sustain to the next end, while some decay and stop in between, which suggests a stochastic nature of the waves (extract from Brian Hagen's experiment).

The role of SERCA in spark-induced Ca^{2+} wave was tested, as shown in Figure 17. With uniform distribution of SERCA along the longitudinal direction, more Ca^{2+} will be sequestered back to the SR along the pathway of calcium diffusion. It is in agreement with a previous study that SERCA inhibition should enhance the wave velocity (Jafri 1995). Given the fact the cytosolic calcium diffuse faster than calcium in the SR, the inhibition of SERCA should facilitate the diffusion of calcium to the next release site to trigger the opening of RyR2 there. After applying UV-flash photolysis of ‘caged’ Nmc-DBHQ or the blocking of SERCA affecting the activation of CRUs (a precursor of SERCA-inhibitor DBHQ (Rossi and Kao 1997)), Kelly and co-workers found a decrease in Ca^{2+} wave velocity. The authors suggested that calcium overloaded at one CRU due to the activity of SERCA pump lead to RyR sensitization ahead of cytosolic Ca^{2+} wave, which explains the reason why blocking SERCA decrease Ca^{2+} wave (Keller, Kao et al. 2007). However, this doesn’t follow CICR mechanism. Based on a computational study, Ramay and co-workers concluded that this ‘sensitization’ only occurs at slow diffusion of SR Ca^{2+} (Ramay, Jafri et al. 2010). However, this slow diffusion was not found in other studies (Picht, Zima et al. 2011). As the activation of one CRU, during a Ca^{2+} wave, depend on the Ca^{2+} released from CRUs not only from the adjacent Z-line, which in turns depends on the distance, but also from activated CRUs on the same Z-line. Thus, one possible explanation for this when SERCA is blocked is when they measure the velocity, the CRU distance is longer for the Ca^{2+} to reach and also the blocking of SERCA reduce the activated CRUs on the same Z-line which in turns reduce diffusing Ca^{2+} to activate the release site.

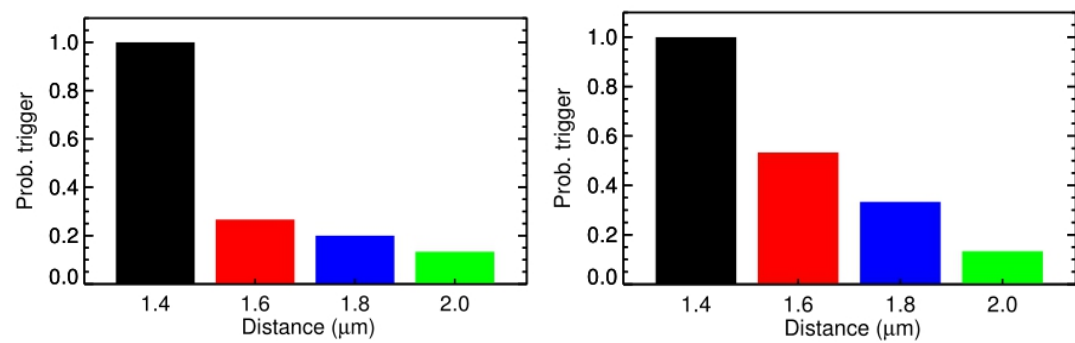
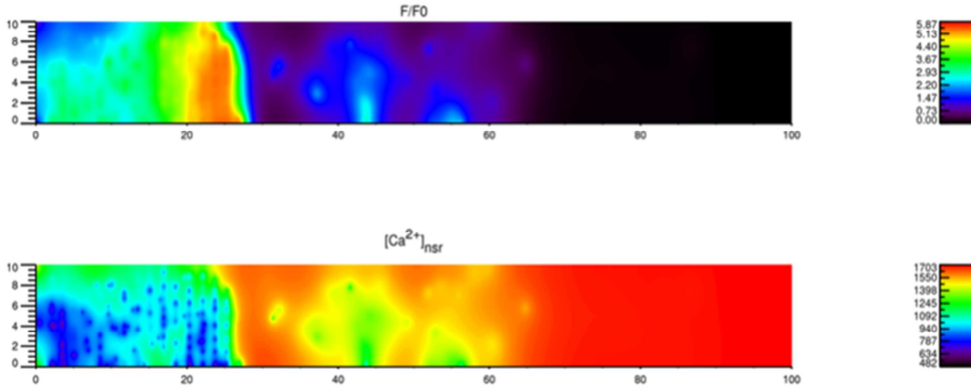
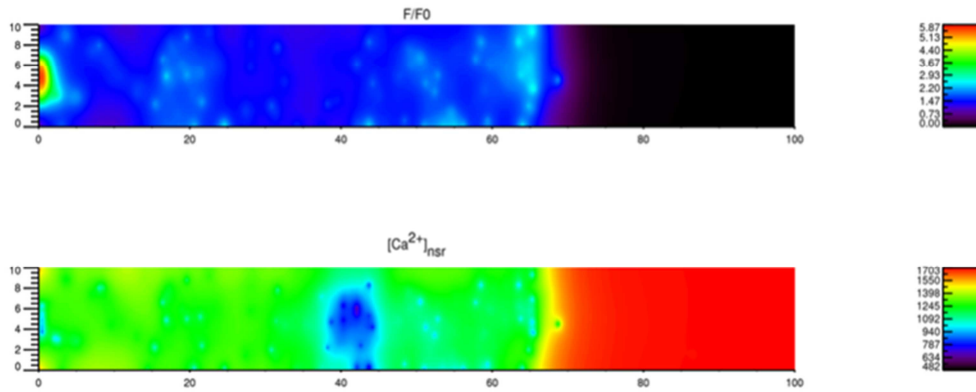


Figure 17. (A) uniform SERCA; (B) block SERCA 90%

Calcium (CaF, Cansr) – Times: 1097.80(ms)



Calcium (CaF, Cansr) – Times: 2141.33(ms)



Calcium (CaF, Cansr) – Times: 2214.27(ms)

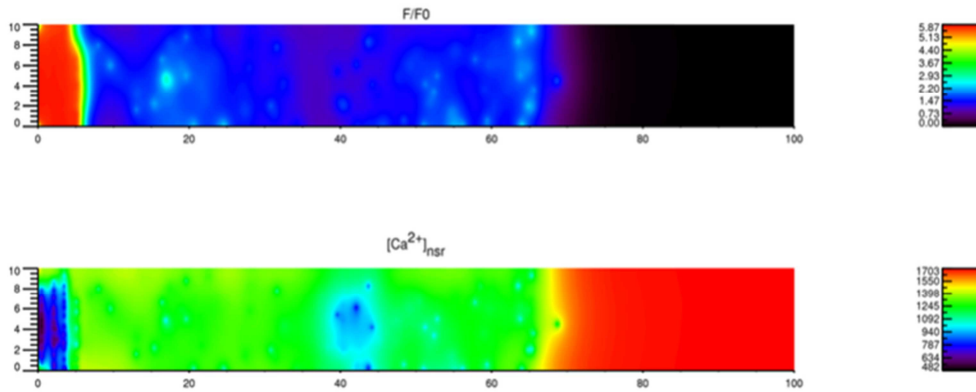


Figure 18. Given the initial $[Ca]_{nsr}=1.7mM$, to derive the triggering of the wave, the simulation suggested that an overload of 1.5M is enough to trigger the repetitive calcium waves.

Conclusion

The 3D spatiotemporal model has been used to study spark-induced spark and spark-induced Ca^{2+} waves. The model was developed using available data for rat ventricular myocytes from the literatures. The model is superior than other models in many ways. First, the gating of ion channels is modelled stochastically with the kinetics of RyRs fitted to give the proper fidelity of spark generation that matches the experimental data, i.e. ~ 100 sparks/cell/sec at rest. The second is the detailed 3D spatialtemporal representation of the cell at the resolution of 200 nm. Thirdly, the non-uniform distribution of SL, SR buffers and NCX were incorporated in the model. Fourthly, the dynamics of calcium buffering in the subspace is modelled explicitly, not fast binding assumption. In addition to that, the ultra-fast MCMC method allows us to obtain a better statistics of spark-induced spark compared to other studies which only enable the examining one, two or a few pairs of CRUs at a time.

The model details were required to give the accurate results. The first is the realistic spark models that has been tested to reproduce proper pump/leak balance in rat ventricular myocyte (Williams, Chikando et al. 2011). Secondly, the role of satellite clusters was also tested, which imply a heterogeneity in RyR cluster arrangements. The widely used assumption is that a single connected RyR cluster forming a planar array for each release site. However, the recent data have showed RyR arrangement is more heterogeneous and that a functional release sites can be the result of one main RyR cluster and a few smaller size of RyR clusters at a distance 100-200 nm apart (Brochet, Yang et al. 2005; Baddeley, Jayasinghe et al. 2009; Brochet and Lederer 2014; Macquaide, Tuan et al. 2014). By using a model with one central cluster with 2 satellite clusters, we was able to reproduce the proper FWHM of a Ca^{2+} spark. In addition, the high

diffusion constant of fluorescence ($\sim 90 \mu\text{m}^2/\text{s}$) is important for triggering the satellite cluster at 200 nm apart, and for reproducing proper FWHM.

The model's results are in agreement with other studies that the Ca^{2+} wave velocity vary upon the condition of the setting, in particularly the loading of Ca^{2+} . The important role of intermediate cluster has been showed in the model as well, which has not been investigated before. This is ingreement with recent data showing that T-tubules is a far more complicated structure that branches not only transversal but also longitudinal (Soeller and Cannell 1999). Using the local control model, the results showed how SR Ca^{2+} can induces Ca^{2+} waves based on stochastic gating of RyR2 channels. In the current model, we suggest an activation of 7-9 CRUs is required to trigger a wave from one Z-line to another. However, the probability of activation depend on the distance. The diffusion constant of ATP as well as CaATP is significant $168 \mu\text{m}^2/\text{s}$ (Baylor and Hollingworth 1998). However the high-valued $K_d=200 \mu\text{M}$ exceeds the peak calcium sparks (Bers 2001; Hake, Edwards et al. 2012). Thus its role in affecting calcium dynamics is non-significant. Currently, the space consumed by the T-tubule has not been considered, i.e. assumed to be zero. Adding these to the model, it may help boosting Ca^{2+} diffusion as a fraction of space is now consumed by T-tubule and the diffusion of calcium is facilitated by Ca-ATP. Thus, it may help spreading Ca^{2+} , which makes the wave initiation and propagation even easier. Other factors that may affect Ca^{2+} wave or arrhythmias that has not been included in the model is the presence of mitochondria and the nucleus (Dedkova and Blatter 2008; Aon, Cortassa et al. 2009; O'Rourke and Blatter 2009).

The current model hasn't incorporated the different oligomers of CSQ, thus the total free SR $[\text{Ca}^{2+}]$ during a calcium wave has not been investigated. However, we was able to produce, for the first time, a repetitive Ca^{2+} wave at $[\text{Ca}^{2+}]_{\text{SR}} = 1.7 \text{ mM}$ and $[\text{Ca}^{2+}]_{\text{myo}} = 0.0156 \mu\text{M}$. The

simulation showed that the local high elevation of cytosolic calcium, which was much underestimated using the back-calculation method, may play an important role in regulating the cellular signals. Lastly, the non-uniform placement of CRU is important for calcium wave initiation and propagation under calcium overload.

(Keller, Kao et al. 2007) proposed the concept of RyR ‘sensitization’ as a possible for decreasing Ca^{2+} wave velocity. We did the test with (1) reducing SERCA during Ca^{2+} wave, (2) different SR Ca^{2+} diffusion constant, however the result follows CICR. As we pointed out in that the Ca^{2+} velocity depends not only on the CRU distance but also the role of intermediate CRU. Thus, it’s possible that the increase/decrease in Ca^{2+} wave velocity is the result of the presence of an intermediate RyR cluster or a longer CRU distance. Another possible explanation is that with SERCA blocking, the number of activated CRUs on one Z-line can be smaller, thus reduce the mass Ca^{2+} release, which in turn reduces the Ca^{2+} wave velocity. We thus reject the hypothesis that Ca^{2+} diffusion constant is higher in the SR side.

Using the Ca^{2+} -sensitive of RyR2 compatible with experimental measurements, the model has successfully explained the difference in wave speed, the mechanism and conditions at which Ca^{2+} waves are initiated. In an earlier 2D model, Ca^{2+} -bound fluorescence had not declined to the baseline level after the wave (Izu, Wier et al. 2001). The model, for the first time, is able to reproduce repetitive Ca^{2+} wave, without any change to RyR channel Ca^{2+} -sensitivity and SERCA pump. The model is the first of its kind at this level of details and promises to be able to provide further understanding of different pathophysiological conditions, such as T-tubule remodelling or different channel mutations.

Appendix

Program design

In order to keep track which grid-points contains the sarcolemma or the T-tubule, two arrays are used. This will allows the program to quickly determines what fluxes contribute to each grid-point during the simulation.

```
INTEGER :: numgrid_is_membrane !! keep the number of grid-point which belong to  
SARCOLEMMMA (SURFACE + T-TUBULE)  
INTEGER, DIMENSION(:), ALLOCATABLE, device :: map_membrane2offset_lin !map the  
index of gridpoint in membrane array to offset in linear representation of 3D structure  
(outerDIMX, outerDIMY, outerDIMZ)  
INTEGER, DIMENSION(:), ALLOCATABLE, device :: map_offset2membrane_lin !map the  
offset in linear representation of 3D structure (outerDIMX, outerDIMY, outerDIMZ) to index of  
gridpoint in membrane array
```

On GPU, the 1D arrays that contains the different values of density of a given species are saved in ‘constant’ memory, which has almost the same speed as shared/cache memory and much faster than accessing from global memory. Due to the small size of the arrays, this perfectly fits into the limited size of constant memory on GPU. Currently, we only consider two cases: (1) uniform where the arrays have only 1 value, (2) non-uniform where the arrays have 2 values: one represent the density at grid-points of lower-density, and one represent the density at grid-points of higher density.

```
REAL(KIND=dp), DIMENSION(DATA_SIZE_GRID), constant :: NCX_distribution  
REAL(KIND=dp), DIMENSION(DATA_SIZE_GRID), constant :: SERCA_distribution  
REAL(KIND=dp), DIMENSION(DATA_SIZE_GRID), constant :: SRbuffer_distribution  
REAL(KIND=dp), DIMENSION(DATA_SIZE_GRID), constant :: SLbuffer_distribution  
REAL(KIND=dp), DIMENSION(DATA_SIZE_GRID), constant :: TrpnC_distribution
```

In the case of SL buffers, for example, the grid-points near the release sites are assumed to have much higher SL buffers than other grid-points, so the value in **gridpoint_data[]** links to the array index of bigger value.

```
INTEGER, PARAMETER :: bitshift_NCX = 0  
INTEGER, PARAMETER :: bitshift_SERCA = 4
```

```

INTEGER, PARAMETER :: bitshift_SRbuffer = 8
INTEGER, PARAMETER :: bitshift_SLbuffer = 12
INTEGER, PARAMETER :: bitshift_TPN_C = 16
INTEGER, PARAMETER :: bitshift_GridType = 20
INTEGER, DIMENSION(:, :, :), ALLOCATABLE :: gridpoint_data !!! keep the bit-groups, each
group of bits is the index to the much smaller array
INTEGER, PARAMETER :: DATA_SIZE_GRID = 4 ! maximum is 16 (as we use 4 bits)
INTEGER, PARAMETER :: SIZE_BITGROUP = 4 ! number of bits arranged for each group

```

In order to deal with CRUs placement, two arrays are used. The first one, SFU_in_lingrid_dev[ii], tells the location of the SFU ii-th on the grid, and the second one lingrid_with_SFU_dev[x] tells whether the grid-point of offset x contains a release site. This allows us to place the release sites any where in the 3D model of the cell, which enables us to study the effect of T-tubule remodelling. The location of the CRUs can be read-in from an input files, or generate on-the-fly and then save it to the text-file for reuse.

```

INTEGER, DIMENSION(:), ALLOCATABLE, device :: SFU_in_lingrid_dev
INTEGER, DIMENSION(:), ALLOCATABLE, device :: lingrid_with_SFU_dev

```

The 3D arrays of different species in the cells are used. If the species are mobile, then a double-buffer strategy is used, where one is used to keep the present values, and one is used to keep the new values in the next time step. For stationary species, a single 3D array is used. Here, all the 3D arrays are organized as linear 1D arrays to avoid logical mapping from 3D to 1D memory linear representation.

```

REAL(KIND=dp), DIMENSION(:), ALLOCATABLE, device :: Ca_myo_2_dev, Ca_myo_1_dev
REAL(KIND=dp), DIMENSION(:), ALLOCATABLE, device :: Ca_nsr_2_dev, Ca_nsr_1_dev
REAL(KIND=dp), DIMENSION(:), ALLOCATABLE, device :: CaF_2_dev, CaF_1_dev !Ca-
bound fluorescence
REAL(KIND=dp), DIMENSION(:), ALLOCATABLE, device :: F_2_dev, F_1_dev !fluorescence
(dyes) REAL(KIND=dp), DIMENSION(:), ALLOCATABLE, device :: CaBhtrpn_dev
REAL(KIND=dp), ALLOCATABLE, DIMENSION(:), device :: CaSL_dev, CaCalm_dev,
CaSR_dev

```

Methods to place CRUs

The CRUs were generated following the below steps:

1. *Read in the Z-line distance data:* Based on the histogram given in Figure 4, the probability density function (PDF) is generated. Then, for the distances within each bin, a given probability is assigned. For example: from 1.4-1.5 μm , the probability is 1.38%; while from 1.5-1.6 μm , the probability is 2.51%. This is saved in matrix **Zdist_probs**.
2. *Read-in the CRU transversal distance data:* a data structure (array) **CRUdist_probs** is generated to keep the information include (the distance-bin, the probability, the expected number of SFU whose nearest neighbors falls into that bin, the number of generated SFU whose nearest neighbors falls into that bin)
3. *Generate Z-line data:* a pseudo-random number is generated that is used to determine the distance to the next Z-disc. The idea is to generate a uniform pseudo-random number, and depending on the value compared to that in **Zdist_probs**, we can estimate the distance.
4. *On the T-tubules of the same Z-disc, generate the CRUs location:* Again, a pseudo-random number is generated to determine the distance between 2 nearest-neighbor CRUs. The last column of the array **CRUdist_probs** is updated to reflect the current distribution of nearest neighbor distances between CRUs along the T-tubules. **Assumption:** the code was designed in a way that T-tubules invaginate along the Y-direction. The distance between adjacent T-tubule was assumed to be either 0.8 μm or 0.9 μm , and was randomly selected.
5. *Add CRUs off the Z-discs:* a given fraction of CRUs (5.62%) are randomly placed in between the 2 Z-discs.

6. *Add peripheral CRU, i.e. CRUs between 2 Z-discs*: a certain given fraction of CRUs along the external surface of the sarcolemma are generated between two Z-discs.
7. *Add rogue-RyR2 location*: The locations of a certain fraction of rogue-RyR2 cluster can be added.
8. Write the location of CRUs to file, so that it can be read-in and map to grid-point index for further simulation.

Parameters

Table 2. Parameters in the model

Parameter	Definition	Value
V_{cell}	Cell volume	24.96(pL)
V_{myo}	Myoplasmic volume	50% * V_{cell}
V_{nsr}	Network SR volume	3.2% * V_{cell}
V_{jsr}	Junctional SR volume	0.5% * V_{cell}
Dyad_height	The distance between jSR and T-tubule	12 nm
Couplon_size	The size of the subspace	300 nm
X_len	Cell dimension	120 μm
Y_len	Cell dimension	20.8 μm
Z_len	Cell dimension	10.0 μm
$D_{\text{myo}}(x,y,z)$	Free cytosolic calcium diffusion	270 $\mu\text{m}^2/\text{sec}$
$D_{\text{nsr}}(x,y,z)$	Free SR calcium diffusion	60 $\mu\text{m}^2/\text{sec}$
$D_{\text{dye}}(x,y,z)$	Fluorescence and Calcium-bound fluorescence diffusion	90 $\mu\text{m}^2/\text{sec}$
F_{T}	Total fluorescence (Fluo-3)	50 μM
k_{on}	Binding constant for fluorescence	80 $\mu\text{M}^{-1}.\text{sec}^{-1}$
k_{off}	Unbinding constant for fluorescence	72 sec^{-1}
E_{cc}	Change in free energy between closed RYR pairs	-0.872 $k_{\text{B}}T$
E_{oo}	Change in free energy between open RYR pairs	-1.15 $k_{\text{B}}T$
k_{B}	Boltzmann constant	1.381x10 ⁻²³ J/K

T	Temperature	295.15 K
$[K^+]_o$	Extracellular potassium concentration	5.4 mM
$[Na^+]_o$	Extracellular sodium concentration	140 mM
$[Ca^{2+}]_o$	Extracellular calcium concentration	1.8 mM
$[K^+]_i$	Cytosolic potassium concentration	143.72 mM
$[Na^+]_i$	Cytosolic sodium concentration	10.2 mM
$[Ca^{2+}]_i$	Cytosolic calcium concentration	0.096 μ M
$[Ca^{2+}]_{sr}$	SR calcium concentration	1.02 mM
B_{myoT}	Total myoplasmic buffer concentration	3.703026e2 μ M
$K_{m,myo}$	Disassociation constant of myoplasm buffer	1.1900 μ M
[Trpn]	Troponin Ca^{2+} binding sites concentration ($k^+=2.37 \mu M^{-1}.s^{-1}$, $k^-=0.032 s^{-1}$)	140 μ M
[Calm]	The dynamics buffers with $K_d=2.38 \mu$ M ($k^+=30 \mu M^{-1}.s^{-1}$, $k^-=71.4 s^{-1}$)	24 μ M
$[B]_{SL}$	The SL buffer ($k^+=115 \mu M^{-1}.s^{-1}$, $k^-=1000 s^{-1}$)	750 μ M
$[B]_{SR}$	The SR buffer with $K_d=0.86 \mu$ M ($k^+=115 \mu M^{-1}.s^{-1}$, $k^-=100 s^{-1}$)	47 μ M
A_{pump}	Concentration of SERCA pump	300 μ M
$K_{p,myo}$	The binding affinity of cytosolic calcium to SERCA	900 μ M
$K_{p,nsr}$	The binding affinity of SR calcium to SERCA	2,150 μ M
V_{refill}^T	Total refill rate for 20,000 CRUs	3 (1/sec/(L-cyt))
V_{efflux}^T	Total efflux rate for 20,000 CRUs	120 (1/sec/(L-cyt))
i_{ryr}	Single channel RyR current	0.2 (pA)
g_{bCa}	Background Ca^{2+} conductance	2.9e-4 (mS/ μ F)
g_{bNa}	Background Na^+ conductance	1.066e-4 (mS/ μ F)
g_{bK}	Background K^+ conductance	0 (mS/ μ F)
g_{Na}	Na^+ conductance	13 (mS/ μ F)
g_{K1}	K1 conductance	0.2 (mS/ μ F)
g_{Kss}	Kss conductance	4.21e-2 (mS/ μ F)
g_{Ktof}	Ktof conductance	0.0798 (mS/ μ F)
g_{Ktos}	Ktos conductance	6.29e-2 (mS/ μ F)
A_m	Cell surface area	
I_{pmca}	Maximum PMCA current density	0.10 (μ A/ μ F)
I_{ncx}	Maximum NCX current density	750 (μ A/ μ F)
I_{NaK}	Maximum NaK current density	0.88 (μ A/ μ F)
eta_RyR	Hill coefficient of Ca^{2+} -dependent in RyR	2.2
eta_LCC	Hill coefficient of Ca^{2+} -dependent in LCC	2.0
E_j	Coupling strength energy (for 49 RyRs)	0.0714
Ecc	Coupling energy between 2 closed-channels	-0.78 ($k_B T$)
Eoo	Coupling energy between 2 open-channels	-1.26 ($k_B T$)

References

- Allbritton, N. L., T. Meyer, et al. (1992). "Range of messenger action of calcium ion and inositol 1,4,5-trisphosphate." Science **258**(5089): 1812-1815.
- Andersen, O. S. and R. E. Koeppe, 2nd (2007). "Bilayer thickness and membrane protein function: an energetic perspective." Annu Rev Biophys Biomol Struct **36**: 107-130.
- Aon, M. A., S. Cortassa, et al. (2009). "From mitochondrial dynamics to arrhythmias." Int J Biochem Cell Biol **41**(10): 1940-1948.
- Backx, P. H., P. P. de Tombe, et al. (1989). "A model of propagating calcium-induced calcium release mediated by calcium diffusion." The Journal of general physiology **93**: 963-977.
- Baddeley, D., I. D. Jayasinghe, et al. (2009). "Optical single-channel resolution imaging of the ryanodine receptor distribution in rat cardiac myocytes." Proceedings of the National Academy of Sciences of the United States of America **106**: 22275-22280.
- Baylor, S. M. and S. Hollingworth (1998). "Model of sarcomeric Ca²⁺ movements, including ATP Ca²⁺ binding and diffusion, during activation of frog skeletal muscle." J Gen Physiol **112**(3): 297-316.
- Berlin, J. R. (1995). "Spatiotemporal changes of Ca²⁺ during electrically evoked contractions in atrial and ventricular cells." Am J Physiol **269**(3 Pt 2): H1165-1170.
- Berridge, M. J. (1993). "Inositol triphosphate and calcium signalling." Nature **361**: 315-425.
- Bers, D. M. (2001). Excitation-Contraction Coupling and Cardiac Contractile Force. Dordrecht, Netherlands, Kluwer Academic Publishers.
- Blatter, L. A., J. Huser, et al. (1997). "Sarcoplasmic reticulum Ca²⁺ release flux underlying Ca²⁺ sparks in cardiac muscle." Proc Natl Acad Sci U S A **94**(8): 4176-4181.
- Brette, F. and C. Orchard (2003). "T-tubule function in mammalian cardiac myocytes." Circulation research **92**: 1182-1192.
- Brochet, D. X. P. and W. J. Lederer (2014). "Decomposition of a Calcium Spark in Cardiac Myocytes." Biophys. J. **104**(2): 483a.
- Brochet, D. X. P., D. Yang, et al. (2005). "Ca²⁺ blinks: rapid nanoscopic store calcium signaling." Proceedings of the National Academy of Sciences of the United States of America **102**: 3099-3104.
- Chen-izu, Y., S. L. McCulle, et al. (2006). "Three-dimensional distribution of ryanodine receptor clusters in cardiac myocytes." Biophysical journal **91**: 1-13.

- Cheng, H., M. R. Lederer, et al. (1996). "Calcium sparks and $[Ca^{2+}]_i$ waves in cardiac myocytes." The American journal of physiology **270**: C148-159.
- Cheng, H. and W. J. Lederer (2008). "Calcium sparks." Physiological reviews **88**: 1491-1545.
- Cheng, H., W. J. J. Lederer, et al. (1993). "Calcium Sparks: Elementary Events Underlying Excitation-Contraction Coupling in Heart Muscle." Science **262**: 740-744.
- Dedkova, E. N. and L. a. Blatter (2008). "Mitochondrial Ca^{2+} and the heart." Cell calcium **44**: 77-91.
- Delbridge, L. M., H. Satoh, et al. (1997). "Cardiac myocyte volume, Ca^{2+} fluxes, and sarcoplasmic reticulum loading in pressure-overload hypertrophy." Am J Physiol **272**(5 Pt 2): H2425-2435.
- Despa, S., F. Brette, et al. (2003). "Na/Ca exchange and Na/K-ATPase function are equally concentrated in transverse tubules of rat ventricular myocytes." Biophys J **85**(5): 3388-3396.
- Diaz, M. E., D. A. Eisner, et al. (2002). "Depressed ryanodine receptor activity increases variability and duration of the systolic Ca^{2+} transient in rat ventricular myocytes." Circ Res **91**(7): 585-593.
- Diaz, M. E., S. C. O'Neill, et al. (2004). "Sarcoplasmic reticulum calcium content fluctuation is the key to cardiac alternans." Circ Res **94**(5): 650-656.
- Drago, G. A., J. Colyer, et al. (1998). "Immunofluorescence Localization of SERCA2a and the Phosphorylated Forms of Phospholamban in Intact Rat Cardiac Ventricular Myocytes." Annals of the New York Academy of Sciences **853**: 273-279.
- Forbes, M. S., L. A. Hawkey, et al. (1984). "The transverse-axial tubular system (TATS) of mouse myocardium: its morphology in the developing and adult animal." Am J Anat **170**(2): 143-162.
- Frank, J. S., G. Mottino, et al. (1992). "Distribution of the Na^{+} - Ca^{2+} exchange protein in mammalian cardiac myocytes: an immunofluorescence and immunocolloidal gold-labeling study." J Cell Biol **117**(2): 337-345.
- Greene, A. L., M. J. Lalli, et al. (2000). "Overexpression of SERCA2b in the heart leads to an increase in sarcoplasmic reticulum calcium transport function and increased cardiac contractility." J Biol Chem **275**(32): 24722-24727.
- Guo, A., C. Zhang, et al. (2013). "Emerging mechanisms of T-tubule remodelling in heart failure." Cardiovasc Res **98**(2): 204-215.
- Gyorke, S., S. C. Stevens, et al. (2009). "Cardiac calsequestrin: quest inside the SR." J Physiol **587**(Pt 13): 3091-3094.

- Hake, J., A. G. Edwards, et al. (2012). "Modelling cardiac calcium sparks in a three-dimensional reconstruction of a calcium release unit." J Physiol **590**(Pt 18): 4403-4422.
- Harkins, A. B., N. Kurebayashi, et al. (1993). "Resting myoplasmic free calcium in frog skeletal muscle fibers estimated with fluo-3." Biophysical journal **65**: 865-881.
- HDF-group. (2014). "<http://www.hdfgroup.org/HDF5/>." from <http://www.hdfgroup.org/HDF5/>.
- Heinzel, F. R., V. Bito, et al. (2008). "Remodeling of T-tubules and reduced synchrony of Ca²⁺ release in myocytes from chronically ischemic myocardium." Circulation research **102**: 338-346.
- Izu, L. T., J. R. H. Mauban, et al. (2001). "Large currents generate cardiac Ca²⁺ sparks." Biophysical journal **80**: 88-102.
- Izu, L. T., W. G. Wier, et al. (2001). "Evolution of Cardiac Calcium Waves from Stochastic Calcium Sparks." **80**: 103-120.
- Jaffe, L. F. (1991). "The path of calcium in cytosolic calcium oscillations: a unifying hypothesis." Proceedings of the National Academy of Sciences of the United States of America **88**: 9883-9887.
- Jafri, M. S. (1995). "On the Roles of Ca²⁺ + Diffusion , Ca²⁺ + Buffers , and the Endoplasmic Reticulum in IP₃-Induced Ca²⁺ + Waves." **69**.
- Kaneko, T., H. Tanaka, et al. (2000). "Three distinct types of Ca(2+) waves in Langendorff-perfused rat heart revealed by real-time confocal microscopy." Circ Res **86**(10): 1093-1099.
- Kargacin, G. and F. S. Fay (1991). "Ca²⁺ movement in smooth muscle cells studied with one- and two-dimensional diffusion models." Biophys J **60**(5): 1088-1100.
- Kawai, M., M. Hussain, et al. (1999). "Excitation-contraction coupling in rat ventricular myocytes after formamide-induced detubulation." Am J Physiol **277**(2 Pt 2): H603-609.
- Keizer, J. and G. D. Smith (1998). "Spark-to-wave transition: saltatory transmission of calcium waves in cardiac myocytes." Biophysical chemistry **72**: 87-100.
- Keizer, J., G. D. Smith, et al. (1998). "Saltatory propagation of Ca²⁺ waves by Ca²⁺ sparks." Biophysical journal **75**: 595-600.
- Keller, M., J. P. Kao, et al. (2007). "Calcium waves driven by "sensitization" wave-fronts." Cardiovasc Res **74**(1): 39-45.
- Kieval, R. S., R. J. Bloch, et al. (1992). "Immunofluorescence localization of the Na-Ca exchanger in heart cells." Am J Physiol **263**(2 Pt 1): C545-550.

- Kockskamper, J., K. A. Sheehan, et al. (2001). "Activation and propagation of Ca^{2+} release during excitation-contraction coupling in atrial myocytes." Biophys J **81**(5): 2590-2605.
- Koh, X., B. Srinivasan, et al. (2006). "A 3D Monte Carlo analysis of the role of dyadic space geometry in spark generation." Biophysical journal **90**: 1999-2014.
- Kong, C. H. T., D. R. Laver, et al. (2013). "Extraction of Sub-microscopic Ca Fluxes from Blurred and Noisy Fluorescent Indicator Images with a Detailed Model Fitting Approach." PLoS Computational Biology **9**: e1002931.
- Kort, A. A., M. C. Capogrossi, et al. (1985). "Frequency, amplitude, and propagation velocity of spontaneous Ca^{++} -dependent contractile waves in intact adult rat cardiac muscle and isolated myocytes." Circ Res **57**(6): 844-855.
- Kubalova, Z., I. Györke, et al. (2004). "Modulation of cytosolic and intra-sarcoplasmic reticulum calcium waves by calsequestrin in rat cardiac myocytes." J Physiol **561**(Pt 2): 515-524.
- Kushmerick, M. J. and R. J. Podolsky (1969). "Ionic mobility in muscle cells." Science **166**(3910): 1297-1298.
- Laver, D. R., C. H. T. Kong, et al. (2013). "Termination of calcium-induced calcium release by induction decay: an emergent property of stochastic channel gating and molecular scale architecture." Journal of molecular and cellular cardiology **54**: 98-100.
- Li, P., M. Lancaster, et al. (2007). "A Three Dimensional Ventricular E-Cell (3Dv E-Cell) with Stochastic Intracellular Ca^{2+} Handling." 180-189.
- Lipp, P. and E. Niggli (1993). "Microscopic spiral waves reveal positive feedback in subcellular calcium signaling." Biophysical journal **65**: 2272-2276.
- Loughrey, C. M., K. E. MacEachern, et al. (2003). "Measurement of the dissociation constant of Fluo-3 for Ca^{2+} in isolated rabbit cardiomyocytes using Ca^{2+} wave characteristics." Cell Calcium **34**: 1-9.
- Lukyanenko, V. and S. Györke (1999). " Ca^{2+} sparks and Ca^{2+} waves in saponin-permeabilized rat ventricular myocytes." The Journal of physiology **521 Pt 3**: 575-585.
- Lukyanenko, V., S. Viatchenko-Karpinski, et al. (2001). "Dynamic regulation of sarcoplasmic reticulum Ca^{2+} content and release by luminal Ca^{2+} -sensitive leak in rat ventricular myocytes." Biophysical journal **81**: 785-798.
- Lyon, A. R., K. T. MacLeod, et al. (2009). "Loss of T-tubules and other changes to surface topography in ventricular myocytes from failing human and rat heart." PNAS **106**(16): 6854-6859.

- MacQuaide, N., H. R. Ramay, et al. (2010). "Differential sensitivity of Ca^{2+} wave and Ca^{2+} spark events to ruthenium red in isolated permeabilised rabbit cardiomyocytes." J Physiol **588**(Pt 23): 4731-4742.
- Macquaide, N., H.-T. M. Tuan, et al. (2014). "Functional consequences of RyR cluster fragmentation and redistribution in persistent atrial fibrillation." (in preparation).
- Michailova, A., F. DelPrincipe, et al. (2002). "Spatiotemporal Features of Ca^{2+} Buffering and Diffusion in Atrial Cardiac Myocytes with Inhibited Sarcoplasmic Reticulum." Biophysical Journal **83**: 3134-3151.
- Niggli, E. and N. Shirokova (2007). "A guide to sparkology: the taxonomy of elementary cellular Ca^{2+} signaling events." Cell calcium **42**: 379-387.
- Nivala, M., E. de Lange, et al. (2012). "Computational modeling and numerical methods for spatiotemporal calcium cycling in ventricular myocytes." Frontiers in physiology **3**: 114.
- O'Rourke, B. and L. A. Blatter (2009). "Mitochondrial Ca^{2+} uptake: tortoise or hare?" J Mol Cell Cardiol **46**(6): 767-774.
- Orchard, C. H., D. A. Eisner, et al. (1983). "Oscillations of intracellular Ca^{2+} in mammalian cardiac muscle." Nature **304**(5928): 735-738.
- Padmala, S. and S. S. Demir (2003). "Computational model of the ventricular action potential in adult spontaneously hypertensive rats." J Cardiovasc Electrophysiol **14**(9): 990-995.
- Page, E. (1978). "Quantitative ultrastructural analysis in cardiac membrane physiology." Am J Physiol **235**(5): C147-158.
- Page, E. and M. Surdyk-droske (1979). "Distribution , Surface Density , and Membrane Area of Diadic Junctional Contacts between Plasma Membrane and Terminal Cisterns in Mammalian Ventricle." Circulation Research: 260-267.
- Pandit, S. V., R. B. Clark, et al. (2001). "A mathematical model of action potential heterogeneity in adult rat left ventricular myocytes." Biophysical journal **81**: 3029-3051.
- Parker, I., W.-J. Zang, et al. (1996). " Ca^{2+} sparks involving multiple Ca^{2+} release sites along Z-lines in rat heart cells." Journal of Physiology **497**: 31-38.
- Pasek, M., F. Brette, et al. (2008). "Quantification of t-tubule area and protein distribution in rat cardiac ventricular myocytes." Prog Biophys Mol Biol **96**(1-3): 244-257.
- Periasamy, M. and S. Huke (2001). "SERCA pump level is a critical determinant of Ca^{2+} homeostasis and cardiac contractility." Journal of molecular and cellular cardiology **33**: 1053-1063.
- Picht, E., A. V. Zima, et al. (2011). "Dynamic calcium movement inside cardiac sarcoplasmic reticulum during release." Circulation research **108**: 847-856.

- Polakova, E. and E. A. Sobie (2013). "Alterations in T-tubule and dyad structure in heart disease: challenges and opportunities for computational analyses." Cardiovasc Res **98**(2): 233-239.
- Pratusevich, V. R. and C. W. Balke (1996). "Factors shaping the confocal image of the calcium spark in cardiac muscle cells." Biophysical journal **71**: 2942-2957.
- Qin, J., G. Valle, et al. (2008). "Luminal Ca²⁺ regulation of single cardiac ryanodine receptors: insights provided by calsequestrin and its mutants." J Gen Physiol **131**(4): 325-334.
- Ramay, H. R., M. S. Jafri, et al. (2010). "Predicting local SR Ca(2+) dynamics during Ca(2+) wave propagation in ventricular myocytes." Biophysical journal **98**: 2515-2523.
- Ramos-Franco, J., M. Fill, et al. (1998). "Isoform-specific function of single inositol 1,4,5-trisphosphate receptor channels." Biophysical journal **75**: 834-839.
- Restrepo, J. G. and A. Karma (2009). "Spatiotemporal intracellular calcium dynamics during cardiac alternans." Chaos **19**: 1-15.
- Restrepo, J. G., J. N. Weiss, et al. (2008). "Calsequestrin-mediated mechanism for cellular calcium transient alternans." Biophysical journal **95**: 3767-3789.
- Ridgway, E. B., J. C. Gilkey, et al. (1977). "Free calcium increases explosively in activating medaka eggs." Proc Natl Acad Sci U S A **74**(2): 623-627.
- Rossi, F. M. and J. P. Kao (1997). "Nmoc-DBHQ, a new caged molecule for modulating sarcoplasmic/endoplasmic reticulum Ca²⁺ ATPase activity with light flashes." J Biol Chem **272**(6): 3266-3271.
- Rovetti, R., X. Cui, et al. (2010). "Spark-induced sparks as a mechanism of intracellular calcium alternans in cardiac myocytes." Circulation research **106**: 1582-1591.
- Satoh, H., L. M. Delbridge, et al. (1996). "Surface:volume relationship in cardiac myocytes studied with confocal microscopy and membrane capacitance measurements: species-dependence and developmental effects." Biophysical journal **70**: 1494-1504.
- Scriven, D. R., P. Dan, et al. (2000). "Distribution of proteins implicated in excitation-contraction coupling in rat ventricular myocytes." Biophys J **79**(5): 2682-2691.
- Shah, M., M. B. Sikkil, et al. (2012). "Flecainide reduces wave frequency and mean spark amplitude in isolated rat ventricular cardiomyocytes." Cardiovascular Research **93**(Suppl. 1): S90.
- Shen, J. X., S. Wang, et al. (2004). "Polymorphism of Ca²⁺ sparks evoked from in-focus Ca²⁺ release units in cardiac myocytes." Biophys J **86**(1 Pt 1): 182-190.

- Shiferaw, Y. and A. Karma (2006). "Turing instability mediated by voltage and calcium diffusion in paced cardiac cells." Proceedings of the National Academy of Sciences of the United States of America **103**: 5670-5675.
- Smith, G. D., J. E. Keizer, et al. (1998). "A simple numerical model of calcium spark formation and detection in cardiac myocytes." Biophysical journal **75**: 15-32.
- Smith, G. L. and S. C. O'Neill (2001). "A comparison of the effects of ATP and tetracaine on spontaneous Ca^{2+} release from rat permeabilised cardiac myocytes." J Physiol **534**(Pt 1): 37-47.
- Sobie, E. A., K. W. Dilly, et al. (2002). "Termination of Cardiac Ca^{2+} Sparks: An Investigative Mathematical Model of Calcium-Induced Calcium Release." Biophysical Journal **83**: 59-78.
- Sobie, E. a., S. Guatimosim, et al. (2006). "The Ca^{2+} leak paradox and rogue ryanodine receptors: SR Ca^{2+} efflux theory and practice." Progress in biophysics and molecular biology **90**: 172-185.
- Sobie, E. a. and W. J. Lederer (2012). "Dynamic local changes in sarcoplasmic reticulum calcium: physiological and pathophysiological roles." Journal of molecular and cellular cardiology **52**: 304-311.
- Soeller, C. and M. B. Cannell (1999). "Examination of the Transverse Tubular System in Living Cardiac Rat Myocytes by 2-Photon Microscopy and Digital Image Processing Techniques." Circulation Research **84**: 266-275.
- Soeller, C., I. D. Jayasinghe, et al. (2009). "Three-dimensional high-resolution imaging of cardiac proteins to construct models of intracellular Ca^{2+} signalling in rat ventricular myocytes." Experimental physiology **94**: 496-508.
- Stewart, J. M. and E. Page (1978). "Improved stereological techniques for studying myocardial cell growth: application to external sarcolemma, T system, and intercalated disks of rabbit and rat hearts." J Ultrastruct Res **65**(2): 119-134.
- Stuyvers, B. D., P. A. Boyden, et al. (2000). "Calcium Waves. Physiological Relevance in Cardiac Function." Circulation Research **86**: 1016-1018.
- Swietach, P., K. W. Spitzer, et al. (2008). " Ca^{2+} -mobility in the sarcoplasmic reticulum of ventricular myocytes is low." Biophysical journal **95**: 1412-1427.
- Swietach, P., K. W. Spitzer, et al. (2010). "Modeling calcium waves in cardiac myocytes : importance of calcium diffusion." Frontiers in Biociencia **15**: 661-680.
- Swift, F., T. A. Stromme, et al. (2006). "Slow diffusion of K^{+} in the T tubules of rat cardiomyocytes." J Appl Physiol (1985) **101**(4): 1170-1176.

- Terentyev, D., S. Viatchenko-Karpinski, et al. (2003). "Calsequestrin determines the functional size and stability of cardiac intracellular calcium stores: Mechanism for hereditary arrhythmia." Proceedings of the National Academy of Sciences of the United States of America **100**: 11759-11764.
- Thul, R., S. Coombes, et al. (2012). "Subcellular calcium dynamics in a whole-cell model of an atrial myocyte." PNAS **109**: 2150-2155.
- Trafford, A. W., P. Lipp, et al. (1995). "Propagating calcium waves initiated by local caffeine application in rat ventricular myocytes." J Physiol **489 (Pt 2)**: 319-326.
- Wagner, E., M. a. Lauterbach, et al. (2012). "Stimulated emission depletion live-cell super-resolution imaging shows proliferative remodeling of T-tubule membrane structures after myocardial infarction." Circulation research **111**: 402-414.
- Wang, J. H. (1953). "Tracer-diffusion in Liquids. IV. Self-diffusion of Calcium Ion and Chloride Ion in Aqueous Calcium Chloride Solutions." J. Am. Chem. Soc **75(7)**: 1769–1770.
- Wang, S. Q., M. D. Stern, et al. (2004). "The quantal nature of Ca²⁺ sparks and in situ operation of the ryanodine receptor array in cardiac cells." Proceedings of the National Academy of Sciences of the United States of America **101**: 3979-3984.
- Wei, S., A. Guo, et al. (2010). "T-tubule remodeling during transition from hypertrophy to heart failure." Circ Res **107(4)**: 520-531.
- Wier, W. G. and L. A. Blatter (1991). "Ca(2+)-oscillations and Ca(2+)-waves in mammalian cardiac and vascular smooth muscle cells." Cell Calcium **12(2-3)**: 241-254.
- Wier, W. G., M. B. Cannell, et al. (1987). "Cellular and subcellular heterogeneity of [Ca²⁺]_i in single heart cells revealed by fura-2." Science **235(4786)**: 325-328.
- Wier, W. G., H. E. ter Keurs, et al. (1997). "Ca²⁺ 'sparks' and waves in intact ventricular muscle resolved by confocal imaging." Circ Res **81(4)**: 462-469.
- Williams, G. S. B., A. C. Chikando, et al. (2011). "Dynamics of Calcium Sparks and Calcium Leak in the Heart." Biophysical journal **101**: 1287-1296.
- Woods, N. M., K. S. Cuthbertson, et al. (1986). "Repetitive transient rises in cytoplasmic free calcium in hormone-stimulated hepatocytes." Nature **319(6054)**: 600-602.
- Woods, N. M., K. S. Cuthbertson, et al. (1987). "Agonist-induced oscillations in cytoplasmic free calcium concentration in single rat hepatocytes." Cell Calcium **8(1)**: 79-100.
- Wu, X. and D. M. Bers (2006). "Sarcoplasmic reticulum and nuclear envelope are one highly interconnected Ca²⁺ store throughout cardiac myocyte." Circulation research **99**: 283-291.

- Yang, Z., C. Pascarel, et al. (2002). "Na⁺-Ca²⁺ exchange activity is localized in the T-tubules of rat ventricular myocytes." Circ Res **91**(4): 315-322.
- Zima, A. V., E. Picht, et al. (2008). "Termination of cardiac Ca²⁺ sparks: role of intra-SR [Ca²⁺], release flux, and intra-SR Ca²⁺ diffusion." Circulation research **103**: e105-115.

CHAPTER 6: CONCLUSION AND FUTURE DIRECTION

Conclusion

This dissertation has presented a novel computational algorithm for simulating stochastic gating of ion channels in a cluster that forms the basis of a calcium release site. Each cluster comprises two types of ion channels: ryanodine receptors (RyRs) and L-type Ca^{2+} channels (LCCs). Each channel is represented by a Markov-model with a finite number of states. The stochastic gating of ion channels requires the small time-step. An adaptive time-step strategy was used, i.e. dt in the range from 10 ns to 0.1 μs . The code was developed in such a way that enables us to incorporate any Markov-based model of single channel RyR or LCC of any given number of states to study different pathophysiological conditions, such as CPVT (catecholaminergic polymorphic ventricular tachycardia) that links to RyR mutations (Chen et al., 2013; George, Jundi, Thomas, Fry, & Lai, 2007; Gyorke, 2009), or Timothy syndrome (LQT8), Brugada syndrome (BrS) that link to LCC mutations (Antzelevitch et al., 2007; Burashnikov et al., 2010).

Together, the clusters of RyRs and LCCs form the calcium release sites, which is essential to the local control of Ca^{2+} release during excitation contraction coupling. The synchronized opening of clustered RyRs results in elevations of local $[\text{Ca}^{2+}]$ known as Ca^{2+} sparks (Cheng, Lederer, & Cannell, 1993). Using the developed algorithm, for the

first time, a whole-cell model can feature a realistic number of Ca^{2+} release sites – 20,000, whose biophysical properties (e.g. Ca^{2+} sensitivity and allosteric interactions) are informed by the latest molecular investigations. The model is able to reproduce this visible Ca^{2+} sparks phenomenon, with the peak of local Ca^{2+} elevation is $\sim 100 \mu\text{M}$ (Williams et al., 2011). More importantly, the model helps to explain the balance of Ca^{2+} homeostasis based on Ca^{2+} sparks and the ‘invisible’ Ca^{2+} leak, the non-spark events, which is the result of stochastic opening of one or a few RyR2 channels. The fully stochastic model now matches the biology and provides what we believe to be new insight into the mechanism by which SR Ca^{2+} leak operates in intact cells. This is important as SR Ca^{2+} content is regulated by Ca^{2+} leak, and is observed to change in response to diverse disease (George, 2008; X. H. Wehrens, Lehnart, & Marks, 2005) or phosphorylation by kinases such as Ca^{2+} -calmodulin-dependent kinase II (CaMKII) or protein kinase A (Marx et al., 2000; Neef et al., 2010).

As RyR is the Ca^{2+} gate, mutations in this channel or proteins involving in the regulation of this channel are found to link to different forms of cellular instability or diseases, e.g. arrhythmogenesis, Ca^{2+} alternans, CPVT (Lehnart et al., 2004; Lehnart et al., 2005; Vest et al., 2005; X. H. T. Wehrens et al., 2006; X. H. T. Wehrens et al., 2004; X. H. T. Wehrens & Marks, 2003). A computational model that offers an explicit means to investigate nanoscale events that cannot be easily measured under experimental settings is critical to our understanding of heart function during both physiological and pathophysiological conditions. In summary, the method and model developed provided the following major new findings. The presence of ‘invisible’ Ca^{2+} leak (Santiago et al.,

2010), that along with visible Ca^{2+} leak, help to explain the balance with diastolic Ca^{2+} uptake via SERCA pump (Tran, Smith, Loiselle, & Crampin, 2009), without using an energetically unfavored back-flux model (Shannon, Ginsburg, & Bers, 2000). Backflux doesn't happen at physiological conditions, unless at very high SR $[\text{Ca}^{2+}]$. The model with fully stochastic activation and termination of RyR-based Ca^{2+} release now obviate the inclusion of an ad-hoc, non-RyR-mediated Ca^{2+} leak flux. The SR $[\text{Ca}^{2+}]$ level depend critically on RyR open probability (P_o); and the increased RyR activity can lead to increase SR Ca^{2+} leak even in the presence of decreased $[\text{Ca}^{2+}]_{\text{SR}}$ (Williams et al., 2011).

Using the model that represents the most detailed level of calcium cycling control so far, we are able to shed light on the mechanism of Ca^{2+} alternans in the cardiac myocyte at high pacing frequency and the role of T-tubule remodelling during heart failure (Wagner et al., 2012). T-tubule networks form the tightly electrically coupled junction between the sarcolemma (SL) and the internal calcium storage SR at universally everywhere in the cell. However, during myocardial infarction, the longitudinal and oblique T-tubules were significantly increased, whereas the transversal components appeared decreased. The transversal components are located where the junctions between the L-type Ca^{2+} channels and the RyRs are formed. The model allows us to study the changes in T-tubule morphology and associated proteins during heart failure (HF) to the functional Ca^{2+} dynamics (Wagner et al., 2012). The altering in junctophilin-2 (Jph2), a protein that mediate the crosstalk between T-tubule membrane and jSR membrane, significantly increase the variability of CRU spacing at T-tubule junctions – a possible orphaning mechanism (Song et al., 2006; van Oort et al., 2011).

The orphaning CRUs were simulated by increasing the subspace volume at which calcium is sensed by the RyR channels. The amount of orphan CRUs was selected as 25%, which is consistent with an earlier study (Song et al., 2006). The simulated condition for heart failure was studied by implementing previously observed (published) changes in ion transport proteins: fast and slow K⁺ currents (I_{to} and I_K) were reduced by 30%; NCX protein expression was increased by 100% (Hasenfuss et al., 1999); SR Ca²⁺ ATPase (SERCA2a) protein was decreased by 30% (Meyer et al., 1995); and RyR2 Ca²⁺ sensitivity was increased by 50% to mimic increased activity from chronic hyperphosphorylation (Lehnart et al., 2005). The results showed a significant prolongation in AP duration in heart failure which is in parallel by a delay in $[Ca^{2+}]$ activation, during diastolic phase and increased SR Ca²⁺ leak during diastolic phase. Importantly, the model reproduced decreased SR Ca²⁺ load, a hallmark of EC coupling pathophysiology in HF, which was blunted by RyR2 orphaning. Unexpectedly, combined RyR2 orphaning with HF improve SR $[Ca^{2+}]$ load in diastole. Whereas RyR2 orphaning by itself did not increase spark dependent Ca²⁺ leak, in HF additional orphaning of RyR2 clusters further increased diastolic Ca²⁺ sparks and Ca²⁺ leak. Therefore, in addition to EC uncoupling in HF, the heterogeneous spatial reorganization of T-tubule and RyR2 clusters may aggravate the experimentally observed delayed and dyssynchronous SR Ca²⁺ release, which promote severe diastolic SR Ca²⁺ leak, which potentially contribute to afterdepolarizations and Ca²⁺-triggered arrhythmias.

In addition, the compartmental whole-cell model is able to reproduce Ca^{2+} alternans at high frequency, and help to explain a novel mechanism that lead to Ca^{2+} alternans. The effect of high pacing rates was first done by Chudin and co-workers using Luo-Rudy-2 model (E. Chudin, Garfinkel, Weiss, Karplus, & Kogan, 1998). Luo-Rudy-2 model is a deterministic common-pool model (Luo & Rudy, 1994). Here, the gradedness of calcium-induced calcium release was formulated using a threshold mechanism which is a phenomenological assumption, not a mechanistic representation of the underlying cellular process. In addition, the LR-2 model wasn't able to explain the cellular mechanism leading to the alternation in $[\text{Ca}^{2+}]_i$ transient and V_m .

The tightly controlled coupling between global calcium elevation and membrane voltage V_m is important for the normal excitation-contraction mechanism. Under rapid pacing, the complex dynamics of both V_m and $[\text{Ca}^{2+}]_i$ can occur. Rapid pacing, which can be the result of intense physical activity or fright, the systole and diastole are shorten. However, at fast rate of contraction, not all ion channels can recover from inactivation fully; nor the recovery of Ca^{2+} from the internal calcium storage – the SR. This results in decreased current, which can cause a less contraction leading to a lack of blood pumping.

At high pacing, the diastolic $[\text{Ca}^{2+}]_i$ is still high, which affect the level of $\text{Ca}^{2+}/\text{Calm}$. The high level of calcium-bound calmodulin ($\text{Ca}^{2+}/\text{Calm}$) affect the Ca^{2+} -dependent inactivation of L-type Ca^{2+} channels (LCCs) gating, or the opening probability (P_o) of LCCs. Another factor that may affect P_o of LCCs is the membrane voltage. The depolarization of membrane voltage is strongly affected by the sodium current. The number of recruited CRUs depends preferentially on the influx via LCCs. Early efforts to

model this by introducing a phenomenological term P_{cicr} (probability of CICR), and another term γ to represent the portion of jSR with Ca^{2+} available for release (E Chudin, Goldhaber, Garfinkel, Weiss, & Kogan, 1999). Clearly, this is not a mechanistic representation that may help to explain the underlying cellular mechanism of Ca^{2+} alternans. In our model, at high pacing frequency, the short basic cycle length (BCL) affects the recovery of the gating variables of Na^+ channels, which in turns reduce the depolarization of membrane potential V_m . As a result of a cascade event, this in turns affect the gating of L-type Ca^{2+} channels which is further disturbed by the high basal level of $Ca^{2+}/Calm$.

Another factor that plays a significant role is the variation in jSR Ca^{2+} recovery at the beginning of each beat at activated CRUs and inactivated CRUs (Diaz, O'Neill, & Eisner, 2004). Bers suggested a theory of nonlinear dependence of Ca^{2+} release on the SR $[Ca^{2+}]$, i.e. a small change in SR $[Ca^{2+}]$ can lead to a large change in Ca^{2+} release (Bers, 2000). Diaz and co-workers were able to demonstrate alternating levels of resting SR Ca^{2+} from beat to beat during Ca^{2+} alternans (Diaz et al., 2004). This is in agreement with the result produced by our model. In another experimental study, Picht and co-workers found 20% of the cases with Ca^{2+} alternans without significant SR Ca^{2+} alterations. This was accounted for the slow SR Ca^{2+} release responsiveness, i.e. RyR refractoriness (Picht, DeSantiago, Blatter, & Bers, 2006), a feature that is not readily available in our current model. Further, their study didn't show an alternation in I_{CaL} . So, the mechanism displayed in the model is supposed to be different. In summary, the developed model help

to provide a mechanistic explanation for the generation of Ca^{2+} alternans, in that not a single element, but the multitude of factors that involve in the Ca^{2+} alternans genesis.

A number of spatial temporal model have been developed previously. They are either 2D (R. Rovetti, Cui, Garfinkel, Weiss, & Qu, 2010; R. J. Rovetti, 2008) or 3D (Nivala, de Lange, Rovetti, & Qu, 2012; Restrepo, Weiss, & Karma, 2008). However, these models can not reproduce Ca^{2+} sparks, the elementary events that underline the basis of excitation-contraction coupling. The failure to control Ca^{2+} release at these local release sites can manifest into life-threatening triggered arrhythmias (Cheng & Lederer, 2008; Hove-Madsen et al., 2004; Stern, Ríos, & Maltsev, 2013). Thus, a ‘good’ model that can help us to provide reliable predictions should incorporates this important feature. The novel 3D temporal spatial model for the ventricular myocyte introduced in this thesis is thus advanced in many ways. First, the gating of ion channels is modelled stochastically with the kinetics of RyRs fitted to give the proper fidelity of spark generation that matches the experimental data, i.e. ~ 100 sparks/cell/sec at rest. Secondly, the non-uniform distribution of SL, SR buffers and NCX were incorporated in the model. Thirdly, the dynamics of calcium buffering in the subspace and the myoplasm, are modelled explicitly, not fast binding assumption.

The couple gating of ion channels implemented in the compartmental model was also extended into this spatial model that incorporates very detailed of excitation-contraction coupling mechanism. This includes spatial placement of calcium release sites, non-uniform distribution of ion channels on the sarcolemma, particularly $\text{Na}^+/\text{Ca}^{2+}$ exchanger, SL buffer, SR buffers. The developed models, both compartmental model and

temporal spatial model, have enabled us to study and explain ionic changes during heart failure, cardiac alternans, atrial fibrillation, and spontaneous calcium waves.

Future directions

Cardiac excitation-contraction coupling occurs primarily at the site of T-tubule/jSR junctions (Fawcett & McNutt, 1969). Even though the majority of the T-tubules are within 0.5 μm from the Z-lines, a significant fraction of T-tubule networks branching in the longitudinal direction as well (Soeller & Cannell, 1999). Thus, the impact of T-tubule remodelling on myocyte Ca^{2+} handling function is expected to be critical (review: (Guo, Zhang, Wei, Chen, & Song, 2013)). T-tubule remodelling has been found during the transition from hypertrophy to heart failure. Regardless of the loss of transverse elements, there is a gain in longitudinal elements, giving rise to a chaotic appearance in the T-tubule networks (Song et al., 2006). This may disturb the crosstalk between LCCs and RyR2s (Bito, Heinzel, Biesmans, Antoons, & Sipido, 2008). A subcellular gradient in $[\text{Ca}^{2+}]_i$ was showed in an experimental study in neonatal rabbit ventricular myocytes which lack T-tubule systems (Haddock et al., 1999). It was thus suggested that T-tubule remodelling is not a secondary modification after heart failure, but instead an important early event during heart-failure progression. Using the developed 3D model, we can help to explain the role of T-tubule remodelling at different regions of the cell to the normal function of EC coupling.

Early evidences of subcellular heterogeneity of $[\text{Ca}^{2+}]_i$ was reported in late 1980s (Wier, Cannell, Berlin, Marban, & Lederer, 1987). Here, the spatial uniformity of Ca^{2+} elevation was interrupted by Ca^{2+} waves. Recently, there are several experimental results

that showed subcellular Ca^{2+} alternans, and suggested its role in the generation of arrhythmogenic Ca^{2+} waves (Aistrup, Shiferaw, Kapur, Kadish, & Wasserstrom, 2009; Blatter et al., 2002; Kocksamper & Blatter, 2002). The mechanism for the formation of spatiotemporal evolution of these phase-mismatched CRUs is not known. Using the developed model, we hope it can shed a light on the underlying mechanism for this dynamical phenomenon.

Apart from the given scientific questions that can be resolved using the developed model, the 3D model can be extended to answer other scientific questions

1. Developing a novel RyR2 model that incorporate CSQ2 dependent and Calm dependent to study arrhythmogenesis of CPVT and other cardiac diseases syndrome.
2. A computational model for the atrial myocyte to study atrial fibrillation can be developed by removing the T-tubule from the model. One way to do this is to block L-type Ca^{2+} channels in the T-tubule, and remove the subspace so that RyR sense cytosolic calcium from one or more neighboring gridpoints.
3. An ambitious plan is to incorporate the 3D cells into a tissue model to study discordant alternans. This requires an extremely high computational demand, and thus multi-GPGPUs or an upcoming hybrid CPU-GPU architecture can be used to run the model.

REFERENCES

- Aistrup, G. L., Shiferaw, Y., Kapur, S., Kadish, A. H., & Wasserstrom, J. A. (2009). Mechanisms underlying the formation and dynamics of subcellular calcium alternans in the intact rat heart. *Circulation research*, 104, 639-649. doi: 10.1161/CIRCRESAHA.108.181909
- Antzelevitch, C., Pollevick, G. D., Cordeiro, J. M., Casis, O., Sanguinetti, M. C., Aizawa, Y., . . . Wolpert, C. (2007). Loss-of-function mutations in the cardiac calcium channel underlie a new clinical entity characterized by ST-segment elevation, short QT intervals, and sudden cardiac death. [Research Support, Non-U.S. Gov't]. *Circulation*, 115(4), 442-449. doi: 10.1161/CIRCULATIONAHA.106.668392
- Bers, D. M. (2000). Calcium Fluxes Involved in Control of Cardiac Myocyte Contraction. *Circulation Research*, 87, 275-281. doi: 10.1161/01.RES.87.4.275
- Bito, V., Heinzel, F. R., Biesmans, L., Antoons, G., & Sipido, K. R. (2008). Crosstalk between L-type Ca²⁺ channels and the sarcoplasmic reticulum: alterations during cardiac remodelling. [Research Support, Non-U.S. Gov't Review]. *Cardiovasc Res*, 77(2), 315-324. doi: 10.1093/cvr/cvm063
- Blatter, L. a., Kockskamper, J., Sheehan, K. a., Zima, a. V., Huser, J., & Lipsius, S. L. (2002). Local calcium gradients during excitation-contraction coupling and alternans in atrial myocytes. *The Journal of Physiology*, 546, 19-31. doi: 10.1113/jphysiol.2002.025239
- Burashnikov, E., Pfeiffer, R., Barajas-Martinez, H., Delpon, E., Hu, D., Desai, M., . . . Antzelevitch, C. (2010). Mutations in the cardiac L-type calcium channel associated with inherited J-wave syndromes and sudden cardiac death. [Research Support, N.I.H., Extramural Research Support, Non-U.S. Gov't]. *Heart Rhythm*, 7(12), 1872-1882. doi: 10.1016/j.hrthm.2010.08.026
- Chen, H., Valle, G., Furlan, S., Nani, A., Gyorke, S., Fill, M., & Volpe, P. (2013). Mechanism of calsequestrin regulation of single cardiac ryanodine receptor in

- normal and pathological conditions. *The Journal of general physiology*, 142, 127-136. doi: 10.1085/jgp.201311022
- Cheng, H., & Lederer, W. J. (2008). Calcium sparks. *Physiological reviews*, 88, 1491-1545. doi: 10.1152/physrev.00030.2007
- Cheng, H., Lederer, W. J. J., & Cannell, M. B. (1993). Calcium Sparks: Elementary Events Underlying Excitation-Contraction Coupling in Heart Muscle. *Science*, 262, 740-744.
- Chudin, E., Garfinkel, A., Weiss, J., Karplus, W., & Kogan, B. (1998). Wave propagation in cardiac tissue and effects of intracellular calcium dynamics (computer simulation study). [Research Support, U.S. Gov't, P.H.S.
- Review]. *Prog Biophys Mol Biol*, 69(2-3), 225-236.
- Chudin, E., Goldhaber, J. I., Garfinkel, A., Weiss, J. N., & Kogan, B. (1999). Intracellular Ca(2+) dynamics and the stability of ventricular tachycardia. *Biophysical journal*, 77, 2930-2941. doi: 10.1016/S0006-3495(99)77126-2
- Diaz, M. E., O'Neill, S. C., & Eisner, D. A. (2004). Sarcoplasmic reticulum calcium content fluctuation is the key to cardiac alternans. [Research Support, Non-U.S. Gov't]. *Circ Res*, 94(5), 650-656. doi: 10.1161/01.RES.0000119923.64774.72
- Fawcett, D. W., & McNutt, N. S. (1969). The ultrastructure of the cat myocardium. I. Ventricular papillary muscle. *J Cell Biol*, 42(1), 1-45.
- George, C. H. (2008). Sarcoplasmic reticulum Ca²⁺ leak in heart failure: mere observation or functional relevance? *Cardiovascular research*, 77, 302-314. doi: 10.1093/cvr/cvm006
- George, C. H., Jundi, H., Thomas, N. L., Fry, D. L., & Lai, F. A. (2007). Ryanodine receptors and ventricular arrhythmias: emerging trends in mutations, mechanisms and therapies. *Journal of molecular and cellular cardiology*, 42, 34-50. doi: 10.1016/j.yjmcc.2006.08.115
- Guo, A., Zhang, C., Wei, S., Chen, B., & Song, L. S. (2013). Emerging mechanisms of T-tubule remodelling in heart failure. [Research Support, N.I.H., Extramural Research Support, Non-U.S. Gov't
- Review]. *Cardiovasc Res*, 98(2), 204-215. doi: 10.1093/cvr/cvt020
- Gyorke, S. (2009). Molecular basis of catecholaminergic polymorphic ventricular tachycardia. [Research Support, N.I.H., Extramural

Review]. *Heart Rhythm*, 6(1), 123-129. doi: 10.1016/j.hrthm.2008.09.013

Haddock, P. S., Coetzee, W. A., Cho, E., Porter, L., Katoh, H., Bers, D. M., . . . Artman, M. (1999). Subcellular $[Ca^{2+}]_i$ gradients during excitation-contraction coupling in newborn rabbit ventricular myocytes. [Research Support, Non-U.S. Gov't

Research Support, U.S. Gov't, P.H.S.]. *Circ Res*, 85(5), 415-427.

Hasenfuss, G., Schillinger, W., Lehnart, S. E., Preuss, M., Pieske, B., Maier, L. S., . . . Just, H. (1999). Relationship between Na^+ - Ca^{2+} -exchanger protein levels and diastolic function of failing human myocardium. [Comparative Study

In Vitro

Research Support, Non-U.S. Gov't]. *Circulation*, 99(5), 641-648.

Hove-Madsen, L., Llach, A., Bayes-Genís, A., Roura, S., Rodriguez Font, E., Arís, A., & Cinca, J. (2004). Atrial fibrillation is associated with increased spontaneous calcium release from the sarcoplasmic reticulum in human atrial myocytes. *Circulation*, 110, 1358-1363. doi: 10.1161/01.CIR.0000141296.59876.87

Kockskamper, J., & Blatter, L. a. (2002). Subcellular Ca^{2+} alternans represents a novel mechanism for the generation of arrhythmogenic Ca^{2+} waves in cat atrial myocytes. *The Journal of Physiology*, 545, 65-79. doi: 10.1113/jphysiol.2002.025502

Lehnart, S. E., Wehrens, X. H. T., Laitinen, P. J., Reiken, S. R., Deng, S.-X., Cheng, Z., . . . Marks, A. R. (2004). Sudden death in familial polymorphic ventricular tachycardia associated with calcium release channel (ryanodine receptor) leak. *Circulation*, 109, 3208-3214. doi: 10.1161/01.CIR.0000132472.98675.EC

Lehnart, S. E., Wehrens, X. H. T., Reiken, S., Warrier, S., Andriy, E., Harvey, R. D., . . . Marks, R. (2005). Phosphodiesterase 4D deficiency in the Ryanodine-Receptor Complex Promotes Heart Failure and Arrhythmias. *Cell*, 123, 25-35. doi: 10.1016/j.cell.2005.07.030.Phosphodiesterase

Luo, C. H., & Rudy, Y. (1994). A dynamic model of the cardiac ventricular action potential. I. Simulations of ionic currents and concentration changes. *Circulation research*, 74, 1071-1096.

Marx, S. O., Reiken, S., Hisamatsu, Y., Jayaraman, T., Burkhoff, D., Rosemblyt, N., & Marks, A. R. (2000). PKA phosphorylation dissociates FKBP12.6 from the calcium release channel (ryanodine receptor): defective regulation in failing hearts. *Cell*, 101, 365-376.

- Meyer, M., Schillinger, W., Pieske, B., Holubarsch, C., Heilmann, C., Posival, H., . . . et al. (1995). Alterations of sarcoplasmic reticulum proteins in failing human dilated cardiomyopathy. [Research Support, Non-U.S. Gov't]. *Circulation*, 92(4), 778-784.
- Neef, S., Dybkova, N., Sossalla, S., Ort, K. R., Fluschnik, N., Neumann, K., . . . Maier, L. S. (2010). CaMKII-dependent diastolic SR Ca²⁺ leak and elevated diastolic Ca²⁺ levels in right atrial myocardium of patients with atrial fibrillation. [Research Support, Non-U.S. Gov't]. *Circ Res*, 106(6), 1134-1144. doi: 10.1161/CIRCRESAHA.109.203836
- Nivala, M., de Lange, E., Rovetti, R., & Qu, Z. (2012). Computational modeling and numerical methods for spatiotemporal calcium cycling in ventricular myocytes. *Frontiers in physiology*, 3, 114. doi: 10.3389/fphys.2012.00114
- Picht, E., DeSantiago, J., Blatter, L. A., & Bers, D. M. (2006). Cardiac alternans do not rely on diastolic sarcoplasmic reticulum calcium content fluctuations. [Research Support, N.I.H., Extramural Research Support, Non-U.S. Gov't]. *Circ Res*, 99(7), 740-748. doi: 10.1161/01.RES.0000244002.88813.91
- Restrepo, J. G., Weiss, J. N., & Karma, A. (2008). Calsequestrin-mediated mechanism for cellular calcium transient alternans. *Biophysical journal*, 95, 3767-3789. doi: 10.1529/biophysj.108.130419
- Rovetti, R., Cui, X., Garfinkel, A., Weiss, J. N., & Qu, Z. (2010). Spark-induced sparks as a mechanism of intracellular calcium alternans in cardiac myocytes. *Circulation research*, 106, 1582-1591. doi: 10.1161/CIRCRESAHA.109.213975
- Rovetti, R. J. (2008). Stochastic models of intracellular calcium release and alternans (pp. 24).
- Santiago, D. J., Curran, J. W., Bers, D. M., Lederer, W. J., Stern, M. D., Ríos, E., & Shannon, T. R. (2010). Ca sparks do not explain all ryanodine receptor-mediated SR Ca leak in mouse ventricular myocytes. *Biophysical journal*, 98, 2111-2120. doi: 10.1016/j.bpj.2010.01.042
- Shannon, T. R., Ginsburg, K. S., & Bers, D. M. (2000). Reverse mode of the sarcoplasmic reticulum calcium pump and load-dependent cytosolic calcium decline in voltage-clamped cardiac ventricular myocytes. *Biophysical journal*, 78, 322-333. doi: 10.1016/S0006-3495(00)76595-7
- Soeller, C., & Cannell, M. B. (1999). Examination of the Transverse Tubular System in Living Cardiac Rat Myocytes by 2-Photon Microscopy and Digital

- Image Processing Techniques. *Circulation Research*, 84, 266-275. doi: 10.1161/01.RES.84.3.266
- Song, L. S., Sobie, E. A., McCulle, S., Lederer, W. J., Balke, C. W., & Cheng, H. (2006). Orphaned ryanodine receptors in the failing heart. [Research Support, N.I.H., Extramural Research Support, Non-U.S. Gov't]. *Proc Natl Acad Sci U S A*, 103(11), 4305-4310. doi: 10.1073/pnas.0509324103
- Stern, M. D., Ríos, E., & Maltsev, V. a. (2013). Life and death of a cardiac calcium spark. *The Journal of general physiology*, 142, 257-274. doi: 10.1085/jgp.201311034
- Tran, K., Smith, N. P., Loiselle, D. S., & Crampin, E. J. (2009). A Thermodynamic Model of the Cardiac Sarcoplasmic/ Endoplasmic Ca²⁺ (SERCA) Pump. *Biophysical journal*, 96, 2029-2042. doi: 10.1016/j.bpj.2008.11.045
- van Oort, R. J., Garbino, A., Wang, W., Dixit, S. S., Landstrom, A. P., Gaur, N., . . . Wehrens, X. H. (2011). Disrupted junctional membrane complexes and hyperactive ryanodine receptors after acute junctophilin knockdown in mice. [Comparative Study]. *Circulation*, 123(9), 979-988. doi: 10.1161/CIRCULATIONAHA.110.006437
- Vest, J. A., Wehrens, X. H., Reiken, S. R., Lehnart, S. E., Dobrev, D., Chandra, P., . . . Marks, A. R. (2005). Defective cardiac ryanodine receptor regulation during atrial fibrillation. [Research Support, Non-U.S. Gov't Research Support, U.S. Gov't, P.H.S.]. *Circulation*, 111(16), 2025-2032. doi: 10.1161/01.CIR.0000162461.67140.4C
- Wagner, E., Lauterbach, M. a., Kohl, T., Westphal, V., Williams, G. S. B., Steinbrecher, J. H., . . . Lehnart, S. E. (2012). Stimulated emission depletion live-cell super-resolution imaging shows proliferative remodeling of T-tubule membrane structures after myocardial infarction. *Circulation research*, 111, 402-414. doi: 10.1161/CIRCRESAHA.112.274530
- Wehrens, X. H., Lehnart, S. E., & Marks, A. R. (2005). Intracellular calcium release and cardiac disease. [Review]. *Annu Rev Physiol*, 67, 69-98. doi: 10.1146/annurev.physiol.67.040403.114521
- Wehrens, X. H. T., Lehnart, S. E., Reiken, S., Vest, J. a., Wronska, A., & Marks, A. R. (2006). Ryanodine receptor/calcium release channel PKA phosphorylation: a critical mediator of heart failure progression. *Proceedings of the National*

Academy of Sciences of the United States of America, 103, 511-518. doi: 10.1073/pnas.0510113103

Wehrens, X. H. T., Lehnart, S. E., Reiken, S. R., Deng, S.-X., Vest, J. a., Cervantes, D., . . . Marks, A. R. (2004). Protection from cardiac arrhythmia through ryanodine receptor-stabilizing protein calstabin2. *Science (New York, N.Y.)*, 304, 292-296. doi: 10.1126/science.1094301

Wehrens, X. H. T., & Marks, A. R. (2003). Altered function and regulation of cardiac ryanodine receptors in cardiac disease. *Trends in biochemical sciences*, 28, 671-678. doi: 10.1016/j.tibs.2003.10.003

Wier, W. G., Cannell, M. B., Berlin, J. R., Marban, E., & Lederer, W. J. (1987). Cellular and subcellular heterogeneity of [Ca]²⁺ in single heart cells revealed by Fura-2. *Science (New York, N.Y.)*, 235, 325-328.

Williams, G. S. B., Chikando, A. C., Tuan, H.-T. M., Sobie, E. a., Lederer, W. J., & Jafri, M. S. (2011). Dynamics of Calcium Sparks and Calcium Leak in the Heart. *Biophysical journal*, 101, 1287-1296. doi: 10.1016/j.bpj.2011.07.021

BIOGRAPHY

Hoang-Trong Minh Tuan was born on July, 7th 1982 in Hue city, Vietnam. graduated from Quoc Hoc High School for the Gifted, Hue, Vietnam, in 2000. He finished his Bachelor of Science in Computer Science from HoChiMinh City University of Technology in Vietnam on May, 2005. After 6-months working for a software company, in 2006, he received a scholarship at Chonnam National University, South Korea. He completed the Master in Computer Engineering in March, 2008. From 2008-2014, he is a PhD student and PhD candidate in the Department of Bioinformatics and Computational Biology, George Mason University, USA.

Published/In-preparation works

1. Williams, G. S. B., Chikando, A. C., **Tuan, H.-T. M.**, Sobie, E. a, Lederer, W. J., & Jafri, M. S. (2011). Dynamics of Calcium Sparks and Calcium Leak in the Heart. *Biophysical Journal*, 101(6), 1287–96. doi:10.1016/j.bpj.2011.07.021
2. **Tuan M. Hoang-Trong**, George S.B. Williams, Aristide C. Chikando, Eric A. Sobie, W.J. Lederer, M. Saleet Jafri, “Stochastic Simulation of Cardiac Calcium Dynamics and Waves” (33rd IEEE-EMBC Conference, Boston, Aug. 2011)
3. Wagner, E., Lauterbach, M. a, Kohl, T., Westphal, V., Williams, G. S. B., Steinbrecher, J. H., Korff, Brigitte, **Tuan, Hoang-Trong M.**, Hagen, Brian, Luther, Stefan, Hasenfuss, Gerd, Parltitz, Ulrich, Jafri, M Saleet, Hell, Stefan W, Lederer, W Jonathan, Lehnart, S. E. (2012). Stimulated emission depletion live-cell super-resolution imaging shows proliferative remodeling of T-tubule membrane structures after myocardial infarction. *Circulation Research*, 111(4), 402–14. doi:10.1161/CIRCRESAHA.112.274530
4. **Tuan M. Hoang-Trong**, George Blair Williams, Saleet Jafri, “Methods and Systems for Utilizing Markov-chain Monte-carlo simulations” (patent pending)
5. Niall Macquaide, **Hoang-Trong Minh Tuan**, Jun-ichi Hotta, Wouter Sempels, Ilse Lenaerts, Patricia Holemans, Johan Hofkens, M. Saleet Jafri, Rik Willems, Karin R. Sipido, “Functional consequences of RyR cluster fragmentation and redistribution in persistent atrial fibrillation” (2014) (in preparation)
6. **Hoang-Trong Minh Tuan**, Aman Ullah, Brian Hagen, John Lederer, Saleet Jafri “Three dimensional computational model for rat ventricular myocyte to study Ca²⁺ wave” (in preparation)

7. Aman Ullah*, **Hoang-Trong Minh Tuan***, John Lederer, Saleet Jafri “A small number of cells is sufficient to trigger a cardiac arrhythmia: stochastic computational studies” (in preparation) [* = equal contribution]
8. **Hoang-Trong Minh Tuan**, Saleet Jafri, “Ultra-fast Markov-chain Monte carlo method: a novel algorithm to study Ca^{2+} dynamics” (in preparation)